

Study of fluid flows around a stretching cylinder



By

Abid Majeed

Reg. No. 10-FBAS/PHDMA/S12

**Department of Mathematics and Statistics
Faculty of Basic and Applied Sciences
International Islamic University
Islamabad, Pakistan
2017**

Study of fluid flows around a stretching cylinder



By
Abid Majeed

Supervised By
Dr. Tariq Javed

**Department of Mathematics and Statistics
Faculty of Basic and Applied Sciences
International Islamic University
Islamabad, Pakistan
2017**

Study of fluid flows around a stretching cylinder

A dissertation
submitted in the partial fulfillment of the
requirements for the degree of
DOCTOR OF PHILOSOPHY
IN
MATHEMATICS

Submitted By
Abid Majeed

Supervised By
Dr. Tariq Javed

Department of Mathematics and Statistics
Faculty of Basic and Applied Sciences
International Islamic University
Islamabad, Pakistan
2017

Author's Declaration

I, Abid Majeed Reg. No. 10-FBAS/PHDMA/S12 hereby state that my Ph.D. thesis titled: Study of fluid flows around a stretching cylinder is my own work and has not been submitted previously by me for taking any degree from this university (International Islamic University, Sector H-10, Islamabad, Pakistan) or anywhere else in the country/world.

At any time if my statement is found to be incorrect even after my doctorate, the university has the right to withdraw my Ph.D. degree.

Name of Student: (Abid Majeed)

Reg. No. 10-FBAS/PHDMA/S12

Dated: 02-03-2017

Plagiarism Undertaking

I solemnly declare that research work presented in the thesis titled: **Study of fluid flows around a stretching cylinder** is solely my research work with no significant contribution from any other person. Small contribution/help wherever taken has been duly acknowledged and that complete thesis has been written by me. I understand the zero tolerance policy of the HEC and University, **International Islamic University, Sector H-10, Islamabad, Pakistan** towards plagiarism. Therefore, I as an Author of the above titled thesis declare that no portion of my thesis has been plagiarized and any material used as reference is properly referred/cited. I undertake that if I am found guilty of any formal plagiarism in the above titled thesis even after award of Ph.D. degree, the university reserves the rights to withdraw/revoke my Ph.D. degree and that HEC and the University has the right to publish my name on the HEC/University Website on which names of students are placed who submitted plagiarized thesis.

Student/Author Signature: _____

Name: **(Abid Majeed)**

Certificate of Approval

This is to certify that the research work presented in this thesis, entitled: Study of Fluid Flows around a Stretching Cylinder was conducted by Mr. Abid Majeed, Reg. No. 10-FBAS/PHDMA/S12 under the supervision of Dr. Tariq Javed no part of this thesis has been submitted anywhere else for any other degree. This thesis is submitted to the Department of Mathematics & Statistics, FBAS, IIU, Islamabad in partial fulfillment of the requirements for the degree of Doctor of Philosophy in Mathematics, Department of Mathematics & Statistics, Faculty of Basic & Applied Science, International Islamic University, Sector H-10, Islamabad, Pakistan.

Student Name: Abid Majeed

Signatures: majeed

Examination Committee:

a) **External Examiner 1:**

Name/Designation/Office Address)

Signatures: Tasawar Hayat

Prof. Dr. Tasawar Hayat

Professor of Mathematics, QAU, Islamabad.

b) **External Examiner 2:**

Name/Designation/Office Address)

Signatures: Mazhar Hussain

Dr. Mazhar Hussain

Associate Professor of Mathematics, NUCES (FAST), Islamabad.

c) **Internal Examiner:**

Name/Designation/Office Address)

Signatures: Nasir Ali

Dr. Nasir Ali

Associate Professor of Mathematics, IIU, Islamabad.

Supervisor Name:

Dr. Tariq Javed

Signatures: Tariq Javed

Name of Dean/HOD

Prof. Dr. Muhammad Arshad Zia

Signatures: M. Arshad Zia

Dedicated

To

My Father, Abdul Majeed (late)

Preface

The study of the flow field produced by the moving surface in a quiescent fluid is relevant to several practical applications in the field of metallurgy and chemical engineering. The stretching causes the entrainment of the adjacent fluid, which in turn affects the resistance and the solidification of the extruded material. The properties of the final product depend to a great extent on the stretching and rate of cooling which governed by the structure of the boundary layer near the moving strips. It is therefore, the basic objective of this dissertation is to study of boundary layer flows over a geometry of stretching cylinder in this dissertation. We analyzed the effects of stretching cylinder as hyperbolic function with entropy generation, unsteady oscillatory wall temperature with mixed convection over a stretching cylinder, Casson fluid with partial slip and prescribed surface heat flux over a stretching cylinder, hydromagnetic heat transfer analysis of stagnation point flow of Walters-B fluid over a stretching cylinder, Soret and Dufour effects over second grade fluid flow over a stretching cylinder with linear radiation and finally the non-linear radiation effects on Maxwell fluid flow over a stretching cylinder with heat generation/absorption. The governing non-linear partial/ordinary differential equations are solved by means of very efficient numerical techniques such as Keller box method, spectral method and shooting method.

Chapter 1, includes some basic knowledge about the fluid flows, fundamental laws of fluid dynamics, relevant mathematical models, a comprehensive literature survey and numerical methods which are used in this dissertation.

In chapter 2, a comprehensive study of entropy generation over hyperbolic stretching cylinder is performed. The numerical results are obtained for the partial differential equations by an implicit finite difference scheme known as Keller box method. The influence of emerging parameters namely: curvature parameter and Prandtl number on velocity and temperature profiles, skin friction coefficient and the Nusselt number are presented through graphs. Moreover, the effects of different physical parameters on entropy generation number and Bejan number are also drawn graphically. The contents of this chapter are published in **Alexandria Engineering Journal (2016) 55, 1333–1339**.

In chapter 3, heat transfer analysis is presented for mixed convection stagnation point flow over a vertical stretching cylinder with sinusoidal wall temperature. The governing partial differential equations are converted into dimensionless form by using suitable transformations. For the numerical solution of the reduced dimensionless partial differential equations,

the Keller Box method is applied. To show the accuracy and authenticity of our results, a comparison is made with literature for some special cases. The skin friction and Nusselt number are plotted against unsteadiness parameter and amplitude of surface temperature oscillations against time. It is appeared that as the values of amplitude of surface temperature oscillations drop, the amplitude of oscillations in skin friction and Nusselt number also drops. These observations are published in **Revista Mexicana de Fisica 62 (2016) 290–298**.

Chapter 4 is focused to analyze the combine effects of partial slip and prescribed surface heat flux when the fluid is moving due to stretching cylinder. A very moderate and powerful technique namely Chebyshev Spectral Newton Iterative Scheme is used to determine the solution of the present mathematical model. The accuracy and convergence of the method is ensure through comparison of its computed results with that of Keller box method through tables. The CPU time is calculated for both schemes. It is observed that CSNIS is efficient, less time consuming, stable and rapid convergent. Involved physical parameters, namely: the slip parameter, Casson fluid parameter, curvature parameter and Prandtl number are utilized to control the fluid movement and temperature distribution. The results show that the fluid velocity and the skin friction coefficient on the stretching cylinder are strongly influenced by the slip parameter. These results are published in **Alexandria Engineering Journal (2015) 54, 1029–1036**.

In chapter 5, heat transfer analysis of two dimensional hydromagnetic flow of Walters-B fluid towards stagnation point region over a stretching cylinder is discussed. Importantly, the Walters-B model is transformed into cylindrical coordinates and then solved by Spectral Quasi Linearization Method (SQLM). The flow and heat transfer characteristics are analyzed through governing parameters representing curvature of cylinder, velocity ratio parameter, magnetic parameter and Weissenberg number. It is noticed that the curvature of the cylinder has significant impact on the velocity and temperature. Magnetic field applied externally suppress the bulk motion and alters the momentum boundary layer thickness. The drag and heat transfer rate on the surface of cylinder are examined through skin friction and heat transfer coefficients. Furthermore, streamlines are drawn to see the flow pattern. The contents of this chapter are published in **Canadian Journal of Physics. 94: 1-9 (2016) dx.doi.org/10.1139/cjp–2015–0511**.

Chapter 6 presents the analysis of Soret and Dufour effects on two dimensional flow of second grade fluid due to stretching cylinder. It is further assumed that the flow is subjected to

thermal radiation, which is another aspect of the study. Mathematical model for second grade fluid in cylindrical coordinate system is developed in terms of nonlinear partial differential equations and solved numerically. It is predicted that the simultaneous increase in Dufour and Soret numbers help to enhance both the temperature and concentration in the boundary layer region around the cylinder. Also concurrent occurring of increasing Dufour and decreasing Soret numbers on heat transfer and mass transfer rates have opposite effects. Moreover, the radiation effects are elaborated through the variation of effective Prandtl number. The increase in effective Prandtl number results in decrease of the temperature of the fluid. These observations are published in **Journal of Molecular Liquids 221 (2016) 878–884**.

In chapter 7, we presented the combined effects of linear and non-linear Rosseland thermal radiations on Maxwell nanofluid flow due to stretching cylinder. Notable difference in the heat transfer enhancement can be observed through temperature profiles and tables of Nusselt number. From the computation, it is concluded that the nonlinear radiation enhances significant heat transfer rate at the surface of cylinder as compared to the linear or in the case of absence of radiation effects. The presented results are submitted for possible publication in **Canadian Journal of Physics**.

Contents

Nomenclature	3
Chapter 1	6
Introduction	6
1.1 Fluid mechanics	6
1.2 Governing Equations	6
1.2.1 Newtonian fluids	7
1.2.2 Non-Newtonian fluid	8
1.2.3 Buongiorno nanofluid model	10
1.3 Literature Survey	10
1.4 Methodology	17
Chapter 2	20
Heat transfer analysis of fluid flow over a hyperbolic stretching cylinder	20
2.1 Problem formulation	20
2.2 Entropy Generation Analysis	23
2.3 Solution Methodology	24
2.4 Results and Discussion	32
2.5 Conclusions	42
Chapter 3	43
Mixed convection stagnation point flow over a stretching cylinder	43
3.1 Problem formulation	43
3.2 Solution Methodology	45
3.3 Results and Discussion	51
3.4 Conclusions	61
Chapter 4	62
Heat transfer analysis of Casson fluid flow due to stretching cylinder	62
4.1 Problem formulation	62

4.2	Numerical Scheme	64
4.3	Results and Discussion	65
4.4	Conclusions	75
Chapter 5	76
Heat transfer analysis of Walters-B fluid flow over a stretching cylinder	76
5.1	Formulation of problem.....	76
5.2	Numerical procedure	79
5.3	Results and discussion.....	81
5.4	Conclusions	96
Chapter 6	97
Study of non-Newtonian fluid flow due to stretching cylinder under Soret and Dufour effects	97
6.1	Mathematical formulation	97
6.2	Solution methodology	101
6.3	Results and Discussion	108
6.4	Conclusions	116
Chapter 7	117
Study of Maxwell nanofluid flow around a stretching cylinder	117
7.1	Mathematical Formulation	117
7.2	Numerical Scheme	119
7.3	Results and discussion.....	120
7.4	Conclusion.....	128
References:	129

Nomenclature

a, c	Dimensionless constants
a/c	Velocity ratio parameter
A^*	Coefficient of space dependent heat source/sink
B^*	Coefficient of temperature dependent heat source/sink
B	Velocity slip parameter
C	Concentration of fluid
B_0	Magnetic field strength
Be	Bejan number
$Be\Omega^{*-1}$	Group parameter
b	Body force
c_p	Specific heat at constant pressure
C_f	Skin friction coefficient
D_B	Brownian diffusion coefficient
De	Maxwell fluid parameter, Deborah number
D_T	Thermophoretic diffusion coefficient
E_0	Characteristic entropy generation
E_G	Local volumetric rate of entropy generation
f	Dimensionless stream function
k	Thermal conductivity of fluid
K	Viscoelastic parameter
l	Reference length
M	Magnetic parameter
N_b	Brownian motion parameter
N_E^*	Entropy generation number
N_t	Thermophoresis parameter
n^*	Temperature index or exponent
Nu_z	Local Nusselt number
p	Pressure
Pr	Prandtl number
q'''	Non-uniform heat sink/source

q_r	Radiative heat flux
q_w	Surface heat flux
r	Radial coordinate
R^*	Radius of cylinder
Re_ξ, Re_z	Local Reynolds number
Rd	Radiation parameter
S	Suction/injection parameter
Sc	Schmidt number
T	Fluid temperature
\bar{t}	Time
T_w	Temperature at the surface of cylinder
T_∞	Ambient fluid temperature
u_w	Mass flux velocity
u	Radial velocity component
v	Axial velocity component
\mathbf{V}	Velocity vector
V_e	Free stream velocity
V_w	Stretching velocity of cylinder
We	Weissenberg number
z	Axial coordinate

Greek symbols

α	Thermal diffusivity
β	Unsteady parameter
β^*	Casson parameter
β_t	Thermal expansion coefficient
γ	Curvature parameter
ϵ	Amplitude of temperature oscillations
η	Similarity variable
θ	Dimensionless temperature
θ_w	Surface heating parameter
λ	Mixed convection parameter
λ_1	Material relaxation time

μ	Dynamic viscosity
ν	Kinematic viscosity
ρ	Density
σ	Electrical conductivity
τ_w	Surface shear stress
ϕ	Dimensionless concentration
ψ	Stream function
Ω^*	Irreversibility ratio

Subscripts

w	Condition at the surface
∞	Condition at the Infinity
η	Differentiation

Superscripts

$'$	Differentiation w.r.t η
-----	------------------------------

Chapter 1

Introduction

In this chapter, the preliminaries of fluid mechanics and its fundamental laws (White 2006), some mathematical fluid models (Harris 1977), numerical methods (Na 1979; Cebeci and Bradshaw 1985) which are directly related to present research and a comprehensive literature survey beginning from stretching sheet to stretching cylinder is presented for knowledge and understanding of readers. For this purpose, current chapter is arranged as follows:

1.1 Fluid mechanics

Fluid mechanics deals with transport processes in the molecule–dependent motion of fluids (fluid dynamics) or the fluids at rest (fluid statics). Fluid mechanics is a special branch of continuous mechanics which deals with the relationship between forces, motion and statics conditions in a continuous material. In fact, fluid mechanics exists everywhere in our life both in natural or practical environment and we all as a human being observer that this branch of science has significant importance. Life is not possible on earth without flows of fluids and even natural and technical growth would not be possible. Therefore, flows have vital importance like blood in the vessels which transport the essential nutrients to the cells by mass flows, where chemical reactions take place and produces energy for the body, flows of the food chain in flora and fauna, flows into lakes, rivers, and seas, transport of clouds through winds, and a multitude of other examples in natural and technological environments

1.2 Governing Equations

All the physical phenomena are in some way related to the laws of fluid mechanics. Application of these laws to fluid flow problems in terms of mathematics, results in the form of partial differential equations such as continuity equation, the equations of motion or the Navier-Stokes equations, the energy equation and concentration equation. For incompressible fluid flow these laws are given as below:

Continuity equation:

$$\nabla \cdot \mathbf{V} = 0, \quad (1.1)$$

Momentum equation:

$$\rho \frac{d\mathbf{V}}{dt} = \nabla \cdot \boldsymbol{\tau} + \rho \mathbf{f}, \quad (1.2)$$

Energy equation:

$$\rho c_p \frac{dT}{dt} = \nabla \cdot (k \nabla T) + \boldsymbol{\tau} : \nabla \mathbf{V}, \quad (1.3)$$

Concentration equation:

$$\rho c_p \frac{dC}{dt} = \nabla \cdot (D_m \nabla C). \quad (1.4)$$

The above equations are in general form where, $\boldsymbol{\tau}$ is the Cauchy stress tensor and \mathbf{S} is called as the extra stress tensor which represents characteristics and rheological behavior of the considered fluid. d/dt represents material derivative, ρ is the density of the fluid, \mathbf{V} represents the velocity field, ∇ is the gradient operator, \mathbf{f} represents the body forces, c_p represents the specific heat, T represents the fluid temperature, k represents the thermal conductivity of the fluid, C represents the species concentration for mass transfer, $\boldsymbol{\tau} : \nabla \mathbf{V}$ represents the scalar viscous dissipation, D_m represents mass diffusivity in species concentration. In cylindrical coordinate system

$$\begin{aligned} \nabla &= \hat{r} \frac{\partial}{\partial r} + \hat{\theta} \frac{1}{r} \frac{\partial}{\partial \theta} + \hat{z} \frac{\partial}{\partial z} \\ \frac{D}{Dt} &= \frac{\partial}{\partial t} + u_r \frac{\partial}{\partial r} + u_\theta \frac{1}{r} \frac{\partial}{\partial \theta} + u_z \frac{\partial}{\partial z} \end{aligned} \quad (1.5)$$

1.2.1 Newtonian fluids

Fluids in which shear stress is proportional to strain rate (or velocity gradient) are commonly categorized as Newtonian fluids. Mathematically for unidirectional flow it can be written as

$$\boldsymbol{\tau} \propto \frac{du}{dy}, \quad (1.6)$$

or

$$\boldsymbol{\tau} = \mu \frac{du}{dy}, \quad (1.7)$$

where μ is the constant of proportionality known as dynamic viscosity. For Newtonian fluid, stress tensor is given by

$$\boldsymbol{\tau} = -p\mathbf{I} + \mathbf{S}, \quad (1.8)$$

in which p represents the pressure, \mathbf{I} is the unit tensor and the extra stress tensor \mathbf{S} has the following form

$$\mathbf{S} = \mu \mathbf{A}_1, \quad (1.9)$$

where \mathbf{A}_1 represents the first Rivlin-Ericksen tensor and is defined as

$$\begin{aligned} \mathbf{A}_1 &= \nabla \mathbf{V} + (\nabla \mathbf{V})^{tranpose} \\ &= \begin{pmatrix} \frac{\partial u_r}{\partial r} & \frac{\partial u_\theta}{\partial r} & \frac{\partial u_z}{\partial r} \\ \frac{1}{r} \frac{\partial u_r}{\partial \theta} - \frac{u_\theta}{r} & \frac{1}{r} \frac{\partial u_\theta}{\partial \theta} + \frac{u_r}{r} & \frac{1}{r} \frac{\partial u_z}{\partial \theta} \\ \frac{\partial u_r}{\partial z} & \frac{\partial u_\theta}{\partial z} & \frac{\partial u_z}{\partial z} \end{pmatrix} \\ &\quad + \begin{pmatrix} \frac{\partial u_r}{\partial r} & \frac{\partial u_\theta}{\partial r} & \frac{\partial u_z}{\partial r} \\ \frac{1}{r} \frac{\partial u_r}{\partial \theta} - \frac{u_\theta}{r} & \frac{1}{r} \frac{\partial u_\theta}{\partial \theta} + \frac{u_r}{r} & \frac{1}{r} \frac{\partial u_z}{\partial \theta} \\ \frac{\partial u_r}{\partial z} & \frac{\partial u_\theta}{\partial z} & \frac{\partial u_z}{\partial z} \end{pmatrix}^{tranpose} \\ &= \begin{pmatrix} 2 \frac{\partial u_r}{\partial r} & \frac{\partial u_\theta}{\partial r} + \frac{1}{r} \frac{\partial u_r}{\partial \theta} - \frac{u_\theta}{r} & \frac{\partial u_z}{\partial r} + \frac{\partial u_r}{\partial z} \\ \frac{\partial u_\theta}{\partial r} + \frac{1}{r} \frac{\partial u_r}{\partial \theta} - \frac{u_\theta}{r} & 2 \left(\frac{1}{r} \frac{\partial u_\theta}{\partial \theta} + \frac{u_r}{r} \right) & \frac{1}{r} \frac{\partial u_z}{\partial \theta} + \frac{\partial u_\theta}{\partial z} \\ \frac{\partial u_z}{\partial r} + \frac{\partial u_r}{\partial z} & \frac{1}{r} \frac{\partial u_z}{\partial \theta} + \frac{\partial u_\theta}{\partial z} & 2 \frac{\partial u_z}{\partial z} \end{pmatrix} \end{aligned} \quad (1.10)$$

1.2.2 Non-Newtonian fluid

In non-Newtonian fluids, shear stress and deformation rate are not linearly proportional to each other. In practice, most of the fluids behave like a non-Newtonian fluid. These fluids have numerous important industrial applications in chemical, civil, metallurgical engineering, and mining. The common examples of non-Newtonian fluids in our daily life are toothpaste, paints, honey, blood etc. Many mathematical models have been proposed to exhibit the nature of fluids in different circumstances till to date. Some of them which are related to the work in this thesis are as follows

Casson fluid model

The constitutive equation of a Casson fluid model may be defined in simplified form as

$$\begin{aligned} \sqrt{\tau^*} &= (\mu \dot{\gamma}^*)^{\frac{1}{2}} + \sqrt{\tau_0^*} \quad \text{for } \tau^* \geq \tau_0^* \\ \dot{\gamma}^* &= 0, \text{ for } \tau^* \leq \tau_0^*, \end{aligned} \quad (1.11)$$

where τ^* is the shear stress, μ is the viscosity coefficient of Casson fluid, $\dot{\gamma}^*$ is the rate of shear strain and τ_0^* is the yield stress.

Walters-B fluid model

The constitutive equation for Walters-B fluid is given by

$$\mathbf{S} = 2\eta_0\mathbf{A}_1 - 2k_0 \frac{D\mathbf{A}_1}{Dt}. \quad (1.12)$$

Here η_0 is the viscosity at zero shear rate, k_0 is the elasticity of the fluid and $D\mathbf{A}_1/Dt$ is defined as

$$\frac{D\mathbf{A}_1}{Dt} = \frac{\partial \mathbf{A}_1}{\partial t} + (\mathbf{V} \cdot \nabla)\mathbf{A}_1 - \mathbf{A}_1 \cdot (\nabla \mathbf{V}) - (\nabla \mathbf{V})^{transpose} \cdot \mathbf{A}_1 \quad (1.13)$$

Second grade fluid model

The equation which exhibits the rheological behavior of second grade fluid model is as follows

$$\mathbf{S} = \mu\mathbf{A}_1 + \alpha_1\mathbf{A}_2 + \alpha_2\mathbf{A}_1^2, \quad (1.14)$$

where \mathbf{A}_2 is the second Rivlin-Erickson tensor which has the following relation

$$\mathbf{A}_2 = \frac{d\mathbf{A}_1}{dt} + \mathbf{A}_1 \cdot (\nabla \mathbf{V}) + (\nabla \mathbf{V})^{transpose} \cdot \mathbf{A}_1. \quad (1.15)$$

The thermodynamic constraints for stable second grade fluid model are

$$\mu \geq 0, \alpha_1 > 0, \alpha_1 + \alpha_2 = 0. \quad (1.16)$$

Maxwell fluid model

The Maxwell fluid model obeys the following constitutive equation

$$\mathbf{S} + \lambda_1 \frac{D\mathbf{S}}{Dt} = \mu\mathbf{A}_1, \quad (1.17)$$

where, λ_1 represent the time relaxation of the material, which is duration of the time over which significant stress persists after termination of deformation. The derivative D/Dt for the vector and tensor can be define in the following forms:

For a contravariant vector:

$$\frac{D\mathbf{S}}{Dt} = \frac{d\mathbf{S}}{dt} - (\mathbf{V}\nabla)\mathbf{S} \quad (1.18)$$

For a contravariant tensor of rank 2:

$$\frac{D\mathbf{S}}{Dt} = \frac{d\mathbf{S}}{dt} - (\mathbf{V}\nabla)\mathbf{S} - \mathbf{S}(\mathbf{V}\nabla)^{transpose} \quad (1.19)$$

1.2.3 Buongiorno nanofluid model

In the present investigation, Buongiorno model is utilized to study the Brownian motion and thermophoresis effects in the fluid flow. The energy and transport equations of nanoparticles which represent the Buongiorno nanofluid model is as follows

$$\frac{DT}{Dt} = \alpha \nabla^2 T + \tau^* \left(D_B \nabla C \cdot \nabla T + D_T \frac{\nabla T \cdot \nabla T}{T_\infty} \right)$$

(1.20)

and

$$\frac{DC}{Dt} = D_B \nabla^2 C + \left(\frac{D_T}{T_\infty} \right) \nabla^2 T.$$

Here $\tau^* = (\rho c)_p / (\rho c)_f$ is the ratio of effective heat capacity of nanoparticle material and the base fluid, D_B and D_T are the Brownian and thermophoretic diffusion coefficients and T_∞ is the ambient temperature of the fluid.

1.3 Literature Survey

The study of boundary layer flow and heat transfer over stretching surfaces received remarkable attentions due to its numerous applications in modern industrial and engineering practices. The attributes of the end product are greatly reliant on stretching and the rate of heat transfer at the final stage of processing. Due to this real-world importance, interest developed among scientists and engineers to comprehend this phenomenon. Common examples are the extrusion of metals in cooling liquids, food, plastic products, the reprocessing of material in the molten state under high temperature. During the phase of the manufacturing process, the material undergoes elongation (stretching) with cooling process. Such types of processes are very handy in the production of plastic and metallic made apparatus, such as cutting hardware tools, electronic components in computers, rolling and annealing of copper wires, etc. In many engineering and industrial applications, the cooling of a solid surface is a primary tool for minimizing the boundary layer. Due to these useful and realistic impacts, the problem of cooling of solid moving surfaces has turned out to be an area of concern for scientists and engineers. The dynamics of the boundary layer flow over a stretching surface started from the pioneering work of Crane (1970). He solved a primary problem of two-dimensional boundary layer flow of stretching sheet which is extensively used in polymer extrusion industry and assumed that sheet is linearly stretching with a distance from a fixed point. Some representative studies over stretching sheet were presented by Gupta and Gupta (1977), Chakrabarti and Gupta (1979), Dutta and Roy (1985),

Chen and Char (1988), Anderson et al. (1992). They provided their analysis by introducing suction and blowing, heat transfer with uniform heat flux, heat transfer with suction and blowing, MHD and heat transfer, analysis of power-law fluids, respectively. Abundant of literature is available over stretching sheet problem with different geometries, physical situations, fluid models and boundary conditions and will be discussed in proceeding paragraphs where necessary.

For last several years, the analysis of fluid flow and heat transfer over elongating surfaces has gained growing interest of engineers and scientists due to its wide application in industry like wire drawing, cooling of metallic sheets, piping and casting system as well as metal spinning and many others. In this context, Wang (1988) was the first who considered the steady flow caused by elongating cylinder immersed in fluid. After a long time, Ishak et al. (2008, 2009) reestablish the pioneering work of Wang (1988). They produced a numerical solution of laminar boundary layer flow, uniform suction blowing and MHD effects over stretching cylinder in an ambient fluid. Heat transfer in magnetohydrodynamics flow due to a stretching cylinder is analytically tackled by Joneidi et al. (2010) using HAM. Bachok and Ishak (2010) studied the effects of prescribed heat flux at the surface of stretching cylinder. They reported that the heat transfer rate is enhanced over a curved surface as compared to that of flat surface. Time dependent flow over an expanding stretching cylinder is investigated by Fang et al. (2011) and they declared that the reverse flow phenomenon exists due to expansion of cylinder. Munawar et al. (2012) presented thermal analysis over an oscillatory stretching cylinder and they concluded that entropy generation magnifies due to oscillatory motion of cylinder. The effect of magnetic field over horizontal stretching cylinder in the presence of source/sink with suction/injection is studied by Elbashbeshy (2012). Abbas et al. (2013) explained the MHD radiation effects with porous medium over a stretching cylinder. Especially in last few years a lot of research problems have been modeled on the analysis of flow and heat transfer over stretching cylinder. Mukhopadhyay (2011, 2012); Mukhopadhyay and Gorla (2013) and Mukhopadhyay (2013) considered a chemical solute transfer, mixed convection in porous media, and MHD slip flow along a stretching cylinder respectively. Fang and Yao (2011); Vajravelu et al. (2012); Wang 2012; Lok et al. (2012); Butt and Ali (2014) have considered viscous swirling flow, axisymmetric MHD flow, natural convection flow, axisymmetric mixed connection stagnation point flow, and entropy analysis of magnetohydrodynamics flow over stretching cylinder, respectively. Entropy generation is the quantification of thermodynamics irreversibility which exists in all types of heat transfer phenomenon and therefore suffer an efficiency loss. It is need of

the hour to calculate the extent of irreversibility occurring in the dynamical system. Also search is on for finding the ways to minimize the rate of entropy generation so that maximum utilization of available energy is possible. Due to this fundamental importance, **Chapter 2** of the thesis is optimized with the inclusion of entropy generation analysis. In this context, the studies (Matin et al. 2012; Butt et al. 2013; Noghrehabadi et al 2013; Rashidi et al. 2014; Dalir et al. 2015) are quite useful to explore many aspects of entropy generation.

The stagnation point encounters highest pressure, enhancement of heat transfer and rate of mass deposition. Some practical examples are cooling of electronic devices by fans, the aerodynamics of plastic sheets, cooling of nuclear reactors during emergency shutdown, heat exchangers placed in a low velocity environment, solar central receivers exposed to wind current and many others (Burde 1995). Due to these aspects, the study of stagnation point flow and heat transfer has attracted many researchers and engineers. Hiemenz (1911) initiated the study of two-dimensional stagnation point flow over a stationary flat plate. He transformed the Navier-Stokes equations into ordinary differential equations by using similarity transformations and provided the exact solution of the nonlinear differential equations. Homann (1936) extended this work to three-dimensional problem of axisymmetric stagnation-point flow. Schlichting and Bussmann (1943) provided numerical solution of Hiemenz problem. Eckert (1942) also extended the Heimenz flow by incorporating heat transfer rate in the stagnation point flow. Ariel (1994) obtained the analytical solution by introducing suction in flow field. Stagnation point flow over moving surfaces is also significant in practical purposes including paper production, the spinning of fibres, glass blowing, continuous metal casting, manufacturing of sheeting material through extrusion process especially in the polymer extrusion in a melt spinning process, aerodynamic extrusion of plastic sheets etc. Chiam (1994) investigated the two-dimensional stagnation point flow of a viscous fluid over a linear stretching surface. He considered the situation where stretching velocity is equal to straining (free stream) velocity and concluded that no boundary layer exists in this case. Contrary to the Chiam (1994), Mahapatra and Gupta (2001, 2002) analysed the effects of Magnetohydrodynamics and heat transfer respectively, in the region of stagnation point flow towards a stretching surface. They show that the boundary layer is formed when $a/c > 1$ (ratio of straining to stretching velocity) and inverted boundary layer is emerging when $a/c < 1$. Unsteady analysis of flow over a stretching sheet is reported by Nazar et al. (2004). Recently, (Mustafa et al. 2011; Sharma and Singh 2009; Javed et al. 2015) reported the investigations on the stagnation point flow over linear and non-linear stretching sheets in different aspects. In all aforementioned

studies, the investigations on stagnation point flow are carried out with temporally constant surface condition and the transient development of flow and heat transfer over stretching cylinder is not extensively studied. Merkin and Pop (2000) stated that the value of surface temperature does not remain constant, it often fluctuates about some mean value. The influence of time dependent oscillations in surface conditions has received very little attention to date. Therefore, **Chapter 3** is aimed to study the unsteady mixed convection stagnation point flow over a stretching cylinder with sinusoidal time dependent wall temperature.

In literature survey, it is discovered that in general the flow field obeys the no-slip condition. However, certain physical situations exist which do not cope with the said conditions. That is why, the replacement of no-slip boundary condition with slip boundary condition is highly essential. The role of the slip condition is vital in shear skin, hysteresis effects and spurts. Slip comes into existence when the fluid is a rarefied gas (Sharipov and Seleznev 1998), or in the case when it is particulate like blood, foam, emulsion or suspension (Yoshimura and Prud'homme 1988). Slip also arises on hydrophobic surfaces, especially in micro and nano-fluidics (Eijkel 2007). Recently, Mukhopadhyay (2011, 2013), Mukhopadhyay and Gorla (2013) studied the effects of partial slip with MHD, chemically reactive solute transfer, and slip effects with heat transfer over a stretching cylinder respectively. Hayat et al. (2014) have investigated the effect of heat and mass transfer in flow along a vertical stretching cylinder with slip condition. A rheological model of Casson fluid pronounces the properties of many polymers over a wide range of shear rates. Various experimental studies on blood flow with varying haematocrits, anticoagulants, temperature, etc. offer the behavior of blood as a Casson fluid. Recently, in this connection some useful research achievements are made for Casson fluid flow over a stretching cylinder (Hayat et al. 2014, 2015; Hussain et al. 2015). Following this trend in **Chapter 4**, we present the analysis over stretching cylinder considering non-Newtonian Casson model with partial slip and prescribed heat flux using the Chebyshev Spectral Newton Iterative Scheme (CSNIS).

The study of non-Newtonian fluid flow has gained significant attention of researchers in past few decades, due to extensive applications in polymer processing industry, developing process of artificial film, artificial fibres, discharge of industrial waste, drawing of plastic film and wire, thermal oil recovery, glass fibre and paper production, food processing, crystal growing and liquid films in condensation process. Recently, some non-Newtonian fluid models namely Viscoelastic, Jaffrey and Powel-Eyring are formulated in cylindrical coordinates by Hayat et al. (2015). Keeping an eye on previous literature, many non-

Newtonian fluid models are still to be discussed with geometry of stretching cylinder. Among these, the behavior of Walter-B fluid model for a stretching cylinder has not been disclosed yet. Walters and Beard (1964) have presented this viscoelastic fluid model which predicts the flow behavior of various polymer solutions including hydrocarbons, industrial liquids like paints and several others. Therefore, in **Chapter 5**, the study of magnetohydrodynamics flow of Walters-B fluid near a stagnation point over a stretching cylinder is presented. The interest for considering the Walters- B fluid stem from its physical and mathematical significance. The Walters-B fluid model is a subclass of viscoelastic fluids, which can predict the memory effects and secondly, considering it electrically conducting fluid ensures the control of both velocity and boundary layer thickness. It is widely applicable to estimate the flow situations in biotechnology and chemical industrial problems. From a mathematical perspective, its constitutive equation of motion generates one order higher equation than that of Newtonian and others non-Newtonian fluids with no extra boundary conditions available. Secondly, it contains singularity at the starting point of the domain. Therefore, when fluid is slightly viscoelastic, there is no possibility of obtaining a numerical solution by any standard integration scheme like Runge-Kutta method etc. Due to these reasons, we focus our attention to discuss the flow of a Walters B fluid over a stretching cylinder.

In many chemical processes, it is frequently happening that the transport of heat in the flow cannot be coupled with the transport of mass in the system. The simultaneous occurrence of coupled heat and mass transfer in moving fluid generates cross diffusion. As a result, the concentration of one species undergoes a constant change to other species in the chemical process. These changes in heat and mass transfer can be termed as Dufour effects: heat flux incorporated by concentration gradients or diffusion-thermo and Soret effects: mass flux produced by temperature gradient or thermal-diffusion (Soret 1880). Soret and Dufour effects have their importance in physical situations like reactions in reactors, hydrology, petrology and geosciences (Benano-Melly et al. 2001). In this context, the main contributions in many fields were carried out by many researchers including Eckert and Drake (1972), Dursunkaya and Worek (1992), Kafoussias and Williams (1995), Postelnicu (2007, 2010) etc. In last decade, Tsai and Huang (2009) considered the Hiemenz flow to observe the Soret and Dufour effects over a stretching surface through an isotropic porous medium. Their analysis is based on percentage differences of effects on emerging parameters which makes the readers understand their findings quite comfortably. Diffusion-thermo and thermo-diffusion effects are examined by Hayat et al. (2014) on peristaltic

motion of nanofluid. They also outlined the thermophoresis effects and Brownian motion of nanoparticles. The computations were carried out by NDSolve command through Mathematica software in the study. Mahdy and Ahmed (2015) modelled the hydromagnetic Marangoni boundary layer flow problem and numerically simulated. For this purpose, they used R-K scheme to solve the reduced first order differential equations and missing initial conditions were calculated by means of Newton's iterative method. In their study, the coupled effects of Soret on mass transfer and Dufour on heat transfer were observed. The study of Soret and Dufour effects on stretching cylinder was encountered by Ramazan et al. (2015). Some other physical phenomenon like chemical reaction, heat generation/absorption and magnetic field effects were also investigated by them in the study. The physical model was converted into ODE's and then solved by a semi analytical method commonly known as a homotopy analysis method. Mahdy (2015) investigated the diffusion-thermo and thermo-diffusion effects on the Casson fluid flow over the porous stretching cylinder. He found the numerical solution of the modelled problem by shooting algorithm. Ali et al. (2016) simulated the Soret and Dufour influence over an oscillatory stretching sheet. They assumed the flow of electrically conducting fluid under orthogonally imposed magnetic field over the porous sheet. They predicted that the larger values of Soret number results in higher concentrations. Reddy and Chamkha (2016) considered the hydromagnetic flow and heat transfer in nanofluid with Soret and Dufour effects. In addition, thermal radiation, chemical reaction and heat generation/absorption were also discussed in the study. They used finite element method for the sake of highly convergent solution. For this purpose, firstly, they transformed the whole domain into finite subintervals and the solution is computed on each subinterval. Secondly, these intervals were connected to find the global solution for the whole domain.

In manufacturing processes at high temperature, the mode of heat transfer like thermal radiation plays a vital role and become essentially important and therefore cannot be ignored. These situations include re-entry of vehicles, internal combustion engine, and gas cooled nuclear reactors pointed to the radiation transfer in these processes. Hossain and Takhar (1996) explored the radiation effects on the flow along vertical surface. They reduced the governing equation into dimensionless non-similar form and used finite difference scheme to obtain the results in the form of local Nusselt and Local shear stresses. Hossain et al. (1999) also considered the free convective radiative flow along a permeable vertical plate. The reduced dimensionless non-similar equations are solved analytically and numerically by using justified techniques. Raptis et al. (2004) numerically computed the

influence of radiation on electrically conducting fluid. Mahmoud (2007) discussed the radiation effects on micropolar fluid flowing due to stretching sheet and especially considered the variable thermal conductivity effects within the fluid. Similarly, few other recent studies can be found at (Abbas et al. 2013; Siddiqa et al. 2013; Javed et al. 2015). Therefor **Chapter 6** is devoted to the study of Soret and Dufour effects of non-Newtonian fluid flowing due to stretching cylinder with radiation effects.

The study of non-Newtonian fluid has got considerable attention due to their elastic, shear thinning, shear thickening, thixotropic and Rheopectic behavior. Different non-Newtonian fluid models have been developed experimentally to predict such flow behavior of the fluids. Maxwell fluid model is one of the non-Newtonian fluid model which predict the elastic behavior of the fluid. This fluid model can be explained for large elastic effects. However, it does not predict the creep accurately. In last decade, the study on Maxwell fluid model has been considered by many researchers. Wenchang and Mingyu (2002) have considered the constitutive equations of Maxwell fluid model to study the viscoelastic behavior of the fluid. They assumed no slip condition and the fluid near the surface is moving with the surface velocity. They found the exact solution by using discrete inverse transform method and concluded that for small time, viscoelastic effects are more significant as compared to the larger time. Vieru et al. (2008) studied the time dependent flow of fractional Maxwell fluid. The flow is considered between two side walls which are perpendicular to the moving plat. They found exact solution of obtained differential equations by using Fourier and Laplace transform method. Hayat et al. (2008) have considered magnetic effect on the Maxwell fluid flow through a porous medium in a rotating frame. They establish the time dependent analytical solution by means of Fourier sine transform method for different emerging dimensionless parameters. Hayat and Qasim (2010) considered the hydromagnetic flow and heat transfer of Maxwell fluid influenced by radiation and joule heating. They presented the series solution and estimated the values of local Nusselt and Sherwood numbers. The reduction in boundary layer is reported with the increment of Deborah number, and velocity is observed as decreasing function of magnetic parameter. The time dependent two-dimensional heat transfer analysis of Maxwell fluid flow over a stretching surface was studied by Mukhopadhyay (2012). The several other studies of Maxwell fluid are reported in the literature and few of them are Hayat et al. (2012), Prasad et al. (2012), Javed et al. (2016).

In the recent era, the development in the field of nanofluid technology have gained the attention by the scientists and engineers owing to their vast industrial applications. The

enhancement in thermal conductivity of the fluids is always a major issue for the researchers and many attempts have been made for enhancement in the thermal conductivity of the fluids. Masuda (1993) reported that the saturation of ultra-fine particles in base fluid surprisingly enhance the fluid thermal conductivity. In later study, Choi (1995) named these fluids as nanofluids. Buongiorno (2006) studied the thermal conductivity of the nanofluids. He concluded that two slip mechanisms, Brownian diffusion and thermophoresis are important factor in the study of nanofluids. Kuznetsov and Nield (2010) studied the effect of nanoparticles on free convection flow using Buongiorno model. In this study, Brownian and thermophoresis effects are investigated and they concluded that nanoparticles enhance the thermal conductivity of the weak conducting fluids. In another study Kuznetsov and Nield (2011) considered double-diffusive convection flow. In this article, temperature and nanoparticles concentration at the wall is assumed constant and found that the reduced Nusselt number drop due to increase in thermophoresis and Brownian motion parameter. More recently, Sheikholeslami (2015) has calculated the effective thermal conductivity and viscosity of the nanofluid by Koo–Kleinstreuer–Li (KKL) model and provided the nanofluid heat transfer analysis over the cylinder. Dhanai et al. (2016) investigated mixed convection nanofluid flow over inclined cylinder. They utilized Buongiorno's model of nanofluid and found dual solutions of the problem under thermal slip effects in presence of MHD. Major contribution in the area of nanofluid was discussed later by many researchers, few of them are Abolbashari et al. (2014), Rashidi et al. (2014), Ghaffari et al. (2015), Garoosi et al. (2015), Mustafa et al. (2016). In **Chapter 7**, the idea of combined effects of linear and non-linear Rosseland thermal radiations on Maxwell nanofluid flow due to stretching cylinder is presented.

1.4 Methodology

In the present study, attention is given to utilize the numerical techniques like implicit finite difference scheme (Keller Box method), Spectral Quasi Linearization Method, Chebyshev Spectral Newton Iterative Scheme and Shooting method. Previously, different analytical method like homotopy analysis method, and Adomian decomposition method with Pade approximations have been vastly used by the researchers. Although these methods are efficient but are time consuming. Since, we will be dealing with very complex equations in this study; we prefer to use these numerical techniques instead of analytical methods. These techniques are briefly summarized in the following paragraphs.

1.4.1 Keller Box method

This finite difference scheme developed by Cebeci and Bradshaw (1984) is very famous due to its accuracy and rapid convergence. The steps through which the solution is computed are as follows:

Step-1: The system of nonlinear differential equations are reduced to the system of first order differential equations.

Step-2: Functions and their derivatives are replaced by mean value and central difference formula respectively. Which results in a system of nonlinear algebraic difference equation for the number of unknown equals to the number of difference equations and number of boundary conditions.

Step-3: The nonlinear terms are linearized by means of Newton's quasi-linearization technique.

Step-4: The obtained system of linear algebraic equations is then solved by block tri-diagonal scheme.

We have successfully employed the Keller Box method for the problems in **Chapter 2, 3** and **6**. The detailed implementation of this method on PDE's is given in **Chapter 2, 3** and on ODE's is given in **Chapter 6**.

1.4.2 Spectral Collocation method

Spectral methods (Canuto et al. 2000) are rated amongst the best methods for the numerical simulations of PDE's. The basic theme of this method is to represent the solution of the nonlinear equation as a sum of certain trial/basis functions with unknown coefficients to be found subject to satisfy the differential equation at different nodes and boundary condition. The main feature of the Spectral methods is to form orthogonal systems of basis function (or trial functions) with some weight function. It is noted that every single choice of trial functions forms a different Spectral approximation. Like "trigonometric polynomials" are chosen for bounded periodic problems, "Legendre and Chebyshev polynomials" are for non-periodic problems, "Laguerre polynomials" are for problems developed on the half line, and "Hermite polynomials" are for problems on the whole line. Spectral methods cannot be implemented directly for nonlinear differential equations. To tackle this situation nonlinear differential equations are first transformed to linear form by a suitable technique like Quasi-linearization method, Newton's iterative scheme or successive linearization scheme etc. In this study we utilized the Newton's iterative scheme and Quasi-linearization method for

linearization process. The detail for these schemes can be seen in forthcoming **Chapter 4** and **Chapter 5** as **Spectral Quasi-Linearization Method** and **Chebyshev Spectral Newton Iterative Scheme**.

1.4.3 Shooting method

The solution of BVP's related to the fluid flow can be obtained by any numerical technique. Shooting method is one of the oldest efficient numerical techniques in which BVP firstly reduced to system of first order IVP. Secondly, the missing initial conditions at initial point are assumed as an initial guess. This reduced IVP is then solved by an efficient fourth order Runge-Kutta integrator. The accuracy of the obtained solution is then checked by comparing the given values at the terminal point. If the accuracy is not up to the desired level, then we repeat the whole process by assuming a new initial guess and continue in this way until required level of accuracy is achieved. In spite of randomly choosing the missing condition after every iteration, we used Newton Raphson's technique to calculate the missing conditions for speedy process. This procedure is implemented over a particular problem in **Chapter 7**.

Chapter 2

Heat transfer analysis of fluid flow over a hyperbolic stretching cylinder

In this chapter, heat transfer analysis and entropy generation of boundary layer flow of an incompressible viscous fluid over a hyperbolic stretching cylinder is presented. The governing nonlinear partial differential equations are normalized by using similarity transformations. The numerical results are found for the obtained partial differential equations by an implicit finite difference scheme known by Keller box method. A comparison of the computed results for the flat plate case is given and developed code is validated. The influence of emerging parameters namely: curvature parameter and Prandtl number on velocity and temperature profiles, skin friction coefficient and the Nusselt number are presented through graphs. It is seen that curvature parameter has dominant effect on the flow and heat transfer characteristics. The increment in the curvature of the hyperbolic stretching cylinder increase both the momentum and thermal boundary layer thicknesses. Also skin friction coefficient at the surface of cylinder decreases but Nusselt number shows opposite results. Temperature distribution is decreasing by increasing Prandtl number. Similarly, the effects of different physical parameters on entropy generation number and Bejan number are shown graphically and discussed it detailed in results and discussion section.

2.1 Problem formulation

Let us consider the two-dimensional steady incompressible flow of a Newtonian fluid over a hyperbolic stretching circular cylinder of fixed radius R^* . It is assumed that the cylinder is being stretched hyperbolically with the function $\cosh(z/l)$. The geometry of the problem is shown in Figure 2.1 with cylindrical coordinates are taken into account. The basic equations which governs the flow and heat transfer phenomena will take the form as

$$\frac{\partial(ru)}{\partial r} + \frac{\partial(rv)}{\partial z} = 0, \quad (2.1)$$

$$u \frac{\partial v}{\partial r} + v \frac{\partial v}{\partial z} = \nu \frac{\partial}{\partial r} \left(r \frac{\partial v}{\partial r} \right), \quad (2.2)$$

$$u \frac{\partial T}{\partial r} + v \frac{\partial T}{\partial z} = \alpha \frac{\partial}{\partial r} \left(r \frac{\partial T}{\partial r} \right), \quad (2.3)$$

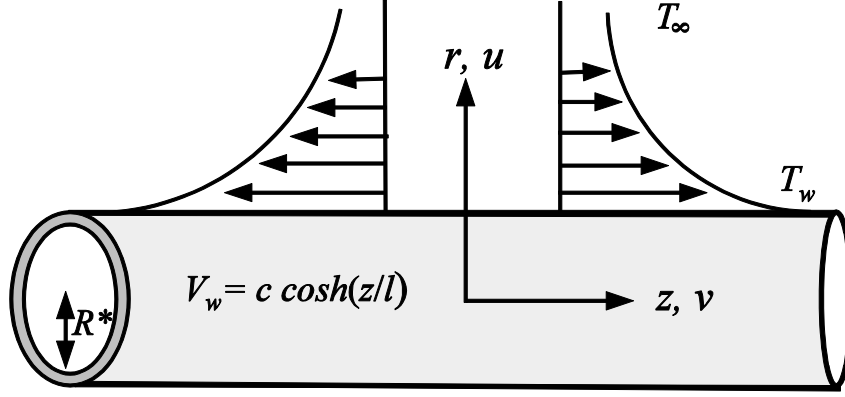


Figure 2.1: Geometry of the flow.

where u and v are the velocity components along r and z directions, T be the temperature of the fluid within boundary layer, $\alpha = k/\rho c_p$ be the thermal diffusivity of the fluid. The boundary conditions relevant to velocity and temperature profile are:

$$\begin{aligned} v(r, z) = V_w(z), u(r, z) = 0, T = T_w = T_\infty + AV_w(z) \text{ at } r = R^*, \\ v(r, z) \rightarrow 0, T = T_\infty \text{ as } r \rightarrow \infty, \end{aligned} \quad (2.4)$$

where A is a constant. Now introducing the dimensionless transformation

$$\begin{aligned} \xi = \frac{z}{l}, \quad \eta = \frac{r^2 - R^{*2}}{2R^*z} Re_z^{1/2}, \quad \psi = \nu R^* Re_z^{1/2} f(\eta, \xi), \\ \theta(\eta, \xi) = \frac{T - T_\infty}{T_w - T_\infty} \end{aligned} \quad (2.5)$$

Where ξ and η are dimensionless variables, $Re_z = zV_w/\nu$ is local Reynolds number, T_w is temperature at surface of cylinder, T_∞ is atmospheric temperature and stream function ψ is the non-dimensional function defined through usual relationship as

$$u = -\frac{\partial \psi}{r \partial z}, \quad v = \frac{\partial \psi}{r \partial r}, \quad (2.6)$$

which satisfies the continuity Eq. (2.1). Upon using Eqs. (2.5) and (2.6) into equations (2.2) and (2.3), we arrived at following transformed equations

$$\begin{aligned} \frac{r^2}{R^{*2}} f_{\eta\eta\eta} + \frac{2\xi}{R^* Re_\xi^{1/2}} f_{\eta\eta} + \left(1 - \frac{\xi}{Re_\xi} \frac{dRe_\xi}{d\xi}\right) f_\eta^2 + \frac{\xi}{2Re_\xi} \frac{dRe_\xi}{d\xi} f f_{\eta\eta} \\ = \xi \left(f_\eta \frac{\partial f_\eta}{\partial \xi} - f_{\eta\eta} \frac{\partial f}{\partial \xi} \right), \end{aligned} \quad (2.7)$$

$$\frac{1}{Pr} \left(\frac{r^2}{R^{*2}} \theta_{\eta\eta} + \frac{2\xi}{R^* Re_\xi^{1/2}} \theta_\eta \right) - \xi (\tanh \xi \theta) f_\eta + \frac{\xi}{2Re_\xi} \frac{dRe_\xi}{d\xi} f \theta_\eta \quad (2.8)$$

$$= \xi \left(f_\eta \frac{\partial \theta}{\partial \xi} - \theta_\eta \frac{\partial f}{\partial \xi} \right),$$

where $Re_\xi = \xi l V_w / \nu$ (local Reynold number) and $Pr = \nu / \alpha$ (Prandtl number). Using the stretching velocity $V_w = c \cosh \xi$ in equations (2.7) and (2.8), we get

$$\left(1 + 2\eta\gamma \sqrt{\frac{\xi}{\cosh \xi}} \right) f_{\eta\eta\eta} + 2\gamma \sqrt{\frac{\xi}{\cosh \xi}} f_{\eta\eta} + \frac{1}{2} (1 + \xi \tanh \xi) f f_{\eta\eta} - \quad (2.9)$$

$$(\xi \tanh \xi) f_\eta^2 = \xi \left(f_\eta \frac{\partial f_\eta}{\partial \xi} - f_{\eta\eta} \frac{\partial f}{\partial \xi} \right),$$

$$\frac{1}{Pr} \left(1 + 2\eta\gamma \sqrt{\frac{\xi}{\cosh \xi}} \right) \theta_{\eta\eta} + \frac{2\gamma}{Pr} \sqrt{\frac{\xi}{\cosh \xi}} \theta_\eta + \frac{1}{2} (1 + \xi \tanh \xi) f \theta_\eta - \quad (2.10)$$

$$\xi \tanh \xi \theta f_\eta = \xi \left(f_\eta \frac{\partial \theta}{\partial \xi} - \theta_\eta \frac{\partial f}{\partial \xi} \right).$$

The boundary conditions take the new form as

$$f(0, \xi) = 0, f_\eta(0, \xi) = 1, \theta(0, \xi) = 1, f_\eta(\infty, \xi) = 0, \theta(\infty, \xi) = 0, \quad (2.11)$$

where $\gamma = \nu l / c R^{*2}$ is curvature parameter and subscripts in Eqs. (2.9)–(2.11) indicate the differentiation with respect to η . If we consider $\xi \rightarrow 0$ and $\gamma = 0$ then Eq. (2.9) reduces to the Sakiadis flow equation (Rees and Pop 1995) given by

$$f_{\eta\eta\eta} + \frac{1}{2} f f_{\eta\eta} = 0 \quad (2.12)$$

with boundary conditions

$$f(0) = 0, f_\eta(0) = 1, f_\eta(\infty) = 0. \quad (2.13)$$

The formula for skin friction coefficient and heat transfer coefficient (Nusselt number) having physical significance are given as

$$C_f = \frac{\tau_w}{\sigma V_w^2}, \quad Nu = \frac{\xi q_w}{k(T_w - T_\infty)}, \quad (2.14)$$

where τ_w be the wall shear stress and q_w is the constant heat flux from the surface, which are formulated as

$$\tau_w = \mu \left(\frac{\partial v}{\partial r} \right)_{r=R^*}, \quad q_w = -k \left(\frac{\partial T}{\partial r} \right)_{r=R^*}. \quad (2.15)$$

Upon using Eq. (2.15) into Eq. (2.14), the expressions in Eq. (2.14) become

$$C_f Re_\xi^{1/2} = f_{\eta\eta}(0, \xi), \quad Nu Re_\xi^{-1/2} = -\theta_\eta(0, \xi). \quad (2.16)$$

2.2 Entropy Generation Analysis

Using the boundary layer assumptions, the local volumetric rate of entropy generation E_G for a Newtonian fluid over a hyperbolic stretching cylinder is defined as:

$$E_G = \underbrace{\frac{k}{T_\infty^2} \left(\frac{\partial T}{\partial r} \right)^2}_{\text{heat transfer}} + \underbrace{\frac{\mu}{T_\infty} \left(\frac{\partial v}{\partial r} \right)^2}_{\text{fluid friction}} \quad (2.17)$$

The first component on the R.H.S of the above equation is for entropy effects due to heat transfer and remaining component is for entropy effects due to fluid friction. After using results of Eq. (2.5) in Eq. (2.17), the following form is obtained

$$E_G = \frac{kr^2(T_w - T_\infty)^2 (\cosh \xi) \left(\theta_\eta(\eta, \xi) \right)^2}{lR^{*2}T_\infty^2 \xi \nu} + \frac{r^2 \mu (\cosh \xi)^3 \left(f_{\eta\eta}(\eta, \xi) \right)^2}{lR^{*2}T_\infty \xi \nu}. \quad (2.18)$$

Above equation can be written as

$$N_E^* = \frac{E_G}{E_0} = \frac{(1 + 2\gamma\eta)Re_l \cosh \xi}{\xi} \left[\left(\theta_\eta(\eta, \xi) \right)^2 + \frac{Br (\cosh \xi)^2 \left(f_{\eta\eta}(\eta, \xi) \right)^2}{\Omega^*} \right], \quad (2.19)$$

where N_E^* is the entropy generation number which is the ratio of local volumetric rate of entropy generation E_G and characteristic entropy generation rate $E_0 = k(T_w - T_\infty)^2 / l^2 T_\infty^2$, $Re_l = cl/\nu$, is the Reynolds number, $Br = \mu c^2 / k(T_w - T_\infty)$ is the Brinkman number, and $\Omega^* = (T_w - T_\infty) / T_\infty$ is the dimensionless temperature difference and the ratio $Be\Omega^{*-1}$ is group parameter. The Bejan number Be serves as a substitute of entropy generation parameter and it represents the ratio between the entropy generation due to heat transfer and the total entropy generation due to combined heat transfer and fluid friction. It is defined by

$$Be = \frac{N_{EHT}}{N_{EHT} + N_{EFF}}. \quad (2.20)$$

Here

$$N_{EHT} = \frac{(1 + 2\gamma\eta)Re_l \cosh \xi}{\xi} \left(\theta_\eta(\eta, \xi) \right)^2, \quad (2.21)$$

$$N_{EFF} = \frac{(1 + 2\gamma\eta)Re_l \cosh^3 \xi}{\xi} Be\Omega^{*-1} \left(f_{\eta\eta}(\eta, \xi) \right)^2, \quad (2.22)$$

where the subscripts EHT and EFF stands for entropy due to heat transfer and entropy due to fluid friction. Bejan number Be can also be presented as $Be = 1/(1 + \Omega^*)$, where $\Omega^* = N_{EFF}/N_{EHT}$ is called irreversibility ratio.

2.3 Solution Methodology

To solve nonlinear system of partial differential equations (2.9) and (2.10) subject to the set of boundary conditions (2.11), we employed a very accurate and efficient implicit finite difference method commonly known as Keller box method (Cebeci and Bradshaw 1984).

For present problem, the solution is obtained through following procedure.

The Eqs. (2.9) and (2.10) are written in terms of system of first order differential equations.

Setting

$$f_\eta = p, \quad p_\eta = q, \quad \theta_\eta = U \quad (2.23)$$

in differential equations (2.9, 2.10) and boundary conditions (2.11) results as:

$$\begin{aligned} \left(1 + 2\eta\gamma \sqrt{\frac{\xi}{\cosh \xi}}\right) q_\eta + 2\gamma \sqrt{\frac{\xi}{\cosh \xi}} q + \frac{1}{2}(1 + \xi \tanh \xi) f q - (\xi \tanh \xi) p^2 \\ = \xi \left(p \frac{\partial p}{\partial \xi} - q \frac{\partial f}{\partial \xi}\right), \end{aligned} \quad (2.24)$$

$$\begin{aligned} \frac{1}{Pr} \left(1 + 2\eta\gamma \sqrt{\frac{\xi}{\cosh \xi}}\right) U_\eta + \frac{2\gamma}{Pr} \sqrt{\frac{\xi}{\cosh \xi}} U + \frac{1}{2}(1 + \xi \tanh \xi) f U \\ - \xi (\tanh \xi) \theta p = \xi \left(f_\eta \frac{\partial s}{\partial \xi} - U \frac{\partial f}{\partial \xi}\right), \end{aligned} \quad (2.25)$$

and new form of boundary conditions will be

$$\begin{aligned} f(0, \xi) = 0, \quad p(0, \xi) = 1, \quad \theta(0, \xi) = 1 \\ f(\infty, \xi) = 0, \quad \theta(\infty, \xi) = 0. \end{aligned} \quad (2.26)$$

A net on the plane (ξ, η) is defined as

$$\begin{aligned} \eta_0 = 0, \eta_j = \eta_{j-1} + \Delta\eta, \eta_j = \eta_\infty, j = 1, 2, \dots, J-1, \\ \xi^0 = 0, \xi^n = \xi^{n-1} + \Delta\xi, n = 1, 2, \dots, \end{aligned} \quad (2.27)$$

where n and j are positive integers, $\Delta\eta$ and $\Delta\xi$ are widths of meshing variables on (ξ, η) plane. The approximate quantities of functions f, p, q, θ , and U at the net point (ξ^n, η_j) are known as net functions whose derivatives in η and ξ -directions are replaced by the central difference formulae and functions itself are replaced by average centered at the midpoint $(\xi^{n-1/2}, \eta_{j-1/2})$ defined as

$$\frac{\partial}{\partial \xi} () \Big|_j^{n-1/2} = \frac{1}{\Delta\xi} (f_j^n - f_j^{n-1}), \quad \frac{\partial}{\partial \eta} () \Big|_{j-1/2}^n = \frac{1}{\Delta\eta} (f_j^n - f_{j-1}^n),$$

and

$$f_j^{n-1/2} = \frac{1}{2}(f_j^n + f_j^{n-1}), \quad f_{j-1/2}^n = \frac{1}{2}(f_j^n + f_{j-1}^n).$$

After discretization, the system of nonlinear partial differential Eqs. (2.24) and (2.25) are converted to the system of difference equations with equal number of unknowns as:

$$\begin{aligned} & \left(1 + (\eta_j + \eta_{j-1})\gamma \sqrt{\frac{\xi^{n-\frac{1}{2}}}{\cosh \xi^{n-\frac{1}{2}}}} \right) \frac{q_j^n - q_{j-1}^n}{\Delta \eta} + 2\gamma \sqrt{\frac{\xi^{n-\frac{1}{2}}}{\cosh \xi^{n-\frac{1}{2}}}} \frac{q_j^n + q_{j-1}^n}{2} \\ & + \frac{1}{8} \left(1 + \xi^{n-\frac{1}{2}} \tanh \xi^{n-\frac{1}{2}} \right) \left(\frac{f_j^n + f_{j-1}^n}{2} \right) \left(\frac{q_j^n + q_{j-1}^n}{2} \right) \\ & - \frac{1}{4} \left(\xi^{n-\frac{1}{2}} \tanh \xi^{n-\frac{1}{2}} \right) (p_j^n + p_{j-1}^n)^2 \\ & - \frac{\xi^{n-\frac{1}{2}}}{4\Delta \xi} \{ (p_j^n + p_{j-1}^n)^2 - (q_j^n + q_{j-1}^n)(f_j^n + f_{j-1}^n) \\ & + (q_j^n + q_{j-1}^n)(f_j^{n-1} + f_{j-1}^{n-1}) - (q_j^{n-1} + q_{j-1}^{n-1})(f_j^n + f_{j-1}^n) \} \\ & = r_{j-\frac{1}{2}}^{n-1}, \end{aligned} \quad (2.28)$$

$$\begin{aligned} & \frac{1}{Pr} \left(1 + (\eta_j + \eta_{j-1})\gamma \sqrt{\frac{\xi^{n-\frac{1}{2}}}{\cosh \xi^{n-\frac{1}{2}}}} \right) \frac{U_j^n + U_{j-1}^n}{2} + \frac{\gamma}{Pr} \sqrt{\frac{\xi^{n-\frac{1}{2}}}{\cosh \xi^{n-\frac{1}{2}}}} (U_j^n + U_{j-1}^n) \\ & + \frac{1}{8} \left(1 + \xi^{n-\frac{1}{2}} \tanh \xi^{n-\frac{1}{2}} \right) \left(\frac{f_j^n + f_{j-1}^n}{2} \right) \left(\frac{U_j^n + U_{j-1}^n}{2} \right) \\ & - \xi^{n-\frac{1}{2}} \left(\tanh \xi^{n-\frac{1}{2}} \right) \left(\frac{\theta_j^n + \theta_{j-1}^n}{2} \right) \left(\frac{p_j^n + p_{j-1}^n}{2} \right) \\ & - \frac{\xi^{n-\frac{1}{2}}}{4\Delta \xi} [(p_j^n + p_{j-1}^n + p_j^{n-1} + p_{j-1}^{n-1})(Q_j^n + Q_{j-1}^n) \\ & - (U_j^n + U_{j-1}^n)(f_j^n + f_{j-1}^n - f_j^{n-1} - f_{j-1}^{n-1})] = m_{j-\frac{1}{2}}^{n-1}. \end{aligned} \quad (2.29)$$

$$f_j^n - f_{j-1}^n = \frac{\Delta \eta}{2} (p_j^n + p_{j-1}^n), \quad (2.30)$$

$$p_j^n - p_{j-1}^n = \frac{\Delta \eta}{2} (q_j^n + q_{j-1}^n), \quad (2.31)$$

$$\theta_j^n - \theta_{j-1}^n = \frac{\Delta \eta}{2} (U_j^n + U_{j-1}^n), \quad (2.32)$$

where

$$\begin{aligned}
r_{j-\frac{1}{2}}^{n-1} = & - \left(1 + (\eta_j + \eta_{j-1}) \gamma \sqrt{\frac{\xi^{n-\frac{1}{2}}}{\cosh \xi^{n-\frac{1}{2}}}} \right) \left(\frac{q_j^{n-1} - q_{j-1}^{n-1}}{\Delta \eta} \right) \\
& + 2\gamma \sqrt{\frac{\xi^{n-\frac{1}{2}}}{\cosh \xi^{n-\frac{1}{2}}}} \left(\frac{q_j^{n-1} + q_{j-1}^{n-1}}{2} \right) \\
& + \frac{1}{2} \left(1 + \xi^{n-\frac{1}{2}} \tanh \xi^{n-\frac{1}{2}} \right) \left(\frac{f_j^n + f_{j-1}^n}{2} \right) \left(\frac{q_j^n + q_{j-1}^n}{2} \right) \\
& - \left(\xi^{n-\frac{1}{2}} \tanh \xi^{n-\frac{1}{2}} \right) \left(\frac{p_j^n + p_{j-1}^n}{2} \right)^2 \\
& + \frac{\xi^{n-\frac{1}{2}}}{4\Delta \xi} \left[-(p_j^{n-1} + p_{j-1}^{n-1})^2 + (q_j^{n-1} + q_{j-1}^{n-1})(f_j^{n-1} + f_{j-1}^{n-1}) \right],
\end{aligned} \tag{2.33}$$

$$\begin{aligned}
m_{j-\frac{1}{2}}^{n-1} = & - \frac{1}{Pr} \left(1 + (\eta_j + \eta_{j-1}) \gamma \sqrt{\frac{\xi^{n-\frac{1}{2}}}{\cosh \xi^{n-\frac{1}{2}}}} \right) \left(\frac{U_j^{n-1} + U_{j-1}^{n-1}}{2} \right) \\
& - \frac{\gamma}{Pr} \sqrt{\frac{\xi^{n-\frac{1}{2}}}{\cosh \xi^{n-\frac{1}{2}}}} (U_j^{n-1} + U_{j-1}^{n-1}) \\
& - \frac{1}{8} \left(1 + \xi^{n-\frac{1}{2}} \tanh \xi^{n-\frac{1}{2}} \right) (f_j^{n-1} + f_{j-1}^{n-1})(U_j^{n-1} + U_{j-1}^{n-1}) \\
& + \xi^{n-\frac{1}{2}} \left(\tanh \xi^{n-\frac{1}{2}} \right) \left(\frac{\theta_j^{n-1} + \theta_{j-1}^{n-1}}{2} \right) \left(\frac{p_j^{n-1} + p_{j-1}^{n-1}}{2} \right) \\
& + \frac{\xi^{n-\frac{1}{2}}}{4\Delta \xi} \left[-(p_j^n + p_{j-1}^n + p_j^{n-1} + p_{j-1}^{n-1})(\theta_j^{n-1} + \theta_{j-1}^{n-1}) \right. \\
& \left. - (U_j^{n-1} + U_{j-1}^{n-1})(f_j^n + f_{j-1}^n - f_j^{n-1} - f_{j-1}^{n-1}) \right],
\end{aligned} \tag{2.34}$$

The boundary conditions (2.26) become

$$f_0^n = 0, p_0^n = 1, \theta_0^n = 1, p_j^n = \theta_j^n = 0 \tag{2.35}$$

The nonlinear algebraic Eqs. (2.28) and (2.29) are linearized by using Newton method by introducing $(i+1)^{th}$ iterates as

$$(f_j^n)^{(i+1)} = (f_j^n)^{(i)} + (\delta f_j^n)^{(i)} \tag{2.36}$$

and similarly for all other dependent (unknown) variables. Here $(f_j^n)^{(i)}$ is known for $0 < j \leq J$ as an initial guess and $(\delta f_j^n)^{(i)}$ is unknown. After using the Newton linearization process and neglecting the terms containing square and higher order of $(\delta f_j^n)^{(i)}, (\delta p_j^n)^{(i)}, (\delta q_j^n)^{(i)}, (\delta \theta_j^n)^{(i)}$ and $(\delta U_j^n)^{(i)}$, the system of linear algebraic equations is obtained which are as follows:

$$\begin{aligned} \delta f_j^n - \delta f_{j-1}^n - \frac{\Delta \eta}{2}(\delta p_j^n + \delta p_{j-1}^n) &= (r_1)_j, \\ (a_1)_j \delta f_{j-1}^n + (a_2)_j \delta f_j^n + (a_3)_j \delta p_{j-1}^n + (a_4)_j \delta p_j^n + (a_5)_j \delta q_{j-1}^n + (a_6)_j \delta q_j^n &= (r_2)_j, \\ (a_7)_j \delta \theta_{j-1}^n + (a_8)_j \delta \theta_j^n + (a_9)_j \delta U_{j-1}^n + (a_{10})_j \delta U_j^n &= (r_3)_j, \\ \delta p_j^n - \delta p_{j-1}^n - \frac{\Delta \eta}{2}(\delta q_j^n + \delta q_{j-1}^n) &= (r_4)_j, \\ \delta \theta_j^n - \delta \theta_{j-1}^n - \frac{\Delta \eta}{2}(\delta U_j^n + \delta U_{j-1}^n) &= (r_5)_j, \end{aligned}$$

The boundary conditions (2.35) take the form as

$$\delta f_0^n = 0, \delta p_0^n = 1, \delta \theta_0^n = 1, \delta p_J^n = \delta \theta_J^n = 0.$$

Finally, the above system of linear algebraic equations with boundary conditions will be written in matrix vector form. The coefficients of unknown functions $\delta f_j^n, \delta p_j^n, \delta q_j^n, \delta \theta_0^n, \delta U_j^n$ in momentum and energy equations and non-homogeneous parts are given as:

Coefficient of momentum equation

Coefficient of δf_{j-1}^n :

$$(a_1)_j = \frac{1}{8} \left(1 + \xi^{n-\frac{1}{2}} \tanh \xi^{n-\frac{1}{2}} \right) (q_j^n + q_{j-1}^n) + \frac{\xi^{n-\frac{1}{2}}}{4\Delta \xi} [(q_j^n + q_{j-1}^n) + (q_j^{n-1} + q_{j-1}^{n-1})]$$

Coefficient of δf_j^n :

$$(a_2)_j = \frac{1}{8} \left(1 + \xi^{n-\frac{1}{2}} \tanh \xi^{n-\frac{1}{2}} \right) (q_j^n + q_{j-1}^n) + \frac{\xi^{n-\frac{1}{2}}}{4\Delta \xi} [q_j^n + q_{j-1}^n + q_j^{n-1} + q_{j-1}^{n-1}]$$

Coefficient of δp_{j-1}^n :

$$(a_3)_j = -\frac{1}{2} \left(\xi^{n-\frac{1}{2}} \tanh \xi^{n-\frac{1}{2}} \right) (p_j^n + p_{j-1}^n) - \frac{\xi^{n-\frac{1}{2}}}{2\Delta \xi} (p_j^n + p_{j-1}^n)$$

Coefficient of δp_j^n :

$$(a_4)_j = -\frac{1}{2} \left(\xi^{n-\frac{1}{2}} \tanh \xi^{n-\frac{1}{2}} \right) (p_j^n + p_{j-1}^n) - \frac{\xi^{n-\frac{1}{2}}}{2\Delta \xi} (p_j^n + p_{j-1}^n)$$

Coefficient of δq_{j-1}^n :

$$\begin{aligned}
(a_5)_j = & -\frac{1}{\Delta\eta} \left[1 + (\eta_j + \eta_{j-1})\gamma \sqrt{\frac{\xi^{n-\frac{1}{2}}}{\cosh\xi^{n-\frac{1}{2}}}} \right] + \gamma \sqrt{\frac{\xi^{n-\frac{1}{2}}}{\cosh\xi^{n-\frac{1}{2}}}} \\
& + \frac{1}{8} \left(1 + \xi^{n-\frac{1}{2}} \tanh\xi^{n-\frac{1}{2}} \right) (f_j^n + f_{j-1}^n) \\
& + \frac{\xi^{n-\frac{1}{2}}}{2\Delta\xi} [(f_j^n + f_{j-1}^n) + (f_j^{n-1} + f_{j-1}^{n-1})]
\end{aligned}$$

Coefficient of δq_j^n :

$$\begin{aligned}
(a_6)_j = & \frac{1}{\Delta\eta} \left[1 + (\eta_j + \eta_{j-1})\gamma \sqrt{\frac{\xi^{n-\frac{1}{2}}}{\cosh\xi^{n-\frac{1}{2}}}} \right] \\
& + \gamma \sqrt{\frac{\xi^{n-\frac{1}{2}}}{\cosh\xi^{n-\frac{1}{2}}}} + \frac{1}{8} \left(1 + \xi^{n-\frac{1}{2}} \tanh\xi^{n-\frac{1}{2}} \right) (f_j^n + f_{j-1}^n) \\
& + \frac{\xi^{n-\frac{1}{2}}}{2\Delta\xi} [(f_j^n + f_{j-1}^n) + (f_j^{n-1} + f_{j-1}^{n-1})]
\end{aligned}$$

Coefficient of energy equation

Coefficient of $\delta\theta_{j-1}^n$:

$$(a_7)_j = -\frac{1}{4} \xi^{n-\frac{1}{2}} \left(\tanh\xi^{n-\frac{1}{2}} \right) (p_j^n + p_{j-1}^n) - \frac{\xi^{n-\frac{1}{2}}}{4\Delta\xi} [p_j^n + p_{j-1}^n + p_j^{n-1} + p_{j-1}^{n-1}]$$

Coefficient of $\delta\theta_j^n$:

$$(a_8)_j = -\frac{1}{4} \xi^{n-\frac{1}{2}} \left(\tanh\xi^{n-\frac{1}{2}} \right) (p_j^n + p_{j-1}^n) - \frac{\xi^{n-\frac{1}{2}}}{4\Delta\xi} [p_j^n + p_{j-1}^n + p_j^{n-1} + p_{j-1}^{n-1}]$$

Coefficient of δU_{j-1}^n :

$$\begin{aligned}
(a_9)_j = & \frac{1}{Pr} \left(1 + (\eta_j + \eta_{j-1})\gamma \sqrt{\frac{\xi^{n-\frac{1}{2}}}{\cosh\xi^{n-\frac{1}{2}}}} \right) + \frac{\gamma}{Pr} \sqrt{\frac{\xi^{n-\frac{1}{2}}}{\cosh\xi^{n-\frac{1}{2}}}} \\
& + \frac{1}{8} \left(1 + \xi^{n-\frac{1}{2}} \tanh\xi^{n-\frac{1}{2}} \right) (f_j^n + f_{j-1}^n)
\end{aligned}$$

Coefficient of δU_j^n :

$$(a_{10})_j = \frac{1}{Pr} \left(1 + (\eta_j + \eta_{j-1})\gamma \sqrt{\frac{\xi^{n-\frac{1}{2}}}{\cosh\xi^{n-\frac{1}{2}}}} \right) + \frac{\gamma}{Pr} \sqrt{\frac{\xi^{n-\frac{1}{2}}}{\cosh\xi^{n-\frac{1}{2}}}} +$$

$$\frac{1}{8} \left(1 + \xi^{n-\frac{1}{2}} \tanh \xi^{n-\frac{1}{2}} \right) (f_j^n + f_{j-1}^n)$$

Non-homogeneous terms

$$(r_1)_j = (f_{j-1}^n - f_j^n) + \frac{\Delta \eta}{2} (p_j^n + p_{j-1}^n),$$

$$\begin{aligned} (r_2)_j = & - \left[1 + (\eta_j + \eta_{j-1}) \gamma \sqrt{\frac{\xi^{n-\frac{1}{2}}}{\cosh \xi^{n-\frac{1}{2}}}} \right] \left(\frac{q_j^{n-1} - q_{j-1}^{n-1}}{2} \right) \\ & - 2\gamma \sqrt{\frac{\xi^{n-\frac{1}{2}}}{\cosh \xi^{n-\frac{1}{2}}}} \left(\frac{q_j^{n-1} + q_{j-1}^{n-1}}{2} \right) \\ & - \frac{1}{8} \left(1 + \xi^{n-\frac{1}{2}} \tanh \xi^{n-\frac{1}{2}} \right) (f_j^{n-1} + f_{j-1}^{n-1}) (q_j^{n-1} + q_{j-1}^{n-1}) \\ & + \left(\xi^{n-\frac{1}{2}} \tanh \xi^{n-\frac{1}{2}} \right) \left(\frac{p_j^{n-1} + p_{j-1}^{n-1}}{2} \right)^2 \\ & + \frac{\xi^{n-\frac{1}{2}}}{4\Delta\xi} \left[-(p_j^{n-1} + p_{j-1}^{n-1})^2 + (q_j^{n-1} + q_{j-1}^{n-1})(f_j^{n-1} + f_{j-1}^{n-1}) \right] \\ & - \left[1 + (\eta_j + \eta_{j-1}) \gamma \sqrt{\frac{\xi^{n-\frac{1}{2}}}{\cosh \xi^{n-\frac{1}{2}}}} \right] \left(\frac{q_j^n - q_{j-1}^n}{\Delta \eta} \right) \\ & - \gamma \sqrt{\frac{\xi^{n-\frac{1}{2}}}{\cosh \xi^{n-\frac{1}{2}}}} (q_j^n + q_{j-1}^n) \\ & - \frac{1}{8} \left(1 + \xi^{n-\frac{1}{2}} \tanh \xi^{n-\frac{1}{2}} \right) (f_j^n + f_{j-1}^n) (q_j^n + q_{j-1}^n) + \frac{1}{4} \left(\xi^{n-\frac{1}{2}} \tanh \xi^{n-\frac{1}{2}} \right) \times \\ & (p_j^n + p_{j-1}^n)^2 + \frac{\xi^{n-\frac{1}{2}}}{4\Delta\xi} \{ (p_j^n + p_{j-1}^n)^2 - (q_j^n + q_{j-1}^n)(f_j^n + f_{j-1}^n) \\ & + (q_j^n + q_{j-1}^n)(f_j^{n-1} + f_{j-1}^{n-1}) - (q_j^{n-1} + q_{j-1}^{n-1})(f_j^n + f_{j-1}^n) \}, \\ (r_3)_j = & - \frac{1}{Pr} \left[1 + (\eta_j + \eta_{j-1}) \gamma \sqrt{\frac{\xi^{n-\frac{1}{2}}}{\cosh \xi^{n-\frac{1}{2}}}} \right] \left(\frac{U_j^{n-1} - U_{j-1}^{n-1}}{2} \right) \end{aligned}$$

$$\begin{aligned}
& -\frac{\gamma}{Pr} \sqrt{\frac{\xi^{n-\frac{1}{2}}}{\cosh \xi^{n-\frac{1}{2}}}} \left(\frac{U_j^{n-1} + U_{j-1}^{n-1}}{2} \right) \\
& -\frac{1}{8} \left(1 + \xi^{n-\frac{1}{2}} \tanh \xi^{n-\frac{1}{2}} \right) (f_j^{n-1} + f_{j-1}^{n-1}) (U_j^{n-1} + U_{j-1}^{n-1}) \\
& + \xi^{n-\frac{1}{2}} \left(\tanh \xi^{n-\frac{1}{2}} \right) \left(\frac{\theta_j^{n-1} + \theta_{j-1}^{n-1}}{2} \right) \left(\frac{p_j^{n-1} + p_{j-1}^{n-1}}{2} \right) \\
& -\frac{1}{Pr} \left[1 + (\eta_j + \eta_{j-1}) \gamma \sqrt{\frac{\xi^{n-\frac{1}{2}}}{\cosh \xi^{n-\frac{1}{2}}}} \right] \left(\frac{U_j^n - U_{j-1}^n}{2} \right) - \frac{\gamma}{Pr} \sqrt{\frac{\xi^{n-\frac{1}{2}}}{\cosh \xi^{n-\frac{1}{2}}}} (U_j^n + U_{j-1}^n) \\
& -\frac{1}{8} \left(1 + \xi^{n-\frac{1}{2}} \tanh \xi^{n-\frac{1}{2}} \right) (f_j^n + f_{j-1}^n) (U_j^n + U_{j-1}^n) \\
& + \frac{\xi^{n-\frac{1}{2}}}{4} \left(\tanh \xi^{n-\frac{1}{2}} \right) (\theta_j^n + \theta_{j-1}^n) (p_j^n + p_{j-1}^n) \\
& + \frac{\xi^{n-\frac{1}{2}}}{4\Delta\xi} [(p_j^n + p_{j-1}^n + p_j^{n-1} + p_{j-1}^{n-1})(\theta_j^n + \theta_{j-1}^n - \theta_j^{n-1} - \theta_{j-1}^{n-1}) \\
& - (U_j^n + U_{j-1}^n + U_j^{n-1} + U_{j-1}^{n-1})(f_j^n + f_{j-1}^n - f_j^{n-1} - f_{j-1}^{n-1})], \\
& (r_4)_j = (p_{j-1}^n - p_j^n) + \frac{\Delta\eta}{2} (q_j^n + q_{j-1}^n), \\
& (r_5)_j = (\theta_{j-1}^n - \theta_j^n) + \frac{\Delta\eta}{2} (U_j^n + U_{j-1}^n).
\end{aligned}$$

In matrix form

$$\bar{A}\bar{\delta} = \bar{r}$$

Where

$$\bar{A} = \begin{bmatrix} D_0 & M_0 & & & & & & & \\ L_1 & D_1 & M_1 & & & & & & \\ & L_2 & D_2 & M_2 & & & & & \\ & & \ddots & \ddots & \ddots & & & & \\ & & & \ddots & \ddots & \ddots & & & \\ & & & & \ddots & \ddots & \ddots & & \\ & & & & & L_{J-1} & D_{J-1} & M_{J-1} & \\ & & & & & & L_J & D_J & \end{bmatrix}, \bar{\delta} = \begin{bmatrix} \delta_0 \\ \delta_1 \\ \delta_2 \\ \vdots \\ \vdots \\ \vdots \\ \delta_{J-1} \\ \delta_J \end{bmatrix}, \bar{r} = \begin{bmatrix} r_0 \\ r_1 \\ r_2 \\ \vdots \\ \vdots \\ \vdots \\ r_{J-1} \\ r_J \end{bmatrix} \quad (2.37)$$

and

$$\begin{aligned}
D_0 &= \begin{bmatrix} 1 & 0 & 0 & 0 & 0 \\ 0 & 1 & 0 & 0 & 0 \\ 0 & 0 & 0 & 0 & 0 \\ 0 & -1 & -\frac{h}{2} & 0 & 0 \\ 0 & 0 & 0 & -1 & -\frac{h}{2} \end{bmatrix}, M_j = \begin{bmatrix} 0 & 0 & 0 & 0 & 0 \\ 0 & 0 & 0 & 0 & 0 \\ 0 & 0 & 0 & 0 & 0 \\ 0 & 1 & -\frac{h}{2} & 0 & 0 \\ 0 & 0 & 0 & 1 & -\frac{h}{2} \end{bmatrix}; \quad j = 0, 1, \dots, J-1 \\
L_j &= \begin{bmatrix} -1 & -\frac{h}{2} & 0 & 0 & 0 \\ (a_1)_j & (a_3)_j & (a_5)_j & 0 & 0 \\ 0 & 0 & 0 & (a_7)_j & (a_9)_j \\ 0 & 0 & 0 & 0 & 0 \\ 0 & 0 & 0 & 0 & 0 \end{bmatrix}; \quad j = 1, 2, \dots, J \\
D_j &= \begin{bmatrix} 1 & -\frac{h}{2} & 0 & 0 & 0 \\ (a_2)_j & (a_4)_j & (a_6)_j & 0 & 0 \\ 0 & 0 & 0 & (a_8)_j & (a_{10})_j \\ 0 & -1 & -\frac{h}{2} & 0 & 0 \\ 0 & 0 & 0 & -1 & -\frac{h}{2} \end{bmatrix}; \quad j = 1, 2, \dots, J-1 \\
D_J &= \begin{bmatrix} 1 & -\frac{h}{2} & 0 & 0 & 0 \\ (a_2)_j & (a_4)_j & (a_6)_j & 0 & 0 \\ 0 & 0 & 0 & (a_8)_j & (a_{10})_j \\ 0 & 1 & 0 & 0 & 0 \\ 0 & 0 & 0 & 1 & 0 \end{bmatrix} \\
r_0 &= \begin{bmatrix} 0 \\ 0 \\ 0 \\ (r_4)_1 \\ (r_5)_1 \end{bmatrix}, \quad r_j = \begin{bmatrix} (r_1)_j \\ (r_2)_j \\ (r_3)_j \\ (r_4)_{j+1} \\ (r_5)_{j+1} \end{bmatrix}, \quad r_J = \begin{bmatrix} (r_1)_J \\ (r_2)_J \\ (r_3)_J \\ 0 \\ 0 \end{bmatrix}, \quad \delta_j = \begin{bmatrix} \delta f_j^n \\ \delta p_j^n \\ \delta q_j^n \\ \delta \theta_j^n \\ \delta U_j^n \end{bmatrix}; \quad j = 0, 1, 2, \dots, j; \quad n = 0, 1, \dots, N.
\end{aligned}$$

The resulting matrix vector form is solved by using block-tridiagonal elimination technique, which consists of two sweeps namely forward sweep and backward sweep. The edge of the boundary layer η_∞ and step sizes $\Delta\eta$ and $\Delta\xi$ in η and ξ respectively are set for different range of parameters involved in the problem. The accuracy of the employed numerical scheme has been established through comparison with the known results obtained by Rees and Pop (1995) for flat plate ($\xi = 0$) as shown in Table 2.1. This comparison gives us confidence that the developed code is correct and has achieved the desired level of accuracy. Moreover, the values of $C_f Re_\xi^{1/2}$ and $Nu Re_\xi^{-1/2}$ against different values of parameters γ are given in Table 2.2.

Table 2.1: Comparison with Rees and Pop (1995)

$\xi = 0$	$C_f Re_\xi^{1/2}$	$Nu Re_\xi^{-1/2}$
Ref. (1995)	-0.4439	-0.3509
Present	-0.4439	-0.3509

Table 2.2: Numerical results for $C_f Re_\xi^{1/2}$ and $Nu Re_\xi^{-1/2}$ at different γ when $Pr = 0.7$ at $\xi = 0.5$.

γ	$C_f Re_\xi^{1/2}$	$Nu Re_\xi^{-1/2}$
0	-0.55387	0.41012
0.5	-0.71911	0.60043
1	-0.88994	0.78894
1.5	-1.05690	0.96676

2.4 Results and Discussion

The governing partial differential equations indicates the presence of two emerging parameters: (a) the curvature parameter γ , (b) and the Prandtl number Pr .

The effects of these parameters are discussed in the forthcoming figures. In Figures 2.2 and 2.3, effects of γ on velocity and temperature profile are plotted. It is observed that curvature has significant effects on velocity and temperature profiles. In Figure 2.2, the trend for velocity profile is rapidly decreasing in the region ($0 < \eta < 0.42$) and then increasing after $\eta = 0.42$ for increasing values of curvature parameter γ and consequently the boundary layer thickness increases with the increase in curvature of the cylinder. Since the curvature γ and radius of cylinder have reciprocal relationship i.e., increase in γ tends to decrease in radius of cylinder, therefore, due to lesser surface area of the cylinder, the increase in velocity gradient at the surface is produced and consequently enhances the shear stress per unit area. Figure 2.2 also depicts that an increase in the curvature of the cylinder leads to augment in boundary layer thickness, as compared to that of flat plate case ($\gamma = 0$). In Figure 2.3, it is seen that the temperature profiles decrease near the surface of the cylinder as γ increases, and afterwards rise significantly and the thermal boundary-layer thickness increases. This variation of the temperature profile is due to the reason that as the curvature increases, the radius of cylinder reduces so the surface area which is intact with the fluid

also decreases. It is also important to mention that heat is transferred into the fluid in modes: conduction at the cylinder surface and convection for the region $\eta > 0$. Now, as the area of surface of the cylinder decreases, a slender reduction in the temperature profile occurs close to the surface of the cylinder owing to the fact that a smaller amount of heat energy is transferred from the surface to the fluid through conduction phenomena. On the other hand, the thermal boundary-layer thickness increases, because of the heat transport in the fluid due to enhanced convection process all around the cylinder, which is evident from Figure 2.3. Figure 2.4 is plotted to observe the consequence of curvature parameter γ on the coefficient of skin friction $C_f Re_\xi^{1/2}$. It is noticed that as γ increases, $C_f Re_\xi^{1/2}$ decreases. This is due to the reason that for larger curvature of the cylinder, the velocity gradient at the surface become increase rapidly and skin friction coefficient decreases as compared to that of flat plate ($\gamma = 0$). Figure 2.5 is plotted to observe the consequence of curvature parameter γ on the Nusselt number $Nu Re_\xi^{-1/2}$. It is noticed that as γ increases the Nusselt number $Nu Re_\xi^{-1/2}$ also increases. It is observed from Figures 2.6 and 2.7 that both velocity and temperature boundary layer thickness decreases by increasing the value of ξ . The effects of different values of Pr on temperature profile have been discussed in Figure 2.8.

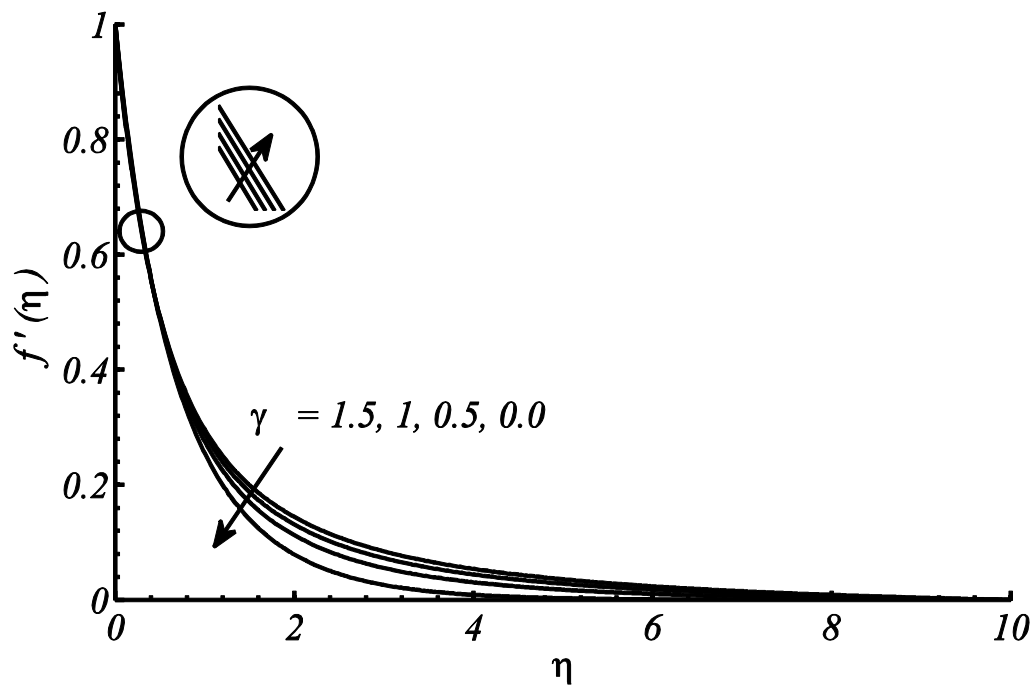


Figure 2.2: Effects on velocity profile due to different values of γ at $\xi = 3$.

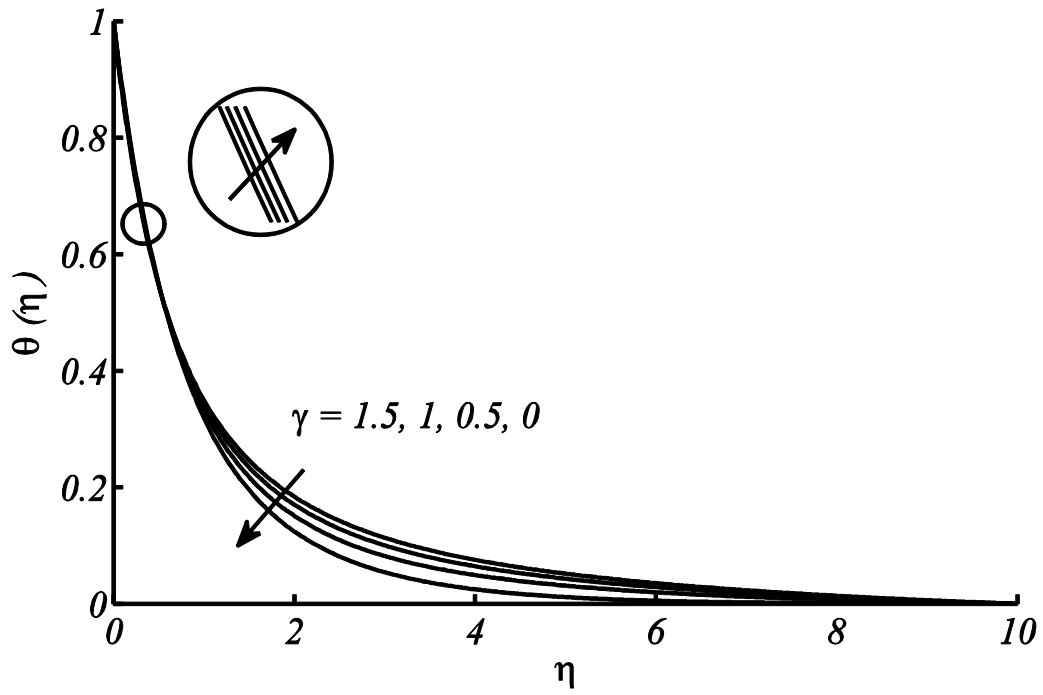


Figure 2.3: Effects of γ on temperature profile while $Pr = 0.7$, $Ec = 0.5$ and $\xi = 3$.

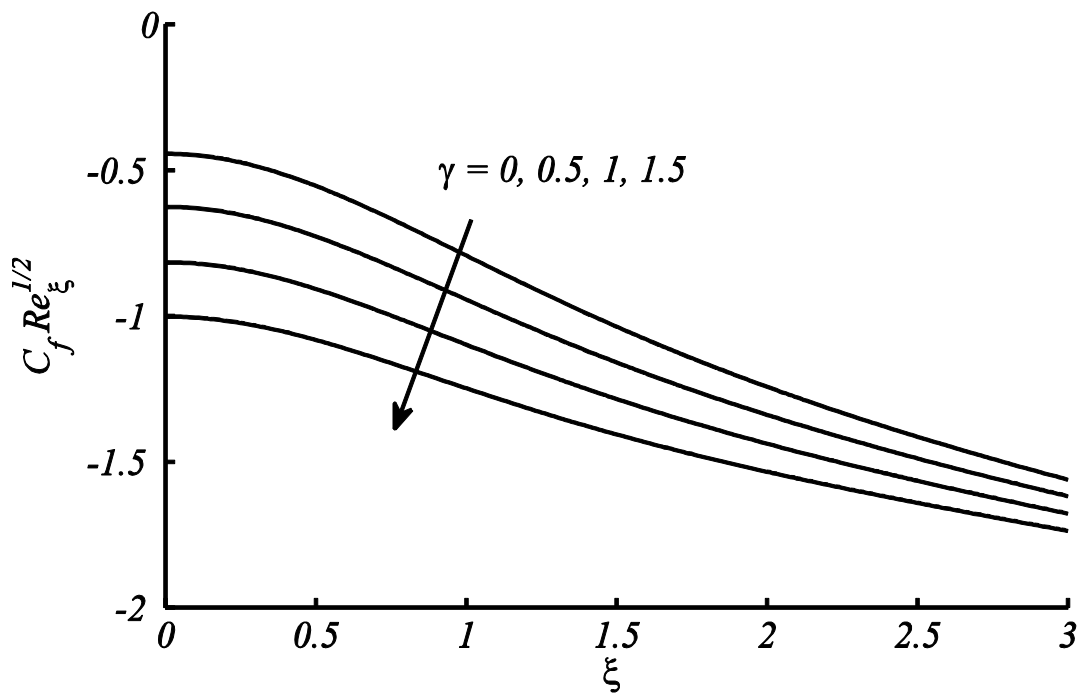


Figure 2.4: Effects on $C_f Re_\xi^{1/2}$ for different γ against ξ .

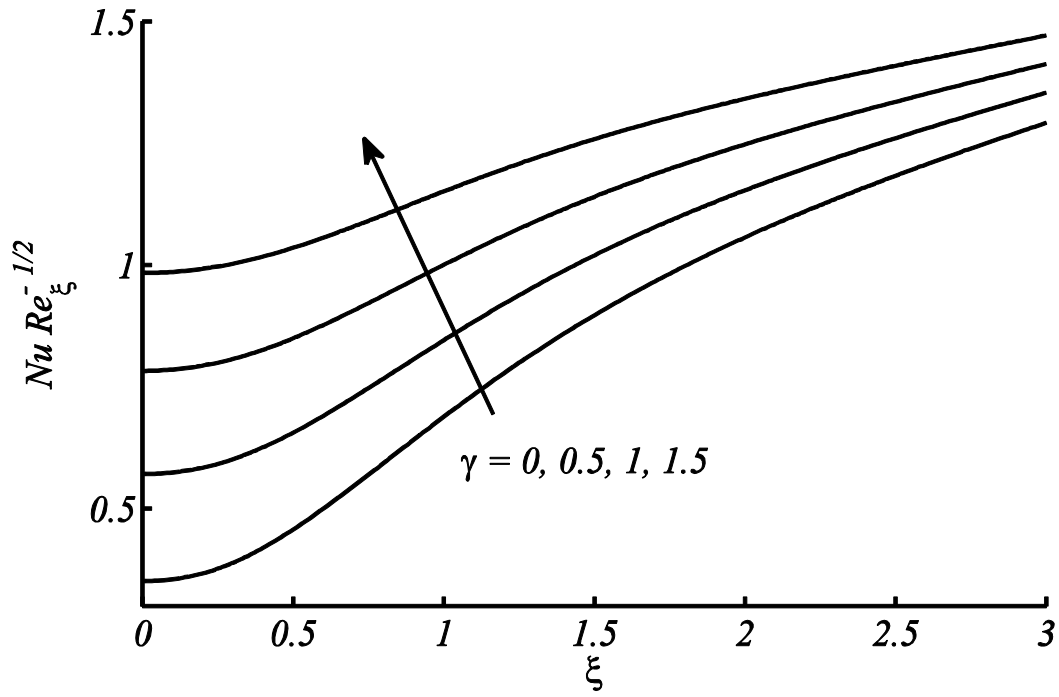


Figure 2.5: Effects on $NuRe_x^{-1/2}$ for different γ against ξ while $Pr = 0.7$.

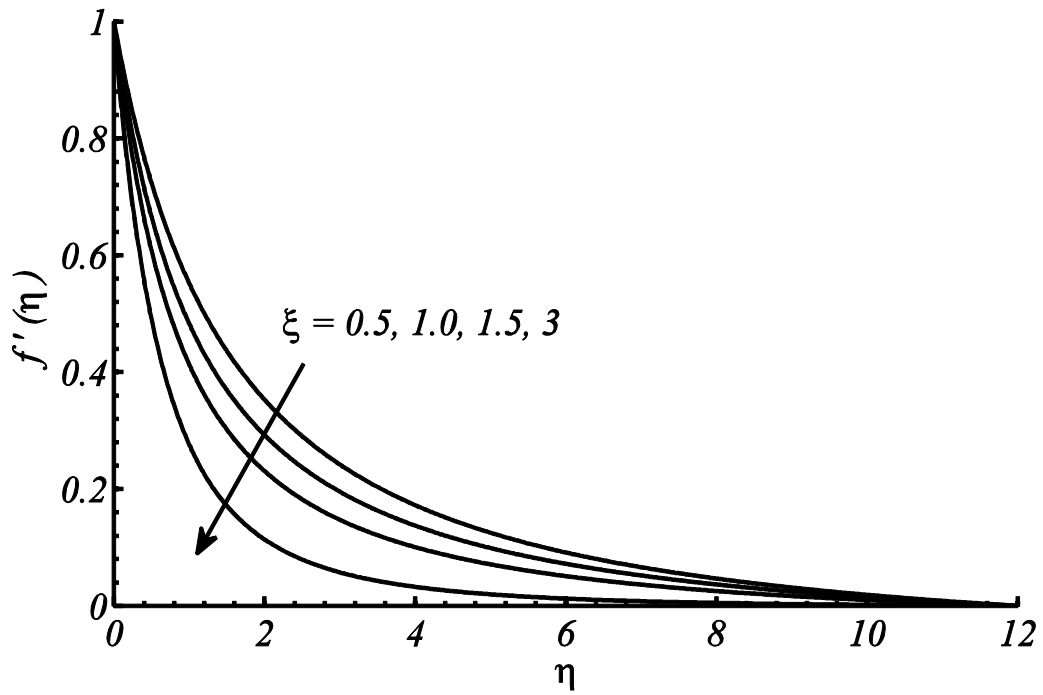


Figure 2.6: Velocity profile at $\xi = 0.5, 1, 1.5, 3$ when $\gamma = 0.5$.

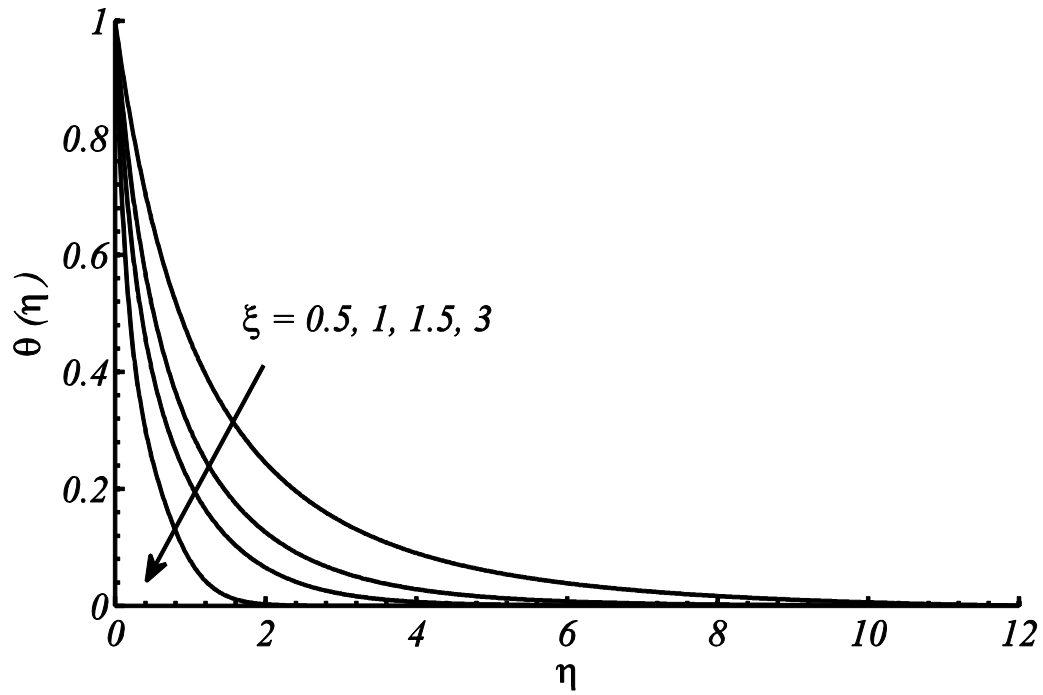


Figure 2.7: Temperature profile at $\xi = 0.5, 1, 1.5, 3$ when $\gamma = 0.5$ and $Pr = 0.7$.

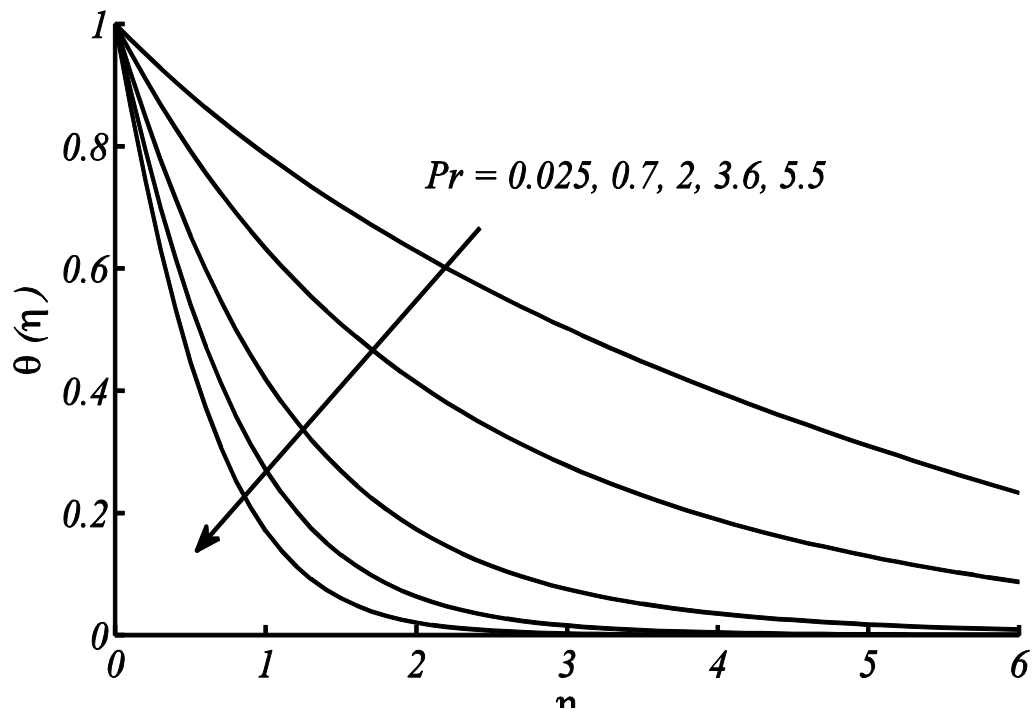


Figure 2.8: Temperature profile at $Pr = 0.025, 0.7, 2, 3.6, 5.5$ when $\xi = 3$.

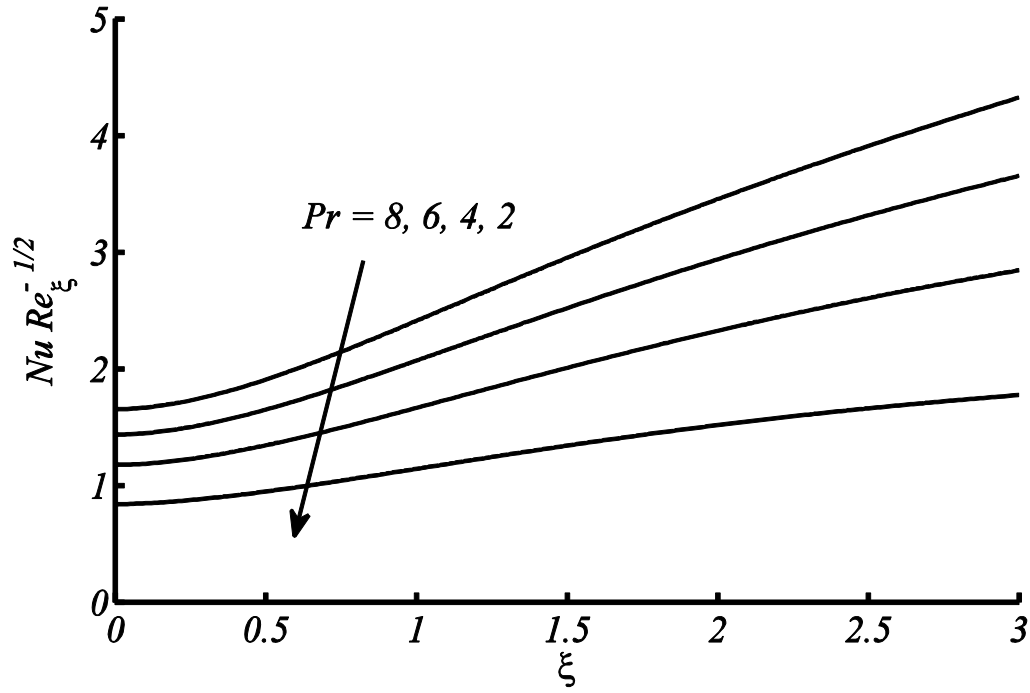


Figure 2.9: Influence on $NuRe_\xi^{-1/2}$ for different Pr against ξ .

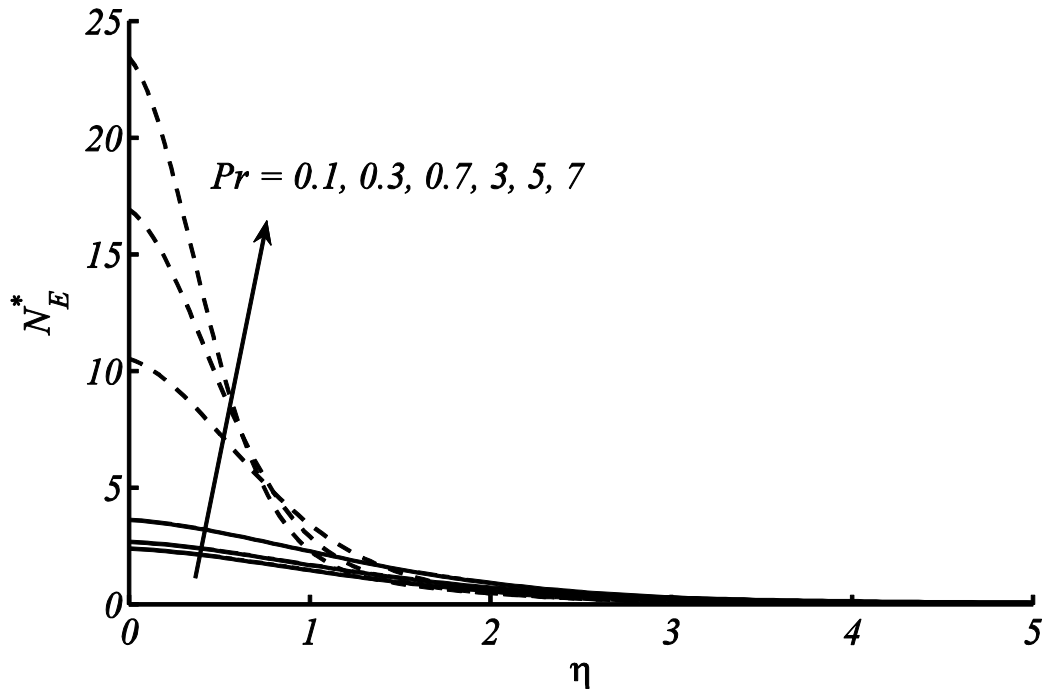


Figure 2.10: Influence of Pr on N_E^* when $\gamma = 0.5$, $Re_l = 2$, $Br\Omega^{*-1} = 1$ at $\xi = 0.2$.

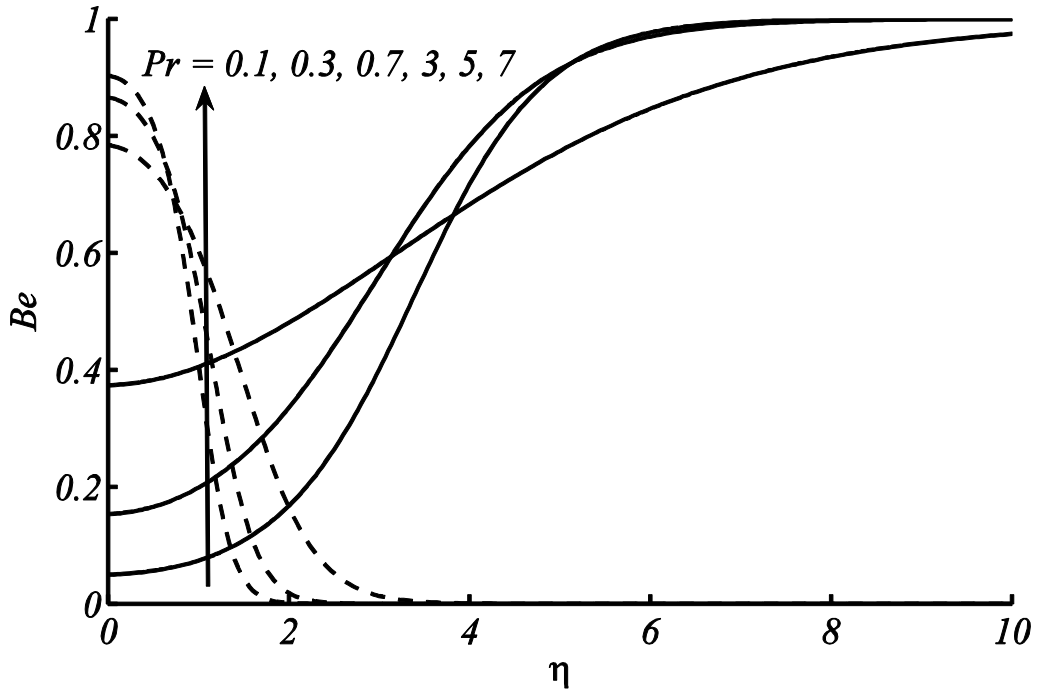


Figure 2.11: Influence of Pr on Be when $\gamma = 0.5, Re_l = 2, Br\Omega^{*-1} = 1$ at $\xi = 0.2$.

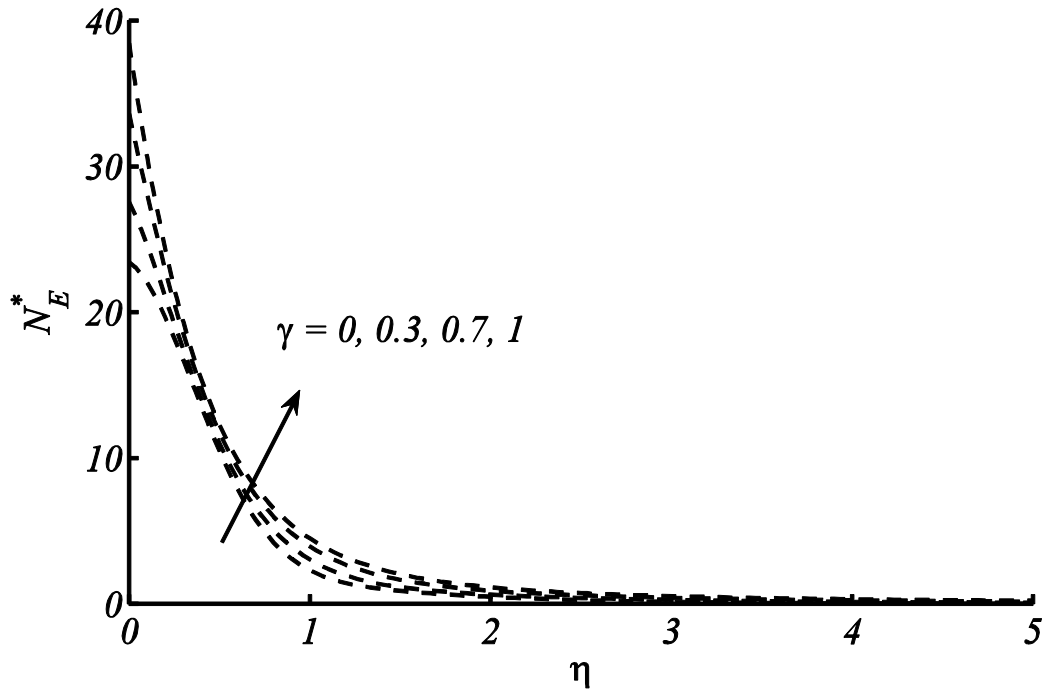


Figure 2.12: Effects of γ on N_E^* when $Re_l = 2, Br\Omega^{*-1} = 1, Pr = 7$ at $\xi = 0.2$.

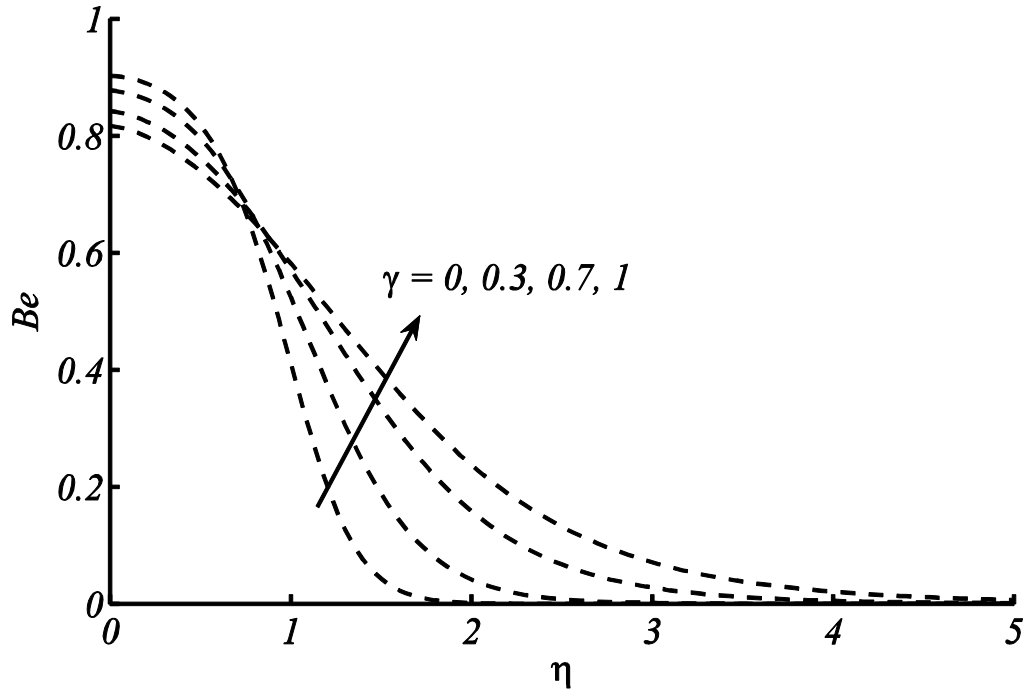


Figure 2.13: Effects of γ on Be when $Br\Omega^{*-1} = 1, Pr = 7$ at $\xi = 0.2$.

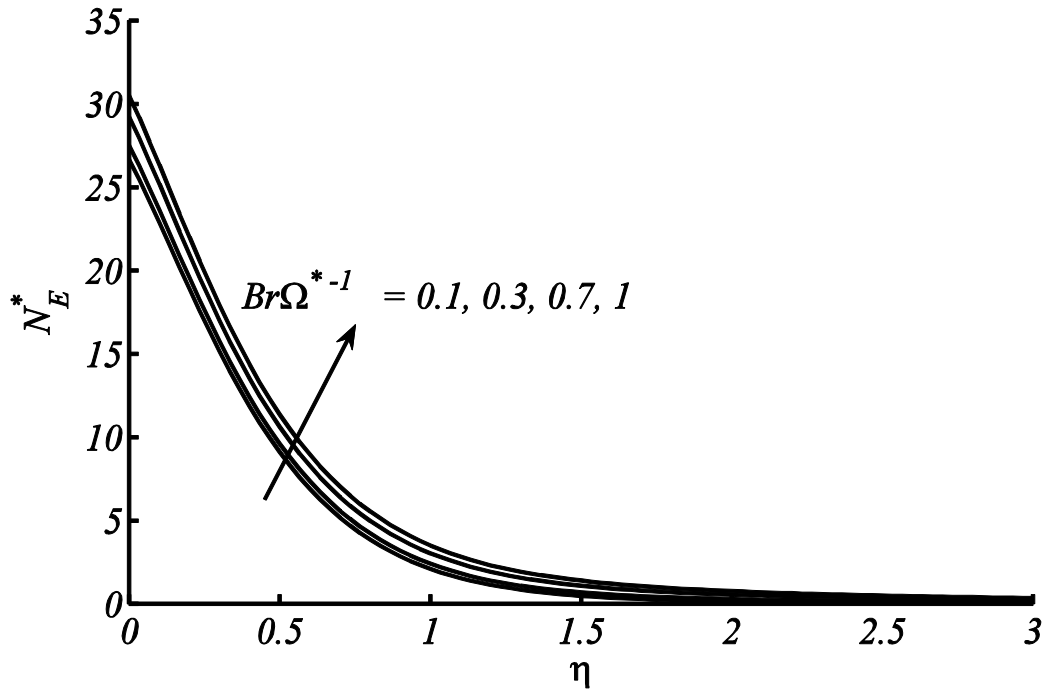


Figure 2.14: Effects of $Br\Omega^{*-1}$ on N_E^* when $Re_l = 2, \gamma = 0.5, Pr = 7$ at $\xi = 0.2$.

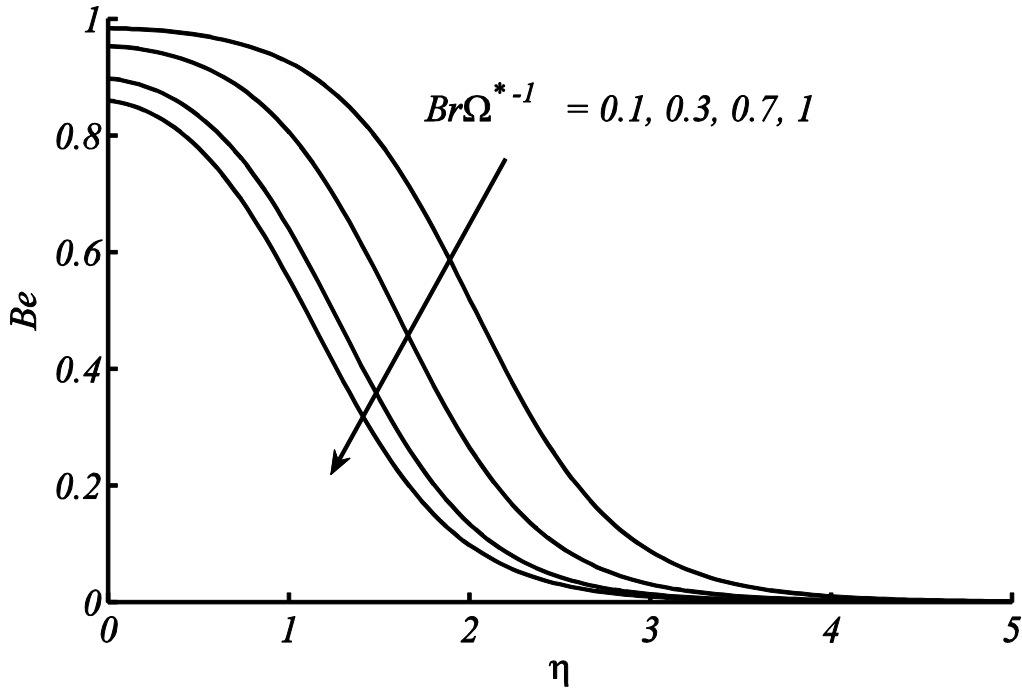


Figure 2.15: Effects of $Br\Omega^{*-1}$ on Be when $\gamma = 0.5, Re_l = 2, Pr = 7$ at $\xi = 0.2$.

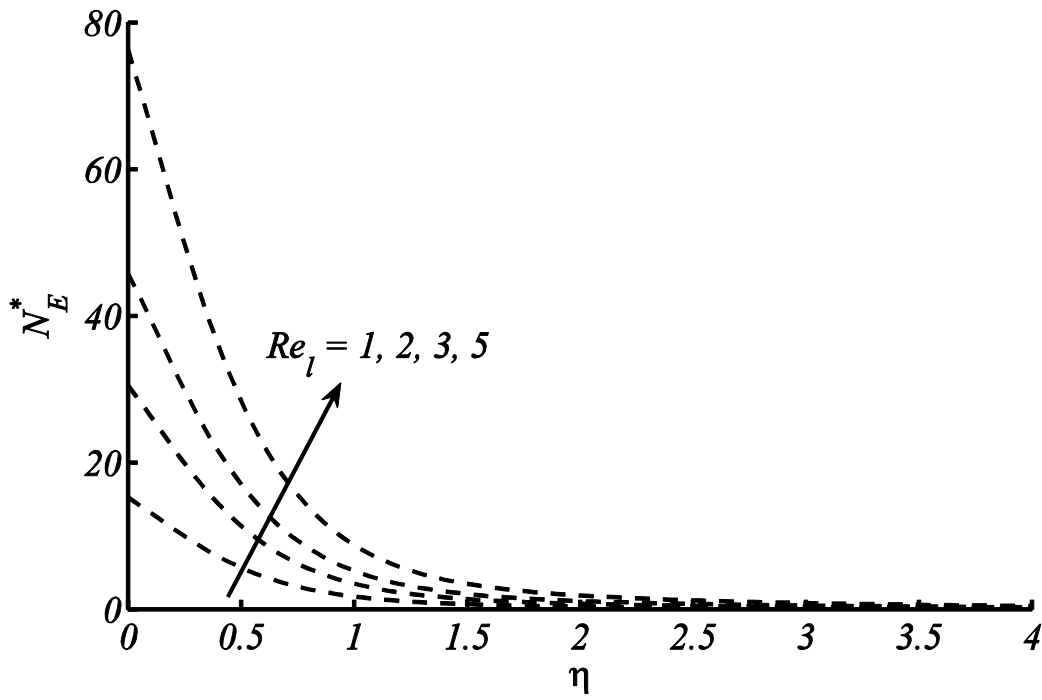


Figure 2.16: Effects of Re_l on N_E^* when $\gamma = 0.5, Pr = 7, Br\Omega^{*-1} = 1$ at $\xi = 0.2$.

It is observed that temperature and thermal boundary layer thickness decreases with increasing Pr . It is obvious from the graph that fluids with low values of Pr slow down the cooling process, and fluids with high Prandtl number expedite the cooling process. Hence this behavior of temperature profile shows that the fluids with high Prandtl number such as oil and lubricants can be used to enhance the cooling process. Figure 2.9 shows that Nusselt number $NuRe_{\xi}^{-1/2}$ increases along the surface of cylinder and against the increase of Pr . This is because of fact that by increasing the value of Pr thermal boundary layer decreases and heat transfer rate enhances. This finding is also visible from the results shown in Figure 2.8. Figures 2.10-2.16 are drawn to discuss the influence of Prandtl number Pr , curvature parameter γ , group parameter $Br\Omega^{*-1}$ and Reynolds number Re_l on entropy generation number N_E^* and Bejan number Be . In Figures 2.10 and 2.11, it is seen that Prandtl number Pr is helpful in enhancing the entropy generation N_E^* and Bejan number Be . This is because the temperature gradient increases with the larger values of Pr . It is also noted that when $Pr < 1$, a small variation in values of Be near the surface of the cylinder is observed and it increases for larger η and attains maximum value i.e., $Be \rightarrow 1$. On the other hand, for the case $Pr > 1$, large values of Be at surface of the cylinder is reported and later start decreasing with $Be \rightarrow 0$ far away from the surface. Figures 2.12 and 2.13 are plotted to see the effects of curvature parameter γ on N_E^* and Be . Both figures depict that entropy generation is more dominant for stretching cylinder case $\gamma > 0$ in comparison with that of flat plat case $\gamma = 0$. In Figure 2.13, Be decrease at the surface of the stretching cylinder ($\eta = 0$) and reverse behavior is observed far away from the surface. The variations of group parameter $Br\Omega^{*-1}$ on N_E^* and Be are depicted in Figures 2.14 and 2.15. The enhancement in $Br\Omega^{*-1}$ results in augmentation of N_E^* and these effects are opposite on Be . The values of Be are decreasing with increase in $Br\Omega^{*-1}$ because the fluid friction dominates when $Br\Omega^{*-1}$ increases and this results in decrement of Be . The effects of Re_l on entropy generation number are expressed in Figure 2.16. The figure reveals that the entropy generation number has gained an increasing trend with increase in Re_l .

2.5 Conclusions

In this chapter we presented the characteristics of flow and heat transfer over a nonlinear stretching cylinder. The nonlinear stretching velocity is considered as hyperbolic function. An analysis of entropy generation is also presented and results are computed numerically with Keller box method. From above study it is perceived that the rise in the values of curvature parameter γ causes increase in velocity and temperature distribution in the boundary layer region. The value of $C_f Re_\xi^{1/2}$ reduces and $Nu Re_\xi^{-1/2}$ enhances with an increase in curvature parameter γ . However, Prandtl number Pr is responsible to reduce the temperature in the boundary layer, and in consequence $Nu Re_\xi^{-1/2}$ enhances. Increasing trend in the values of curvature parameter γ , group parameter $Br\Omega^{*-1}$ and Prandtl number Pr results in enhancement of entropy generation.

Chapter 3

Mixed convection stagnation point flow over a stretching cylinder

In this chapter the analysis of two-dimensional mixed convection flow near the stagnation point over a vertical stretching cylinder is presented. The surface of the cylinder is assumed with temperature as sinusoidal function of time. The governing partial differential equations are converted into dimensionless form by using suitable transformations. The numerical solution of dimensionless partial differential equations is computed with the help of Keller Box method. The details of the method are also given for better implementation and understanding of the readers. To show the accuracy and validity of our results a comparison is also shown as a limiting case with previous studies in the literature. Graphs of velocity and temperature profiles are plotted for assisting and opposing flow cases at different value of time. The assisting buoyant flow augment the momentum boundary layer while opposing buoyant flow controls the momentum boundary layer. The thermal boundary layer thickness grows with the passage of time. Skin friction and Nusselt number are plotted against unsteadiness parameter. The amplitude of surface temperature oscillations is plotted against time. It is apparent that for the small value of surface temperature, the amplitude of oscillations in skin friction and Nusselt number also drops. Furthermore, isotherms are drawn to exhibit the influence of amplitude of surface temperature oscillations on curvature parameter with time.

3.1 Problem formulation

Let us the consider two-dimensional laminar boundary layer fluid flow near the stagnation point over a vertically inclined cylinder as shown in Figure 3.1. The cylinder is of fixed radius R^* is assumed permeable and is being continuously stretching with velocity $V_w(z)$ along its own axis. To perform this analysis, the cylindrical coordinate system is considered as such that the z -axis is taken along the axis of the cylinder and the r -axis is in the radial direction with stagnation point at the origin. It is assumed that the stretching (V_w) and straining (V_e) velocities are proportional to distance z from the stagnation point i.e., $V_w = cz/l$ and $V_e = az/l$. The temperature (T_w) at the surface of cylinder is considered to be

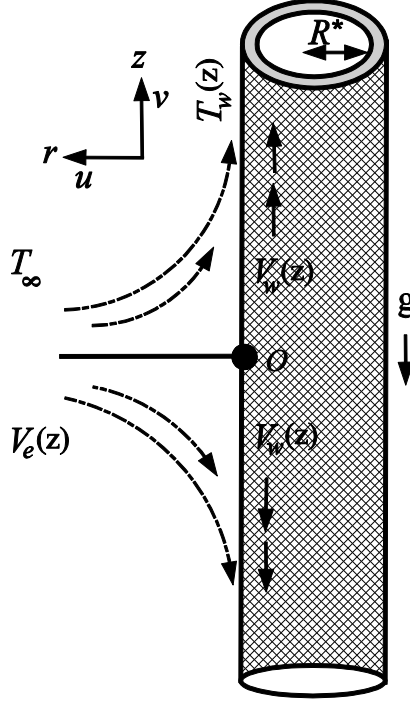


Figure 3.1: Geometry of the problem.

sinusoidal function of time and the ambient fluid temperature is T_∞ . For the present problem, continuity and energy equations are same as described in Eqs. (2.1) and (2.3) while the boundary layer momentum equation with Boussinesq approximation is given by

$$\frac{\partial v}{\partial \bar{t}} + u \frac{\partial v}{\partial r} + v \frac{\partial v}{\partial z} = V_e \frac{\partial V_e}{\partial z} + v \frac{\partial}{\partial r} \left(r \frac{\partial v}{\partial r} \right) + g \beta_t (T - T_\infty). \quad (3.1)$$

The boundary conditions of the assumed flow are

$$\left. \begin{aligned} v &= V_w(z) = \frac{cz}{l}, u(r, z) = u_w, \\ T &= T_w(z) = T_\infty + T_0 \left(\frac{z}{l} \right) (1 + \epsilon \sin \omega \bar{t}) \text{ at } r = R^* \\ v &\rightarrow V_e(z) = \frac{az}{l}, T \rightarrow T_\infty \text{ as } r \rightarrow \infty \end{aligned} \right\} \quad (3.2)$$

where g is the acceleration due to gravity acting downward, β_t is the thermal expansion coefficient, u_w is the mass flux velocity, T_0 is some temperature scale, \bar{t} is the time, ϵ is the amplitude of surface temperature oscillation and ω is the frequency of the oscillation.

Introducing the following non-dimensional variables:

$$\eta = \frac{r^2 - R^{*2}}{2R^*z} \sqrt{\frac{c}{\nu l}}, \psi = \sqrt{\frac{\nu c}{l}} z R^* f(\eta, t), \tau = \omega \bar{t}, T = T_\infty + T_0 \left(\frac{z}{l} \right) \theta(\eta, t), \quad (3.3)$$

here $f(\eta, t)$ is the dimensionless function and $\theta(\eta, t)$ is the dimensionless temperature field.

From relation (2.6), we obtain

$$u = -\frac{R^*}{r} \sqrt{\frac{\nu c}{l}} f(\eta, t) \text{ and } v = \frac{cz}{l} f_\eta(\eta, t) \quad (3.4)$$

Substituting Eqs. (3.3) and (3.4) into Eqs. (3.1) and (2.3), we get the following dimensionless system of partial differential equations

$$(1 + 2\gamma\eta)f_{\eta\eta\eta} + 2\gamma f_{\eta\eta} + f f_{\eta\eta} + \left(\frac{a}{c}\right)^2 - f_\eta^2 + \lambda\theta - \beta f_{\eta t} = 0, \quad (3.5)$$

$$(1 + 2\gamma\eta)\theta_{\eta\eta} + 2\gamma\theta_\eta + Pr(f\theta_\eta - f_\eta\theta - \beta\theta_t) = 0. \quad (3.6)$$

The boundary conditions in Eq. (3.2) take the form

$$\begin{aligned} \eta = 0: \quad f(\eta, t) = S, f_\eta(\eta, t) = 1, \theta(\eta, t) = 1 + \epsilon \sin t, \\ \eta \rightarrow \infty: \quad \theta(\eta, t) = 0, f_\eta(\eta, t) = a/c, \end{aligned} \quad (3.7)$$

where $\gamma = \sqrt{\nu l / c R^{*2}}$ is curvature parameter, a/c is the ratio of straining (free stream) to stretching velocities, $\lambda = Gr_z / Re_z^2$ is the mixed convection parameter where $Gr_z = g\beta_t T_0 z^4 / \nu^2$ and $Re_z = cz^2 / \nu$. It is important to note that $\lambda = 0$ corresponds to forced convection flow, $\lambda > 0$ ($T_0 > 0$) corresponds to assisting flow case (i.e., the buoyancy forces acts parallel to free stream velocity), $\lambda < 0$ ($T_0 < 0$) corresponds to opposing flow case (i.e., the buoyancy forces acts opposite to free stream velocity), $\beta = l\omega / c$ is unsteady parameter (arises due to temperature oscillations), $Pr = \nu / \alpha$ is Prandtl number, $S = -u_w \sqrt{l / \nu c}$ is the suction/injection parameter with $S > 0$ represents suction case and $S < 0$ is for injection case. After utilizing Eq. (2.15) in Eq. (2.14), the expressions of C_f and Nu will be modified as following

$$Re_z^{1/2} C_f = f_{\eta\eta}(0, t), \quad Re_z^{-1/2} Nu_z = -\theta_\eta(0, t). \quad (3.8)$$

3.2 Solution Methodology

The nonlinear system of partial differential equations. (3.5) and (3.6) subject to the boundary conditions (3.7) is solved by using the second order accurate Keller box method. The detailed method has explained in the book by Cebeci and Bradshaw (1984). The main steps are as follows: Setting

$$f_\eta = p, \quad p_\eta = q, \quad \theta_\eta = U. \quad (3.9)$$

in differential equations (3.5, 3.6) and boundary conditions (3.7) resulting as

$$(1 + 2\eta\gamma)q_\eta + 2\gamma q + f q - p^2 + 2\theta - \beta \frac{\partial p}{\partial \xi} = -\left(\frac{a}{c}\right)^2, \quad (3.10)$$

$$U_\eta + 2\gamma U + Pr \left(f U - f' \theta - \beta \frac{\partial p}{\partial \xi} \right) = 0, \quad (3.11)$$

and boundary conditions take the new form as

$$\begin{aligned} f(0, \xi) &= 0, & p(0, \xi) &= 1, & \theta(0, \xi) &= 1, \\ f(\infty, \xi) &= 0, & \theta(\infty, \xi) &= 0. \end{aligned} \quad (3.12)$$

A net on the plane (ξ, η) is defined as

$$\begin{aligned} \eta_0 &= 0, \eta_j = \eta_{j-1} + \Delta\eta, \eta_J = \eta_\infty, j = 1, 2, \dots, J-1, \\ \xi^0 &= 0, \xi^n = \xi^{n-1} + \Delta\xi, n = 1, 2, \dots, \end{aligned} \quad (3.13)$$

where n and j are positive integers, $\Delta\eta$ and $\Delta\xi$ are widths of meshing variables on (ξ, η) plane. The approximate quantities of functions f, p, q, θ and U at the net point (ξ^n, η_j) are known as net functions whose derivatives in η and ξ -directions are replaced by the central difference formulae, and functions itself are replaced by average centered at the midpoint $(\xi^{n-1/2}, \eta_{j-1/2})$ defined as

$$\left. \frac{\partial}{\partial \xi} (\quad) \right|_j^{n-1/2} = \frac{1}{\Delta\xi} (f_j^n - f_j^{n-1}), \quad \left. \frac{\partial}{\partial \eta} (\quad) \right|_{j-1/2}^n = \frac{1}{\Delta\eta} (f_j^n - f_{j-1}^n),$$

and

$$f_j^{n-1/2} = \frac{1}{2} (f_j^n + f_j^{n-1}), \quad f_{j-1/2}^n = \frac{1}{2} (f_j^n + f_{j-1}^n).$$

After discretization, the system of nonlinear partial differential Eqs. (3.10) and (3.11) are converted to the system of difference equations written as

$$\begin{aligned} (1 + (\eta_j + \eta_{j-1})\gamma) \frac{q_j^n - q_{j-1}^n}{\Delta\eta} + \gamma(q_j^n + q_{j-1}^n) + \left(\frac{f_j^n + f_{j-1}^n}{2} \right) \left(\frac{q_j^n + q_{j-1}^n}{2} \right) \\ - \frac{1}{4} (p_j^n + p_{j-1}^n)^2 + \lambda \left(\frac{\theta_j^n + \theta_{j-1}^n}{2} \right) - \frac{2\beta}{\Delta\xi} \{ (p_j^n + p_{j-1}^n)^2 \} \\ = r_{j-\frac{1}{2}}^{n-1}, \end{aligned} \quad (3.14)$$

$$\begin{aligned} (1 + (\eta_j + \eta_{j-1})\gamma) \frac{U_j^n - U_{j-1}^n}{\Delta\eta} + \gamma(U_j^n + U_{j-1}^n) \\ + Pr \left(\frac{f_j^n + f_{j-1}^n}{2} \right) \left(\frac{U_j^n + U_{j-1}^n}{2} \right) \\ - Pr \left(\frac{\theta_j^n + \theta_{j-1}^n}{2} \right) \left(\frac{p_j^n + p_{j-1}^n}{2} \right) - 2Pr\beta \left(\frac{\theta_j^n + \theta_{j-1}^n}{\Delta\xi} \right) = m_{j-\frac{1}{2}}^{n-1}, \end{aligned} \quad (3.15)$$

Eq. (3.9) becomes

$$f_j^n - f_{j-1}^n = \frac{\Delta\eta}{2} (p_j^n + p_{j-1}^n), \quad (3.16)$$

$$p_j^n - p_{j-1}^n = \frac{\Delta\eta}{2} (q_j^n + q_{j-1}^n), \quad (3.17)$$

$$\theta_j^n - \theta_{j-1}^n = \frac{\Delta\eta}{2} (U_j^n + U_{j-1}^n), \quad (3.18)$$

where

$$\begin{aligned} r_{j-\frac{1}{2}}^{n-1} = & -2 \left(\frac{a}{c} \right)^2 + [1 + \gamma(\eta_j + \eta_{j-1})] \left(\frac{q_j^{n-1} + q_{j-1}^{n-1}}{\Delta\eta} \right) - \gamma(q_j^{n-1} + q_{j-1}^{n-1}) \\ & - \frac{1}{4} (f_j^{n-1} + f_{j-1}^{n-1})(q_j^{n-1} + q_{j-1}^{n-1}) + \left(\frac{p_j^{n-1} + p_{j-1}^{n-1}}{2} \right)^2 \\ & - \lambda \left(\frac{\theta_j^{n-1} + \theta_{j-1}^{n-1}}{2} \right), \end{aligned} \quad (3.19)$$

$$\begin{aligned} m_{j-\frac{1}{2}}^{n-1} = & -(1 + (\eta_j + \eta_{j-1})\gamma) \left(\frac{U_j^{n-1} + U_{j-1}^{n-1}}{\Delta\eta} \right) - \gamma (U_j^{n-1} + U_{j-1}^{n-1}) \\ & - \frac{Pr}{4} (f_j^{n-1} + f_{j-1}^{n-1})(U_j^{n-1} + U_{j-1}^{n-1}) \\ & + Pr \left(\frac{\theta_j^{n-1} + \theta_{j-1}^{n-1}}{2} \right) \left(\frac{p_j^{n-1} + p_{j-1}^{n-1}}{2} \right). \end{aligned}$$

The boundary conditions (3.12) become

$$f_0^n = 0, p_0^n = 1, \theta_0^n = 1, p_J^n = \theta_J^n = 0 \quad (3.20)$$

The nonlinear algebraic Eqs. (3.14) and (3.15) are linearized by using Newton method by introducing $(i + 1)^{th}$ iterates as

$$(f_j^n)^{i+1} = (f_j^n)^{(i)} + (\delta f_j^n)^{(i)}. \quad (3.21)$$

and similarly, it is same for all other variables in which $(f_j^n)^{(i)}$ is known for $0 < j \leq J$ as an initial guess and $(\delta f_j^n)^{(i)}$ is unknown. After using the Newton linearization process and neglecting the terms containing square and higher order of $(\delta f_j^n)^{(i)}, (\delta p_j^n)^{(i)}, (\delta q_j^n)^{(i)}, (\delta \theta_j^n)^{(i)}$ and $(\delta U_j^n)^{(i)}$, the system of linear algebraic equations is obtained as follows

$$\begin{aligned} & \delta f_j^n - \delta f_{j-1}^n - \frac{\Delta\eta}{2} (\delta p_j^n + \delta p_{j-1}^n) = (r_1)_j, \\ & (a_1)_j \delta f_{j-1}^n + (a_2)_j \delta f_j^n + (a_3)_j \delta p_{j-1}^n + (a_4)_j \delta p_j^n + (a_5)_j \delta q_{j-1}^n + (a_6)_j \delta q_j^n + (a_7)_j \delta \theta_{j-1}^n \\ & \quad + (a_8)_j \delta \theta_j^n = (r_2)_j, \\ & (a_9)_j \delta \theta_{j-1}^n + (a_{10})_j \delta \theta_j^n + (a_{11})_j \delta U_{j-1}^n + (a_{12})_j \delta U_j^n = (r_3)_j, \\ & \delta p_j^n - \delta p_{j-1}^n - \frac{\Delta\eta}{2} (\delta q_j^n + \delta q_{j-1}^n) = (r_4)_j, \\ & \delta \theta_j^n - \delta \theta_{j-1}^n - \frac{\Delta\eta}{2} (\delta U_j^n + \delta U_{j-1}^n) = (r_5)_j. \end{aligned}$$

The boundary conditions (3.24) take the new form as

$$\delta f_0^n = 0, \delta p_0^n = 1, \delta \theta_0^n = 1, \delta p_j^n = \delta \theta_j^n = 0.$$

Finally, the above system of linear algebraic equations with boundary conditions will be written in matrix vector form. The coefficients in momentum and energy equations of unknown functions δf_j^n , δp_j^n , δq_j^n , $\delta \theta_0^n$, δU_j^n and non-homogeneous parts are given as:

Coefficient of momentum equation:

coefficient of δf_{j-1}^n :

$$(a_1)_j = \frac{1}{4}(q_j^n + q_{j-1}^n)$$

Coefficient of δf_j^n :

$$(a_2)_j = \frac{1}{4}(q_j^n + q_{j-1}^n)$$

Coefficient of δp_{j-1}^n :

$$(a_3)_j = -\frac{1}{2}(p_j^n + p_{j-1}^n) - \frac{2\beta}{2\Delta\xi}$$

Coefficient of δp_j^n :

$$(a_4)_j = -\frac{1}{2}(p_j^n + p_{j-1}^n) - \frac{2\beta}{2\Delta\xi}$$

Coefficient of δq_{j-1}^n :

$$(a_5)_j = -\frac{1}{\Delta\eta}[1 + \gamma(\eta_j + \eta_{j-1})] + \gamma + \frac{1}{4}(f_j^n + f_{j-1}^n)$$

Coefficient of δq_j^n :

$$(a_6)_j = -\frac{1}{\Delta\eta}[1 + \gamma(\eta_j + \eta_{j-1})] + \gamma + \frac{1}{4}(f_j^n + f_{j-1}^n)$$

Coefficient of $\delta \theta_{j-1}^n$:

$$(a_7)_j = \frac{\lambda}{2}$$

Coefficient of $\delta \theta_j^n$:

$$(a_8)_j = \frac{\lambda}{2}$$

Coefficient of energy equation:

Coefficient of $\delta \theta_{j-1}^n$:

$$(a_9)_j = -\frac{Pr}{4}(p_j^n + p_{j-1}^n) - \frac{2Pr\beta}{\Delta\xi}$$

Coefficient of $\delta\theta_j^n$:

$$(a_{10})_j = -\frac{Pr}{4}(p_j^n + p_{j-1}^n) - \frac{2Pr\beta}{\Delta\xi}$$

Coefficient of δU_{j-1}^n :

$$(a_{11})_j = -\frac{[1 + \gamma(\eta_j + \eta_{j-1})]}{\Delta\eta} + \frac{Pr}{4}(f_j^n + f_{j-1}^n)$$

Coefficient of δU_j^n :

$$(a_{12})_j = \frac{[1 + \gamma(\eta_j + \eta_{j-1})]}{\Delta\eta} + \frac{Pr}{4}(f_j^n + f_{j-1}^n)$$

Non-homogeneous terms

$$\begin{aligned} (r_1)_j &= (f_{j-1}^n - f_j^n) + \frac{\Delta\eta}{2}(p_j^n + p_{j-1}^n), \\ (r_2)_j &= -2\left(\frac{a}{c}\right)^2 + [1 + \gamma(\eta_j + \eta_{j-1})]\left(\frac{q_j^{n-1} + q_{j-1}^{n-1}}{\Delta\eta}\right) - \gamma(q_j^{n-1} + q_{j-1}^{n-1}) \\ &\quad - \frac{1}{4}(f_j^{n-1} + f_{j-1}^{n-1})(q_j^{n-1} + q_{j-1}^{n-1}) + \left(\frac{p_j^{n-1} + p_{j-1}^{n-1}}{2}\right)^2 - \left(\frac{\theta_j^{n-1} + \theta_{j-1}^{n-1}}{2}\right) \\ &\quad - [1 + \gamma(\eta_j + \eta_{j-1})]\left(\frac{q_j^n + q_{j-1}^n}{\Delta\eta}\right) - \gamma(q_j^n + q_{j-1}^n) \\ &\quad - \frac{1}{4}(f_j^n + f_{j-1}^n)(q_j^n + q_{j-1}^n) + \frac{1}{4}(p_j^n + p_{j-1}^n)^2 - \frac{\lambda}{2}(T_j^n + T_{j-1}^n) \\ &\quad + \frac{\beta}{\Delta\xi}\{(p_j^n + p_{j-1}^n) - (p_j^{n-1} + p_{j-1}^{n-1})\}, \\ (r_3)_j &= -[1 + \gamma(\eta_j + \eta_{j-1})]\left(\frac{U_j^{n-1} - U_{j-1}^{n-1}}{\Delta\eta}\right) - \gamma(U_j^{n-1} + U_{j-1}^{n-1}) \\ &\quad - \frac{Pr}{4}(f_j^{n-1} + f_{j-1}^{n-1})(U_j^{n-1} + U_{j-1}^{n-1}) + \frac{Pr}{4}(p_j^{n-1} + p_{j-1}^{n-1})(\theta_j^{n-1} + \theta_{j-1}^{n-1}) \\ &\quad - \frac{1}{\Delta\eta}[1 + \gamma(\eta_j + \eta_{j-1})](U_j^n + U_{j-1}^n) - \gamma(U_j^n + U_{j-1}^n) \\ &\quad - \frac{Pr}{4}(f_j^n + f_{j-1}^n)(U_j^n + U_{j-1}^n) + \frac{Pr\beta}{\Delta\xi}\{(\theta_j^n + \theta_{j-1}^n) - (\theta_j^{n-1} + \theta_{j-1}^{n-1})\}, \\ (r_4)_j &= (p_{j-1}^n - p_j^n) + \frac{\Delta\eta}{2}(q_j^n + q_{j-1}^n), \\ (r_5)_j &= (\theta_{j-1}^n - \theta_j^n) + \frac{\Delta\eta}{2}(U_j^n + U_{j-1}^n). \end{aligned}$$

The resulting matrix vector form is solved by using block-tridiagonal elimination technique, which is explained in the previous chapter. The edge of boundary layer thickness η_∞ is

Table 3.1: Numerical values of $f_{\eta\eta}(0)$ for different a/c when $\gamma = \lambda = S = \beta = t = 0$ with Mahapatra and Gupta (2002) and Nazar et al. (2004)

a/c	Mahapatra and Gupta (2002)	Nazar et al. (2004)	Present study
0.01		-0.9980	-0.9980
0.02		-0.9958	-0.9958
0.05		-0.9876	-0.9876
0.10	-0.9694	-0.9694	-0.9694
0.20	-0.9181	-0.9181	-0.9181
0.50	-0.6673	-0.6673	-0.6673
2.00	2.0175	2.0176	2.0175
3.00	4.7293	4.7296	4.7294
5.00		11.7537	11.7524
10.00		36.2687	36.2603
20.00		106.5744	106.5239
50.00		430.6647	430.1501

Table 3.2: Comparison of $-\theta_{\eta}(0)$ for different a/c and Pr when $\gamma = a/c = S = \beta = t = \epsilon = 0$ with (Ishak et al. 2009)

λ	Pr	Ishak et al. (2009)	Present study
0	0.01	0.0197	0.0198
	0.72	0.8086	0.8086
	1.0	1.0000	1.0000
	3.0	1.9237	1.9237
	7.0	3.0723	3.0723
	10	3.7207	3.7208
	100	12.2941	12.3004
1	1	1.0873	1.0873
2		1.1423	1.1423
3		1.1853	1.1853

chosen according to the values of the parameters. The iteration is continued for refinement in the solution until we achieved the difference between two consecutive iterations is less

than 10^{-6} . The employed technique is validated after comparing the numerical values of $f_{\eta\eta}(0)$ with Mahapatra and Gupta (2002) and Nazar et al. (2004) as shown in Table 3.1 as a limiting case. Table 3.2 gives the comparison of $-\theta_\eta(0)$ with Ishak et al. (2009) for limited cases. These tables show that the computed results are in good agreement that gives us a confidence in accuracy of the employed numerical technique.

3.3 Results and Discussion

The non-linear partial differential equations (3.7)–(3.8) subject to the boundary conditions (3.9) are solved numerically using Keller Box method for various values of emerging dimensionless parameters namely, curvature parameter (γ), velocity ratio parameter (a/c), mixed convection parameter (λ), suction/injection parameter (S), unsteadiness parameter (β), Prandtl number (Pr) and amplitude of oscillation in temperature (ϵ). The numerical results are computed in terms of velocity profile $f_\eta(\eta, t)$, temperature profiles $\theta(\eta, t)$, skin friction coefficient $Re_z^{1/2} C_f$ and Nusselt number $Re_z^{-1/2} Nu_z$. Figure 3.2 exhibits the velocity profile against η for different values of a/c for assisting flow ($\lambda = 1$) and opposing flow ($\lambda = -1$) cases at different time steps levels ($t = 0, \pi/4, \pi/2$). It is observed that velocity increases for increasing values of time (t) in assisting flow case ($\lambda = 1$) and opposite behavior is observed in opposing flow case ($\lambda = -1$) for all values of velocities ratio parameter (a/c). This is due to the reason that in assisting flow, buoyant force assists the flow and in opposing flow, buoyant force delays the flow. Figures 3.3 and 3.4 show the velocity and temperature profiles respectively for various values of curvature parameter (γ) and suction/injection parameter (S). In Figure 3.3, it is noted that the velocity profile decreases near the surface of cylinder and increases far away from the surface due to increase in curvature parameter (γ) for both suction ($S = 0.5$) and injection ($S = -0.5$) cases. It is also observed that in case of injection ($S = -0.5$), the velocity and corresponding momentum boundary layer thickness become higher as compare to the case of suction ($S = 0.5$). This is because injection enhances the flow near the surface. In Figure 3.4 for both values of parameter (S), the temperature profile increases with increase in curvature of the cylinder (γ). Furthermore, it is noted that, thermal boundary layer thickness can be increased with increase in curvature parameter (γ) both for injection and suction cases. Figure 3.5 demonstrates the effects on temperature profiles against η for various values of

parameter a/c at different time step levels $t = 0$ and $t = \pi/2$. The temperature profile increases with the increasing value of time (t) for all values of a/c which is obviously due

Table 3.3: Values of $Re_z^{1/2}C_f$ and $(Re_z^{-1/2}Nu_z)$ for the various parameter γ ,
 $a/c, \lambda, S, \beta, \epsilon$ and Pr

Pr	γ	a/c	λ	β	ϵ	S	$t = 0$	$t = \pi/4$	$t = \pi/2$	$t = \pi$					
0.7	0.2	0	1	1	1	0.5	-0.8034	-0.5861	-0.4110	-0.6803					
							(1.1508)	(2.3036)	(2.4750)	(0.8097)					
		0.2					-0.7140	-0.4985	-0.3280	-0.6007					
							(1.1857)	(2.3446)	(2.5236)	(0.8530)					
		0		0			-0.2075	-1.2075	-1.2075	-1.2075					
							(1.1158)	(2.2353)	(2.3479)	(0.7137)					
	1.0	0.4		1.5			-0.2075	-1.2075	-1.2075	-1.2075					
							(1.1158)	(2.3632)	(2.4180)	(0.5696)					
				1.5			-0.2075	-1.2075	-1.2075	-1.2075					
							(1.1158)	(2.9870)	(3.0691)	(0.2965)					
				-1			-1.7312	-1.9999	-2.2780	-2.1029					
							(1.3039)	(3.5290)	(3.5352)	(0.1079)					
1.0	0.4	1		2	2	-0.5	-1.8222	-2.0928	-2.3769	-2.2172					
							(1.3628)	(3.6805)	(3.7137)	(0.1349)					
		1					-0.3432	-0.5936	-0.8064	-0.4937					
							(1.7024)	(4.1352)	(4.3674)	(0.8606)					
		2					-0.3432	-0.5706	-0.7776	-0.5163					
							(1.7024)	(4.3265)	(4.4671)	(0.6346)					
	7.0	0.6		1.5	-0.5		-0.3432	-0.6465	-0.9241	-0.5777					
							(1.7024)	(5.1987)	(5.3753)	(0.2686)					
		1.2					0.3530	0.6352	0.8990	0.5762					
							(1.9770)	(7.6830)	(6.9611)	(-1.4708)					
		0.6					0.3526	0.6346	0.8982	0.5761					
							(2.0626)	(7.8986)	(7.2232)	(-1.3965)					
7.0	1.2	1.2					0.6807	0.9606	1.2176	0.8896					
							(2.1204)	(7.9825)	(7.3444)	(-1.2899)					

to input temperature at the wall at that time. It is further important to note that the temperature profile decreases due to increase in velocity ratio parameter (a/c) and hence thermal boundary layer thickness become smaller for large values of velocity ratio parameter a/c . In Figure 3.6, the temperature profile increases at any point within the boundary layer for increasing time steps levels in both assisting and opposing flow cases. In opposing flow case, the thermal boundary layer thickness is larger as compared to assisting flow case for all time steps levels $t = 0, \pi/4$ and $\pi/2$. Influence of curvature parameter (γ) on velocity and temperature profile is shown in Figures 3.7 and 3.8 respectively for $\lambda = 0.5$ (assisting flow) and $\lambda = -0.5$ (opposing flow). As curvature parameter (γ) increases the surface of cylinder squeezes due to which surface area reduces and consequently the velocity of the fluid increases as shown in Figure 3.7. Similarly, temperature of the fluid also enhances at any point within the boundary layer region due to increase in curvature parameter (γ) as shown in Figure 3.8. In addition, momentum boundary layer is maximum in case of $\lambda = 0.5$ (assisting flow) in comparison with $\lambda = -0.5$ (opposing flow), but very little change is observed in thermal boundary layer for $\lambda = 0.5$ (assisting flow) and $\lambda = -0.5$ (opposing flow) cases. Figures 3.9 and 3.10 illustrate the variations in $Re_z^{1/2}C_f$ and $Re_z^{-1/2}Nu_z$ respectively against time (t) for different values of unsteadiness parameter (β). It is noted that due to sinusoidal nature of temperature, the amplitude of skin friction enhanced as well as reduced for Nusselt number with backward phase shift against time (t) with increase in unsteadiness parameter (β) as shown in Figures 3.9 and 3.10. Figures 3.11 and 3.12 show the variation of $Re_z^{1/2}C_f$ and $Re_z^{-1/2}Nu_z$ respectively against t for different values of ϵ . It is noted that amplitude of oscillations in the values of $Re_z^{1/2}C_f$ and $Re_z^{-1/2}Nu_z$ increases with increase in ϵ . It is also perceived that as the values of ϵ drop, the amplitude of oscillations in $Re_z^{1/2}C_f$ and $Re_z^{-1/2}Nu_z$ also diminish. However, for $\epsilon = 0$, the case of constant surface temperature is recovered as shown in Figures 3.11 and 3.12. The effect of Prandtl number (Pr) on heat transfer rate is observed in Figure 3.13. The heat transfer rate enhances due to increase in Pr and amplitude of oscillation become larger for large values of Pr against time t . Figures 3.14 and 3.15 demonstrate the isotherms for curvature parameter (γ) and amplitude of temperature oscillations (ϵ) respectively. Due to increase in curvature parameter (γ) and amplitude of temperature oscillations (ϵ), a pattern of increasing behavior in sinusoidal nature of isotherms is clearly visible. Table 3.3 is constructed to exhibit the behavior of sundry

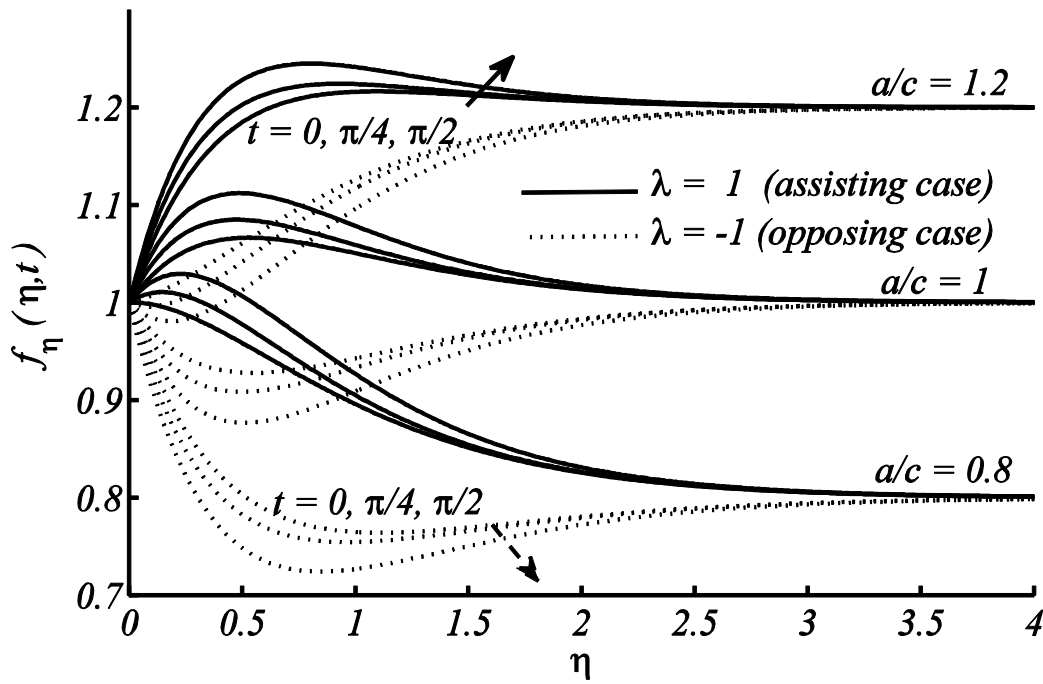


Figure 3.2: Velocity profile for $\lambda = 1$ and $\lambda = -1$ at $\gamma = 0.2, \beta = 2, \epsilon = 1, Pr = 1$.

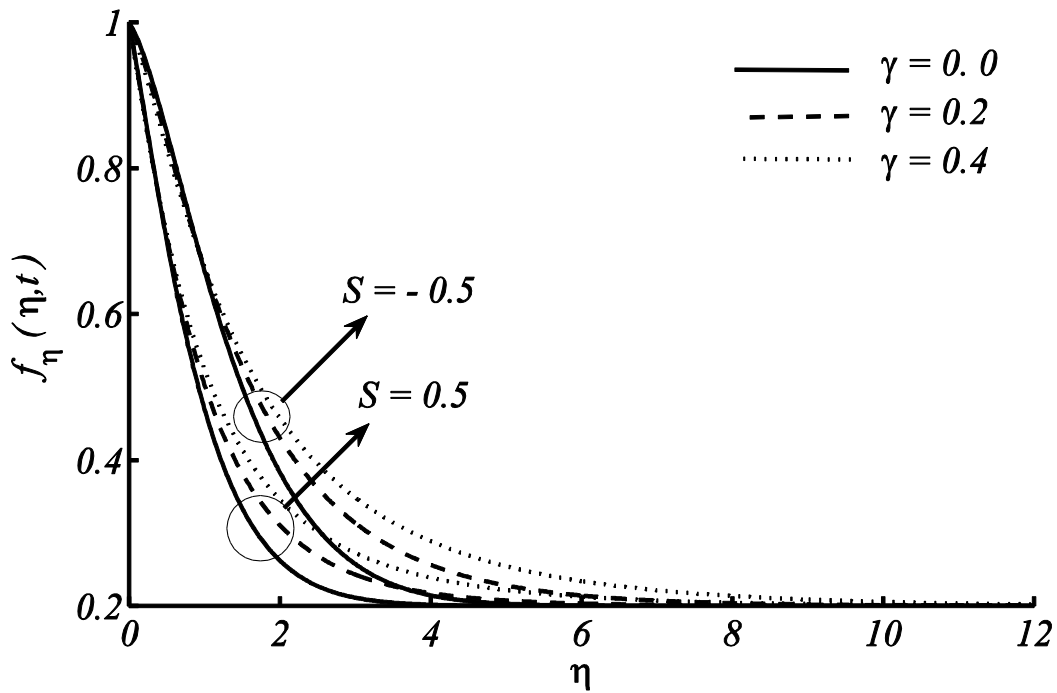


Figure 3.3: Velocity profile for different γ at $S = 0.5$ (suction) and $S = -0.5$ (injection) while $\beta = 2, \epsilon = 1, \lambda = 1, a/c = 0.2, t = \pi/4$.

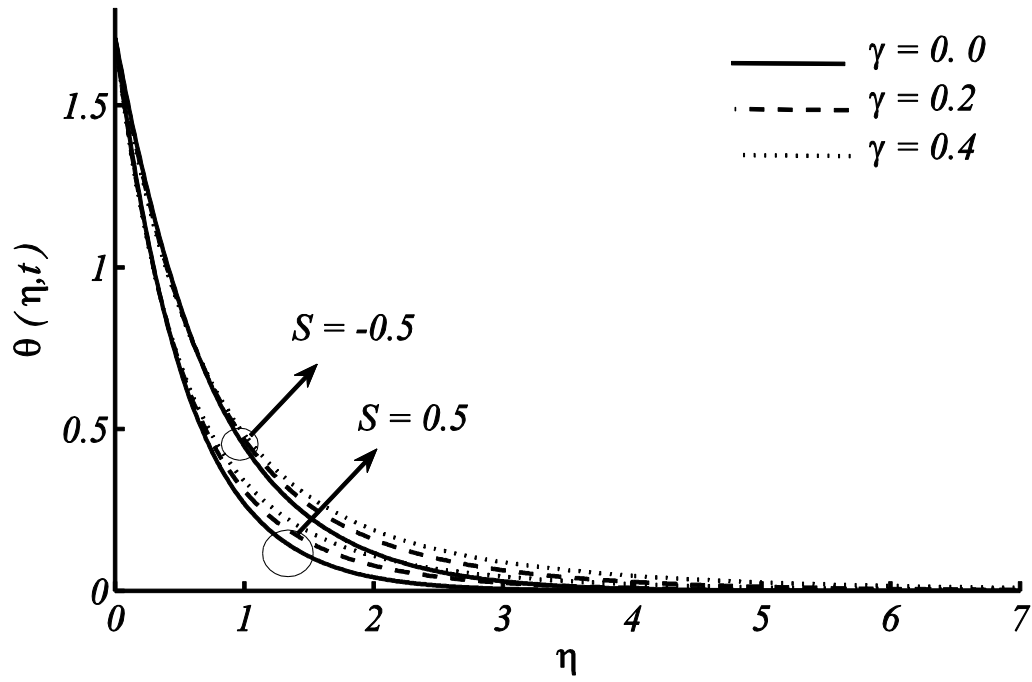


Figure 3.4: Temperature profile for different γ at $S = 0.5$ (suction) and $S = -0.5$ (injection) while $\beta = 2, \epsilon = 1, \lambda = 1, a/c = 0.2, t = \pi/4, Pr = 1$.

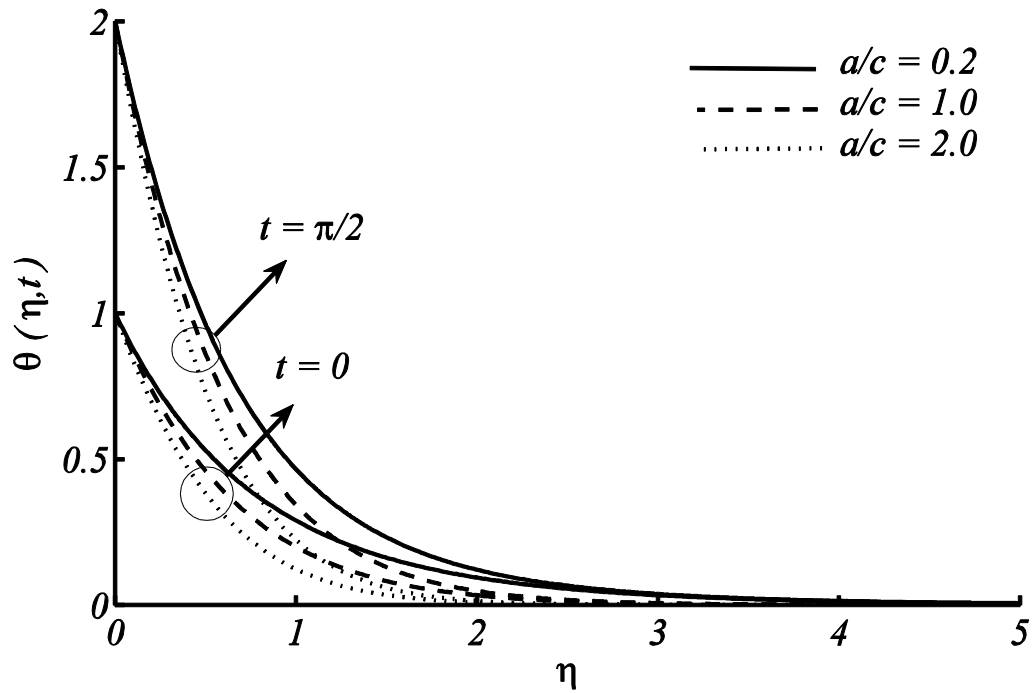


Figure 3.5: Temperature profile for different a/c at $t = 0$ and $t = \pi/2$ while $\gamma = 0.2, \beta = 2, \epsilon = 1, \lambda = 1, S = 0.2, Pr = 1$.

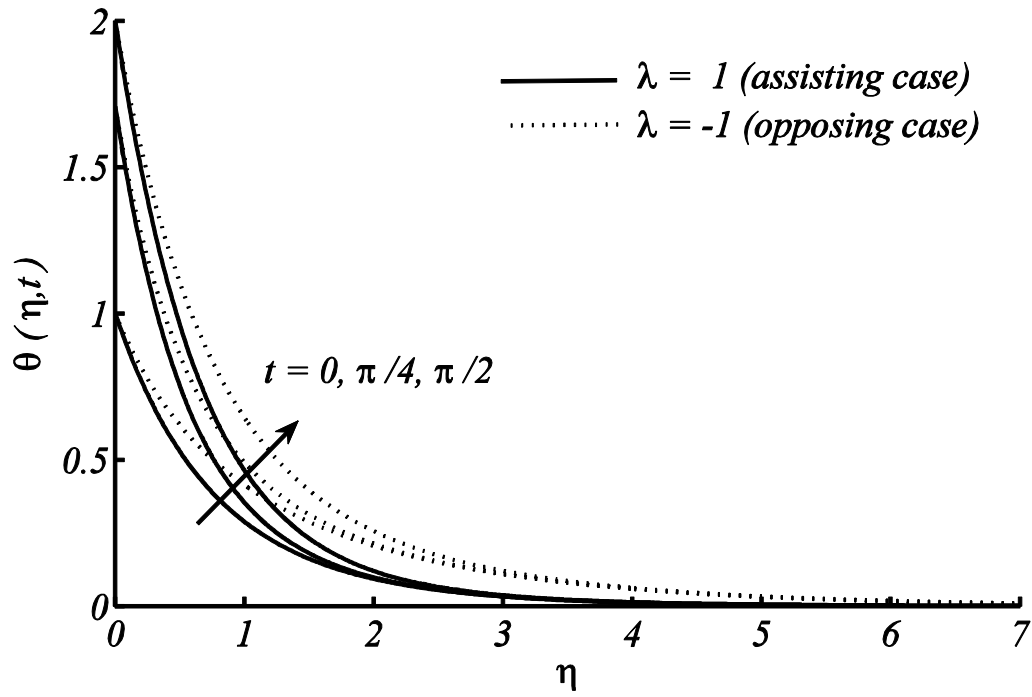


Figure 3.6: Temperature profile at $t = 0, \pi/4, \pi/2$ while $\gamma = 0.2, \beta = 2, \epsilon = 1, a/c = 0.2, S = 0.2, Pr = 1$.

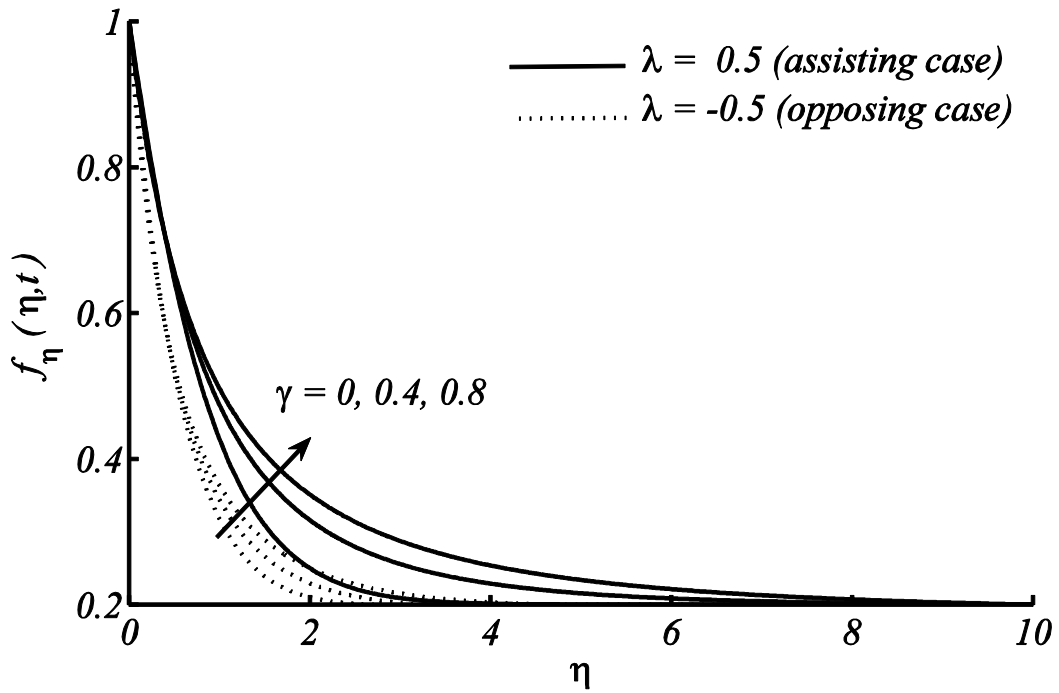


Figure 3.7: Velocity profile at $\gamma = 0, 0.4, 0.8$ while $\beta = 2, \epsilon = 1, S = 0.5, a/c = 0.2, t = \pi/4, Pr = 1$.

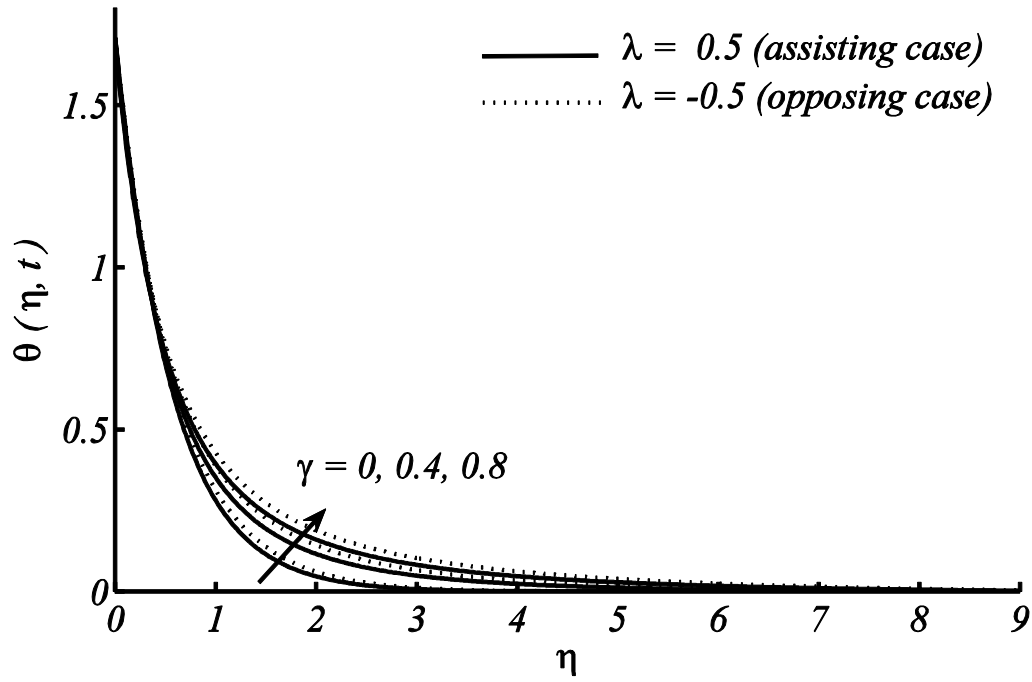


Figure 3.8: Temperature profile at $\gamma = 0, 0.4, 0.8$ while $\beta = 2, \epsilon = 1, S = 0.5, a/c = 0.2, t = \pi/4, Pr = 1$.

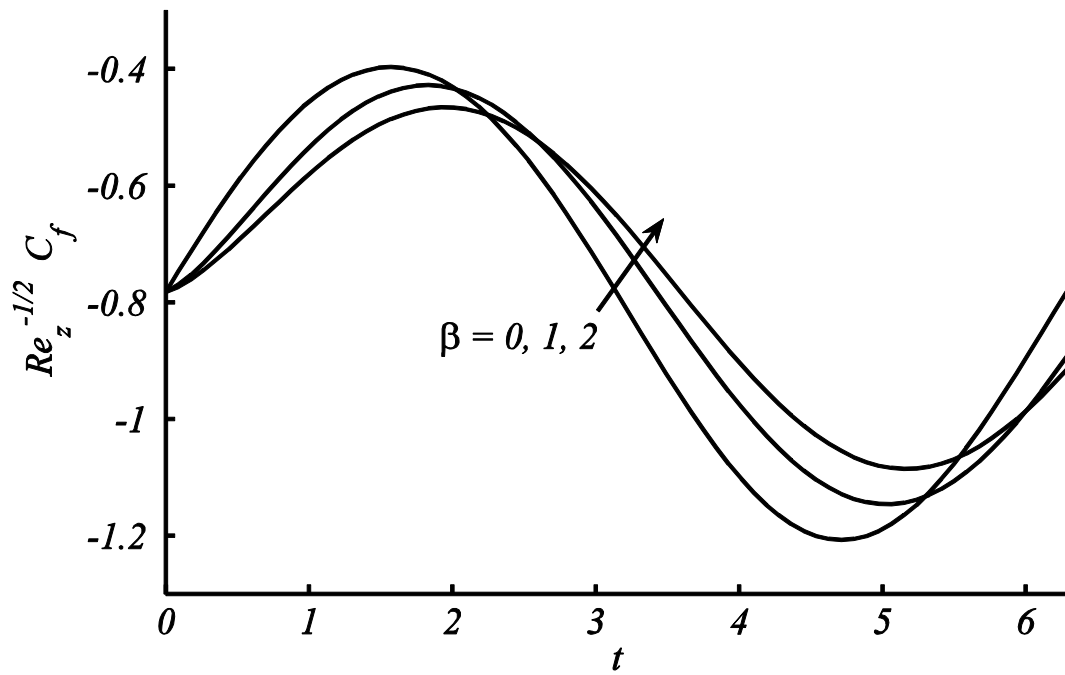


Figure 3.9: Variations in $Re_z^{1/2} C_f$ against time for different β while $\gamma = 0.2, \epsilon = 1, S = 0.5, a/c = 0.2, Pr = 1, \lambda = 1$.

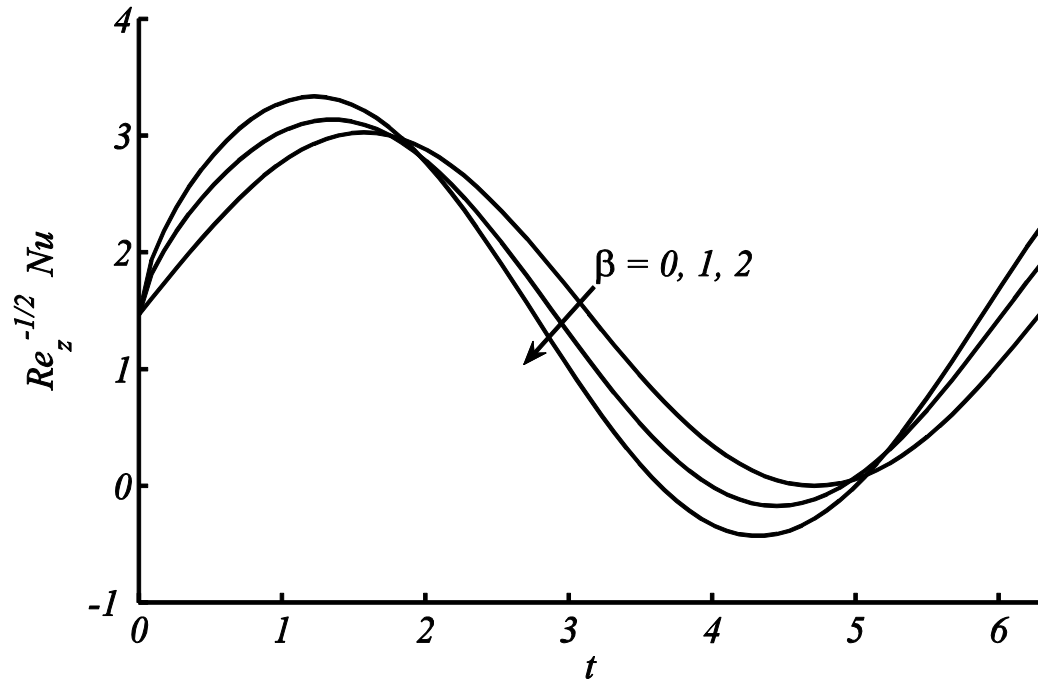


Figure 3.10: Variations in $Re_z^{-1/2} Nu_z$ against time for different β while $\gamma = 0.2, \epsilon = 1, S = 0.5, a/c = 0.2, Pr = 1, \lambda = 1$.

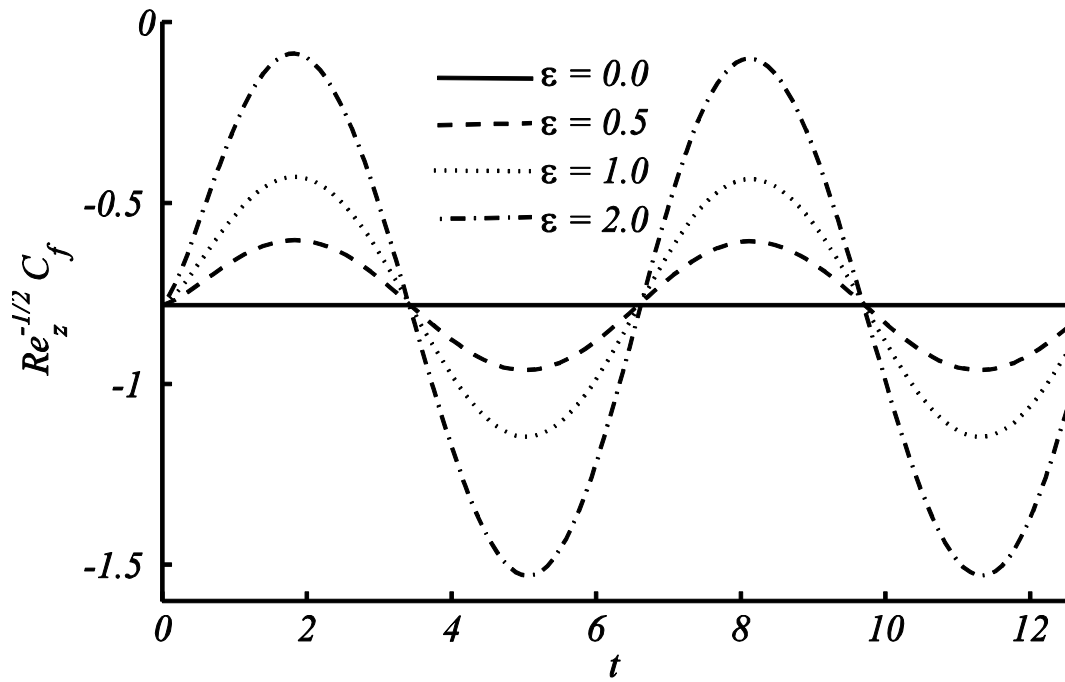


Figure 3.11: Variations in $Re_z^{1/2} C_f$ against time for different ϵ while $\gamma = 0.2, \beta = 1, S = 0.5, a/c = 0.2, Pr = 1, \lambda = 1$.

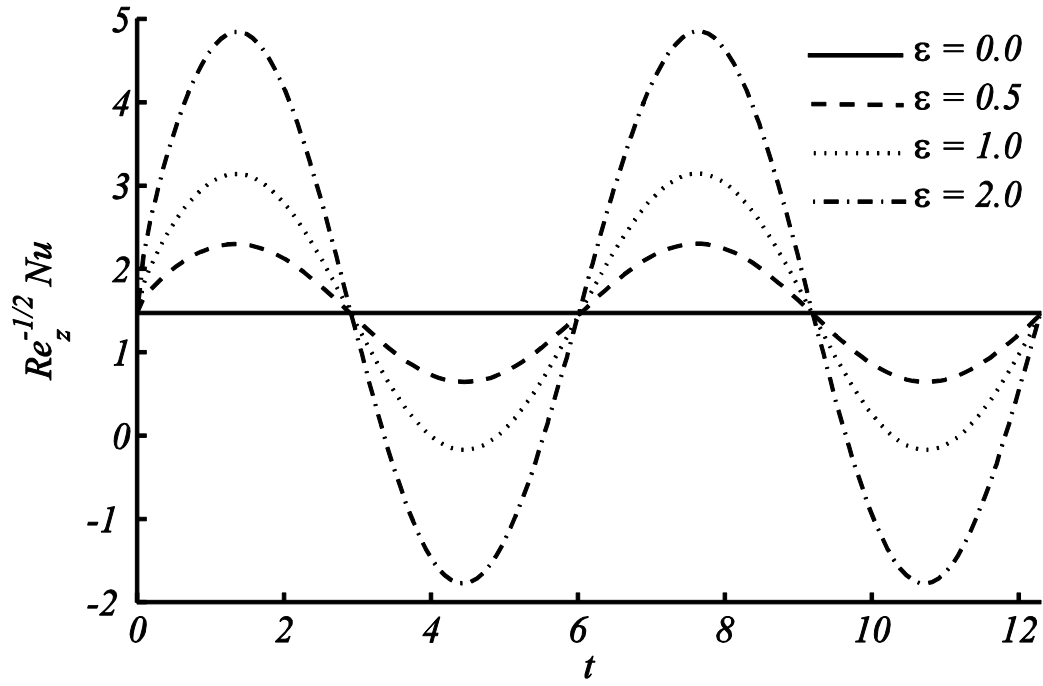


Figure 3.12: Variations in $Re_z^{-1/2} Nu_z$ against time for different ϵ while $\gamma = 0.2, \beta = 1, S = 0.5, a/c = 0.2, Pr = 1, \lambda = 1$.

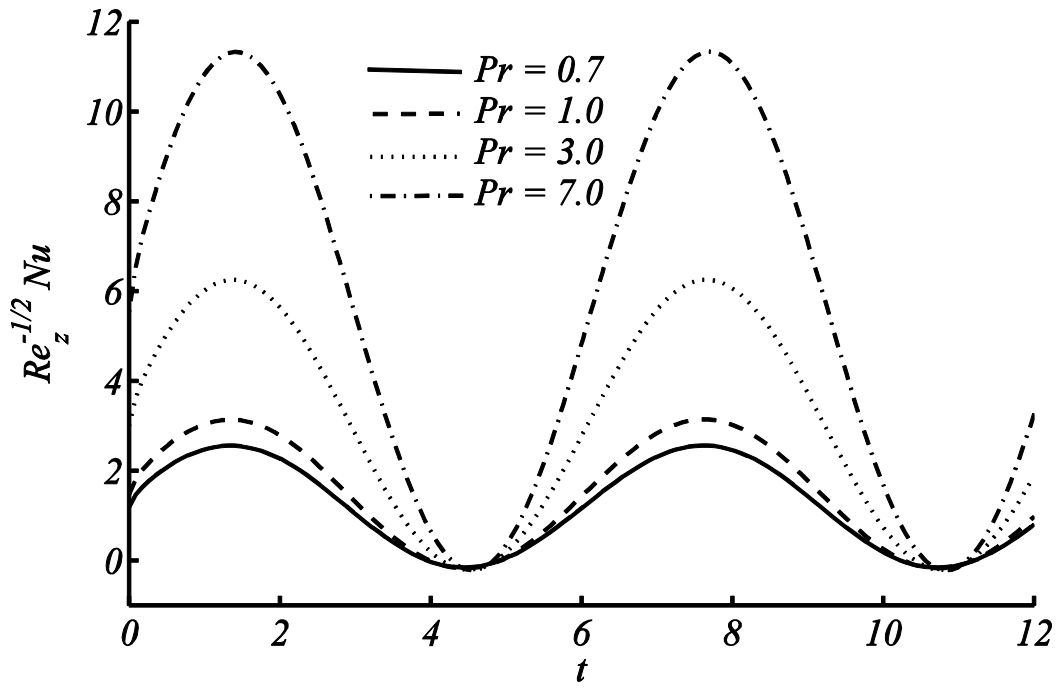


Figure 3.13: Variations in $Re_z^{-1/2} Nu_z$ against time for different Pr while $\gamma = 0.2, \beta = 1, S = 0.5, \epsilon = 1, a/c = 0.2, \lambda = 1$.

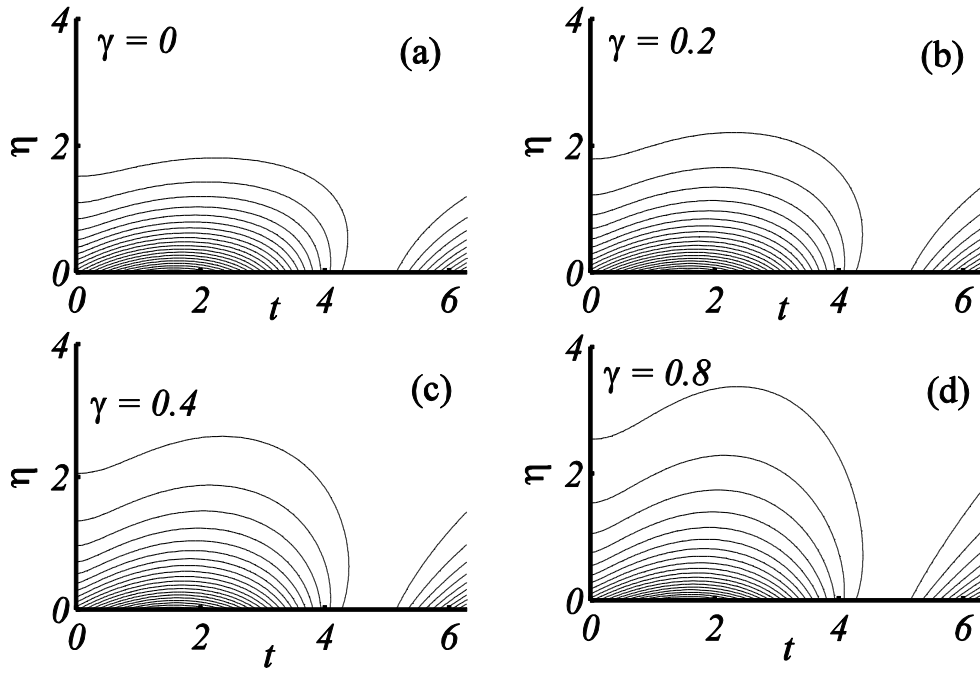


Figure 3.14: Isotherms for different γ while $\beta = 1, S = 0.5, \epsilon = 1, a/c = 0.2, \lambda = 1, Pr = 1$.

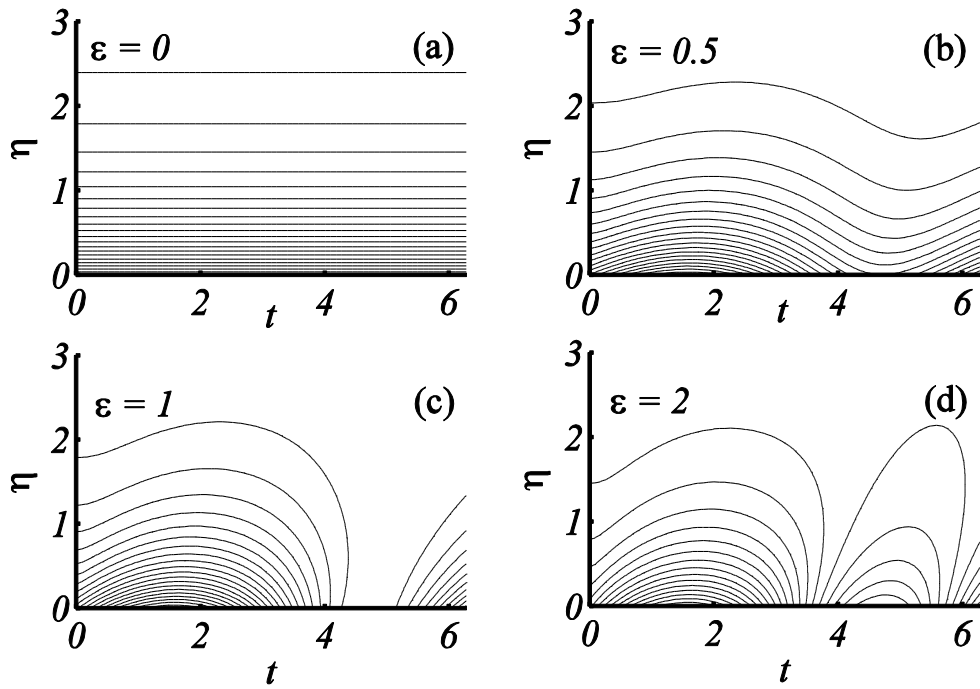


Figure 3.15: Isotherms for different ϵ while $\gamma = 0.2, \beta = 1, S = 0.5, a/c = 0.2, \lambda = 1, Pr = 1$.

3.4 Conclusions

In this chapter, the analysis of unsteady mixed convection stagnation point flow due to stretching cylinder with sinusoidal wall temperature is presented. The modeled equations are reduced into dimensionless form as partial differential equations and solved numerically with the help of Keller box method. The analysis is made in term of velocity, temperature profiles, skin friction and Nusselt number against different parameters of the problem. It is noted that the assisting buoyant flow increases the velocity profile and opposing buoyant flow decreases the velocity profile. The heat transfer rate increases due to increase in Prandtl number and amplitude of oscillation also increases with passage of time. Most importantly, this phenomenon of maximizing heat transfer near the stagnation point flow over a stretching cylinder can be enhanced by introducing the sinusoidal heat at the surface of the cylinder.

Chapter 4

Heat transfer analysis of Casson fluid flow due to stretching cylinder

This chapter analyses the combine effects of partial slip and prescribed surface heat flux on the heat transfer analysis of Casson fluid flow around the stretching cylinder. The physical model is represented as a system of ordinary differential equations. A very moderate and powerful technique namely Chebyshev Spectral Newton Iterative Scheme (CSNIS) is used to determine the solution of the governing equations. The comparison of computed numerical values of skin friction coefficient and the local Nusselt number is made with the results available in the literature. The accuracy and convergence of Chebyshev Spectral Newton Iterative Scheme is compared with finite difference scheme (Keller box method) through tables. The CPU time is calculated for both schemes. It is observed that CSNIS is efficient, less time consuming, stable and rapid convergent. Involved physical parameters, namely: the slip parameter, Casson fluid parameter, curvature parameter and Prandtl number are utilized to analyze the fluid movements and temperature distribution. The results show that the fluid velocity and the skin friction coefficient around the stretching cylinder are strongly influenced by the slip parameter. It is analysed that hydrodynamic boundary layer decreases and thermal boundary layer increases with the slip parameter. Influence of Casson fluid parameter on temperature profile provides the opposite behavior as compare to the slip parameter.

4.1 Problem formulation

Considered the flow of non-Newtonian Casson fluid outside the stretching cylinder of fixed radius R^* . The flow is assumed as steady, axi-symmetric and is subjected to laminar boundary layer assumptions. The surface of the cylinder is heated due to prescribed heat flux q_w . The physical model of the flow situation is shown in Figure 2.1. It is further assumed that cylinder is stretched in the axial direction with velocity V_w with wall temperature T_w and ambient temperature T_∞ . It is assumed that the wall temperature is larger than that of ambient temperature i.e., $T_w > T_\infty$. The rheological equations for non-Newtonian Casson fluid model are described in Eq. (1.11). For the problem under

consideration, the continuity and energy equations are same as in Eqs. (2.1) and (2.3). By means of boundary layer approximations, the momentum equation for Casson fluid model is

$$u \frac{\partial v}{\partial r} + v \frac{\partial v}{\partial z} = v \left(1 + \frac{1}{\beta^*} \right) \left(\frac{\partial}{\partial r} \left(r \frac{\partial v}{\partial r} \right) \right), \quad (4.1)$$

where $\beta^* = \mu_B \sqrt{2\pi}/p_y$ is known as Casson parameter. The boundary conditions which are imposed to the velocity components and temperature profile are

$$\begin{aligned} v = V_w + B_1 v \left(1 + \frac{1}{\beta^*} \right) \frac{\partial v}{\partial r}, \quad k \frac{\partial T}{\partial r} = -q_w(z), \quad u = 0 \text{ at } r = R^*, \\ v \rightarrow 0, \quad T \rightarrow T_\infty \text{ as } r \rightarrow R^*. \end{aligned} \quad (4.2)$$

Here $V_w = cz/l$ is the stretching velocity, B_1 is velocity slip factor with dimension $[T/L]$. Following the similarity transformation of Bachok and Ishak (2010) as

$$\eta = \frac{r^2 - R^{*2}}{2R^*} \sqrt{\frac{V_w}{vz}}, \quad \psi = \sqrt{vzV_w} R^* f(\eta), \quad T_w = T_\infty + \frac{q_w}{k} \sqrt{\frac{vz}{V_w}} \theta(\eta). \quad (4.3)$$

Utilizing the transformation (4.3), the velocity components in stream function notation given in Eq. (2.5) will be of the form

$$v = V_w f'(\eta) \text{ and } u = -\frac{R^*}{r} \sqrt{\frac{vz}{l}} f(\eta). \quad (4.4)$$

After substituting Eqs. (4.3) and (4.4) into Eqs. (4.1) and (2.3), we get the following governing equations in terms of ordinary differential equations

$$(1 + 2\gamma\eta) \left(1 + \frac{1}{\beta^*} \right) f''' + 2 \left(1 + \frac{1}{\beta^*} \right) \gamma f'' + f f'' - (f')^2 = 0, \quad (4.5)$$

$$(1 + 2\gamma\eta) \theta'' + 2\gamma\theta' + Pr(f\theta' - f'\theta) = 0, \quad (4.6)$$

where primes denote differentiation with respect to η . The boundary conditions in Eqs. (4.2) become

$$\begin{aligned} f(0) = 0, f'(0) = 1 + B \left(1 + \frac{1}{\beta^*} \right) f''(0), f'(\infty) = 0, \\ \theta'(0) = -1, \theta(\infty) = 0. \end{aligned} \quad (4.7)$$

where $B = B_1 v \sqrt{c/vl}$ is velocity slip parameter. The wall skin friction and the wall heat flux are

$$\tau_w = \mu_B \left(1 + \frac{1}{\beta^*} \right) \left(\frac{\partial v}{\partial r} \right)_{r=R^*}, \quad q_w = -k \left(\frac{\partial T}{\partial r} \right)_{r=R^*} \quad (4.8)$$

Upon using the similarity transformation (4.3) in Eq. (4.8), the expression for C_f and Nu which are already defined in chapters 2 and 3 can be written as

$$Re_z^{1/2} C_f = \left(1 + \frac{1}{\beta^*}\right) f''(0), \quad Re_z^{-1/2} Nu_z = \frac{1}{\theta(0)}. \quad (4.9)$$

4.2 Numerical Scheme

The system of nonlinear ordinary differential equations Eqs. (4.5) and (4.6) subject to boundary conditions (4.7) is solved for different values of involving parameters by an efficient numerical scheme namely: Chebyshev Spectral Newton Iterative Scheme (CSNIS). This scheme is mathematically simple and can be easily coded in MATLAB algorithm. It is based on Newton iterative scheme having convergence of order 2. It is therefore rapidly convergent as shown in Tables 4.4 and 4.5 and low-cost scheme with less CPU usage. The solution procedure is as follows:

In first step, we linearized Eqs. (4.5)–(4.7) by using Newton iterative scheme. For $(i + 1)^{th}$ iterates, we write

$$f_{i+1} = f_i + \delta f_i, \quad \theta_{i+1} = \theta_i + \delta \theta_i, \quad (4.10)$$

and for all other dependent variables. Using Eq. (4.10) in Eqs. (4.5–4.7), we obtained

$$\begin{aligned} c_{1,i} \delta f_i''' + c_{2,i} \delta f_i'' + c_{3,i} \delta f_i' + c_{4,i} \delta f_i &= R_{1,i}, \\ d_{1,i} \delta \theta_i'' + d_{2,i} \delta \theta_i' + d_{3,i} \theta_i + d_{4,i} \delta f_i' + d_{5,i} \delta f_i &= R_{2,i}, \end{aligned} \quad (4.11)$$

the boundary conditions become

$$\begin{aligned} \delta f_i(0) &= -f_i(0), \\ \delta f_i'(0) - B_1 \left(1 + \frac{1}{\beta^*}\right) \delta f_i''(0) &= 1 - f_i'(0) + B_1 \left(1 + \frac{1}{\beta^*}\right) f_i''(0), \\ \delta f_i'(\infty) &= -f_i'(\infty), \\ \delta \theta_i'(0) &= -1 - \theta_i(\infty), \quad \delta \theta_i(0) = -\theta_i(\infty). \end{aligned} \quad (4.12)$$

The coefficients $c_{j,i}$ ($j = 1, 2, 3, 4$), $d_{m,i}$ ($m = 1, 2, 3, 4, 5$) and $R_{n,i}$ ($n = 1, 2$) are

$$\begin{aligned} c_{1,i} &= (1 + 2\gamma\eta) \left(1 + \frac{1}{\beta^*}\right), \quad c_{2,i} = 2\gamma \left(1 + \frac{1}{\beta^*}\right) + f_i, \\ c_{3,i} &= -2f_i', \quad c_{4,i} = f_i'', \\ d_{1,i} &= (1 + 2\gamma\eta), \quad d_{2,i} = 2\gamma + Pr f_i, \quad d_{3,i} = -Pr f_i', \\ d_{4,i} &= -Pr \theta_i, \quad d_{5,i} = -Pr f_i', \\ R_{1,i} &= -(1 + 2\gamma\eta) \left(1 + \frac{1}{\beta^*}\right) f_i''' - 2\gamma \left(1 + \frac{1}{\beta^*}\right) f_i'' - f_i f_i'' + (f_i')^2, \\ R_{2,i} &= -(1 + 2\gamma\eta) \theta_i'' - 2\gamma \theta_i' - Pr(f \theta' - f' \theta). \end{aligned} \quad (4.13)$$

Now the obtained linear system of equations (4.11) subject to conditions (4.12) is solved by using the Spectral Collocation method with Chebyshev polynomial is used as a basis function (Motsa and Sibanda 2012, Motsa et al. 2014). The physical domain $[0, \infty]$ is shorten to finite domain $[0, L]$ where L is set as sufficiently large to achieve required accuracy. This finite domain again converted to $[-1, 1]$ by using transformation $\xi^* = 2\eta/L - 1$. The grid points between -1 and 1 are defined in term of Gauss-Lobatto collocation points defined by $\xi_j^* = \cos(\pi j/N)$, $j = 0, 1, 2, \dots, N$. The derivatives are calculated by Chebyshev differentiation matrix \mathbf{D} as suggested by Trefethen (2000). The above linear system of equations can be arranged in matrix form as

$$\begin{pmatrix} M_{11} & M_{12} \\ M_{21} & M_{22} \end{pmatrix} \begin{pmatrix} \delta f_i \\ \delta \theta_i \end{pmatrix} = \begin{pmatrix} R_{1,i} \\ R_{2,i} \end{pmatrix} \quad (4.14)$$

where

$$\begin{aligned} M_{11} &= c_{1,i}D^3 + c_{2,i}D^2 + c_{3,i}D + c_{4,i}I, \quad M_{12} = 0, \\ M_{21} &= d_{4,i}D + d_{5,i}I, \quad M_{22} = d_{1,i}D^2 + d_{2,i}D + d_{3,i}I. \end{aligned}$$

The obtained system of linear equations is solved by an iterative Gauss elimination method. MATLAB software is used to develop the algorithm for the above problem.

4.3 Results and Discussion

The nonlinear system of ordinary differential equations (4.5) and (4.6) subject to the boundary conditions (4.7) have been solved numerically using CSNIS. The computed results are compared with the numerical values obtained by Keller box method. The comprehensive study related to Keller box method can be found in the book by (Cebeci and Bradshaw 1984). In Table 4.1, the computed numerical values of the surface temperature $\theta(0)$ are compared with previously published results (Bachok and Ishak 2010) available in the literature. It is observed that the results are in excellent agreement. In Tables 4.2 and 4.3, the comparison of the values of skin friction coefficient and local Nusselt number with the Keller box method is given. The main finding of the tables is that the CSNIS has advantage over Keller box method in terms of time consumption. CSNIS reduces the cost over the time, which is need of the hour and we achieved excellent accuracy. In Tables 4.4 and 4.5, the computed values of $Re_z^{1/2}C_f$ and $\theta(0)$ are presented. These results show the validity and convergence CSNIS. In Table 4.4, it is observed that the values of $Re_z^{1/2}C_f$ converge rapidly after only 3 to 4 iterations. Table 4.5 clearly indicates that after performing few iterations, the present CSNIS results display an outstanding agreement with the results of Bachok and

Ishak (2010). It is also noted through Table 4.5 that for the case of stretching sheet ($\gamma = 0$), the results converge after first iteration. This authenticates the validity of the present scheme.

Figures 4.2–4.7 are plotted for various physical parameters namely: curvature parameter (γ), Casson fluid parameter (β^*), slip parameter (B) and Prandtl number Pr against both velocity $f'(\eta)$ and temperature $\theta(\eta)$ profiles. In Figures 4.2 and 4.3, the domain truncation parameter ' L ' and number of collocation points ' N ' are set as 15 and 82, respectively. Whereas in remaining figures L and N are set as 25 and 120, respectively. In Figure 4.2, influence of velocity profile against various values of curvature parameter (γ) is developed. It depicts that the velocity profile increases with increase of curvature parameter (γ) and growth in boundary layer thickness is noticed. Figure 4.3 demonstrates the variation in the temperature profile $\theta(\eta)$ for various values of curvature parameter (γ). As surface area of the cylinder will squeeze with increase in curvature parameter (γ), consequently, less surface area provides low heat transfer rate in other words temperature profile decreases with increase of curvature parameter (γ) near the surface of the cylinder. In Figure 4.4 effects of Casson fluid parameter (β^*) on velocity profile is presented. It is noticed that the increase in the non-Newtonian parameter (β^*) provides more resistance in fluid motion and resultantly velocity of the fluid gets slow down with an increase in Casson fluid parameter (β^*). Influence of temperature profile with Casson fluid parameter (β^*) is plotted in Figure 4.5. It is important to mention that highly viscous fluid (Casson fluid) provides more heat transfer rate as compare to the Newtonian fluid. These noticeable effects can be observed in Figure 4.5 that with an increase of Casson fluid parameter (β^*) temperature profile increases. In Figure 4.6, the mainstream velocity has been plotted against η for various values of slip parameter B . It is noted that velocity profiles decrease near the wall with increase of B . It is due to the reason that when slip parameter increases in magnitude, the fluid near the wall no longer move with the stretching velocity of surface. By increase in the value of B the surface of the cylinder become smoother so that the pulling of the stretching surface rarely transmitted to the fluid. It is obvious that B has a substantial effect on the solutions. In Figure 4.7, temperature profiles are plotted against η for various values of slip parameter B . It is depicted that temperature of the fluid enhances with increase in slip parameter B . Figure 4.8 presents the variation in temperature profile due to increase in Pr . It is seen that the increment in Pr reduces the thermal boundary layer thickness.

Table 4.1: Variation of $\theta(0)$ for different values of γ and Pr when $\beta^* \rightarrow \infty$ and $B = 0$

γ	Pr	Analytic solution of Eq. (4.8)	Numerical Results Bachok and Ishak (2010)	Present Results (CSNIS)
Bachok and Ishak (2010)				
0	0.72	1.236657472	1.2367	1.2366574712
	1	1.000000000	1.0000	0.9999999999
	6.7	0.3333030614	0.3333	0.3333030614
	10	0.2687685151	0.2688	0.2687685151
1	0.72		0.8701	0.8700421639
	1		0.7439	0.7438521133
	6.7		0.2966	0.2965389644
	10		0.2442	0.2441266335

Table 4.2: Variation of $Re_z^{1/2} C_f$ for different values of γ, β^*, B .

γ	β^*	B	Keller box Scheme	CPU time (seconds)	CSNIS	CPU time (seconds)	Error
0	1	0.1	-1.17286	7.957862	-1.17286	0.070381	10^{-5}
		0.5	-0.72221	12.978531	-0.72221	0.066410	10^{-5}
	10	0.1	-0.90909	5.330466	-0.90909	0.067188	10^{-5}
		0.5	-0.60860	5.911651	-0.60860	0.071580	10^{-5}
	100	0.1	-0.87588	5.324875	-0.87588	0.068287	10^{-5}
		0.5	-0.59300	5.937075	-0.59300	0.078705	10^{-5}
	∞	0.1	-0.87208	5.282584	-0.87208	0.070348	10^{-5}
		0.5	-0.59120	5.956520	-0.59120	0.070998	10^{-5}
1	1	0.1	-1.64185	7.716986	-1.64188	0.051344	3.0×10^{-5}
		0.5	-0.91986	13.686686	-0.91986	0.054036	10^{-5}
	10	0.1	-1.19747	6.673299	-1.19748	0.056144	1.0×10^{-5}
		0.5	-0.75060	6.754250	-0.75061	0.057946	1.0×10^{-5}
	100	0.1	-1.14434	6.735931	-1.14436	0.054190	2.0×10^{-5}
		0.5	-0.72799	6.699626	-0.72799	0.058315	10^{-5}
	∞	0.1	-1.13830	7.448435	-1.13832	0.058091	2.0×10^{-5}
		0.5	-0.72538	6.749316	-0.72539	0.056084	1.0×10^{-5}

Table 4.3: Variation of $Re_z^{-1/2}Nu_z$ for different values of γ , Pr and β^* when $B = 0.5$.

γ	β^*	Pr	Finite difference	CPU time (seconds)	Iterative Scheme	CPU time (seconds)	Error
0	1	0.7	0.69609	12.793637	0.69609	0.0703620	10^{-5}
		7.0	2.51384	12.881962	2.51380	0.070446	4.0×10^{-5}
	10	0.7	0.67216	5.916910	0.67216	0.072338	10^{-5}
		7.0	2.57226	6.022827	2.57222	0.070590	4.0×10^{-5}
	∞	0.7	0.66611	6.098248	0.66611	0.077956	10^{-5}
		7.0	2.57853	6.047961	2.57850	0.077398	3.0×10^{-5}
1	1	0.7	0.97388	13.636132	0.97389	0.052239	1.0×10^{-5}
		7.0	2.68205	13.643384	2.68209	0.054686	4.0×10^{-5}
	10	0.7	0.97410	6.643172	0.97412	0.055505	2.0×10^{-5}
		7.0	2.80726	6.574281	2.80732	0.056434	6.0×10^{-5}
	∞	0.7	0.97143	6.663579	0.97145	0.058720	2.0×10^{-5}
		7.0	2.82221	6.594247	2.82226	0.055463	5.0×10^{-5}

Table 4.4: Values of $Re_z^{1/2}C_f$ at different iteration.

		$\gamma = 0, \beta^* = \infty$		$\gamma = 1, \beta^* = 1$	
		$B = 0.1$	$B = 0.5$	$B = 0.1$	$B = 0.5$
$(Re_z^{1/2}C_f) \rightarrow$	Iterations ↓				
	1	-0.8695652	-0.57142857	-1.53508496	-0.84615333
	2	-0.8720819	-0.59108397	-1.63214914	-0.91558621
	3	-0.872082	-0.59119547	-1.64168650	-0.91981240
	4	-0.8720824	-0.59119548	-1.64187579	-0.91986053
	5	-0.8720824	-0.59119548	-1.64187589	-0.91986054
	6	-0.872082	-0.5911954	-1.641875899	-0.919860545

Since the Prandtl number (Pr) denotes the ratio of kinematic viscosity to thermal diffusivity, so as the viscosity of the fluid increases, the heat transfer rate enhances due to which the temperature of fluid decreases. Figure 4.9 is plotted for $Re_z^{1/2}C_f$ against slip parameter (B) for the different values of β^* . The absolute value of $Re_z^{1/2}C_f$ gives higher friction with the wall for $\beta^* = 0.5$ and 1 as compare to that of Newtonian fluid ($\beta^* \rightarrow \infty$). It is also observed that with increase in the value of B , the drag in the fluid near the surface

Table 4.5: Comparison with analytical and numerical results of Bachok and Ishak (2010) and CSNIS results

		$\gamma = 0$		$\gamma = 1$	
Iterations↓		$Pr = 0.72$	$Pr = 6.7$	$Pr = 0.72$	$Pr = 6.7$
$\theta(0) \rightarrow$	1	1.236657471	0.333303061	0.950775246	0.294388703
	2	1.236657471	0.333303061	0.843083154	0.295172498
	3	1.236657471	0.333303061	0.866247457	0.296395959
	4	1.236657471	0.333303061	0.869928748	0.296535240
	5	1.236657471	0.333303061	0.870042029	0.296538958
	6	1.236657471	0.333303061	0.870042164	0.296538963
	7	1.236657471	0.333303061	0.870042164	0.296538963
	8	1.236657471	0.333303061	0.870042164	0.296538963
Analytical→		1.236657472	0.3333030614		
Numerical→		1.2367	0.3333	0.8701	0.2966

increases for both Newtonian and non-Newtonian fluids. Figure 4.10 is plotted for the values of $Re_z^{1/2} C_f$ against Casson fluid parameter for various values of curvature parameter (γ). The value of $Re_z^{1/2} C_f$ is decreasing with the increase of curvature parameter (γ) against any fixed values of Casson fluid parameter (β^*). These results also validate the findings in Figure 4.2. Figure 4.11 is drawn for $Re_z^{-1/2} Nu_z$ against slip parameter B_1 for the different values of β^* . For small value of B , increase of β^* results in reduction of heat transfer rate and for large value of B , heat transfer rate enhances. Figure 4.12 is plotted for $Re_z^{-1/2} Nu_z$ against Casson fluid parameter (β^*) for the different values of curvature parameter γ . With increase in γ , the surface area of cylinder reduces due to which heat transfer rate increases and same effects are observed for increasing values of β^* .

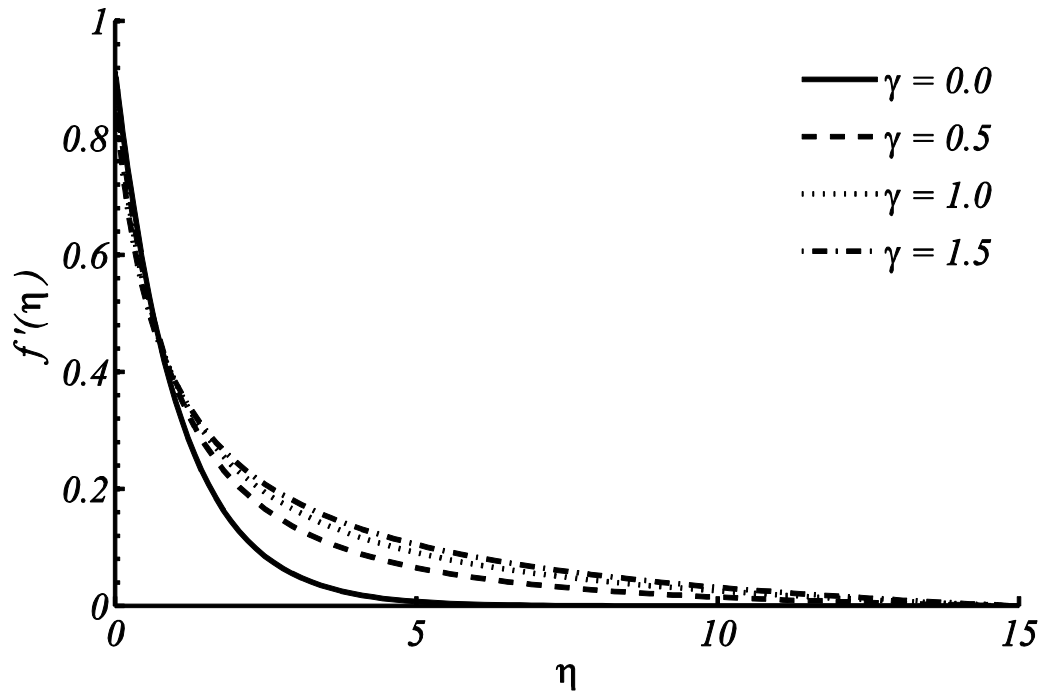


Figure 4.2: Velocity profile for different γ with $B = 0.1$, and $\beta^* \rightarrow \infty$.

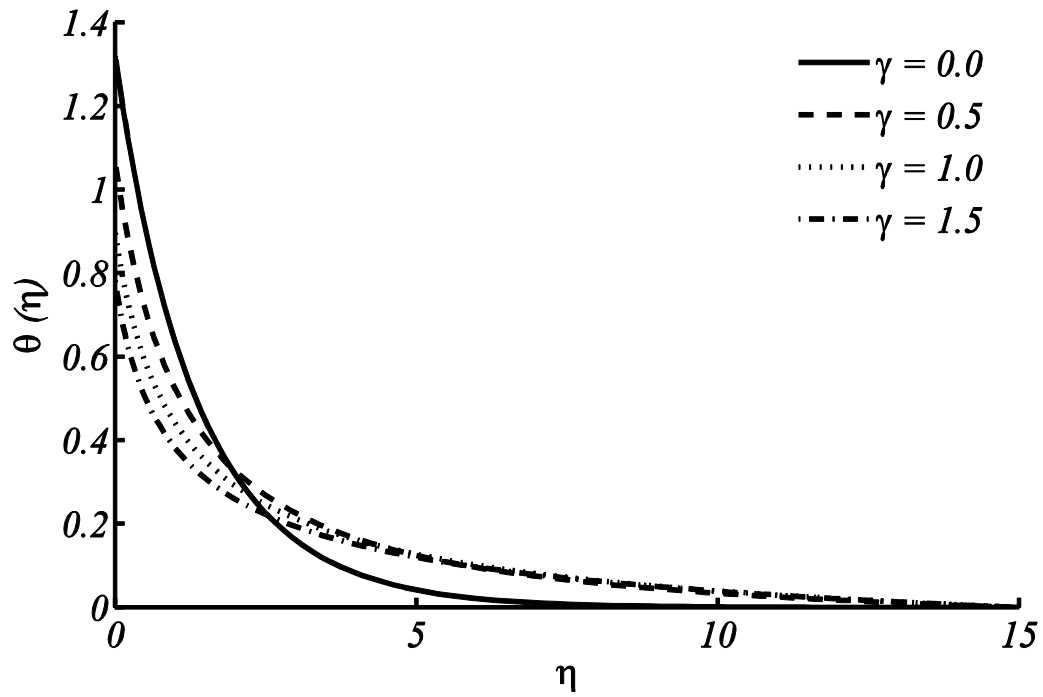


Figure 4.3: Temperature profile for different γ with $Pr = 0.7$, $B = 0.1$, and $\beta^* \rightarrow \infty$.

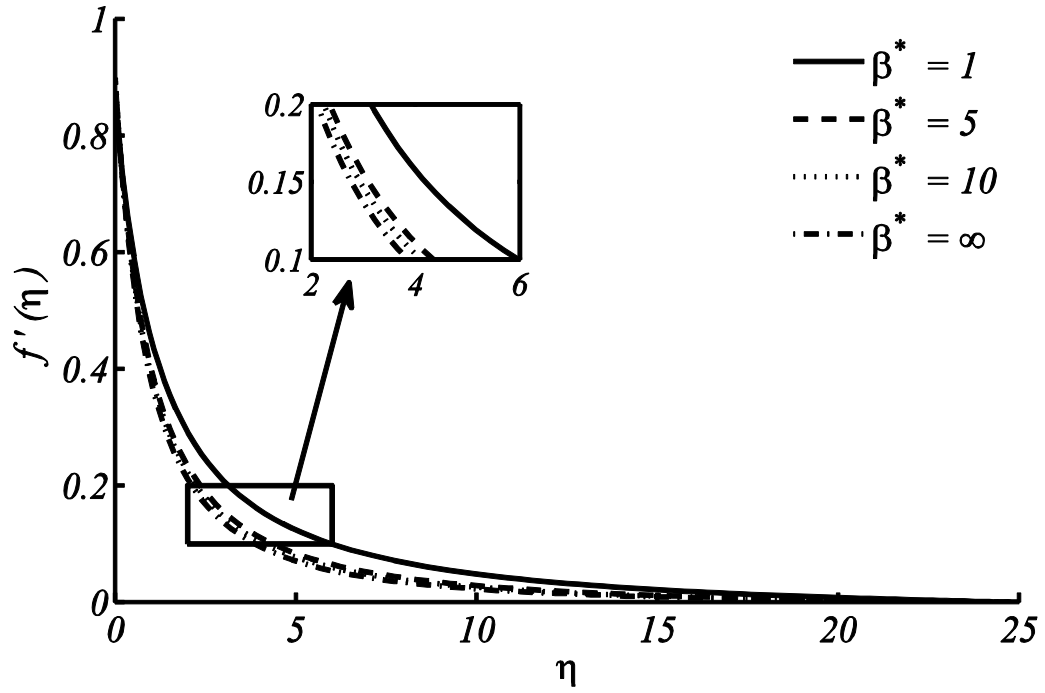


Figure 4.4: Velocity profile at different β^* with $B = 0.1$, and $\gamma = 0.5$.

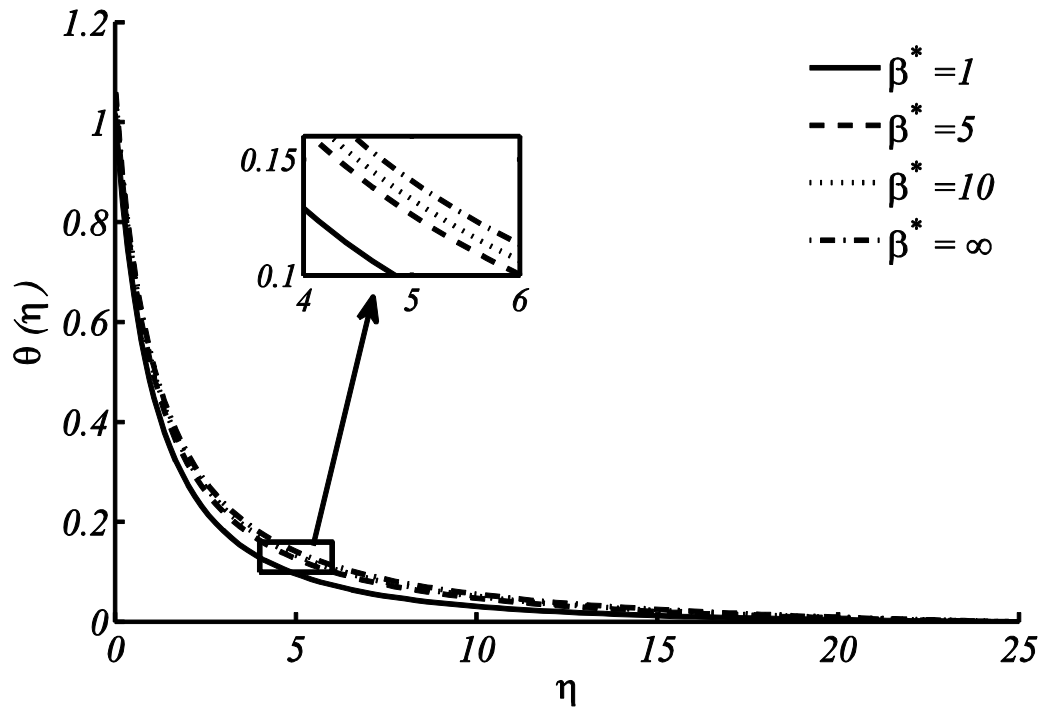


Figure 4.5: Temperature profile at different β^* with $Pr = 0.7$, $B = 0.1$, and $\gamma = 0.5$.

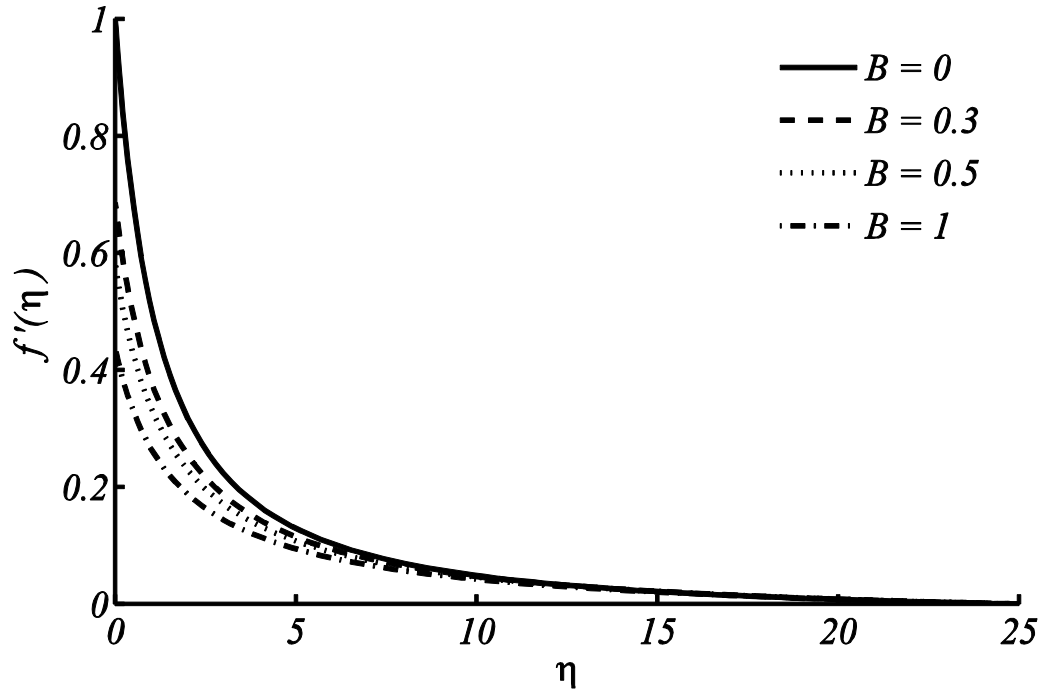


Figure 4.6: Velocity profile at different B with $\beta^* = 1$ and $\gamma = 0.5$.

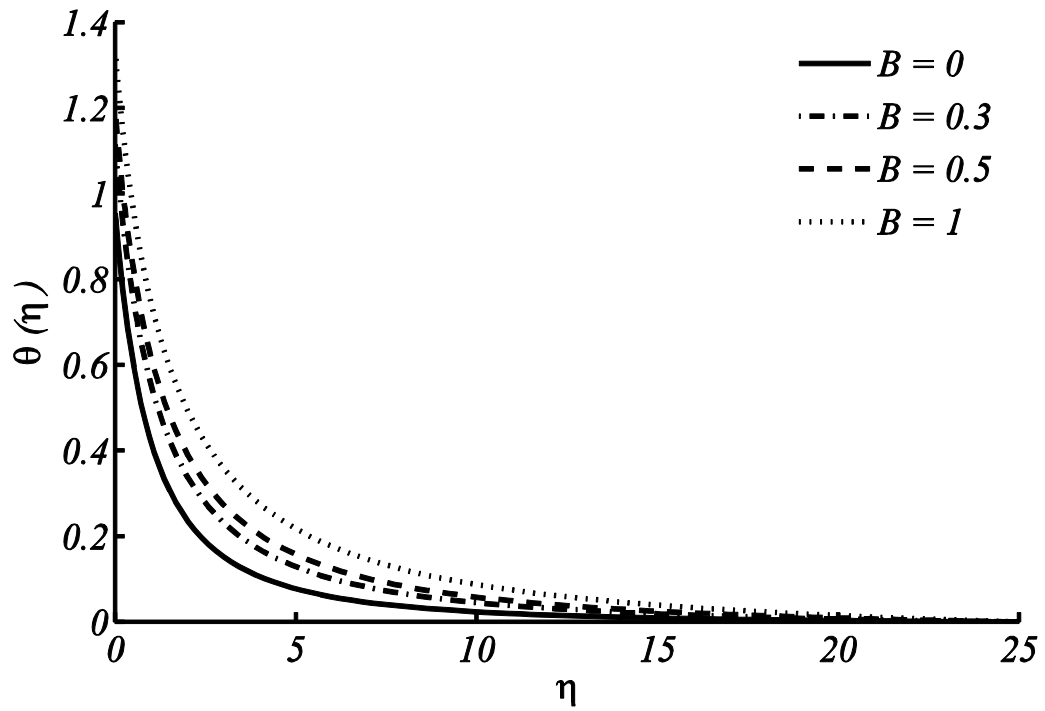


Figure 4.7: Temperature profile at different B with $Pr = 0.7$, $\beta^* = 1$, and $\gamma = 0.5$.

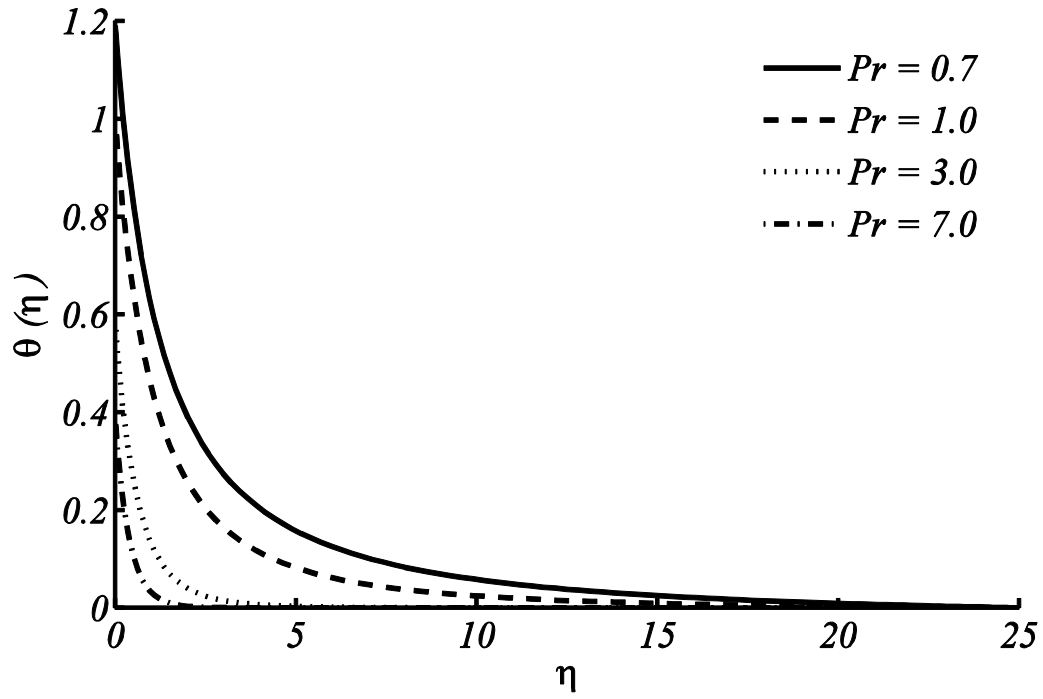


Figure 4.8: Temperature profile at different Pr with $B = 0.5, \beta^* = 1$, and $\gamma = 0.5$.

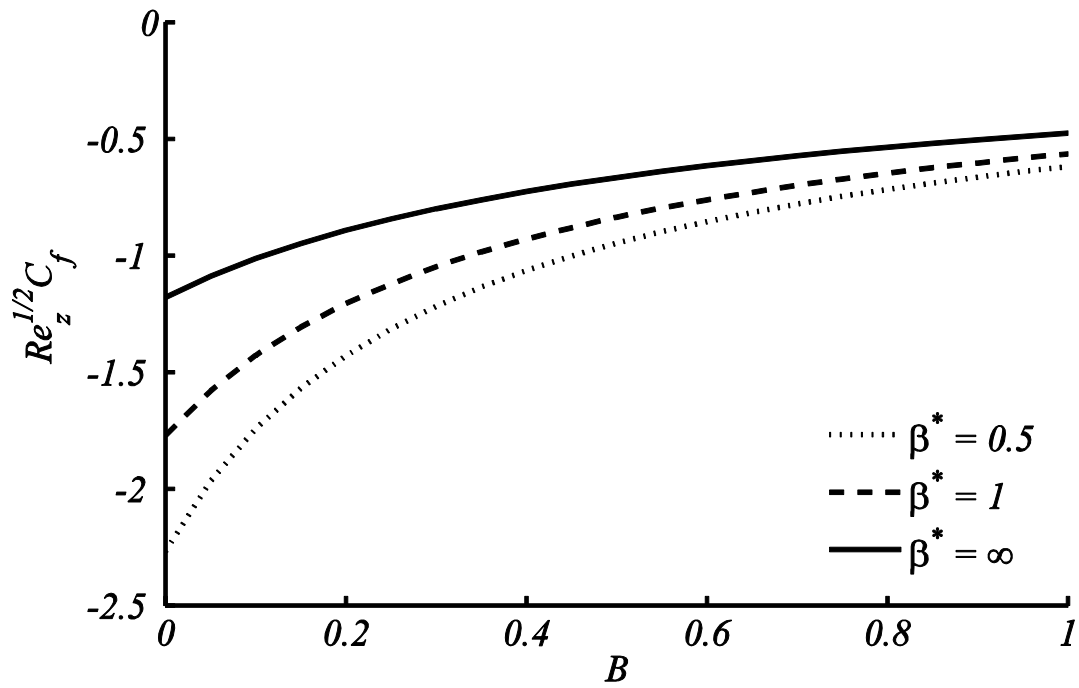


Figure 4.9: Variation in $Re_z^{1/2} C_f$ against slip parameter B at different β^* .

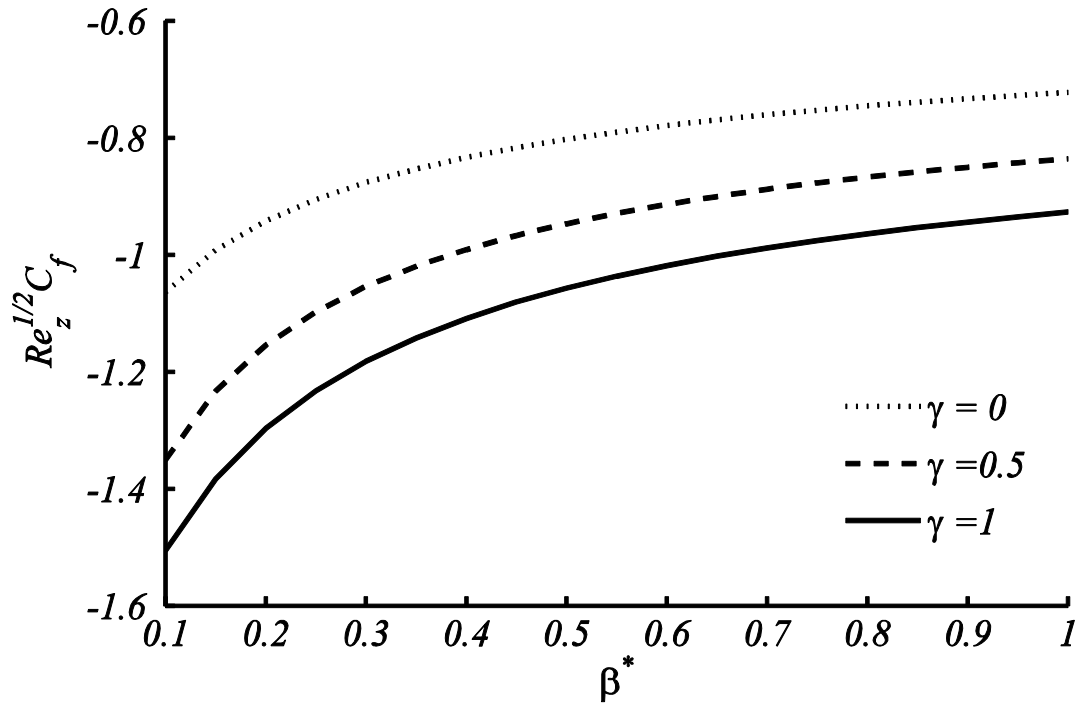


Figure 4.10: Variations in $Re_z^{1/2} C_f$ against Casson fluid parameter β^* at different γ .

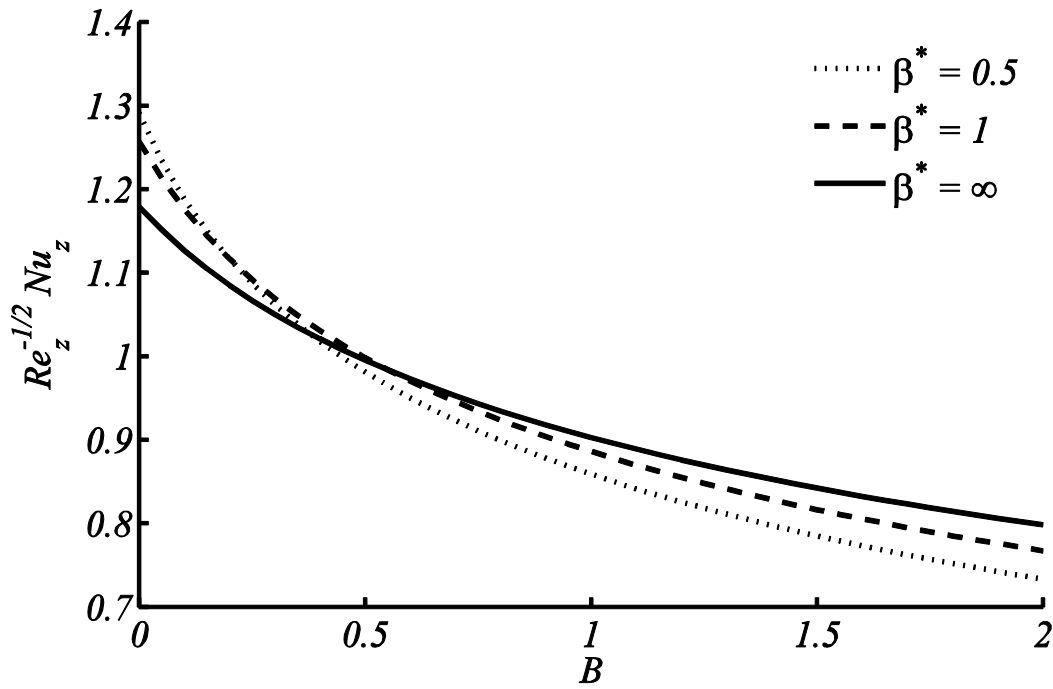


Figure 4.11: Variation in $Re_z^{-1/2} Nu_z$ against slip parameter B at different β^* .

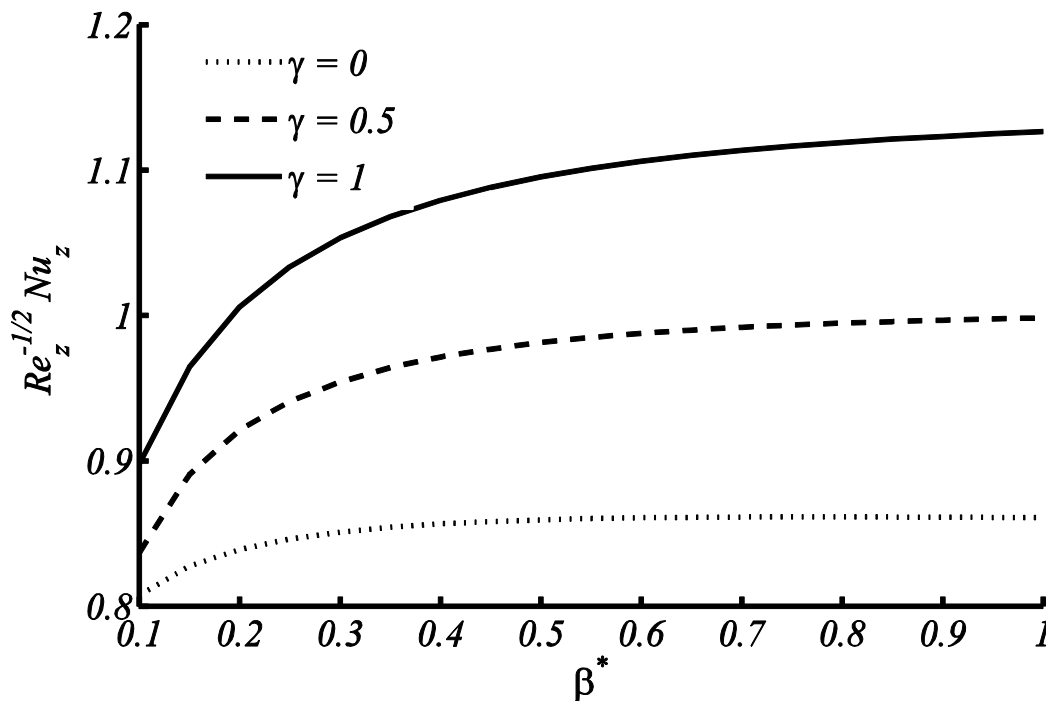


Figure 4.12: Variation in $Re_z^{-1/2} Nu_z$ against Casson fluid parameter β^* at different γ .

4.4 Conclusions

The numerical investigation of heat transfer analysis of non-Newtonian Casson fluid due to stretching cylinder with partial slip and prescribed heat flux is this performed in this chapter. For computation purpose, the Chebyshev Spectral Newton Iteration Scheme (CSNIS) is utilized. It is observed that the CSNIS is efficient, less time consuming, stable and rapid convergent. The computed results by this scheme have excellent agreement with analytical solution (see Table 4.1) and Keller box method (see Table 4.2). The present investigations help to conclude that the velocity is decreasing function of Casson fluid parameter (β^*) and temperature profile is increasing with increase in Casson fluid parameter (β^*). The momentum and thermal boundary layer thickness increases with increase of curvature of cylinder. Absolute skin friction gives higher friction for small non-Newtonian parameter (β^*) as compare that of Newtonian fluid ($\beta^* \rightarrow \infty$) and absolute value of skin friction coefficient increases with the increase of curvature of cylinder. For small values of slip parameter (B), reduction in the values of $Re_z^{-1/2} Nu_z$ has been observed with increase of Casson fluid parameter (β^*).

Chapter 5

Heat transfer analysis of Walters-B fluid flow over a stretching cylinder

In this chapter, two dimensional hydromagnetic flow and heat transfer of Walters-B fluid towards stagnation point region over a stretching cylinder is discussed. Constitutive equations are transformed into dimensionless form by means of suitable similarity transformations. Spectral Quasi Linearization Method (SQLM) is employed to obtain the solution of similarity equations. Comparison of computed results with existing results in limiting case of a flat sheet is also provided through Table. Analysis of obtained results is performed through graphs to discuss the influence of emerging parameters on the velocity and temperature profiles. The flow and heat transfer characteristics are analyzed through parameters representing curvature of cylinder, velocity ratio parameter, magnetic parameter and Weissenberg number. It is obvious that the magnetic field applied externally suppress the bulk motion and alters the momentum boundary layer thickness. The drag and heat transfer rate on the surface of cylinder are examined through skin friction and heat transfer coefficients. Furthermore, streamlines are drawn to see the flow pattern.

5.1 Formulation of problem

Let us consider the steady the flow of Walters-B fluid near the stagnation point over an horizontal stretching cylinder of radius R^* . It is assumed that the surface of the cylinder is at the temperature T_w , the ambient temperature is T_∞ with $T_w > T_\infty$. The cylindrical coordinate system is used to model the flow problem in which z -axis is taken along the horizontal direction and r -axis is along the vertical direction respectively. A constant magnetic field $\mathbf{B}(B_0, 0, 0)$ is applied along the radial direction of the flow. It is assumed that the fluid is electrically conducting in conjecture of low magnetic Reynolds number. Moreover, it is assumed that the effects of induced magnetic field effects are very small as compared to that of applied magnetic field neglected. This whole situation is summarized in Figure 5.1.

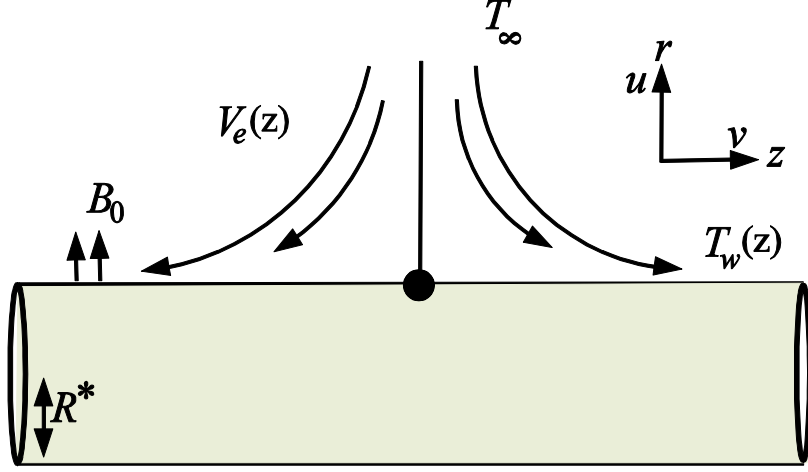


Figure 5.1: Physical model and coordinate system.

The general transport equations for Walters-B fluid are (Beard and Walters 1964; Nandeppanavar et al. 2010)

$$\text{div} \mathbf{V} = 0, \quad (5.1)$$

$$\rho \frac{d\mathbf{V}}{dt} = \text{div} \mathbf{S} - \rho \mathbf{b}, \quad (5.2)$$

$$\rho c_p \left(\frac{\partial T}{\partial t} + \mathbf{V} \cdot \nabla T \right) = \nabla \cdot k \nabla T, \quad (5.3)$$

where \mathbf{V} is time independent velocity vector, ρ is the density of the fluid, \mathbf{S} is Cauchy stress tensor, \mathbf{b} is the external body force, c_p represents specific heat, T is the temperature and k is the fluid thermal conductivity.

The constitutive equation for Walters-B fluid is given by

$$\mathbf{S} = -p\mathbf{I} + \boldsymbol{\tau}, \quad (5.4)$$

$$\boldsymbol{\tau} = 2\eta_0 \mathbf{A}_1 - 2k_0 \frac{d\mathbf{A}_1}{dt} \quad (5.5)$$

here \mathbf{S} is the Cauchy stress tensor, $\boldsymbol{\tau}$ is the extra stress tensor, \mathbf{I} is a unit tensor, η_0 is the viscosity at zero shear rate, k_0 is the elasticity of the fluid, and \mathbf{A}_1 is the first Rivlin-Erickson tensor. Incorporating the usual boundary layer assumption $O(v) = O(z) = 1, O(u) = O(r) = \delta$, and $O(v) = O(k_0) = \delta^2$, where δ represents the boundary layer thickness which is very small as compare to the length of the cylinder (see Schlichting and Gersten 2003). The dominant order terms have been retained and neglected the small order terms (i.e. δ and δ^2 etc.). The Eqs. (5.1)–(5.3) reduce to the following form

$$\frac{\partial(ru)}{\partial r} + \frac{\partial(rv)}{\partial z} = 0, \quad (5.6)$$

$$\begin{aligned}
u \frac{\partial v}{\partial r} + v \frac{\partial v}{\partial z} &= V_e(z) \frac{\partial V_e(z)}{\partial z} + v \left(\frac{\partial v}{r \partial r} + \frac{\partial^2 v}{\partial r^2} \right) \\
&+ \frac{k_0}{\rho} \left(\frac{3}{r} \frac{\partial v}{\partial z} \frac{\partial}{\partial r} \left(r \frac{\partial v}{\partial r} \right) + \frac{\partial v}{r \partial r} \frac{\partial}{\partial r} \left(r \frac{\partial v}{\partial r} \right) - \frac{v}{r} \frac{\partial}{\partial r} \left(r \frac{\partial^2 v}{\partial r \partial z} \right) \right. \\
&\left. - \frac{u}{r} \frac{\partial}{\partial r} \left(r \frac{\partial^2 v}{\partial r^2} \right) \right) - \frac{\sigma B_0^2}{\rho} (V_e(z) - v),
\end{aligned} \tag{5.7}$$

$$u \frac{\partial T}{\partial r} + v \frac{\partial T}{\partial z} = \alpha \frac{\partial}{\partial r} \left(r \frac{\partial T}{\partial r} \right), \tag{5.8}$$

where $u(r, z)$ and $v(r, z)$ are radial and transverse components of velocity, ν is the kinematic viscosity, σ is the electrical conductivity of fluid and α is the fluid thermal diffusivity. The relevant boundary conditions are

$$\begin{aligned}
&\left. \begin{aligned} v(r, z) &= V_w(z) = \frac{cz}{l}, u(r, z) = 0 \\ T(r, z) &= T_w = T_\infty + T_0 \left(\frac{z}{l} \right)^{n^*} \end{aligned} \right\} \text{ at } r = R^*, \\
&v(r, z) = V_w(z) = \frac{az}{l}, T(r, z) \rightarrow T_\infty \text{ as } r \rightarrow \infty.
\end{aligned} \tag{5.9}$$

Eqs. (5.6)–(5.8) governing the two-dimensional flow in the plane $r \geq R^*$, $-\infty < z < +\infty$ subject to boundary condition (5.9) are not amenable to analytic solution. For numerical solution, we introduce the following transformations:

$$\eta = \frac{r^2 - R^{*2}}{2R^*} \sqrt{\frac{c}{\nu l}}, \psi = \sqrt{\frac{\nu c}{l}} z R^* f(\eta), T = T_\infty + T_0 \left(\frac{z}{l} \right)^{n^*} \theta(\eta). \tag{5.10}$$

In above transformations, stream function ψ is related to velocity components as $u = -r^{-1} \partial \psi / \partial z$ and $v = r^{-1} \partial \psi / \partial r$, η is the similarity variable, $f(\eta)$ and $\theta(\eta)$ are the dimensionless velocity function and temperature field. With the help of above transformations, Eq. (5.6) is identically satisfied and Eqs. (5.7) and (5.8) take the following form

$$\begin{aligned}
&(1 + 2\gamma\eta)f'''' + 2\gamma f'' + f f'' - (f')^2 + 4We\gamma(f' f'' + f f''') \\
&+ (1 + 2\gamma\eta)We(f f^{iv} - 2f' f''' + (f'')^2) - M^2 \left(f' - \frac{a}{c} \right) + \left(\frac{a}{c} \right)^2 = 0,
\end{aligned} \tag{5.11}$$

$$(1 + 2\gamma\eta)\theta'' + 2\gamma\theta' + Pr(f\theta' - n^* f' \theta) = 0. \tag{5.12}$$

The corresponding boundary conditions are

$$f(0) = 0, f'(0) = 1, \theta(0) = 1, f'(\infty) = a/c, \theta(\infty) \rightarrow 0. \tag{5.13}$$

The involved non-dimensional parameter are $\gamma = \sqrt{\nu l / c R^{*2}}$ (Curvature parameter), $We = ck_0 / \rho \nu l$ (Weissenberg number), $M = \sqrt{\sigma B_0^2 l / \rho c}$ (Hartman number), a/c (Velocity ratio

parameter) and $Pr = \nu/\alpha$ (Prandtl number). Physical quantities of interest for present study are skin friction coefficient C_f and heat transfer coefficient Nu are given as

$$(Re_z)^{1/2}C_f = (1 - 3We)f''(0) \text{ and } (Re_z)^{-1/2}Nu = -\theta'(0), \quad (5.14)$$

where, $Re_z = cz^2/\nu l$ is the dimensionless local Reynolds number.

5.2 Numerical procedure

Eqs. (5.11) and (5.12) subject to the boundary conditions (5.13) forms a system of nonlinear differential equations and are solved by using Spectral Quasi Linearization Method (SQLM). This method is a generalized Newton-Raphson method that was first brought in use by Bellman and Kalaba (1965) for the solution of functional equations. SQLM can be used in place of traditional methods such as shooting method, finite difference schemes in solving non-linear boundary value problems to achieve better accuracy. The present scheme is based on linearizing the nonlinear component of governing equations using Taylor series expansion with the assumption that difference between the values of unknown function at the current $(r + 1)th$ stage the steps with that of previous represented by $(r)th$ stage is small. The equations in linearized form are

$$a_{1,r}f_{r+1}^{iv} + a_{2,r}f_{r+1}''' + a_{3,r}f_{r+1}'' + a_{4,r}f_{r+1}' + a_{5,r}f_{r+1} = B_{1,r}, \quad (5.15)$$

$$b_{1,r}\theta_{r+1}'' + b_{2,r}\theta_{r+1}' + b_{3,r}\theta_{r+1} + b_{4,r}f_{r+1}' + b_{5,r}f_{r+1} = B_{2,r}, \quad (5.16)$$

and the boundary conditions become

$$\begin{aligned} f_{r+1}(0) &= 0, f_{r+1}' = 1, \theta_{r+1}(0) = 1, \\ f_{r+1}(\infty) &= \frac{a}{c}, f_{r+1}''(\infty) = 0, \theta_{r+1}(\infty) = 0 \end{aligned} \quad (5.17)$$

The coefficients $a_{k,r}$, $b_{k,r}$ and $B_{k,r}$ $k = (1, 2, \dots)$ are given as

$$\begin{aligned} a_{1,r} &= (1 + 2\gamma\eta)We f_r, a_{2,r} = (1 + 2\gamma\eta) + 4We\gamma f_r - 2f_r'(1 + 2\gamma\eta)We, \\ a_{3,r} &= 2\gamma + f_r + 4We\gamma f_r' + 2f_r''(1 + 2\gamma\eta)We, \\ a_{4,r} &= -2f_r' + 4We\gamma f_r - 2We(1 + 2\gamma\eta)f_r''' - M^2, \\ a_{5,r} &= f_r'' + (1 + 2\gamma\eta)We f_r''' + 4We\gamma f_r'', \\ b_{1,r} &= (1 + 2\gamma\eta), b_{2,r} = 2\gamma + Pr f_r, \\ b_{3,r} &= -n^*Pr f_r', \quad b_{4,r} = -n^*Pr \theta_r, \quad b_{5,r} = Pr \theta_r', \end{aligned} \quad (5.18)$$

and

$$B_{1,r} = (1 + 2\gamma\eta)We(f_r f_r''' - 2f_r' f_r'' + f_r''^2) + 4We\gamma(f_r f_r''' + f_r' f_r'') \quad (5.19)$$

$$+f_r f_r'' - f_r'^2 - M^2 \left(\frac{a}{c}\right) - \left(\frac{a}{c}\right)^2,$$

$$B_{2,r} = -n^* Pr \theta_r f_r' + Pr \theta_r' f_r,$$

For solution of Eqs. (5.15)–(5.17), Chebyshev Spectral Collocation Method is used. It is applied by first reducing the semi-infinite domain $[0, \infty]$ to finite domain say $[0, \eta_\infty]$ and then further transforming it to $[-1, 1]$ by using the transformation $\eta = \eta_\infty(y + 1)/2$, which is a basic need for use of collocation methods. To estimate the derivatives of unknown variables $f(\eta)$ and $\theta(\eta)$ at the collocation points, differentiation matrix \mathbf{D} is used e.g. derivative of $f(\eta)$ is given as

$$\frac{df^j}{d\eta} = \sum_{k=0}^N D_{jk} f(y_k) = Df, \quad j = 0, 1, \dots, N, \quad (5.20)$$

where N is the total number of collocation points, $D = \mathbf{D}/\eta_\infty$ and

$$f = [f(y_0), f(y_1), \dots, f(y_N)]^t. \quad (5.21)$$

For higher order derivatives, the following relation is used

$$f^{(s)} = \mathbf{D}^{(s)} f, \quad (5.22)$$

where ‘ s ’ is the order of the derivative. Matrix \mathbf{D} is of size $(N \times 1) \times (N \times 1)$ and the collocation points are defined as

$$y_j = \cos\left(\frac{\pi j}{N}\right), \quad j = 0, 1, \dots, N. \quad (5.23)$$

Applying Collocation method to Eqs. (5.15-5.17), the following matrix is obtained.

$$\begin{bmatrix} A_{11} & A_{12} \\ A_{21} & A_{22} \end{bmatrix} \begin{bmatrix} f^{r+1} \\ \theta^{r+1} \end{bmatrix} = \begin{bmatrix} B_{1r} \\ B_{2r} \end{bmatrix}. \quad (5.24)$$

In which

$$A_{11} = a_{1,r} D^4 + a_{2,r} D^3 + a_{3,r} D^2 + a_{4,r} D + a_{5,r} I, \quad A_{12} = \mathbf{0}$$

$$A_{21} = b_{4,r} D + b_{5,r} I, \quad A_{22} = b_{1,r} D^2 + b_{2,r} D + b_{3,r} I. \quad (5.25)$$

In which I is identity matrix, and $a_{i,r}$, $b_{i,r}$, B_{1r} and B_{2r} ($i = 1, 2, \dots, 5$) are given by set of Eqs. (5.18) and (5.19) respectively. In order to ensure that the solution of the present problem is grid independent, computed numerical values of $f''(0)$ against different refinement levels of grid points are given in Table 5.1. It is observed that percentage error is reducing by increasing the grid points and is minimum at fourth refinement level. Therefore the fourth refinement level (i.e., $N = 40$) is used for the solution in present study.

Table 5.1: Validity of computed $f''(0)$ at different grid points

Refinement levels	Grid Points (N)	$f''(0)$	%Error
First	10	-0.6325	—
Second	20	-0.9706	35
Third	30	-0.9736	0.3
Fourth	40	-0.9735	0.01

5.3 Results and discussion

The grid independent solution of the problem has been computed with the help of Spectral Quasi Linearization Method. Main focus of study is how fluid flow varies about stagnation point under the influence of traverse magnetic field. In order to get the clear insight of fluid flow and heat transfer principle, a parametric study is conducted in the prescribed domain with the variation of non-dimensional factors i.e. curvature parameter (γ), Magnetic parameter (M), velocities ratio parameter (a/c), Weissenberg number (We) and Prandtl number (Pr). Tables 5.2–5.6 are drawn to show the validity and accuracy of computed results. In which, Table 5.2 shows a comparison of computed numerical values of $f''(0)$ with Sharma and Singh (2009) for different values of a/c , when other parameters are fixed as $\gamma = We = M = 0$.

Table 5.2: Present results of $f''(0)$ as compared to (Sharma and Singh 2009) for different values of a/c when $\gamma = We = M = 0$.

a/c	Sharma and Singh (2009)	Present results (SQLM)
0.1	-0.969386	-0.969386
0.2	-0.918106	-0.918107
0.5	-0.667263	-0.667264
2.0	2.017490	2.01750
3.0	4.729226	4.729282

In Table 5.3, comparison has been shown for computed numerical values of $f''(0)$ with Sharma and Singh (2009) when $\gamma = We = 0$ are fixed against various values of parameters M and a/c . In Table 5.4, comparison has been shown for computed numerical values of $-\theta'(0)$ with Elbashbeshy et al. (2012) when $\gamma = We = M = a/c = 0$ are fixed. Table 5.5 shows a comparison of numerical values of $f''(0)$ with the results computed by Pillai et al.

(2004) and Nandeppanavar et al. (2010) for different values of We when $\gamma = M = a/c = 0$. It is observed through all these tables that the computed solution is convergent, grid independent and highly accurate. Computed numerical values of $f''(0)$ are listed in Table 5.6 for different values of M . It is important to mention that these values are also validated by another numerical scheme known as Hybrid method (Areal 1992). These tabulated values are new results in literature and will be helpful in future references.

The Figures 5.2 and 5.3 are plotted to observe the effects of curvature parameter γ on velocity and temperature profiles respectively. It is noticed that by increasing the curvature of the cylinder, the velocity and temperature profiles increase in the boundary layer. It is because by enhancing γ , the cylinder surface area squeezes and the motion of the fluid adjacent to the surface speeds up which consequently increases the temperature of the fluid within the boundary layer. The increase in γ further helps to control the momentum and thermal boundary layer thickness as shown in these figures. Figures 5.4 and 5.5 demonstrate

Table 5.3: Present results of $f''(0)$ compared to (Sharma and Singh 2009) for different values of M and a/c when $\gamma = We = 0$.

a/c	M	Sharma and Singh (2009)	Present results
0.1	0.1	-0.973508	-0.973508
0.2	0.1	-0.921466	-0.921534
0.5	0.1	-0.669102	-0.669102
2.0	0.1	2.019932	2.019944
3.0	0.1	4.733399	4.733455
0.1	0.5	-1.067898	-1.067898
0.2	0.5	-1.000469	-1.000469
0.5	0.5	-0.711890	-0.711891
2.0	0.5	2.077711	2.077724
3.0	0.5	4.832501	4.832520
0.1	1.0	-1.321111	-1.321111
0.2	1.0	-1.215622	-1.215622
0.5	1.0	-0.832125	-0.832126
2.0	1.0	2.240857	2.249103
3.0	1.0	5.130344	5.130380

Table 5.4: Present results of $-\theta'(0)$ compared to Elbashbeshy et al. 2012 for different values of M when $\gamma = We = M = a/c = 0$.

Pr	n^*	Elbashbeshy et al. 2012	Present results (SQLM)
1	-2	-1.0000	-1.0000
	-1	0.0000	0.0000
	0	0.5820	0.5819
	1	1.0000	1.0000
	2	1.3333	1.3333
10	-2	-10.0000	-10.0000
	-1	0.0000	0.0000
	0	2.3080	2.3080
	1	3.7207	3.7207
	2	4.7969	4.7969
0.9	2	—	1.25046
0.8	2	—	1.16276
0.7	2	—	1.06932

Table 5.5: Present results of $f''(0)$ compared to Pillai et al. 2004 and Nandeppanavar et al. 2010 for different values of We when $\gamma = M = a/c = 0$.

We	Pillai et al. 2004	Nandeppanavar et al. 2010	Present results (SQLM)
0	1.0	1.0	1.0
0.0001	1.00005	1.00005	1.00005
0.001	1.0050	1.00500	1.00500
0.005	—	1.00251	1.00250
0.01	1.00504	1.00504	1.00504
0.03	—	1.01535	1.01534
0.05	—	1.02598	1.02597
0.1	1.05409	1.05409	1.05406
0.2	1.11803	1.11803	1.11797
0.3	1.19523	1.19523	1.19512
0.4	1.29099	1.29099	1.29079
0.5	1.41421	1.41421	1.41390

Table 5.6: Numerical values of $f''(0)$ for different values of $\gamma, a/c, M$ and We .

γ	a/c	M	We	Present results	
				SQLM	Hybrid Method (Areal 1992)
0.0	0.1	0.1	0.1	-1.0317	-1.0317
	0.2	0.1		-0.9832	-0.9832
	0.5	0.1		-0.7320	-0.7320
0.5	0.1	0.5	0.2	-1.7450	-1.7450
	0.2	0.5		-1.6627	-1.6627
	0.5	0.5		-1.2701	-1.2701
1.0	0.1	1.0	0.3	-3.5380	-3.5380
	0.2	1.0		-3.4028	-3.4028
	0.5	1.0		-2.8108	-2.8108

the effects of We on velocity and temperature profiles respectively. The case when $a/c < 1$; the velocity profile decreases for larger values of We and for the case $a/c > 1$; the velocity profile increases for larger values of We . This behavior of We is quite opposite in the temperature profile as shown in Figure 5.5. It is also noted that when the value of $a/c > 1$, the temperature variation is very small for increasing values of We . For a/c close to unity, the velocity $f'(\eta)$ is almost constant and independent of We . Due to this fact, the temperature inside the boundary layer is independent of We for $a/c = 1$. To show the importance of Lorentz force on the velocity profile of Walters-B fluid near a stagnation point over a stretching cylinder, Figure 5.6 is plotted. It depicts the variation in velocity profile for different values of magnetic parameter M . Physically, the presence of transverse magnetic field to an electrically conducting fluid develops a body force known as Lorentz force. It acts like a resistive force which decelerates the fluids velocity. This effect differs due to boundary layer structure and due to the velocities ratio parameter a/c . When $a/c = 0.4 < 1$ (i.e. free stream velocity is less than stretching velocity and inverted boundary layer structure develops), the velocity profile decreases with increase in M . When $a/c = 0.4 > 1$ (i.e. free stream velocity is greater than stretching velocity and boundary layer structure develops), the velocity profile increases with increase in M . Also when $a/c = 1$ (i.e. free stream velocity is equal to stretching velocity and no boundary layer exists), the velocity profile for different values of M coincides. In other words, the velocity profile is independent of the applied magnetic field when free stream velocity is equal to stretching

velocity. Mathematically, this behavior of velocity profile can be related to the factor $-M(F' - a/c)$ in the flow Eq. (5.11). Figure 5.7 is plotted to predict the temperature distribution against the impact of Lorentz force. The observation reflects that the temperature in boundary layer region is enhanced by strengthening magnetic field. It is because of this reason that by increasing strength of magnetic field (i.e. increase in Lorentz force) the heat transfer rate reduces which falls out as enhancement of temperature in boundary layer region. In addition, the variation in heat transfer rate against M is discussed later in this section. Figure 5.8 depicts the variation in velocity profile against the velocity ratio parameter a/c . It is noted from the figure that when $a/c > 1$, the flow has boundary layer structure. Also with increase in a/c , the boundary layer thickness shrinks. Physically, it means that for large value of free stream velocity as compare to stretching velocity (such that $a/c > 1$), the fluid near the surface of cylinder moves with free stream velocity which leads to thinning of momentum boundary layer. When $a/c < 1$, the flow has an inverted boundary layer structure, which is because of the reason that the stretching velocity exceeds the free stream velocity. When $a/c = 1$, no boundary layer structure is formed. Temperature profile for various values of n^* is shown in Figure 5.9. It is seen from the figure that temperature profile decreases and thermal boundary layer is controlled by increasing n^* . Figure 5.10 shows that the temperature of the fluid is reduced for larger values of Pr . Physically it is due to the fact that the fluids with large Pr have the ability to reduce the temperature of the surface. Therefore, in automobiles and industrial mechanisms, the fluids with high Prandtl number are frequently used as a cooling agent. Numerical results for physical parameters like skin friction coefficient ($Re_z^{1/2}C_f$) and heat transfer coefficient ($Re_z^{-1/2}Nu$) are plotted in Figures 5.11-5.15 against curvature parameter (γ), magnetic parameter (M) and Weissenberg number (We) for various ranges of We and Pr respectively by taking other parameters fixed. It is noted in Figure 5.11 that the skin friction coefficient ($Re_z^{1/2}C_f$) increases by increasing the prescribed values of We . This implies that the drag between fluid and surface of cylinder is getting stronger in going from Newtonian to non-Newtonian behavior of the fluid ($We = 0 \rightarrow 0.3$). However, a small amount of reduction in drag is noted with large value of We against each γ . It is illustrated from Figure 5.12 that heat transfer coefficient ($Re_z^{-1/2}Nu$) is an increasing function of γ for prescribed values of We . This affirms the reduction in heat transfer rate in going from Newtonian to non-Newtonian behavior of fluid ($We = 0 \rightarrow 0.3$). The dominating effects of M are shown

in Figure. 5.13. By increasing the strength of magnetic field, the absolute value of $Re_z^{1/2} C_f$ increases. Also the effects of M are more pronounced for $We = 0$ in comparison with $We = 0.3$. In Figure 5.14, the heat transfer rate is found to be decreasing function of M which validates the effects achieved in Figure 5.7. Figure 5.15 shows that the heat transfer coefficient ($Re_z^{-1/2} Nu$) is an increasing function of Prandtl number Pr and heat transfer rate slightly decreases against large values of We . The flow developments through streamlines are observed in Figures 5.16–5.19 within the restricted domain. Variation in streamlines in the absence of stagnation and in the presence of stagnation point are plotted in Figures 5.16(a) and (b), respectively. When $a/c = 0$, the fluid moves due to stretching of surface, and no potential flow occurs. Due to this, the streamlines are stagnant in the region beyond the surface and near the surface the fluid is moving away from dividing streamline in both directions. When $a/c = 0$, the potential flow exists but the case $a/c < 1$ means the stretching velocity effects are more dominant than straining velocity effects. Because of this, streamlines are more concentrated towards dividing streamline beyond the surface and expanding near the surface. The resulting patterns of streamlines for (a) stretching sheet $\gamma = 0$ and (b) stretching cylinder $\gamma = 1$ are shown in Figure 5.17. Streamlines are getting closer and concentrated near dividing stream in case of stretching cylinder $\gamma = 1$ in comparison with that of stretching sheet $\gamma = 0$. This shows a dominant fluid flow around stretching cylinder due to small surface area. Figure 5.18 (a, b) shows the streamlines in case of Newtonian ($We = 0$) and non-Newtonian Walter-B fluid ($We = 0.3$), respectively. Figure 5.18 (b) shows that the streamlines are more diverging from dividing stream line for Walter-B fluid ($We = 0.3$) than the Newtonian fluid ($We = 0$) in Figure 18 (a). In Figure 5.19 (a, b), the streamlines are plotted for $M = 0$ (absence of magnetic field effects) and for $M = 2$ (presence of magnetic field effects), respectively. In Figure 5.19(a), the minimum and maximum values of $|\psi|$ are observed as $|\psi|_{min} = 1.6748$ and $|\psi|_{max} = 7.6748$, and the streamlines are concentrated in this domain, which is indication of high flow rate. In Figure 19 (b), $|\psi|_{max} = 5.6748$ which is smaller than the $|\psi|_{max}$ in absence of magnetic field, this leads to the fact that magnetic field reduces the flow rate. It is noted through Figures 5.18 and 5.19 that We and M have same impact on fluid flow.

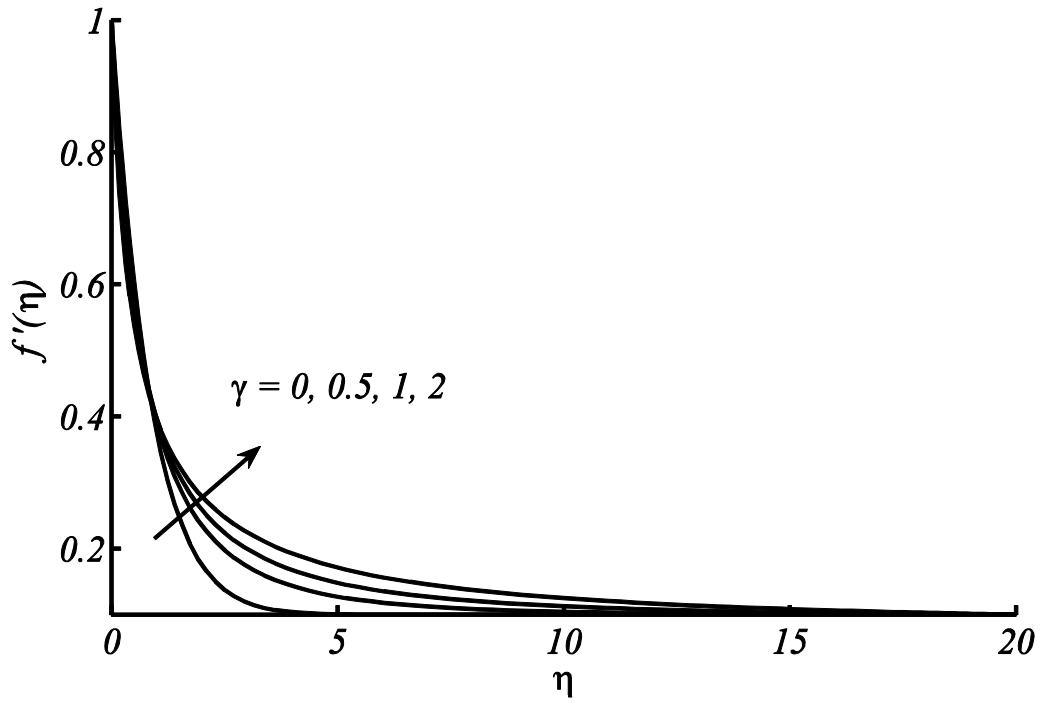


Figure 5.2: Curvature effects on velocity profile at $M = 0.1, a/c = 0.1, We = 0.1$.

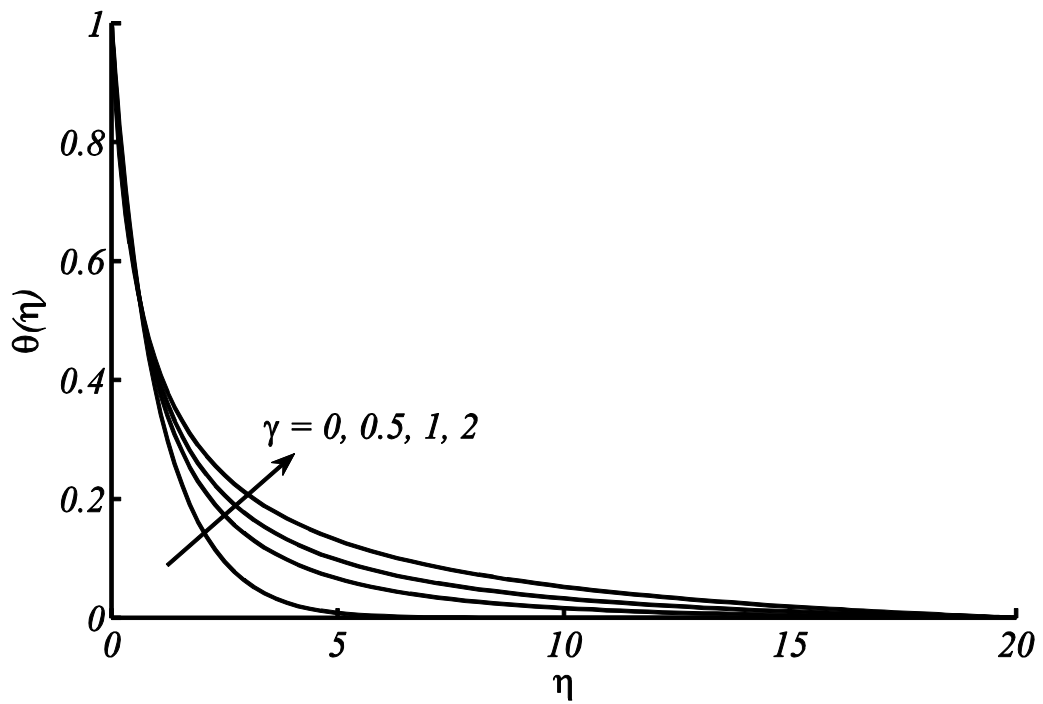


Figure 5.3: Curvature effects on temperature distribution at $M = 0.1, a/c = 0.1, We = 0.1, n^* = 2, Pr = 0.7$.

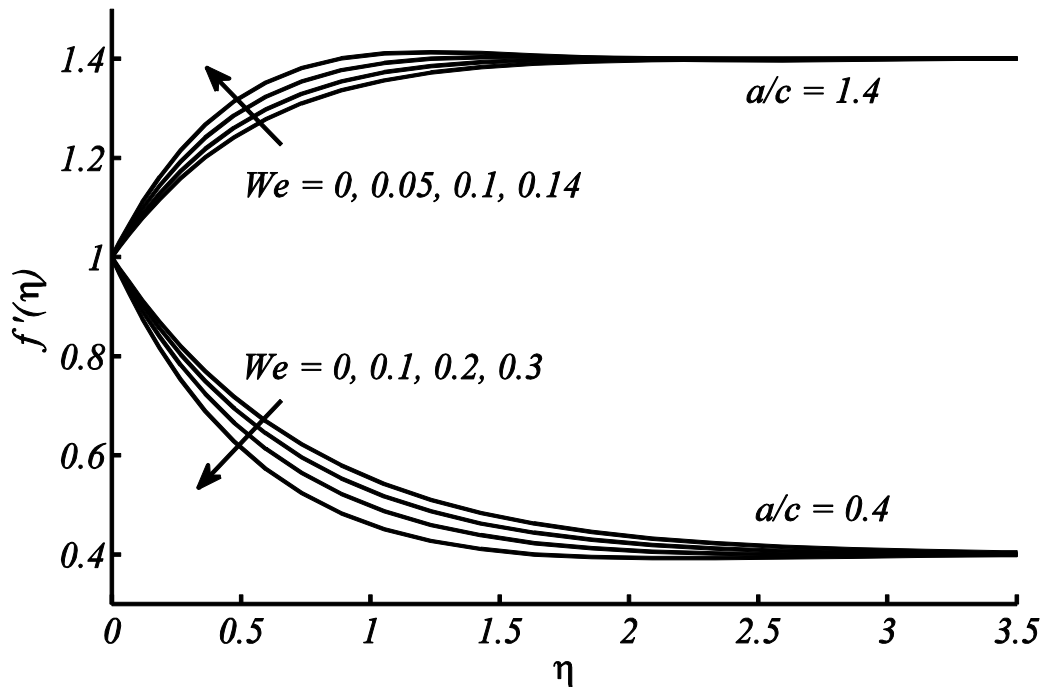


Figure 5.4: Viscoelastic effects on velocity profile at $\gamma = 0.1, M = 0.1$.

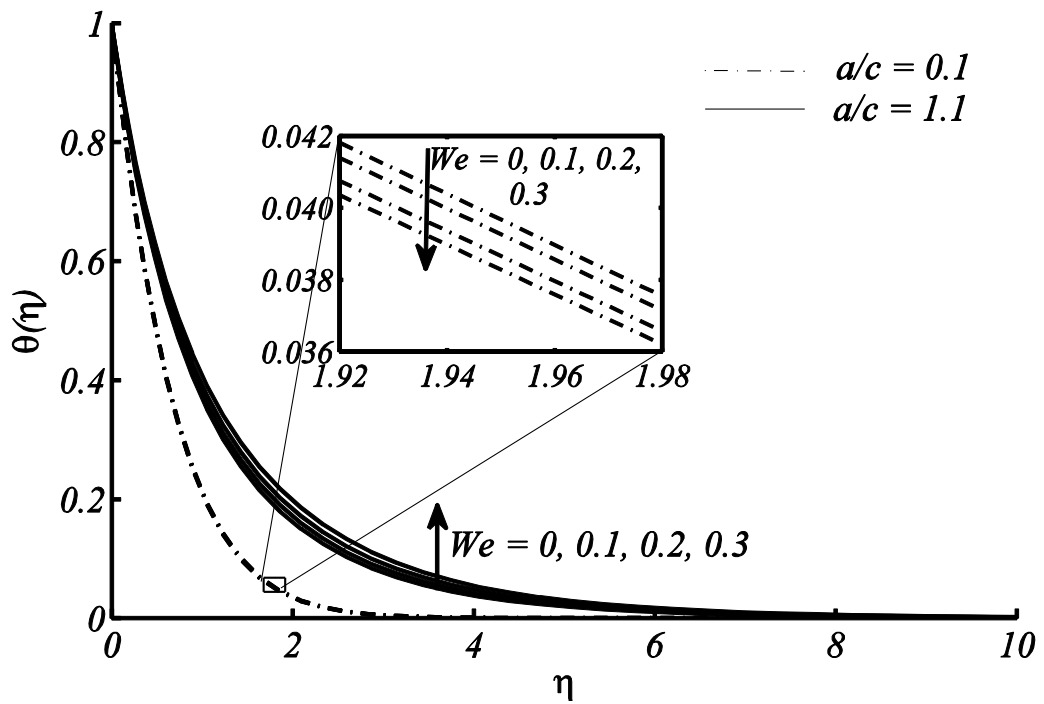


Figure 5.5: Viscoelastic effects on temperature distribution $\gamma = 0.1, M = 0.1, n^* = 2, Pr = 0.7$.

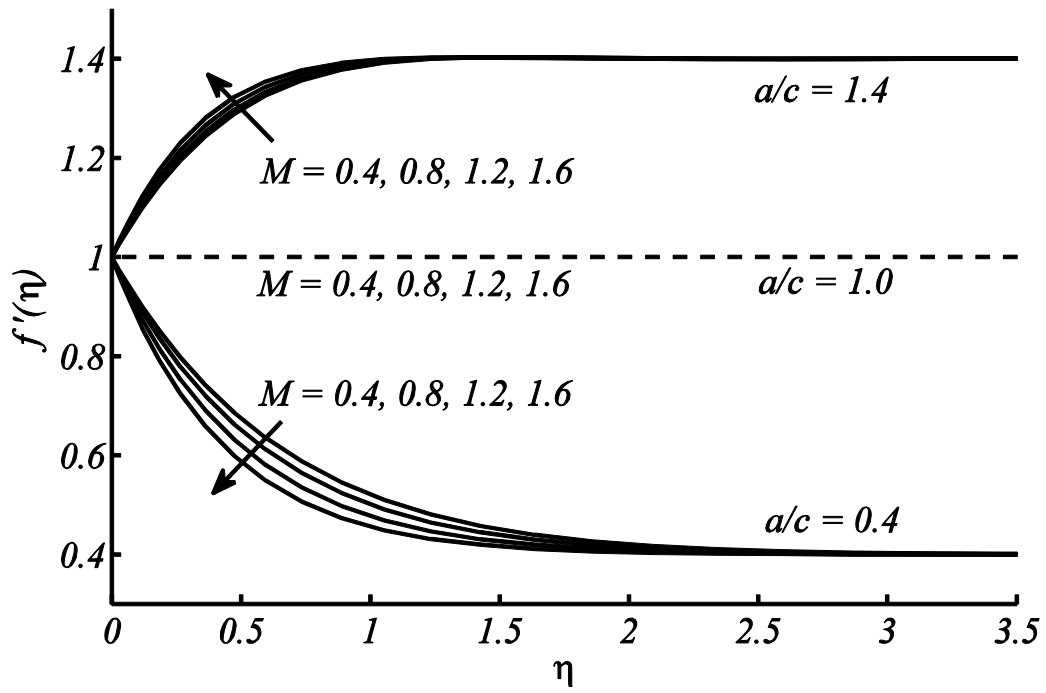


Figure 5.6: Magnetic field influence on velocity profile at $\gamma = 0.1, We = 0.1$.

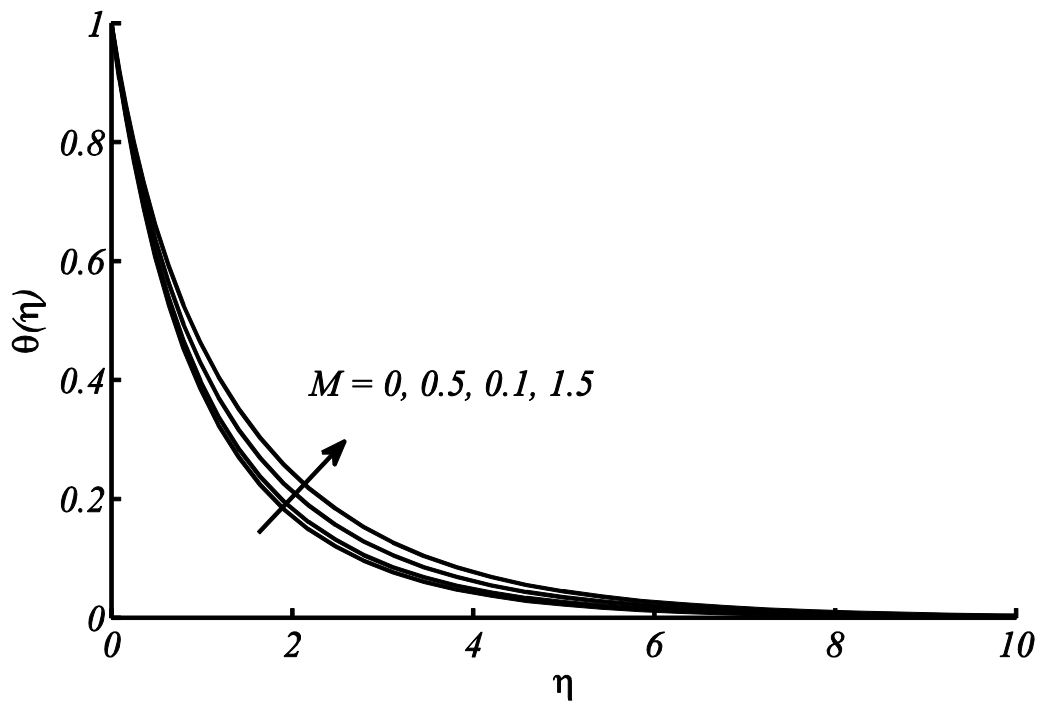


Figure 5.7: Magnetic field influence on temperature distribution at $\gamma = 0.1, a/c = 0.1, We = 0.1, n^* = 2, Pr = 0.7$.

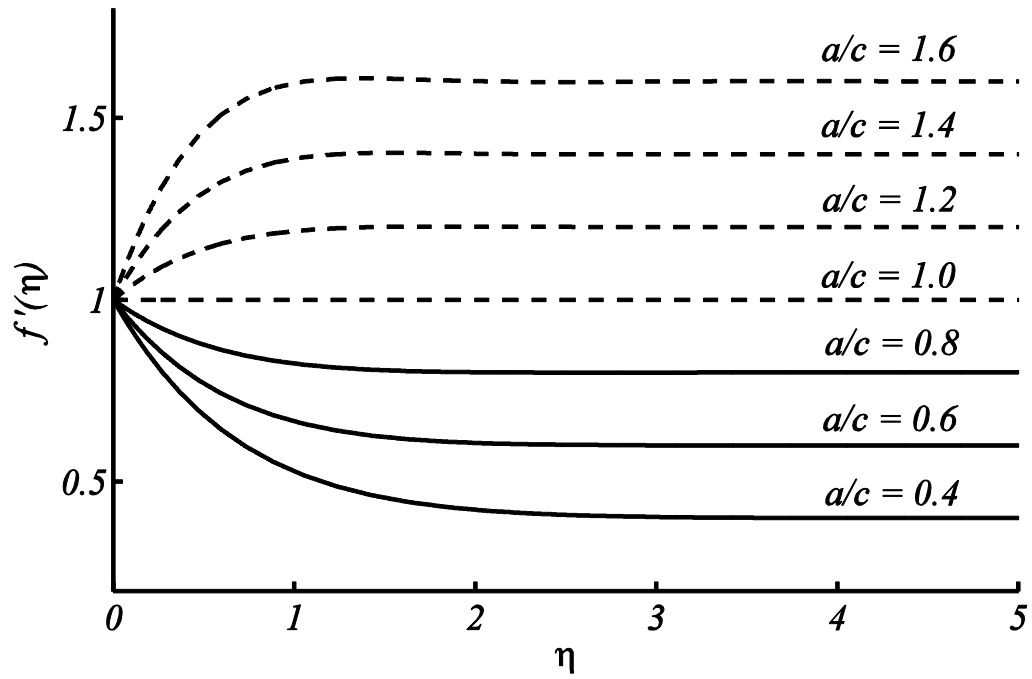


Figure 5.8: Velocity behavior due to variation of a/c at $\gamma = 0.1, M = 0.1, We = 0.1$.

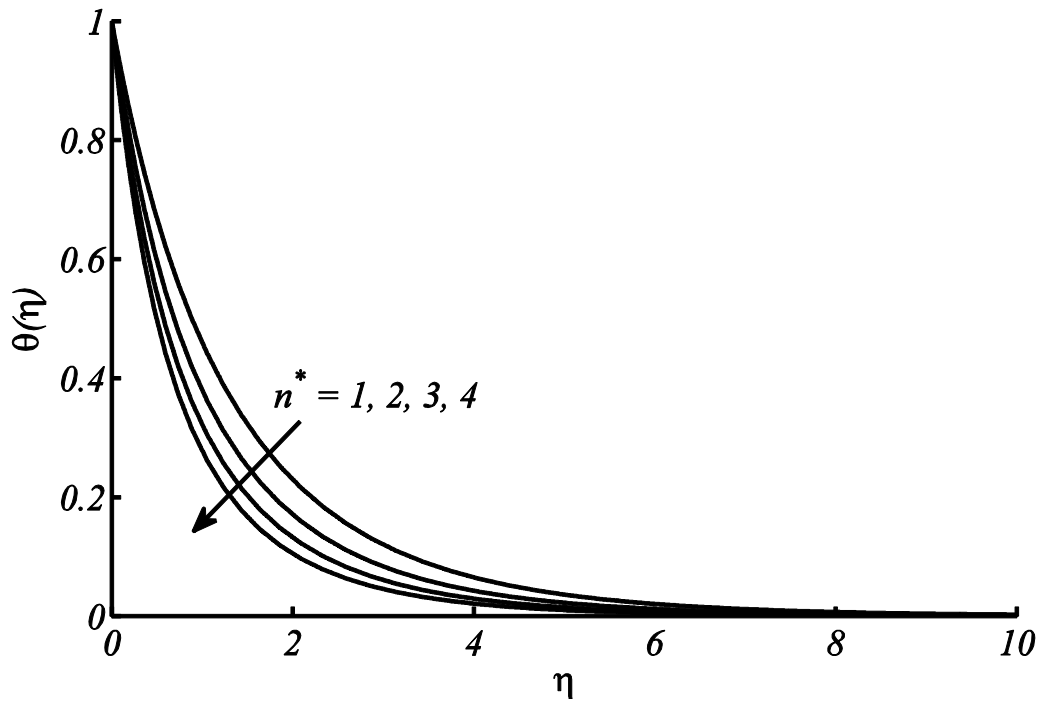


Figure 5.9: Influence of n on temperature distribution at $\gamma = 0.1, M = 0.1, a/c = 0.1, We = 0.1, Pr = 0.7$.

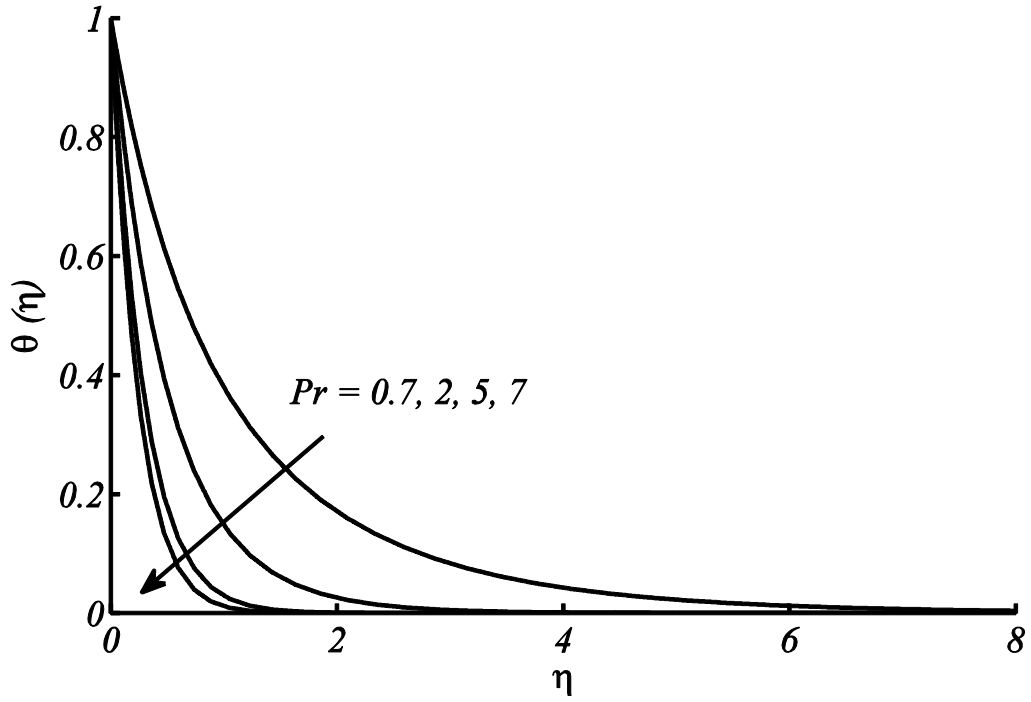


Figure 5.10: Effect of Pr on temperature distribution at $\gamma = 0.1, M = 0.1, a/c = 0.1$, $We = 0.1, Pr = 0.7$.

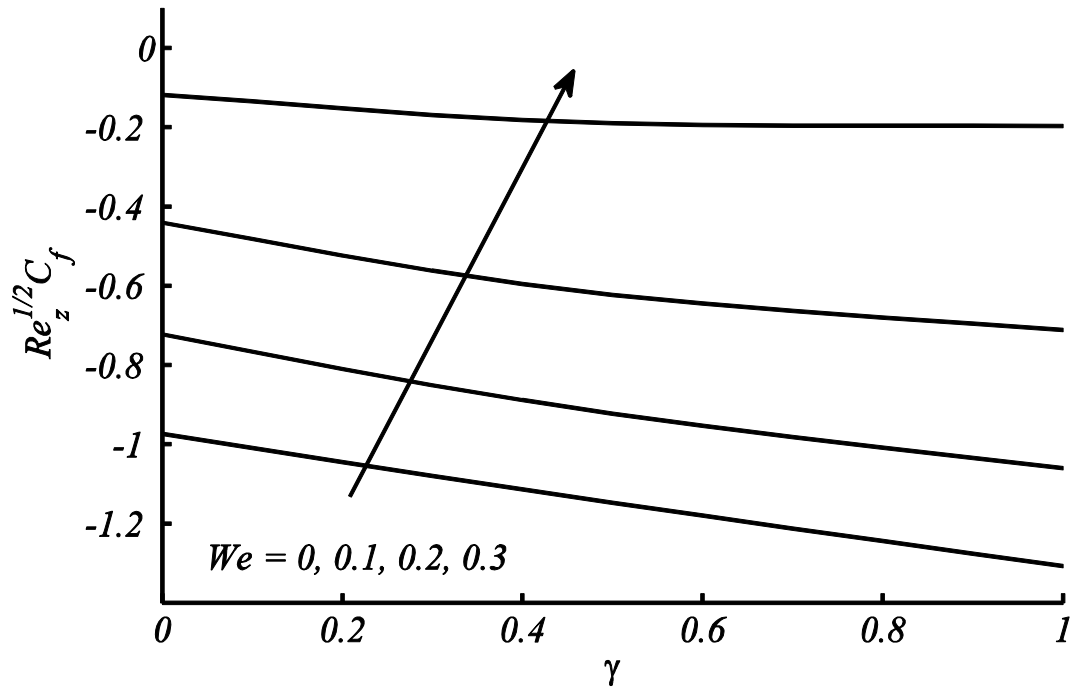


Figure 5.11: Variation in $Re_z^{1/2} C_f$ with γ at different We for $M = 0.1, a/c = 0.1$.

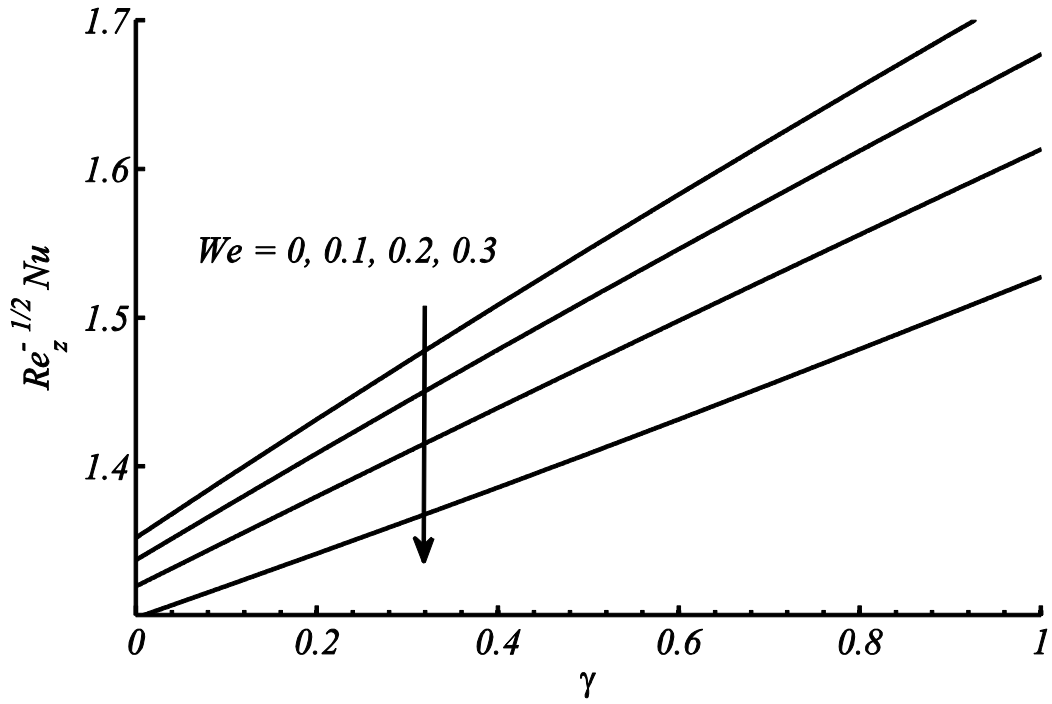


Figure 5.12: Variation in $Re_z^{-1/2} Nu$ with γ at different We for $M = 0.1, a/c = 0.1, n^* = 2, Pr = 0.7$.

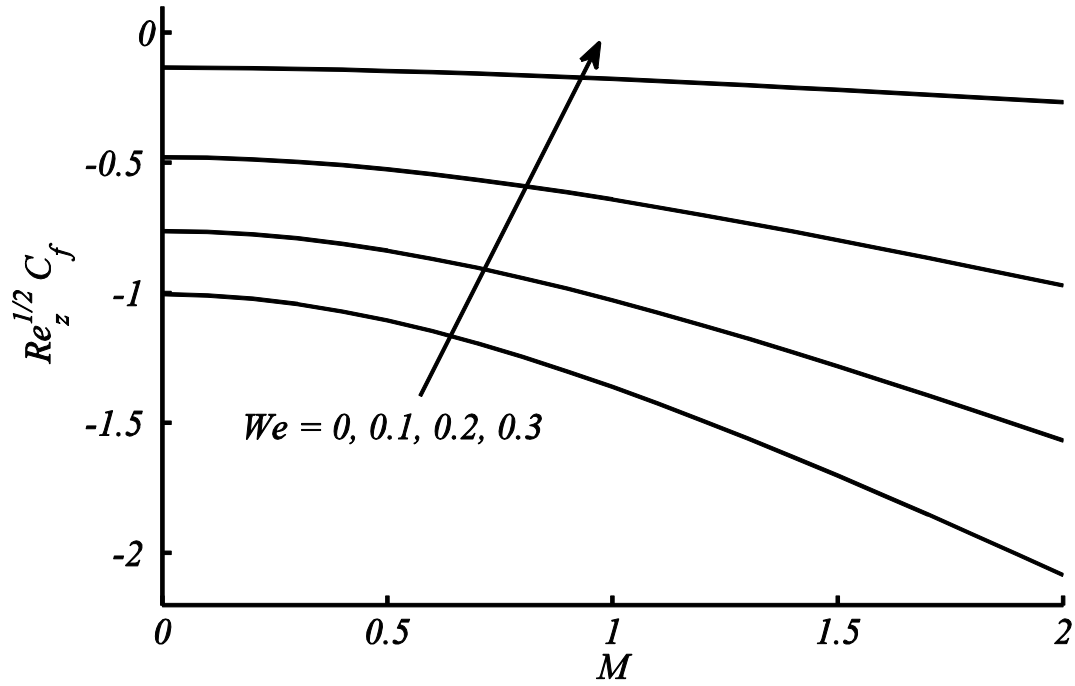


Figure 5.13: Variation in $Re_z^{1/2} C_f$ with M at different We for $\gamma = 0.1, a/c = 0.1$.

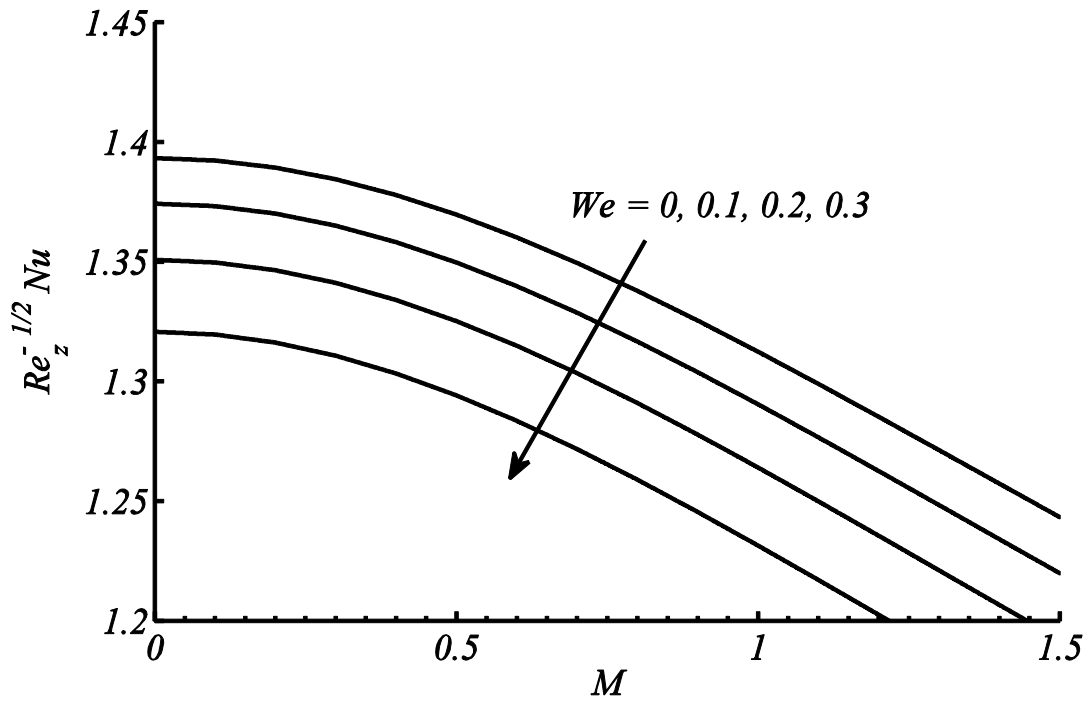


Figure 5.14: Variation in $Re_z^{-1/2} Nu$ with M at different We for $\gamma = 0.1, a/c = 0.1, n^* = 2, Pr = 0.7$.

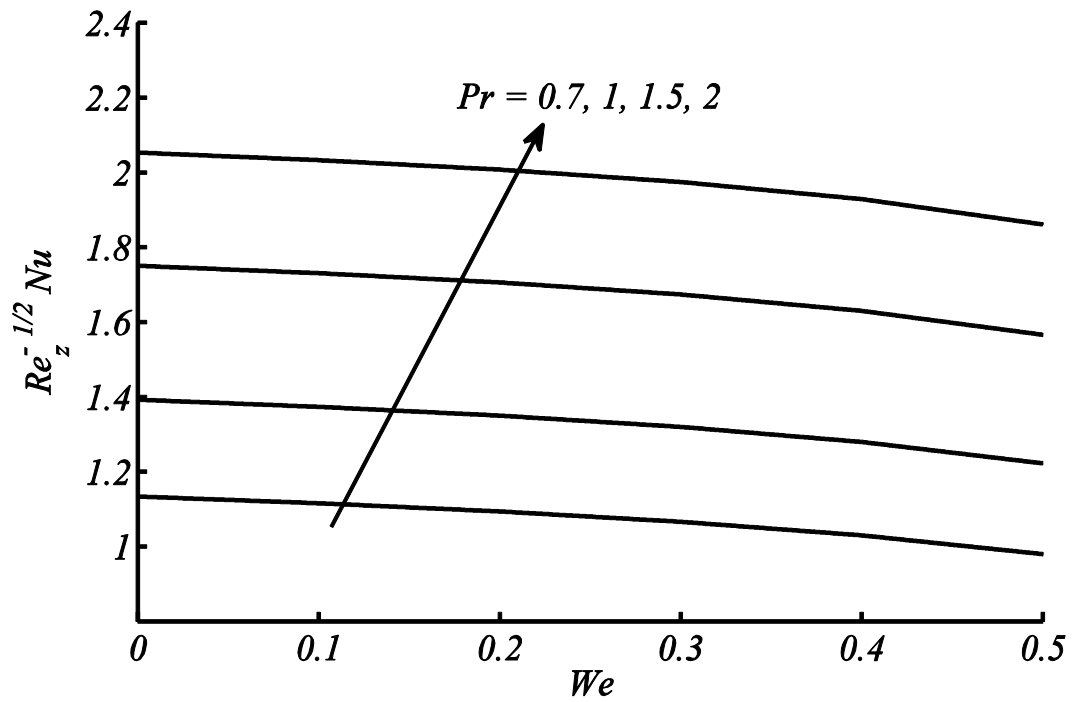


Figure 5.15: Variation in $Re_z^{-1/2} Nu$ with We at different Pr for $\gamma = 0.1, a/c = 0.1, n^* = 2, M = 0.1$.

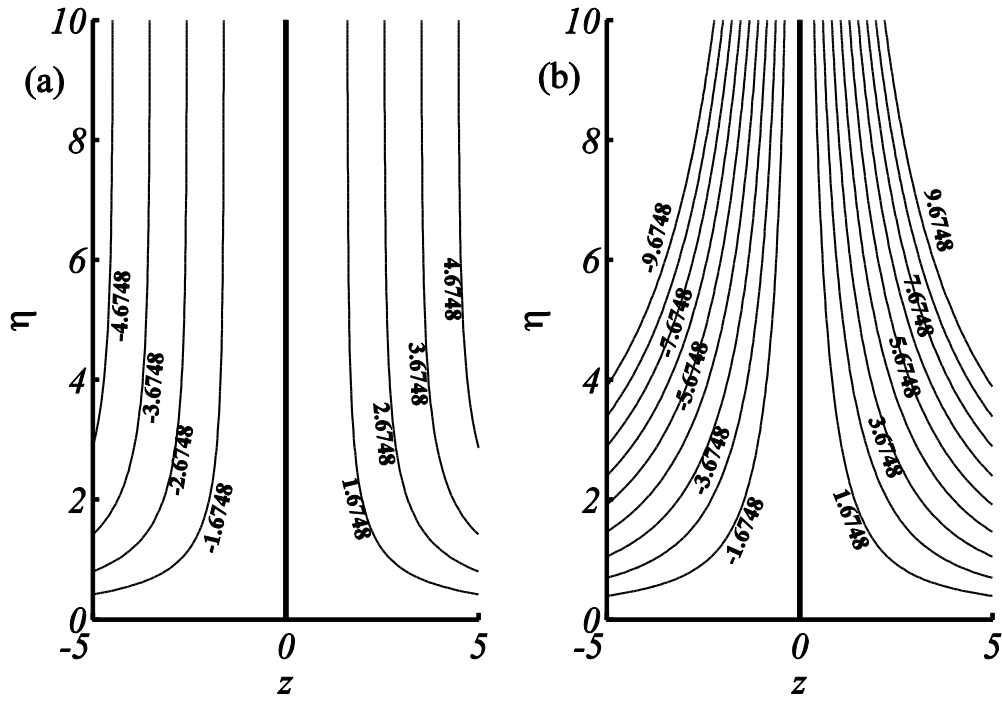


Figure 5.16: Streamlines for (a) $a/c = 0$, and (b) $a/c = 0.4$.

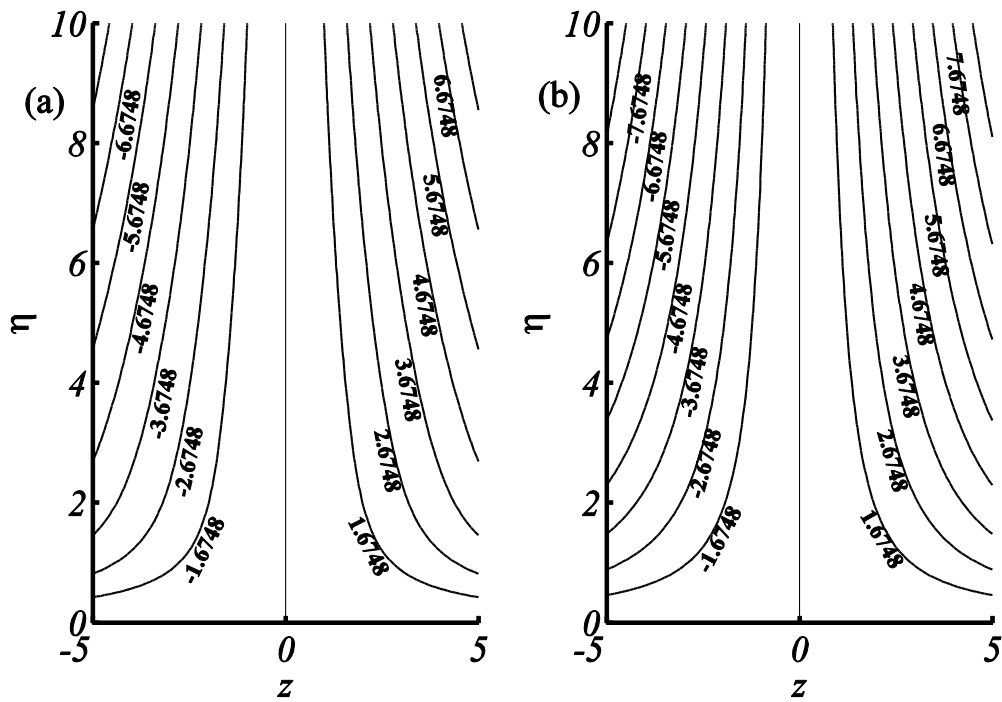


Figure 5.17: Streamlines for (a) $\gamma = 0$, and (b) $\gamma = 1$.

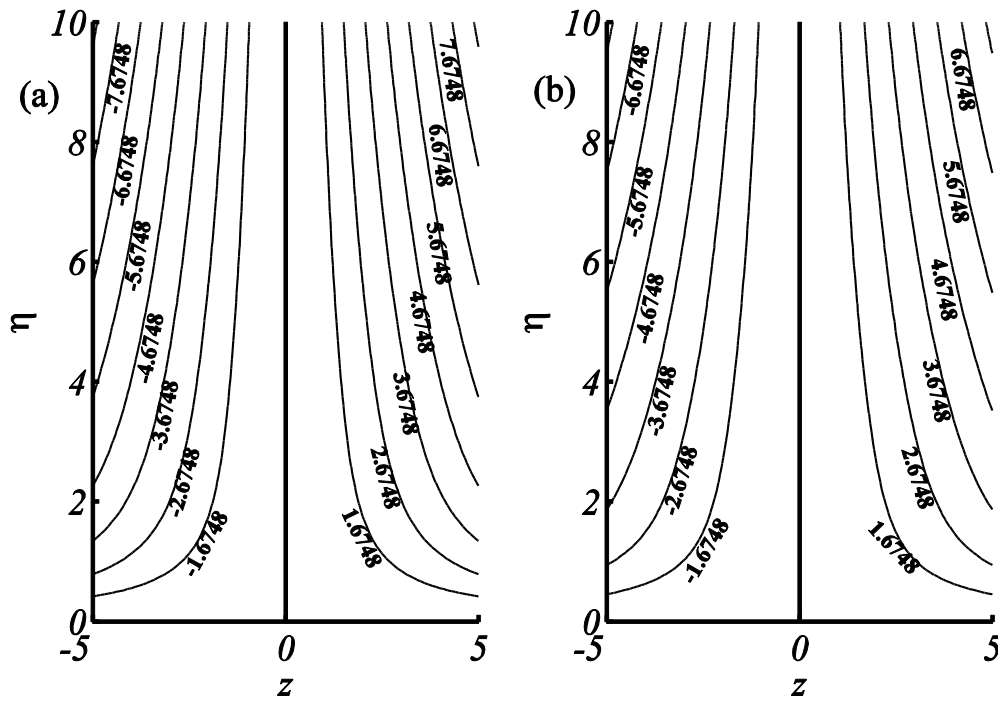


Figure 5.18: Streamlines for (a) $We = 0$, and (b) $We = 0.3$.

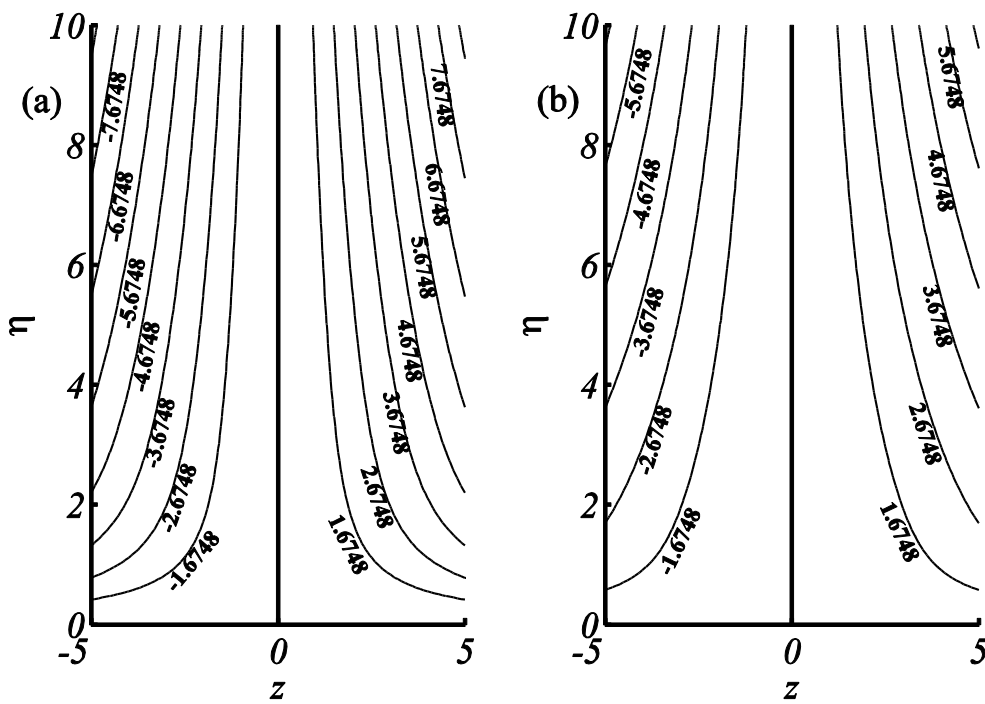


Figure 5.19: Streamlines for (a) $M = 0$, and (b) $M = 2$.

5.4 Conclusions

A computational study is performed to investigate the two-dimensional, laminar, MHD stagnation point flow of Walters B fluid over a stretching cylinder. The main theme is to model the Walters B fluid constitutive equation in cylindrical coordinate system subject to flow over stretching cylinder. For this purpose, the Spectral Quasi Linearization Method (SQLM) has successfully employed to perform a comparative study of present problem in limiting case with that of previous studies. It is observed that SQLM is accurate, rapidly convergent, time saving and easy to implement in MATLAB coding. It is concluded that the implemented method reflects an abundant prospective to widely use in non-linear science and engineering problems. In present study, mainly the effects of curvature parameter (γ), velocity ratio parameter (a/c), Weissenberg parameter (We) and Prandtl number (Pr) with constant magnetic field are discussed. The developed Walters-B fluid model over a stretching cylinder can be extended for the nanofluid by incorporating the nanoparticles and mixed convection flows. We noted that the curvature of cylinder has significant effect over velocity and temperature profiles as compared to that of flat plate case when $\gamma = 0$. The application of an external magnetic field generates Lorentz force which decelerate the fluid flow and accelerate temperature of the fluid. The velocity profile decreases significantly and momentum boundary layer gets thin for large values of Weissenberg number (We). It is because viscous forces dominate the elastic forces. With increasing values of Weissenberg number (We), the drag force over the surface increases and it reduces against each value of cylinder Curvature parameter (γ). Reduction in heat transfer rate is noted with increase in the values of Weissenberg number (We), while enhancement in the heat transfer rate is observed with increasing curvature of cylinder.

Chapter 6

Study of non-Newtonian fluid flow due to stretching cylinder under Soret and Dufour effects

This chapter presents the analysis of Soret and Dufour effects on the two-dimensional flow of second grade fluid due to stretching cylinder. It is further considered that the flow is subjected to thermal radiation, which is another aspect of the study. Mathematical model for second grade fluid in cylindrical coordinate system is developed in terms of nonlinear partial differential equations. These modelled equations are first transformed to a system of nonlinear coupled ordinary differential equations after using similarity transformation, and then the solution is computed numerically by using Keller box scheme for the wide range of physical parameters. The computed results are validated with the existing literature for limiting case. The drag coefficient on surface, heat transfer, and mass transfer rates are analyzed through the graphs and tables. It is predicted that the simultaneous increase in Dufour and Soret numbers help to enhance the temperature and the concentration in the boundary layer region around the cylinder, respectively. Also concurrent occurring of increasing Dufour and decreasing Soret numbers on heat transfer and mass transfer rates have opposite effects. Moreover, the radiation effects are elaborated through the variation of effective Prandtl number. The increase in effective Prandtl number results in decrease of the temperature of the fluid.

6.1 Mathematical formulation

Let us consider the two-dimensional flow of second grade fluid due to stretching cylinder. To generalize the scope of the study, the effects of thermal radiation, Soret and Dufour phenomena are also made a part of this work. Moreover, the properties of the fluid are assumed to be constant. Geometry of the problem is constructed in such a way that axis of cylinder (z -axis) is taken in horizontal direction and r -axis is considered normal to it. The cylinder is assumed of fixed radius R^* and the surface is subjected to stretching with velocity cz/l . The Schematic of flow model is presented in Figure 4.1. After invoking the boundary layer approximation, the governing equations for the momentum (in component form), energy and concentration are reduced to:

z-component of momentum equation

$$v \frac{\partial v}{\partial z} + u \frac{\partial v}{\partial r} = -\frac{\partial p}{\partial z} + v \left(\frac{\partial^2 v}{\partial r^2} + \frac{1}{r} \frac{\partial v}{\partial r} \right) + \frac{\alpha_1}{\rho} \left(\frac{1}{r} \left\{ \frac{\partial v}{\partial z} \frac{\partial v}{\partial r} - \frac{\partial u}{\partial r} \frac{\partial v}{\partial r} + v \frac{\partial^2 v}{\partial r \partial z} + u \frac{\partial^2 v}{\partial r^2} \right\} + \frac{\partial^3 v}{\partial r^3} + v \frac{\partial^3 v}{\partial r^2 \partial z} - \frac{\partial v}{\partial z} \frac{\partial^2 u}{\partial r^2} + \frac{\partial v}{\partial z} \frac{\partial^2 v}{\partial r^2} \right), \quad (6.1)$$

r-component of momentum equation

$$0 = -\frac{1}{\rho} \frac{\partial p}{\partial r} + \frac{\alpha_1}{\rho} \left(\frac{1}{r} \left(\frac{\partial v}{\partial r} \right)^2 + 2 \frac{\partial v}{\partial z} \frac{\partial^2 v}{\partial r^2} \right), \quad (6.2)$$

Energy equation

$$\rho c_p \left(u \frac{\partial T}{\partial r} + v \frac{\partial T}{\partial z} \right) = k \left(\frac{\partial^2 T}{\partial r^2} + \frac{\partial T}{r \partial r} \right) + \frac{\rho D_m k_t}{c_s} \left(\frac{\partial^2 C}{\partial r^2} + \frac{\partial C}{r \partial r} \right) - \frac{\partial}{\partial r} (r q_r), \quad (6.3)$$

Concentration equation

$$\left(u \frac{\partial C}{\partial r} + v \frac{\partial C}{\partial z} \right) = D_m \left(\frac{\partial^2 C}{\partial r^2} + \frac{\partial C}{r \partial r} \right) + \frac{D_m k_t}{T_m} \left(\frac{\partial^2 T}{\partial r^2} + \frac{\partial T}{r \partial r} \right). \quad (6.4)$$

The corresponding boundary conditions against the fluid flow, temperature and concentration are

$$\left. \begin{aligned} v(r, z) &= \frac{cz}{l}, \\ u(r, z) &= 0, \\ T(r, z) &= T_\infty + \left(\frac{z}{l} \right)^{n^*} \Delta T, \\ C(r, z) &= C_\infty + \left(\frac{z}{l} \right)^{n^*} \Delta C \end{aligned} \right\} \text{ at } r = R^*, \quad (6.5)$$

and

$$\left. \begin{aligned} v(r, z) &= 0, \\ u(r, z) &= 0, \\ T(r, z) &= T_\infty, \\ C(r, z) &= C_\infty \end{aligned} \right\} \text{ as } r \rightarrow \infty.$$

The symbols used in above equations are listed below as:

p : pressure	c_s : concentration susceptibility
α_1 : material parameter of second grade fluid	c_p : specific heat capacity
D_m : molecular diffusivity of the species concentration	q_r : radiative heat flux
k_t : thermal diffusion ratio	n^* : temperature index.
	T_m : mean fluid temperature

l : characteristic length of the cylinder	C : concentration of fluid
C_∞ : ambient concentration	c : dimensional constant

The radiative heat flux q_r is obtained by means of Rosseland approximation (Rosseland 1931) as follows

$$q_r = -\frac{4\sigma^*}{3(\alpha_r + \sigma_s)} \frac{\partial T^4}{\partial r}, \quad (6.6)$$

where σ^* is the Stefan-Boltzman constant, α_r is the Rosseland mean absorption coefficient, and σ_s is the scattering coefficient. For the flow over hot stretching cylinder, the reduced form of radiative heat flux (Magyari and Pantokratoras 2011) is

$$q_r = -\frac{16\sigma^*T^3}{3(\alpha_r + \sigma_s)} \frac{\partial T}{\partial r}. \quad (6.7)$$

Upon utilizing Eq. (6.6) in Eq. (6.3), we get

$$\begin{aligned} \left(u \frac{\partial T}{\partial r} + v \frac{\partial T}{\partial z}\right) &= \frac{k}{\rho c_p} \left(1 + \frac{16\sigma^*T^3}{3k(\alpha_r + \sigma_s)}\right) \left(\frac{\partial^2 T}{\partial r^2} + \frac{\partial T}{r \partial r}\right) \\ &+ \frac{\rho D_m k_t}{c_p c_s} \left(\frac{\partial^2 C}{\partial r^2} + \frac{\partial C}{r \partial r}\right). \end{aligned} \quad (6.8)$$

It is assumed that temperature difference in the fluid-phase within the flow is sufficiently small and k is considered as constant. Linearizing the radiative heat flux about the ambient temperature T_∞ will bring Eq. (6.8) to the following form:

$$\begin{aligned} \left(u \frac{\partial T}{\partial r} + v \frac{\partial T}{\partial z}\right) &= \frac{k}{\rho c_p} \left(1 + \frac{16\sigma^*T_\infty^3}{3k(\alpha_r + \sigma_s)}\right) \left(\frac{\partial^2 T}{\partial r^2} + \frac{\partial T}{r \partial r}\right) \\ &+ \frac{\rho D_m k_t}{c_p c_s} \left(\frac{\partial^2 C}{\partial r^2} + \frac{\partial C}{r \partial r}\right). \end{aligned} \quad (6.9)$$

Introducing the following appropriate similarity transformations

$$\begin{aligned} \eta &= \frac{r^2 - R^{*2}}{2R^*} \sqrt{\frac{c}{\nu l}}, \quad u = -\frac{R^*}{r} \sqrt{\frac{c\nu}{l}} f(\eta), \quad v = \frac{cz}{l} f'(\eta), \\ \theta(\eta) &= \frac{T - T_\infty}{T_w - T_\infty}, \quad \theta(\eta) = \frac{C - C_\infty}{C_w - C_\infty}, \end{aligned} \quad (6.10)$$

After eliminating pressure terms from Eq. (6.1) and Eq. (6.2) and upon using similarity transformation, Eqs. (6.1-6.4) take the following dimensionless form:

$$\begin{aligned} (1 + 2\gamma\eta)f^{iv} - f'f'' + ff''' + 4\gamma f''' + 4\gamma K f'f''' - \\ 6\gamma K f f^{iv} + (1 + 2\gamma\eta)K(f'f^{iv} - ff^v) = 0, \end{aligned} \quad (6.11)$$

$$\frac{1}{Pr_{eff}}((1 + 2\gamma\eta)\theta'' + 2\gamma\theta') + (f\theta' - n^*f'\theta) + Du((1 + 2\gamma\eta)\phi'' + 2\gamma\phi') = 0, \quad (6.12)$$

$$((1 + 2\gamma\eta)\phi'' + 2\gamma\phi') + Sc(f\phi' - n^*f'\phi) + ScSr((1 + 2\gamma\eta)\theta'' + 2\gamma\theta') = 0. \quad (6.13)$$

The boundary conditions (6.5) reduce to:

$$f(0) = 0, f'(0) = 1, f'(\infty) = f''(\infty) = f'''(\infty) = 0, \quad (6.14)$$

$$\theta(0) = 1, \theta(\infty) = 0, \phi(0) = 1, \phi(\infty) = 0,$$

where, $K = \alpha_1 c / \rho \nu l$ (Viscoelastic parameter), $Nr = 16\sigma^* T_\infty^3 / 3k(\alpha_r + \sigma_s)$ (Radiation parameter), $Pr_{eff} = Pr / (1 + Nr)$ (Prandtl effective number), $Du = D_m k_t (C_w - C_\infty) / c_p c_s (T_w - T_\infty)$ (Dufour number), $Sr = D_m k_t (T_w - T_\infty) / T_m \nu (C_w - C_\infty)$ (Soret number), and $Sc = \nu / D_m$ (Schmidt number).

It is important to mention here that for $\gamma = 0$, Eq. (6.11) reduces to the case of flat sheet problem, i.e.

$$f^{iv} - f'f'' + ff''' + K(f'f^{iv} - ff^v) = 0. \quad (6.15)$$

Integrating above equation w.r.t η we get:

$$f''' + ff'' - f'^2 + K(2ff''' - f''^2 - ff^{iv}) + c = 0. \quad (6.16)$$

here constant $c = 0$, due to boundary condition specified at infinity. The above Eq. (6.16) is a typical form of second grade fluid model as reported by (Vajravelu and Roper 2011).

The important physical quantities which are used to measure the skin-friction, heat and mass transfer are given as

$$C_f = \frac{\tau_w}{\rho V_w^2}, \quad Nu = \frac{zq_w}{k_{eff}(T_w - T_\infty)}, \quad Sh = \frac{zq_m}{D_m(C_w - C_\infty)}, \quad (6.17)$$

where τ_{rz} represents the shear stress along the cylinder, k_{eff} is the combination of k_{cond} with k_{rad} , q_w represents the heat flux and q_m is mass flux at the wall, which are defined as

$$\tau_w = \mu \left(\frac{\partial v}{\partial r} \right)_{r=R} + \alpha_1 \left(v \frac{\partial^2 v}{\partial z \partial r} + u \frac{\partial^2 v}{\partial r^2} - \frac{\partial v}{\partial r} \frac{\partial v}{\partial z} + \frac{\partial v}{\partial r} \frac{\partial u}{\partial r} \right)_{r=R}, \quad (6.18)$$

$$k_{eff} = k + \frac{16\sigma T^3}{3(\alpha_r + \sigma_s)}, \quad q_w = -k_{eff} \left(\frac{\partial T}{\partial r} \right)_{r=R}, \quad q_m = -D_m \left(\frac{\partial C}{\partial r} \right)_{r=R}.$$

In view of Eq. (6.18), Eq. (6.17) become

$$\text{Skin friction coefficient: } Re_z^{1/2} C_f = (1 + 3K)f''(0), \quad (6.19)$$

$$\text{Local Nusselt number: } Re_z^{-1/2} Nu = -\theta'(0),$$

Local Sherwood number: $Re_z^{-1/2} Sh = -\phi'(0)$,

where $Re_z = cz^2/l\nu$ is the local Reynolds number.

6.2 Solution methodology

The numerical simulation of nonlinear ordinary differential equations (6.11–6.13) subject to the boundary conditions (6.14) is performed by means of Keller box method (Cebeci and Bradshaw 1984). The steps through which the solution is computed are as follows:

The system of equations (6.13–6.15) are reduced to the system of first order ODE's. For this purpose, let us introduce the new variables p, q, s, d, U, V which are defined as:

$$f' = p, p' = q, q' = s, s' = d, \theta' = U, \phi' = V. \quad (6.20)$$

After using above functions in Eqs. (6.11–6.14), we get

$$(1 + 2\gamma\eta)d - pq + fs + 4\gamma s + 4\gamma Kps - 6\gamma Kfd + (1 + 2\gamma\eta)K(pd - fd') = 0, \quad (6.21)$$

$$\frac{1}{p_{ref}} [(1 + 2\gamma\eta)U' + 2\gamma U] + (fU - n^*p\theta) + Du[(1 + 2\gamma\eta)V' + 2\gamma V] = 0, \quad (6.22)$$

$$[(1 + 2\gamma\eta)V' + 2\gamma V] + Sc(fV - n^*p\phi) + ScSr[(1 + 2\gamma\eta)U' + 2\gamma U] = 0, \quad (6.23)$$

$$f(0) = 0, p(0) = 1, p(\infty) = q(\infty) = s(\infty) = 0, \quad (6.24)$$

$$\theta(0) = 1, \theta(\infty) = 0, \phi(0) = 1, \phi(\infty) = 0.$$

A net on η is defined as

$$\eta_0 = 0, \eta_j = \eta_{j-1} + \Delta\eta, \eta_J = \eta_\infty, j = 1, 2, \dots, J - 1 \quad (6.25)$$

where j is positive integer and $\Delta\eta$ is the width of meshing variables on η . The approximate quantities of functions p, q, s, d, U , and V at the net point η_j are known as net functions whose derivatives in η -direction are replaced by the central difference formulae and functions itself are replaced by average centered at the midpoint $\eta_{j-1/2}$ defined as $f'_{j-1/2} = (f_j - f_{j-1})/\Delta\eta$, and $f_{j-1/2} = (f_j + f_{j-1})/\Delta\eta$. After discretization, the system of first order nonlinear ordinary differential Eqs. (6.21–6.23) are converted to difference equations in terms of nonlinear algebraic equations as follows

$$\begin{aligned} & \frac{1}{2}(1 + (\eta_j + \eta_{j-1})\gamma)(d_j + d_{j-1}) - \frac{1}{4}(p_j + p_{j-1})(q_j + q_{j-1}) \\ & + \frac{1}{4}(f_j + f_{j-1})(s_j + s_{j-1}) + 2\gamma(s_j + s_{j-1}) + \gamma K(p_j + p_{j-1})(s_j + s_{j-1}) \\ & - \frac{3\gamma K}{2}(f_j + f_{j-1})(d_j + d_{j-1}) - \frac{3\gamma K}{2}(f_j + f_{j-1})(d_j + d_{j-1}) \end{aligned} \quad (6.26)$$

$$+ (1 + (\eta_j + \eta_{j-1})\gamma) K \left(\frac{1}{4} (p_j + p_{j-1})(d_j + d_{j-1}) - \frac{1}{2\Delta\eta} (f_j + f_{j-1})(d_j - d_{j-1}) \right) = 0,$$

$$\frac{1}{pr_{eff}} \left((1 + (\eta_j + \eta_{j-1})\gamma) \left(\frac{U_j - U_{j-1}}{\Delta\eta} \right) + \gamma(U_j + U_{j-1}) \right) + \left(\frac{1}{4} (f_j + f_{j-1})(U_j + U_{j-1}) - \frac{n^*}{4} (p_j + p_{j-1})(\theta_j + \theta_{j-1}) \right) \quad (6.27)$$

$$+ Du \left((1 + (\eta_j + \eta_{j-1})\gamma) \left(\frac{V_j - V_{j-1}}{\Delta\eta} \right) + \gamma(V_j + V_{j-1}) \right) = 0,$$

$$\left((1 + (\eta_j + \eta_{j-1})\gamma) \left(\frac{V_j - V_{j-1}}{\Delta\eta} \right) + \gamma(V_j + V_{j-1}) \right) + Sc \left(\frac{1}{4} (f_j + f_{j-1})(V_j + V_{j-1}) - \frac{n^*}{4} (p_j + p_{j-1})(\phi_j + \phi_{j-1}) \right) \quad (6.28)$$

$$+ ScSr \left((1 + (\eta_j + \eta_{j-1})\gamma) \left(\frac{U_j - U_{j-1}}{\Delta\eta} \right) + \gamma(U_j + U_{j-1}) \right) = 0$$

and Eq. (6.20) becomes

$$\begin{aligned} f_j - f_{j-1} &= \frac{\Delta\eta}{2} (p_j + p_{j-1}), \\ p_j - p_{j-1} &= \frac{\Delta\eta}{2} (q_j + q_{j-1}), \\ q_j - q_{j-1} &= \frac{\Delta\eta}{2} (s_j + s_{j-1}), \\ s_j - s_{j-1} &= \frac{\Delta\eta}{2} (d_j + d_{j-1}), \\ \theta_j - \theta_{j-1} &= \frac{\Delta\eta}{2} (U_j + U_{j-1}), \\ \phi_j - \phi_{j-1} &= \frac{\Delta\eta}{2} (V_j + V_{j-1}). \end{aligned} \quad (6.29)$$

The nonlinear algebraic Eqs. (6.26)–(6.28) are linearized using Newton method by introducing $(i + 1)^{th}$ iterates as

$$f_j^{i+1} = f_j^{(i)} + \delta f_j^{(i)} \quad (6.30)$$

and similarly for all other variables. Here $f_j^{(i)}$ is known for $0 \leq j < J$ as an initial guess and $\delta f_j^{(i)}$ is unknown. After using the Newton linearization process and neglecting the terms

containing square and higher order of $\delta f_j^{(i)}, \delta p_j^{(i)}, \delta q_j^{(i)}, \delta s_j^{(i)}, \delta d_j^{(i)}, \delta \theta_j^{(i)}, \delta U_j^{(i)}, \delta \phi_j^{(i)}$, and $\delta V_j^{(i)}$, the system of linear algebraic equations is obtained as follows:

$$\begin{aligned}
& \delta f_j - \delta f_{j-1} - \frac{\Delta\eta}{2}(\delta p_j + \delta p_{j-1}) = (r_1)_j, \\
& (a_1)_j \delta f_{j-1} + (a_2)_j \delta f_j + (a_3)_j \delta p_{j-1} + (a_4)_j \delta p_j + (a_5)_j \delta q_{j-1} + (a_6)_j \delta q_j \\
& \quad (a_7)_j \delta s_{j-1} + (a_8)_j \delta s_j + (a_9)_j \delta d_{j-1} + (a_{10})_j \delta d_j = (r_2)_j, \\
& (a_{11})_j \delta \theta_{j-1} + (a_{12})_j \delta \theta_j + (a_{13})_j \delta U_{j-1} + (a_{14})_j \delta U_j + (a_{15})_j \delta V_{j-1} + (a_{16})_j \delta V_j \\
& \quad = (r_3)_j, \\
& (a_{17})_j \delta \phi_{j-1} + (a_{18})_j \delta \phi_j + (a_{19})_j \delta V_{j-1} + (a_{20})_j \delta V_j = (r_4)_j, \\
& \delta p_j - \delta p_{j-1} - \frac{\Delta\eta}{2}(\delta q_j + \delta q_{j-1}) = (r_5)_j, \\
& \delta q_j - \delta q_{j-1} - \frac{\Delta\eta}{2}(\delta s_j + \delta s_{j-1}) = (r_6)_j, \\
& \delta s_j - \delta s_{j-1} - \frac{\Delta\eta}{2}(\delta d_j + \delta d_{j-1}) = (r_7)_j, \\
& \delta \theta_j - \delta \theta_{j-1} - \frac{\Delta\eta}{2}(\delta U_j + \delta U_{j-1}) = (r_8)_j, \\
& \delta \phi_j - \delta \phi_{j-1} - \frac{\Delta\eta}{2}(\delta V_j + \delta V_{j-1}) = (r_9)_j.
\end{aligned}$$

The boundary conditions (6.24) take the form as

$$\delta f_0 = \delta p_0 = \delta \theta_0 = \delta \phi_0 = 0, \delta p_J = \delta q_J = \delta s_J = \delta \theta_J = \delta \phi_J = 0.$$

Finally, the above system of linear algebraic equations with boundary conditions are written in matrix vector form. The coefficients in momentum and energy equations of unknown functions $\delta f_{j-1}, \delta p_{j-1}, \delta q_{j-1}, \delta s_{j-1}, \delta d_{j-1}, \delta \theta_{j-1}, \delta U_{j-1}$ and δV_{j-1} and non-homogeneous parts are given as

Coefficient of momentum equation

Coefficient of δf_{j-1} :

$$\begin{aligned}
(a_1)_j = & -\frac{1}{4}(s_j + s_{j-1}) - \frac{3\gamma K}{2}(d_j + d_{j-1}) \\
& + (1 + \gamma(\eta_j + \eta_{j-1}))K \left(-\frac{1}{2\Delta\eta}(d_j + d_{j-1}) \right)
\end{aligned}$$

Coefficient of δf_j :

$$(a_2)_j = \frac{1}{4}(s_j + s_{j-1}) - \frac{3\gamma K}{2}(d_j + d_{j-1})$$

$$+ \left(1 + \gamma(\eta_j + \eta_{j-1})\right) K \left(-\frac{1}{2\Delta\eta} (d_j + d_{j-1}) \right)$$

Coefficient of δp_{j-1} :

$$(a_3)_j = -\frac{1}{4}(q_j + q_{j-1}) + \gamma K(s_j + s_{j-1}) \\ + \left(1 + \gamma(\eta_j + \eta_{j-1})\right) \frac{K}{4} \left(-\frac{1}{2\Delta\eta} (d_j + d_{j-1}) \right)$$

Coefficient of δp_j :

$$(a_4)_j = -\frac{1}{4}(q_j + q_{j-1}) + \gamma K(s_j + s_{j-1}) \\ + [1 + \gamma(\eta_j + \eta_{j-1})] \frac{K}{4} \left(-\frac{1}{2\Delta\eta} (d_j + d_{j-1}) \right)$$

Coefficient of δq_{j-1} :

$$(a_5)_j = -\frac{1}{4}(p_j + p_{j-1})$$

Coefficient of δq_j :

$$(a_6)_j = -\frac{1}{4}(p_j + p_{j-1})$$

Coefficient of δs_{j-1} :

$$(a_7)_j = \frac{1}{4}(f_j + f_{j-1}) + 2\gamma + \gamma K(p_j + p_{j-1})$$

Coefficient of δs_j :

$$(a_8)_j = \frac{1}{4}(f_j + f_{j-1}) + 2\gamma + \gamma K(p_j + p_{j-1})$$

Coefficient of δd_{j-1} :

$$(a_9)_j = \frac{(1 + \gamma(\eta_j + \eta_{j-1}))}{2} - \frac{3\gamma K}{2} (f_j + f_{j-1}) \\ + \left(1 + \gamma(\eta_j + \eta_{j-1})\right) K \left(\frac{1}{4}(p_j + p_{j-1}) + \frac{1}{2\Delta\eta} (f_j + f_{j-1}) \right)$$

Coefficient of δd_j :

$$(a_{10})_j = \frac{(1 + \gamma(\eta_j + \eta_{j-1}))}{2} - \frac{3\gamma K}{2} (f_j + f_{j-1}) \\ + \left(1 + \gamma(\eta_j + \eta_{j-1})\right) K \left(\frac{1}{4}(p_j + p_{j-1}) - \frac{1}{2\Delta\eta} (f_j + f_{j-1}) \right)$$

Coefficient of energy equationCoefficient of $\delta\theta_{j-1}$:

$$(a_{11})_j = -\frac{n^*}{4}(p_j + p_{j-1})$$

Coefficient of $\delta\theta_j$:

$$(a_{12})_j = -\frac{n^*}{4}(p_j + p_{j-1})$$

Coefficient of δU_{j-1} :

$$(a_{13})_j = \frac{1}{Pr_{eff}} \left(\frac{(1 + \gamma(\eta_j + \eta_{j-1}))}{\Delta\eta} + \gamma \right) + \frac{1}{4}(f_j + f_{j-1})$$

Coefficient of δU_j :

$$(a_{14})_j = \frac{1}{Pr_{eff}} \left(\frac{(1 + \gamma(\eta_j + \eta_{j-1}))}{\Delta\eta} + \gamma \right) + \frac{1}{4}(f_j + f_{j-1})$$

Coefficient of δV_{j-1} :

$$(a_{15})_j = Du \left((1 + \gamma(\eta_j + \eta_{j-1})) \left(\frac{-1}{\Delta\eta} \right) + \gamma \right)$$

Coefficient of δV_j :

$$(a_{16})_j = Du \left((1 + \gamma(\eta_j + \eta_{j-1})) \left(\frac{1}{\Delta\eta} \right) + \gamma \right)$$

Coefficient of concentration equationCoefficient of $\delta\theta_{j-1}$:

$$(a_{17})_j = -Sc \left(\frac{n^*}{4} \right) (p_j + p_{j-1})$$

Coefficient of $\delta\theta_j$:

$$(a_{18})_j = -Sc \left(\frac{n^*}{4} \right) (p_j + p_{j-1})$$

Coefficient of $\delta\phi_{j-1}$:

$$(a_{19})_j = -\frac{n^*}{4}(p_j + p_{j-1})$$

Coefficient of $\delta\phi_j$:

$$(a_{20})_j = -\frac{n^*}{4}(p_j + p_{j-1})$$

Non-homogeneous terms:

$$\begin{aligned}
(r_1)_j &= f_j - f_{j-1} - \frac{\Delta\eta}{2}(p_j + p_{j-1}), \\
(r_2)_j &= -\frac{1}{2}(1 + (\eta_j + \eta_{j-1})\gamma)(d_j + d_{j-1}) + \frac{1}{4}(p_j + p_{j-1})(q_j + q_{j-1}) \\
&\quad - \frac{1}{4}(f_j + f_{j-1})(s_j + s_{j-1}) - 2\gamma(s_j + s_{j-1}) - \gamma K(p_j + p_{j-1})(s_j + s_{j-1}) \\
&\quad - \frac{3\gamma K}{2}(f_j + f_{j-1})(d_j + d_{j-1}) + \frac{3\gamma K}{2}(f_j + f_{j-1})(d_j + d_{j-1}) \\
&\quad - (1 + (\eta_j + \eta_{j-1})\gamma)K \left(\frac{1}{4}(p_j + p_{j-1})(d_j + d_{j-1}) - \frac{1}{2\Delta\eta}(f_j + f_{j-1})(d_j - d_{j-1}) \right), \\
(r_3)_j &= -\frac{1}{pr_{eff}} \left((1 + (\eta_j + \eta_{j-1})\gamma) \left(\frac{U_j - U_{j-1}}{\Delta\eta} \right) + \gamma(U_j + U_{j-1}) \right) \\
&\quad - \left(\frac{1}{4}(f_j + f_{j-1})(U_j + U_{j-1}) - \frac{n}{4}(p_j + p_{j-1})(\theta_j + \theta_{j-1}) \right) \\
&\quad - Du \left((1 + (\eta_j + \eta_{j-1})\gamma) \left(\frac{V_j + V_{j-1}}{\Delta\eta} \right) + \gamma(V_j + V_{j-1}) \right), \\
(r_4)_j &= - \left((1 + (\eta_j + \eta_{j-1})\gamma) \left(\frac{V_j - V_{j-1}}{\Delta\eta} \right) + \gamma(V_j + V_{j-1}) \right) \\
&\quad - Sc \left(\frac{1}{4}(f_j + f_{j-1})(V_j + V_{j-1}) - \frac{n}{4}(p_j + p_{j-1})(\phi_j + \phi_{j-1}) \right), \\
(r_5)_j &= \delta p_j - \delta p_{j-1} - \frac{\Delta\eta}{2}(\delta q_j + \delta q_{j-1}), \\
(r_6)_j &= \delta q_j - \delta q_{j-1} - \frac{\Delta\eta}{2}(\delta s_j + \delta s_{j-1}), \\
(r_7)_j &= \delta s_j - \delta s_{j-1} - \frac{\Delta\eta}{2}(\delta d_j + \delta d_{j-1}), \\
(r_8)_j &= \delta \theta_j - \delta \theta_{j-1} - \frac{\Delta\eta}{2}(\delta U_j + \delta U_{j-1}), \\
(r_9)_j &= \delta \phi_j - \delta \phi_{j-1} - \frac{\Delta\eta}{2}(\delta V_j + \delta V_{j-1}).
\end{aligned}$$

The resulting matrix vector form is solved by using block-tridiagonal elimination technique. The edge of the boundary layer η_∞ and step sizes $\Delta\eta$ are set for different range of parameters. By implementing the above mentioned procedure, the system of equations (6.11-6.14) is solved and the computed results are presented through tables and graphs for wide ranges of physical parameters involved in the equations. Table 6.1, presents the

numerical values of skin friction coefficient against different iterations to ensure the convergence of the adopted method. It is ensured from these results that convergence is achieved after only 5 or 6 number of iterations and these values are validated with Chebyshev Spectral Newton Iterative Scheme (Majeed et al. 2015). This gave us great confidence in accuracy of applied technique. A comparison of the computed numerical values of $-\theta'(0)$ as a limiting case with previous published results is given in Table 6.2. These results are in perfect agreement with Ali (1994), and Mukhopadhyay (2012) for Newtonian case.

Table 6.1: Values of $Re_z^{1/2} C_f$ at different iterations with Keller box method when $\gamma = 0$

<i>Iterations</i> ↓	$Re_z^{1/2} C_f$			
	$K = 0$	$K = 0.5$	$K = 1$	$K = 5$
1	−0.7241	−1.2719	−1.6652	−3.5303
2	−0.9337	−1.7792	−2.3827	−5.1968
3	−0.9768	−1.9431	−2.6521	−5.9641
4	−0.9911	−2.0017	−2.7575	−6.3183
5	−0.9969	−2.0265	−2.8031	−6.4753
6	−0.9993	−2.0373	−2.8225	−6.5259
7	−0.9999	−2.0408	−2.8280	−6.5319
8	−1.0000	−2.0412	−2.8284	−6.5320
9	−1.0000	−2.0412	−2.8284	−6.5320
10	−1.0000	−2.0412	−2.8284	−6.5320
CSNIS (Majeed et al. 2015)	−1.0000	−2.0412	−2.8284	−6.5320

Table 6.2: Numerical values of $-\theta'(0)$ for different n when $\gamma = K = Nr = 0$
and $Pr = Pr_{eff}$

n	Ali (1999)	Mukhopadhyay (2012)	Present
0	0.5821	0.5820	0.5820
1	1.0000	1.0000	1.0000
2	1.3269	1.3332	1.3333

6.3 Results and Discussion

After employing the above discussed numerical scheme, results are found for velocity, temperature and concentration profile against the various values of emerging parameters named as: curvature parameter (γ), viscoelastic parameter (K), Dufour parameter (Du), Soret parameter (Sr), temperature exponent (n^*), effective Prandtl number (Pr_{eff}), and Schmidt parameter (Sc) which are shown in Figures 6.1–6.7. The effects of Curvature, viscoelasticity, Soret and Dufour parameters on $Re_z^{1/2}C_f$, $Re_z^{-1/2}Nu$ and $Re_z^{-1/2}Sh$ are computed and shown in Figures 6.8–6.11. Figures 6.1 and 6.2 illustrate the variations of velocity, temperature and concentration profiles against various values of curvature parameter γ and viscoelastic parameter K , respectively. Figure 6.1 shows that the velocity enhances as the curvature of the cylinder increases. This is evident from practical observation that the fluid flows over the cylinder with relatively small radius is much faster than that of cylinder with large radius or flat surface. As having the reciprocal relationship between curvature and radius, so increase in curvature results in reduction of surface of cylinder. The reduction in surface area enhances the fluid flow over the surface which increases the velocity, temperature and concentration. Figure 6.2 demonstrates that by enhancing the viscoelasticity of the fluid through increasing viscoelastic parameter We , the fluid velocity increases, and opposing effects are seen in case of temperature and concentration profiles. The effects of Du on temperature and Sr on concentration are shown in Figures 6.3 and 6.4 respectively. Temperature and thermal boundary layer thickness is observed an increasing function of Du . On the other hand, Soret number Sr helps to accelerate the concentration in the fluid in the boundary layer region. The effects of temperature exponents n^* on temperature and concentration profiles are demonstrated in Figure 6.5. It is seen that the variation from linear to nonlinear wall temperature helps to reduce the temperature and concentration boundary layer thicknesses. In Figure 6.6, the effects of effective Prandtl number on temperature profile is shown. It is found that with increase in effective Prandtl number the boundary layer gets thin. Since the effective Prandtl number is a combination of both radiation and Prandtl number as proposed by Magyari and Pantokratoras (2011). In their article, they suggested that the prominent effects of radiation can be obtained for the smaller values of effective Prandtl number and increase in Pr_{eff} results in substantial reduce in temperature of the fluid. It is further seen that with increase in Pr_{eff} , thermal boundary layer thickness decreases near the surface of cylinder. Figure 6.7 demonstrates the results of concentration profiles for various values of Sc . It is found

that the increasing values of Sc minimize the concentration in the fluid. This is because of the fact that molecular diffusivity has inverse relation with Sc , in turns increasing Schmidt number has decreases diffusivity effects in flow domain. It is found through Figure 6.8 that values of $Re_z^{1/2}C_f$ is a decreasing function of γ and K . However, it is sharply decreasing for viscoelastic effects. It is due to the reason that increase in curvature of stretching cylinder implies to reduce the surface area of the cylinder, hence skin friction will decrease. It is also seen that with increase in γ , the variation in skin friction remain negligible at $K = 0$. Figure 6.9 shows the effects of curvature parameter γ on $Re_z^{-1/2}Nu$ and $Re_z^{-1/2}Sh$ for different values of K . It is observed that as much we reduce the radius of cylinder heat transfer rate near the surface in the fluid decrease for both Newtonian and non-Newtonian fluid. However, the effects are more dominant in non-Newtonian case. Figure 6.10 shows the effects of K on $Re_z^{-1/2}Nu$ and $Re_z^{-1/2}Sh$ for simultaneous variation of Du (increasing) and Sr (decreasing). To discuss the effects of Dufour and Soret number, keep in mind that their product should be constant for homogeneous mixture. It is seen through Figure 6.10 that by increasing the Du parameter heat transfer rate reduces. On the other hand, Sr parameter is found responsible for increase in $Re_z^{-1/2}Nu$ for all values of We . Variations of mass transfer rate against We for different values of Du and Sr are also presented in Figure 6.11. A development in concentration rate is seen for large values of We . However, the effects for simultaneous variation of Du (increasing) and Sr (decreasing) on the values of $Re_z^{-1/2}Sh$ are observed opposite as that of effects on the values of $Re_z^{-1/2}Nu$. Figure 6.12 illustrates the variations of $Re_z^{-1/2}Nu$ and $Re_z^{-1/2}Sh$ against viscoelastic parameter We for different values of Prandtl effective Pr_{eff} . The values of $Re_z^{-1/2}Nu$ enhance for larger values of Pr_{eff} while opposite trend of it has been observed on $Re_z^{-1/2}Sh$. Figure 6.12 is plotted to show a relationship among the parameters Pr , Pr_{eff} and Nr . This graph shows that $Nr = 0$ implies $Pr_{eff} = Pr$ and with increase in radiation (i.e. $Nr > 0$) the values of Pr_{eff} are decreasing. This behaviour exhibits that the small Prandtl number exalts radiation effects. The computed numerical values of $Re_z^{1/2}C_f$, $Re_z^{-1/2}Nu$, and $Re_z^{-1/2}Sh$ for various values of viscoelastic parameter K and curvature parameter γ is shown in Table 6.3.

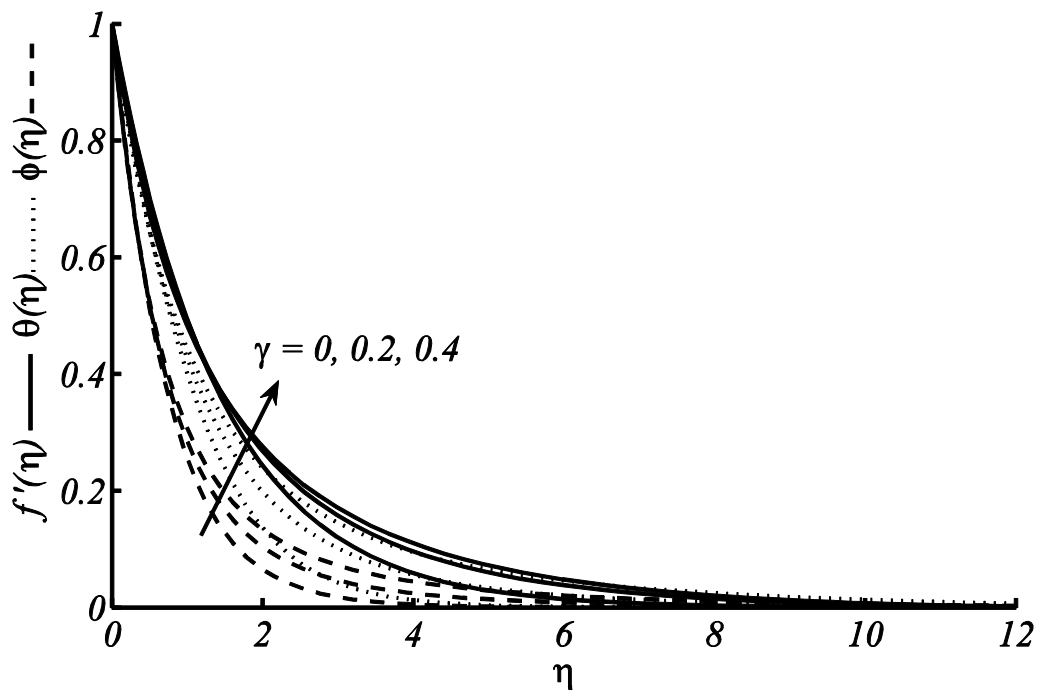


Figure 6.1: Curvature effects on velocity, temperature and concentration profile with fixed values of $K = n^* = Pr_{eff} = 1, Du = 0.3, Sr = 0.2$, and $Sc = 1.6$.

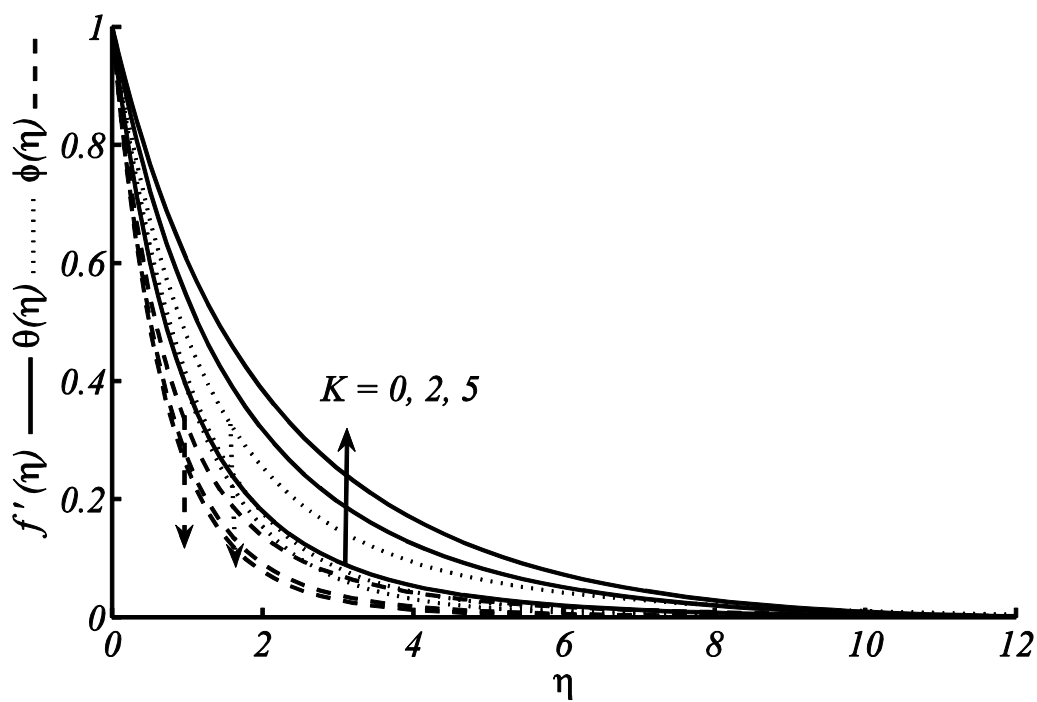


Figure 6.2: Impact of K on velocity, temperature and concentration profile with fixed values of $\gamma = 0.2, n^* = Pr_{eff} = 1, Du = 0.3, Sr = 0.2$, and $Sc = 1.6$.

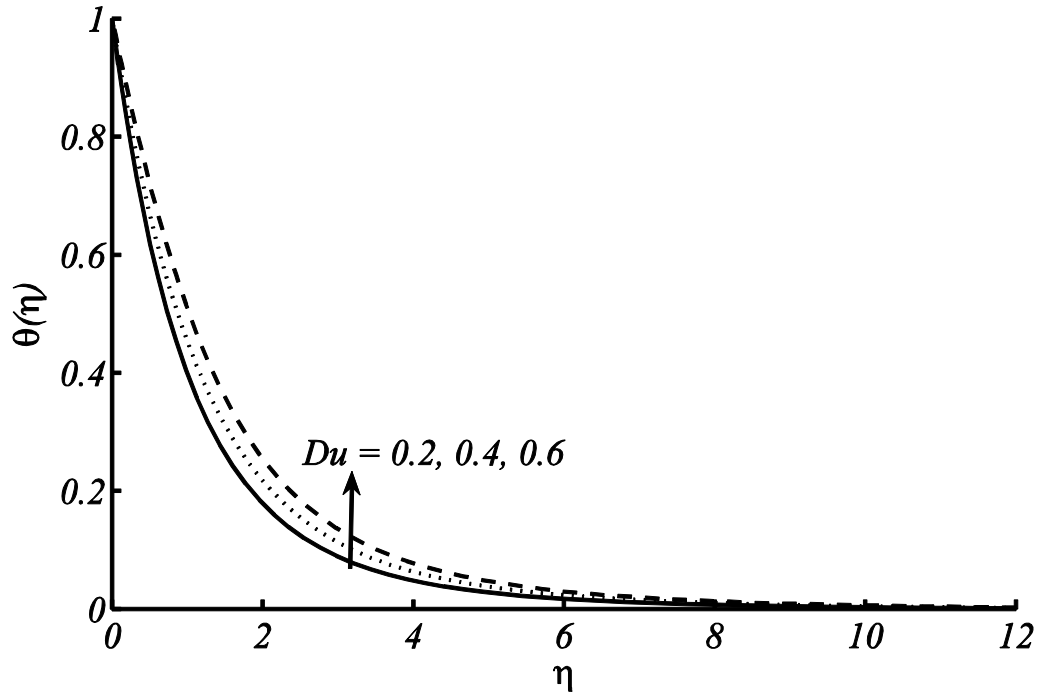


Figure 6.3: Impact of Du on temperature profile with fixed values of $\gamma = 0.2, K = n^* = Pr_{eff} = 1, Sr = 0.2$, and $Sc = 1.6$.

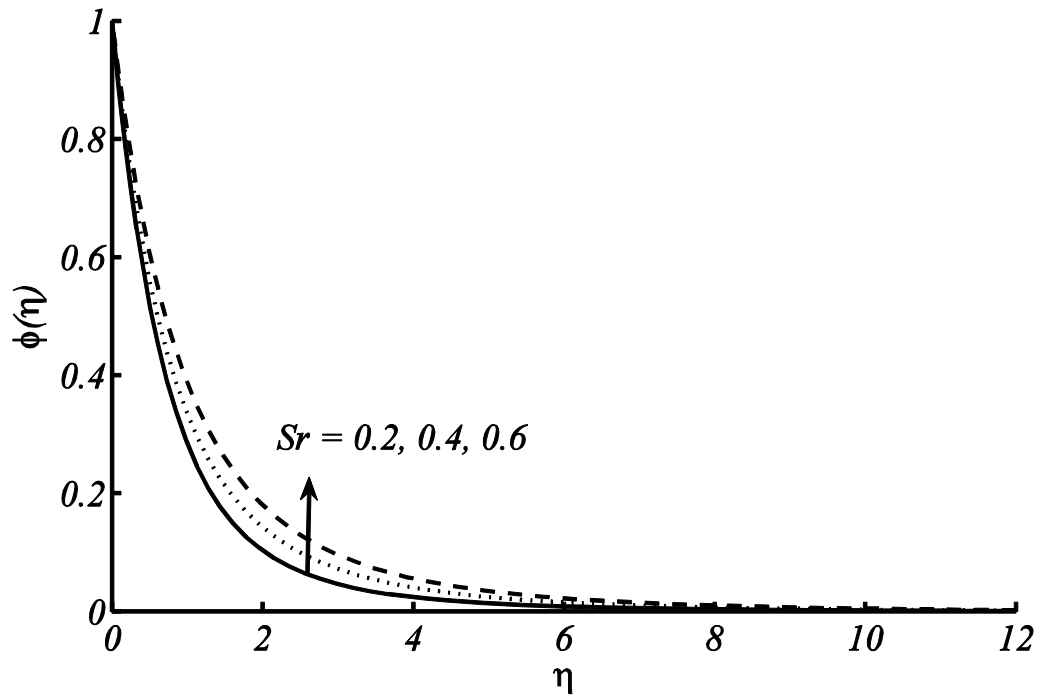


Figure 6.4: Impact of Sr on concentration profile with fixed values of $\gamma = 0.2, K = n^* = Pr_{eff} = 1, Du = 0.3$, and $Sc = 1.6$.

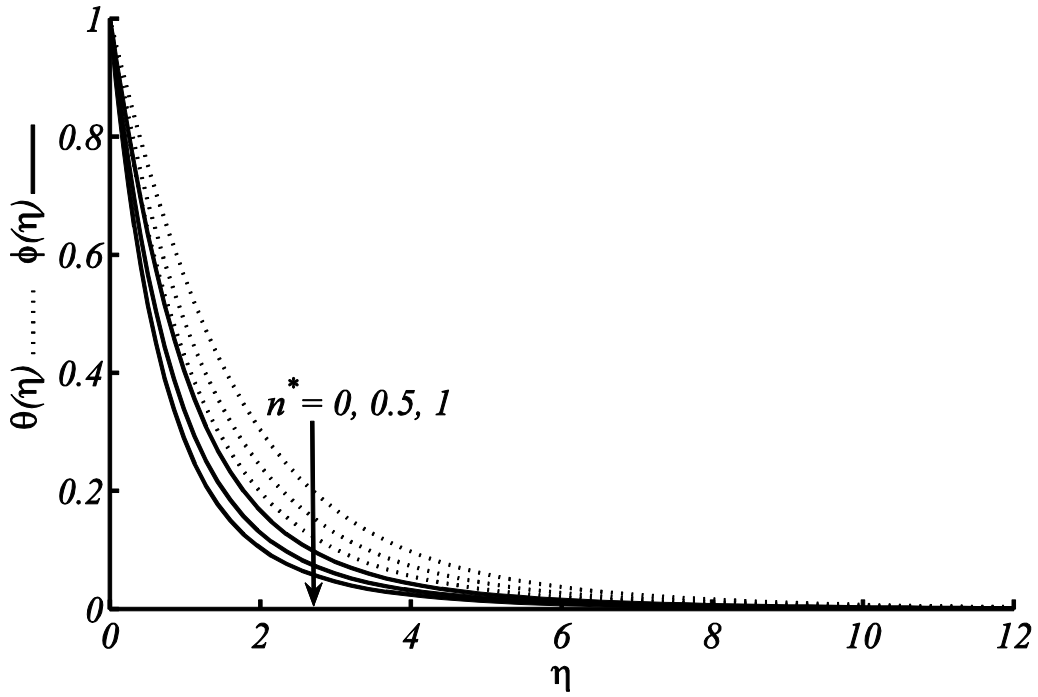


Figure 6.5: Impact of n^* on temperature and concentration when $\gamma = 0.2, K = Pr_{eff} = 1, Du = 0.3, Sr = 0.2$, and $Sc = 1.6$.

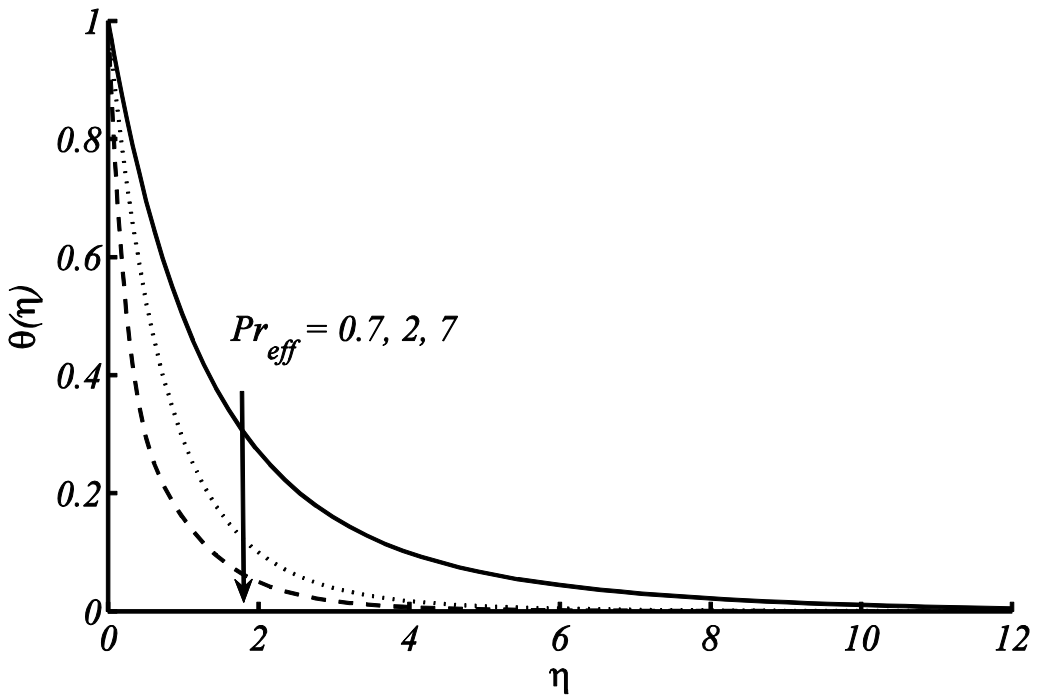


Figure 6.6: Impact of Pr_{eff} on temperature and concentration when $\gamma = 0.2, K = n^* = 1, Du = 0.3, Sr = 0.2$, and $Sc = 1.6$.

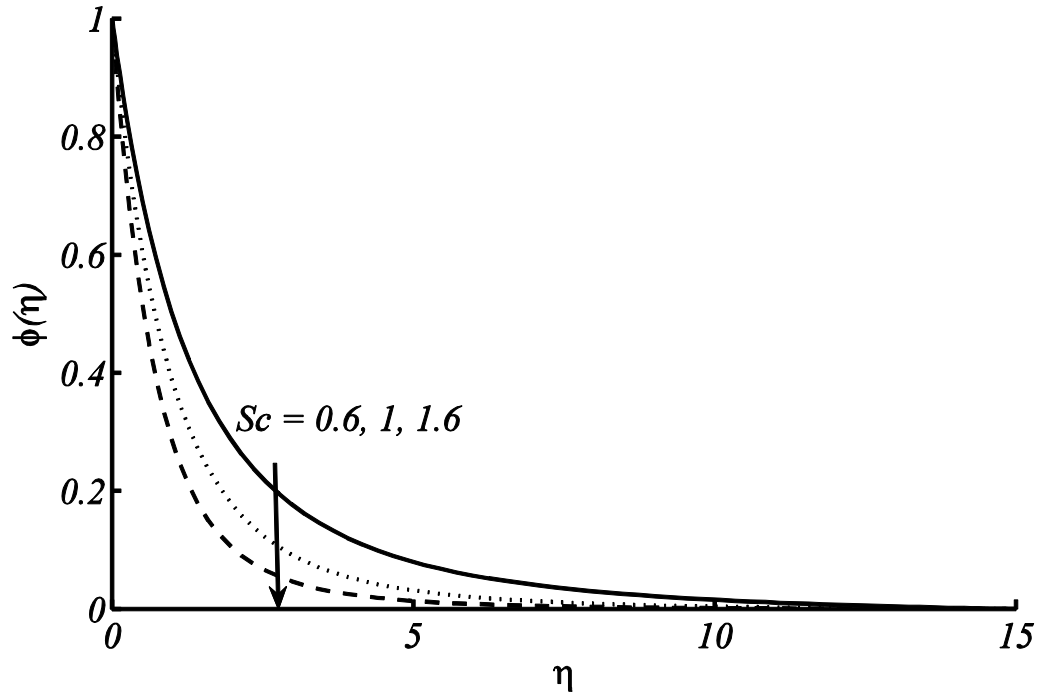


Figure 6.7: Impact of Sc on temperature and concentration when $\gamma = 0.2, K = n^* = Pr_{eff} = 1, Du = 0.3$, and $Sr = 0.2$.

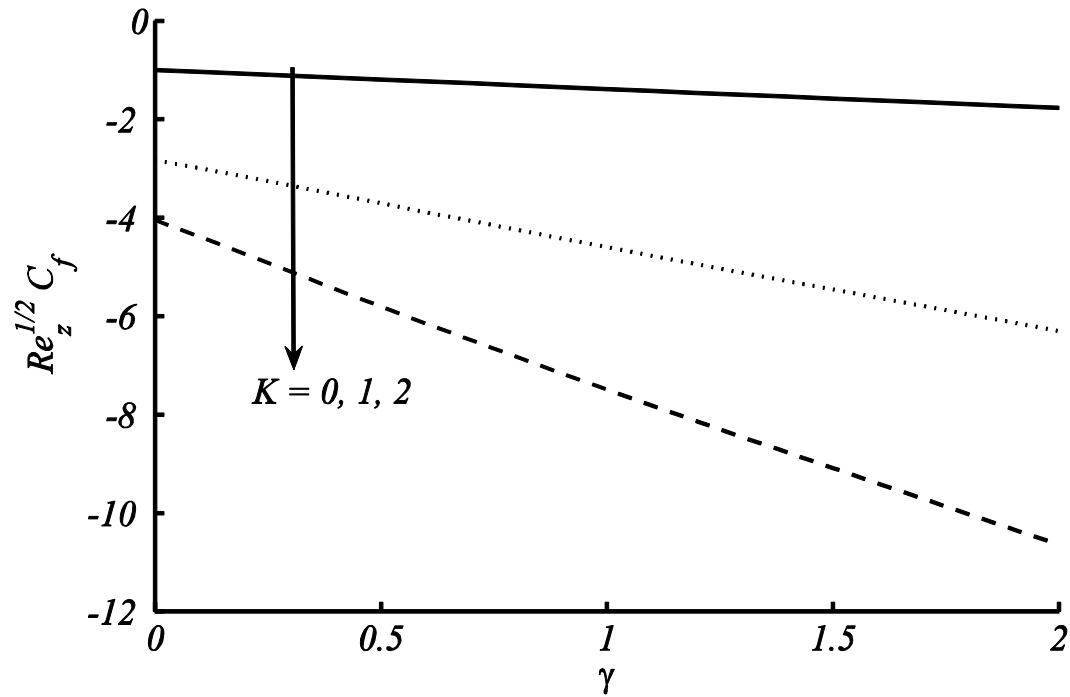


Figure 6.8: Variation in $Re_z^{1/2} C_f$ against γ at different K while $n^* = Pr_{eff} = 1, Du = 0.3, Sr = 0.2$ and $Sc = 1.6$ are fixed.

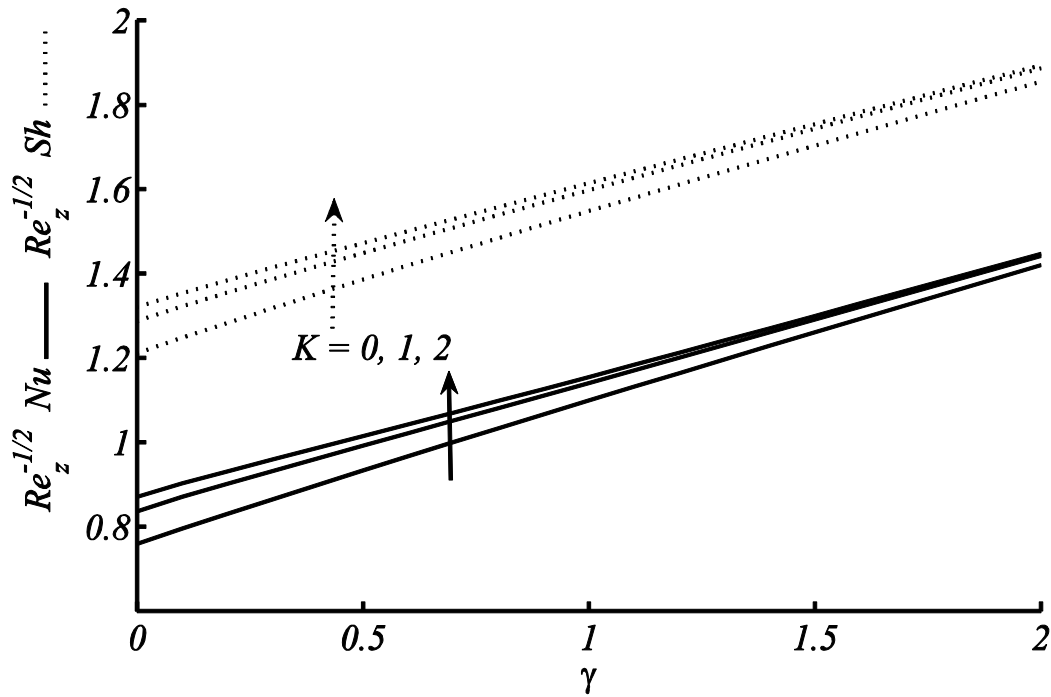


Figure 6.9: Variation in $Re_z^{-1/2} Nu$ and $Re_z^{-1/2} Sh$ against γ at different K while $n^* = Pr_{eff} = 1, Du = 0.3, Sr = 0.2$ and $Sc = 1.6$ are fixed.

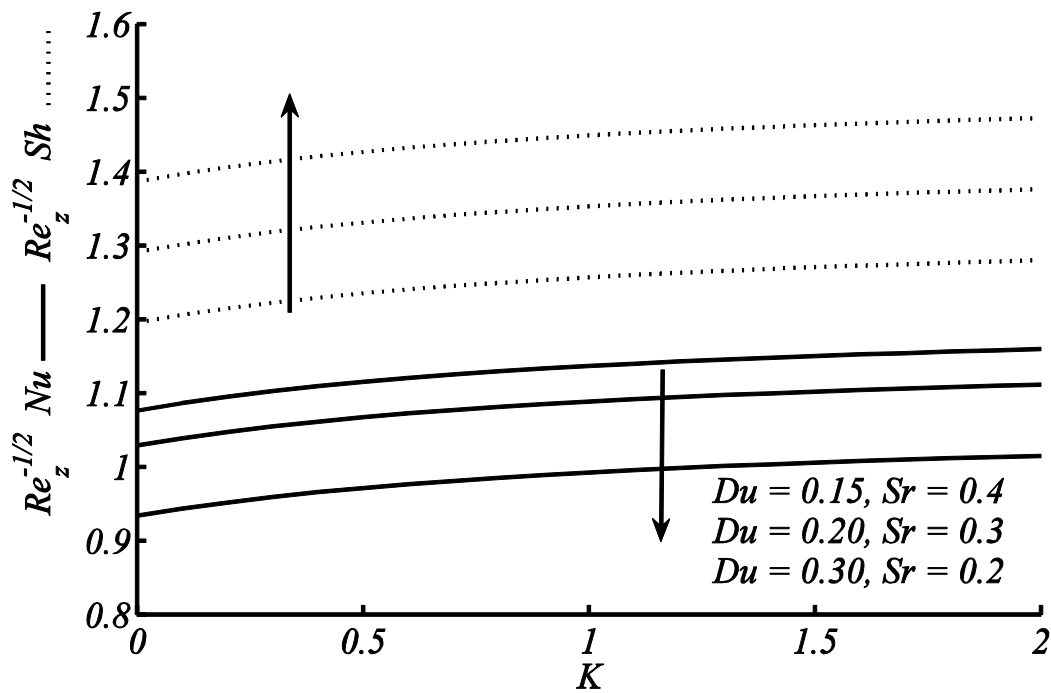


Figure 6.10: Variation in $Re_z^{-1/2} Nu$ and $Re_z^{-1/2} Sh$ against K at different Du , and Sr while $\gamma = 0.5, n^* = Pr_{eff} = 1$, and $Sc = 1.6$ are fixed.

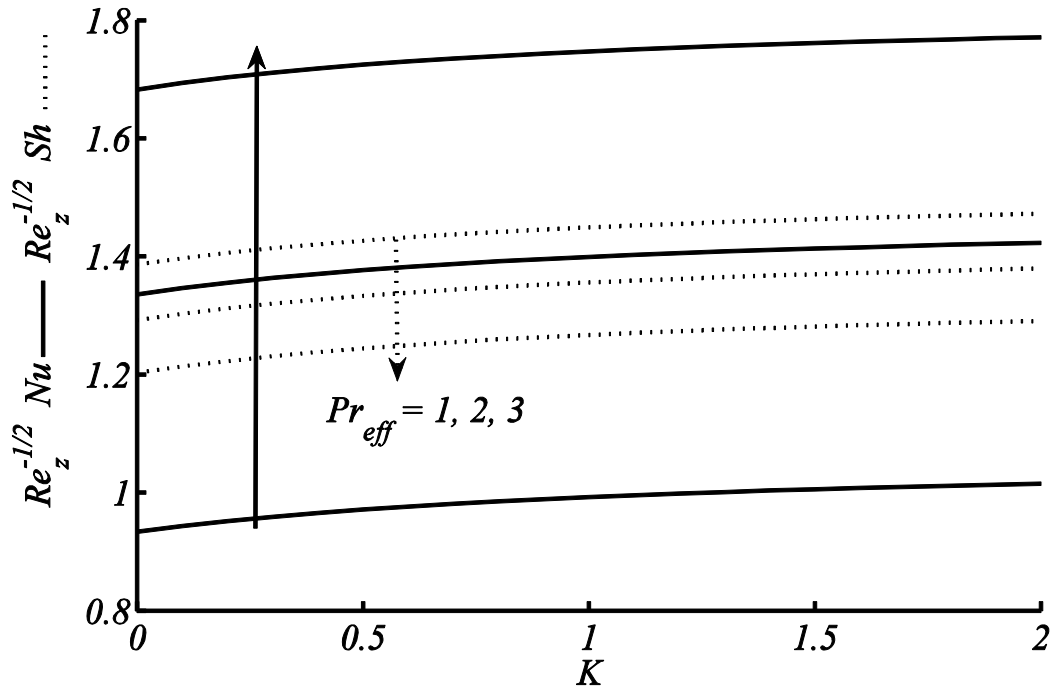


Figure 6.11: Variation in $Re_z^{-1/2} Nu$ and $Re_z^{-1/2} Sh$ against K at different Pr_{eff} while $\gamma = 0.5$, $n^* = 1$, $Du = 0.3$, $Sr = 0.2$, and $Sc = 1.6$ are fixed.

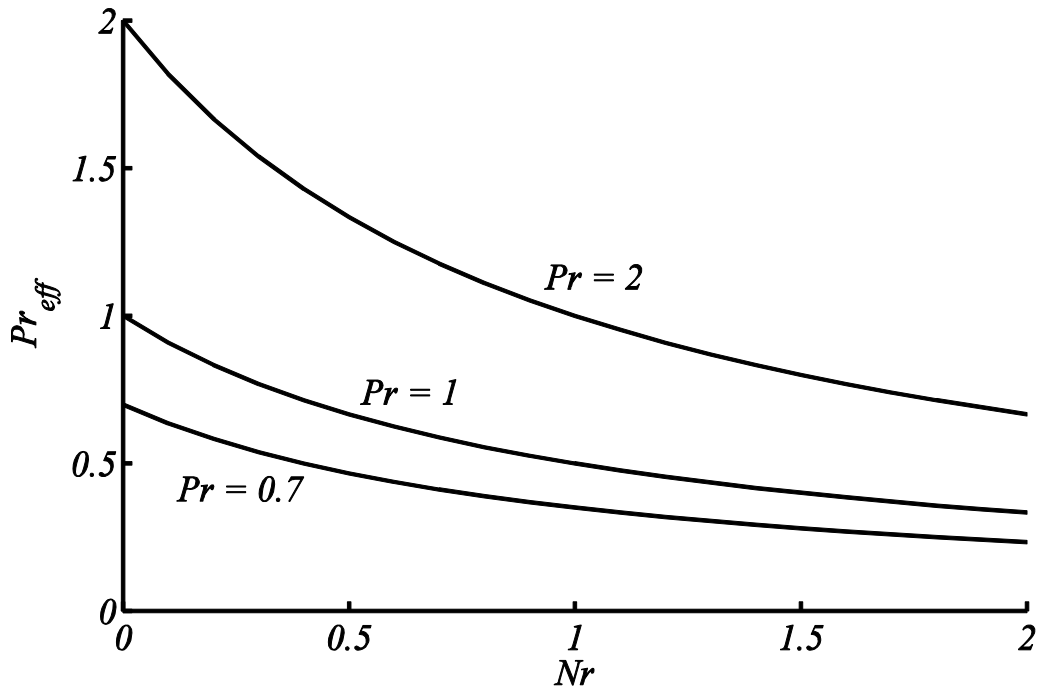


Figure 6.12: Graph of relationship among Nr , Pr , and Pr_{eff} .

Table 6.3: Numerical values of $Re_z^{1/2}C_f$, $Re_z^{-1/2}Nu$, and $Re_z^{-1/2}Sh$ at different K and γ

K	γ	$Re_z^{1/2}C_f$	$Re_z^{-1/2}Nu$	$Re_z^{-1/2}Sh$
0	0	-1.0000	0.4613	0.7151
	0.2	-1.0727	0.4857	0.7737
	0.5	-1.1779	0.5687	0.8615
1	0	-2.8284	0.4926	0.7780
	0.2	-3.1259	0.5482	0.8374
	0.5	-3.5614	0.6297	0.9245
5	0	-6.5320	0.5579	0.8433
	0.2	-7.8801	0.6162	0.9038
	0.5	-9.7687	0.7001	0.9923

6.4 Conclusions

Heat and mass transfer analysis of second grade fluid over an elongating surface of the cylinder has been studied in this chapter. For computational purposes, two numerical schemes, i.e. Keller box and Chebyshev Spectral Newton Iterative Scheme is used. To confirm the validity of obtaining results, the comparison is made with published results and it ensures that the computed solution is highly accurate. The important results of this study are mainly dependent upon the Soret, Dufour, viscoelastic and radiation parameters. We expressed our results in terms of figures and tables. The Curvature parameter (γ) increases the velocity of the fluid in the boundary layer region outside the cylinder. Similarly, temperature, and concentration are also increasing function of γ . The non-Newtonian fluid parameter (K) has an increasing impact on velocity and likewise temperature and concentration. The increase in Du and Sr significantly enhance the temperature and the concentration, respectively. The variations of concurrent occurring of Du (increasing) and Sr (decreasing) on $Re_z^{-1/2}Sh$ are observed opposite as that of effects on $Re_z^{-1/2}Nu$. The concentration boundary layer augments with a decrease in Schmidt number. It is important to write here that increase in Pr_{eff} bring about substantial reduce of temperature of the fluid.

Chapter 7

Study of Maxwell nanofluid flow around a stretching cylinder

In this chapter, attention is given to investigate the combined effects of linear and non-linear Rosseland thermal radiations in Maxwell nanofluid flow due to stretching cylinder. To strengthen the importance of the study, non-linear heat generation/absorption is also considered. These effects are incorporated into momentum, energy and concentration equations, and then these modeled non-linear partial differential equations are converted into ordinary differential equations with the help of suitable transformations. Significant difference in the heat transfer enhancement is observed through temperature profiles and tables of Nusselt number. From the graphs, it is observed that the nonlinear radiation provides better heat transfer rate at the surface of cylinder as compare to that of linear or absence of radiation effects.

7.1 Mathematical Formulation

Let us consider the two-dimensional flow of Maxwell nanofluid around the stretching cylinder of fixed radius R^* . The constitutive equations of Maxwell fluid model are developed in cylindrical coordinate system. The schematic of the flow has been described in chapter 4 and 6. Extra heating factors like nonlinear radiation and non-uniform heat generation/absorption are taken into account. Buongiorno's model is used to investigate the Brownian diffusion and thermophoresis effects on flow, heat and mass transfer of Maxwell nanofluid. This physical situation is modeled into mathematical form and obtained boundary layer equations which governs the flow, heat and mass transfer are as follows:

$$\frac{\partial(ru)}{\partial r} + \frac{\partial(rv)}{\partial z}, \quad (7.1)$$

$$u \frac{\partial v}{\partial r} + v \frac{\partial v}{\partial z} = v \left(\frac{\partial^2 v}{\partial r^2} + \frac{1}{r} \frac{\partial v}{\partial r} \right) + \frac{\lambda_1}{\rho} \left(u^2 \frac{\partial^2 v}{\partial r^2} + 2uv \frac{\partial^2 v}{\partial r \partial z} + v^2 \frac{\partial^2 v}{\partial z^2} \right), \quad (7.2)$$

$$u \frac{\partial T}{\partial r} + v \frac{\partial T}{\partial z} = \frac{k}{\rho c_p} \left(\frac{\partial^2 T}{\partial r^2} + \frac{1}{r} \frac{\partial T}{\partial r} \right) + \tau \left[D_B \frac{\partial C}{\partial r} \frac{\partial T}{\partial r} + \frac{D_T}{T_\infty} \left(\frac{\partial T}{\partial r} \right)^2 \right] - \dots \quad (7.3)$$

$$\frac{1}{\rho c_p} \frac{1}{r} \frac{\partial(r q_r)}{\partial r} + \frac{q'''}{\rho c_p},$$

$$u \frac{\partial C}{\partial r} + v \frac{\partial C}{\partial z} = D_B \left(\frac{\partial^2 C}{\partial r^2} + \frac{1}{r} \frac{\partial C}{\partial r} \right) + \frac{D_T}{T_\infty} \left(\frac{\partial^2 T}{\partial r^2} + \frac{1}{r} \frac{\partial T}{\partial r} \right), \quad (7.4)$$

with boundary conditions

$$\left. \begin{aligned} v(r, z) = V_w = c \left(\frac{z}{l} \right), \quad u(r, z) = 0, \\ T(r, z) = T_w, \quad C(r, z) = C_w \end{aligned} \right\} \text{ at } r = R^*,$$

$$\left. \begin{aligned} v(r, z) = 0, \quad u(r, z) = 0, \\ T(r, z) = T_\infty, \quad C(r, z) = C_\infty \end{aligned} \right\} \text{ as } r \rightarrow \infty. \quad (7.5)$$

The new symbols which are used in equations (7.2-7.5) are defined as

λ_1 : material relaxation time D_B : Brownian diffusion coefficient

D_T : Thermophoretic diffusion coefficient

$q''' = \frac{k V_w(z)}{z v} [A^*(T_w - T_\infty) f' + B^*(T - T_\infty)]$: non-uniform heat sink/source

A^* : coefficient of space dependent heat source/sink

B^* coefficient of temperature dependent heat source/sink

Upon using the radiative heat flux q_r and non-uniform heat sink/source q''' as defined above, Eq. (7.3) takes the following form

$$u \frac{\partial T}{\partial r} + v \frac{\partial T}{\partial z} = \frac{k}{\rho c_p} \left(1 + \frac{16 \sigma^* T^3}{3k(\alpha_r + \alpha_s)} \right) \left(\frac{\partial^2 T}{\partial r^2} + \frac{\partial T}{r \partial r} \right) +$$

$$\tau \left[D_B \frac{\partial C}{\partial r} \frac{\partial T}{\partial r} + \frac{D_T}{T_\infty} \left(\frac{\partial T}{\partial r} \right)^2 \right] + \frac{\frac{k V_w(z)}{z v} [A^*(T_w - T_\infty) f' + B^*(T - T_\infty)]}{\rho c_p}. \quad (7.6)$$

Introducing the following appropriate similarity transformations:

$$\eta = \frac{r^2 - R^{*2}}{2R^*} \sqrt{\frac{c}{v l}}, \quad u = -\frac{R^*}{r} \sqrt{\frac{c v}{l}} f(\eta), \quad v = \frac{c z}{l} f'(\eta),$$

$$\theta(\eta) = \frac{T - T_\infty}{T_w - T_\infty}, \quad \phi(\eta) = \frac{C - C_\infty}{C_w - C_\infty}. \quad (7.7)$$

Utilizing $T = T_\infty(1 + (\theta_w - 1)\theta)$ and $\theta_w = T_w/T_\infty$ (temperature ratio parameter) into Eqs. (7.2)–(7.4), we obtained the following differential equations

$$(1 + 2\gamma\eta) f'''' + 2\gamma f'' + f f'' - (f')^2 - \frac{\gamma De}{(1 + 2\gamma\eta)} f^2 f''$$

$$+ De(2f f' f'' - f^2 f''') = 0, \quad (7.8)$$

$$(1 + 2\gamma\eta) \frac{\partial}{\partial \eta} \left\{ \left(1 + \frac{4}{3} Rd(1 + (\theta_w - 1)\theta)^3 \right) \theta' \right\} \quad (7.9)$$

$$+ \left\{ 2\gamma \left(1 + \frac{4}{3} Rd(1 + (\theta_w - 1)\theta)^3 \right) + Prf \right\} \theta' \\ + (1 + 2\gamma\eta)(N_b \phi' \theta' + N_t \theta'^2) + A^* f' + B^* \theta = 0, \\ (1 + 2\gamma\eta) \phi'' + 2\gamma \phi' + Scf \phi' + \frac{N_t}{N_b} ((1 + 2\gamma\eta) \theta'' + 2\gamma \theta') = 0. \quad (7.10)$$

The boundary conditions (7.5) in dimensionless form are

$$f(0) = 0, f'(0) = 1, f'(\infty) = 0, \\ \theta(0) = 1, \theta(\infty) = 0, \phi(0) = 1, \phi(\infty) = 0. \quad (7.11)$$

Dimensionless symbols used in equations (7.8)–(7.10) are defined as

$\gamma = \sqrt{\nu l / c R^{*2}}$: curvature parameter	$De = \lambda_1 c / l$: Maxwell fluid parameter
$\theta_w = T_w / T_\infty$: surface heating parameter	$Rd = 4\sigma^* T_\infty^3 / k(\alpha_r + \sigma_s)$: radiation parameter
$Pr = \nu / \alpha$: Prandtl number	$N_t = D_T \tau (T_w - T_\infty) / T_\infty \alpha$: Thermophoresis parameter
$N_b = D_B \tau (C_w - C_\infty) / \alpha$: Brownian motion parameter	θ : dimensionless temperature
ϕ : dimensionless concentration	$Sc = \nu / D_B$: Schmidt number

After utilizing the expression of Nu from Eq. (2.15) and expression of Sh from Eq. (6.17) with similarity transformation of present chapter the transformed values of Nu and Sh will be of the form

$$Re_z^{-\frac{1}{2}} Nu_z = - \left(1 + \frac{4Rd}{3} \theta_w^3 \right) \theta'(0), \quad Re_z^{-\frac{1}{2}} Sh = -\phi'(0). \quad (7.12)$$

7.2 Numerical Scheme

Since the system of equations with boundary conditions (7.8)–(7.11) is non-linear, so the presentation of solution in exact form is impossible. Keeping this in view, we obtained the numerical solution of it by using shooting method with Runge-Kutta fourth order integrator. For this purpose, we first need to convert the obtained system of boundary value problem (7.8-7.11) into first order initial value problem such as

$$f' = p, \\ p' = q,$$

$$[(1 + 2\gamma\eta) - Def^2]q' + \left[2\gamma + f - \frac{De\gamma f^2}{(1 + 2\gamma\eta)}\right]q - p^2 + 2Defpq = 0,$$

$$\theta' = U, \phi' = R,$$

$$(1 + 2\gamma\eta) \frac{\partial}{\partial \eta} \left\{ \left(1 + \frac{4}{3} Rd(1 + (\theta_w - 1)\theta)^3 \right) U \right\} + 2\gamma \left(1 + \frac{4}{3} Rd(1 + (\theta_w - 1)\theta)^3 \right) U \\ + PrfU + (N_b RU + N_t Q^2) + A^*p + B^*\theta = 0, \\ (1 + 2\gamma\eta)R' + 2\gamma R + ScfR + \frac{N_t}{N_b} ((1 + 2\gamma\eta)U' + 2\gamma\theta') = 0,$$

with initial conditions

$$f(0) = 0, p(0) = 1, q(0) = s_1,$$

$$\theta(0) = 1, U(0) = s_2,$$

$$\phi(0) = 1, R(0) = s_3.$$

where the constants s_1 , s_2 and s_3 are unknown commonly known as missing initial conditions. These missing conditions are chosen in such a way that the boundary conditions at infinity satisfy. So for the calculation of missing initial conditions Newton Raphson algorithm is utilized. The obtained results are firstly validated by the comparison with published results and then novel results for the considered problem are calculated.

7.3 Results and discussion

Numerical investigation of Maxwell nanofluid with non-linear radiation and non-uniform heat generation/absorption is performed. Obtained system of partial differential equations are transformed into dimensionless form by using suitable similarity transformation. The numerical scheme described previously is applied to get the results. To check the validity of these results, a comparison is given in Tables 7.1-7.3, which show a good agreement with the past studies. Further, the results for different emerging parameters such as Maxwell fluid parameter De , radius of curvature γ , radiation parameter Rd , thermophoresis parameter N_t , Brownian motion parameter N_b , space dependent heat source/sink A^* , temperature dependent heat source/sink B^* , Prandtl number Pr and Schmidt number Sc are presented in Figures 7.1-7.12. Figure 7.1 demonstrate the effects of Maxwell fluid parameter De on dimensionless velocity profile by taking $\gamma = 0$ (Stretching sheet) and $\gamma = 0.5$ (Stretching cylinder). It is clearly seen that with the increase in De the velocity and momentum boundary layer decrease for both stretching sheet and stretching cylinder. It is found that the

Table 7.1: Values of $-f''(0)$ for various values of Maxwell fluid parameter De .

$\gamma \rightarrow$	0.0		0.2	0.5
$De \downarrow$	Abel et al. (2012)	Present \rightarrow		
0.0	0.999962	1.000008	1.073104	1.180682
0.2	1.051948	1.051886	1.121344	1.226009
0.4	1.101850	1.101892	1.168136	1.270075
0.6	1.150163	1.150126	1.213519	1.312934
0.8	1.196692	1.196702	1.257568	1.354648
1.2	1.285257	1.285349	1.341984	1.434921
1.6	1.368641	1.368744	1.421978	1.511338
2.0	1.447617	1.447637	1.498083	1.584367

Table 7.2: Comparison of $-\theta'(0)$ for the various values of N_t and N_b when $\beta = \gamma = Rd = A^* = B^* = 0, Pr = 10$ and $Sc = 10$.

$N_b \rightarrow$	0.1	0.3		0.5		
$N_t \downarrow$	Present	Khan and Pop (2010)	Present	Khan and Pop (2010)	Present	Khan and Pop (2010)
0.1	0.9524	0.9524	0.2521	0.2522	0.0542	0.0543
0.3	0.5201	0.5201	0.1355	0.1355	0.0291	0.0291
0.5	0.3211	0.3211	0.0833	0.0833	0.0179	0.0179

Table 7.3: Comparison of $\phi'(0)$ for the various values of N_t and N_b when $\beta = \gamma = Rd = A^* = B^* = 0, Pr = 10$ and $Sc = 10$.

$N_b \rightarrow$	0.1	0.3		0.5		
$N_t \downarrow$	Present	Khan and Pop (2010)	Present	Khan and Pop (2010)	Present	Khan and Pop (2010)
0.1	2.1294	2.1294	2.4100	2.4100	2.3836	2.3836
0.3	2.5287	2.5286	2.6088	2.6088	2.4984	2.4984
0.5	3.0352	3.0351	2.7519	2.7519	2.5731	2.5731

boundary layer thickness increases with increase of γ . Linear and non-linear radiation effects on temperature and concentration profile over a stretching cylinder are presented in Figure 7.2. It is depicted that temperature enhances and concentration reduces with increase in θ_w . The graph clearly distinguishes between linear and nonlinear radiation effects. Nonlinear radiation greatly increases the temperature of the fluid but little effect can be seen on concentration profile. Figure 7.3 capture the effects of space dependent coefficient of heat generation/absorption on temperature and concentration profiles. It is seen that with

increase of A^* temperature profile increases throughout the boundary layer regime but the concentration profile decreases near the wall and adopted an opposite behavior away from the cylinder surface. Same effects of temperature dependent coefficient of heat generation/absorption B^* are observed in Figure 7.4. Figure 7.5 and 7.6 capture the Brownian motion and thermophoresis effects on temperature $\theta(\eta)$ and nanoparticle volume fraction $\phi(\eta)$. It can be seen that for weak Brownian motion ($N_b = 0.1$) temperature and concentration significantly increase due to increase in thermophoretic parameter. However due to hot surface a particle-free layer occurs near the wall because heated surface drive back the small size particles. However, for small thermophoresis effect with $N_t = 0.1$, due to change in weak to strong Brownian motion, a very small increase in temperature $\theta(\eta)$ and nanoparticle volume fraction $\phi(\eta)$ is observed. Figure 7.7 is developed to show the variation in wall shear stress against Maxwell fluid parameter at different orientations of geometry from sheet ($\gamma = 0$) to cylinder ($\gamma > 0$). It clearly describes that wall shear stress decreases for the curved surface ($\gamma > 0$) and same is happening with Maxwell fluid parameter. Due to increase in curvature parameter the cylinder surface reduces, consequently drag on the surface will reduce. The variation in Nu and Sh against Deborah number De is plotted for $\gamma = 0, 0.5, 1$ and is shown in Figure 7.8. With increase in curvature parameter γ , the values of Nu and Sh both increase while these quantities reduce for increase in De . Linear and nonlinear radiation effects on heat transfer rate are presented in Figure 7.9 for different values of N_t and N_b . This figure depicts that heat transfer rate due to nonlinear radiation is more prominent than that of linear radiation. Moreover, the increase in radiation parameter also enhances the rate of heat transfer. This figure depicts that the radiation effects enhances the heat transfer rate and this enhancement in case of nonlinear radiation is higher than that of linear radiation. It can also be seen that by increasing the thermophoresis and Brownian motion effects of the nanoparticles the cylinder surface rapidly gets cool as compare to Maxwell fluid alone. To show the flow pattern at the surface of sheet and cylinder, the streamlines are displayed in Figures 7.10 and 7.11 for both $\gamma = 0$ and $\gamma = 10$.

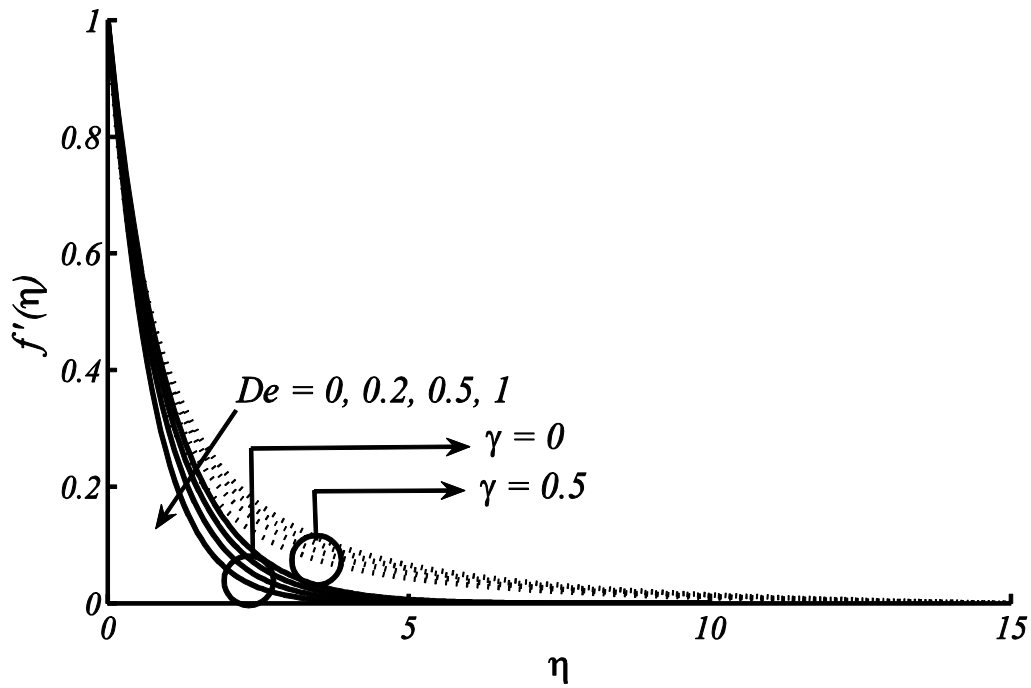


Figure 7.1: Impact of De on velocity distribution.

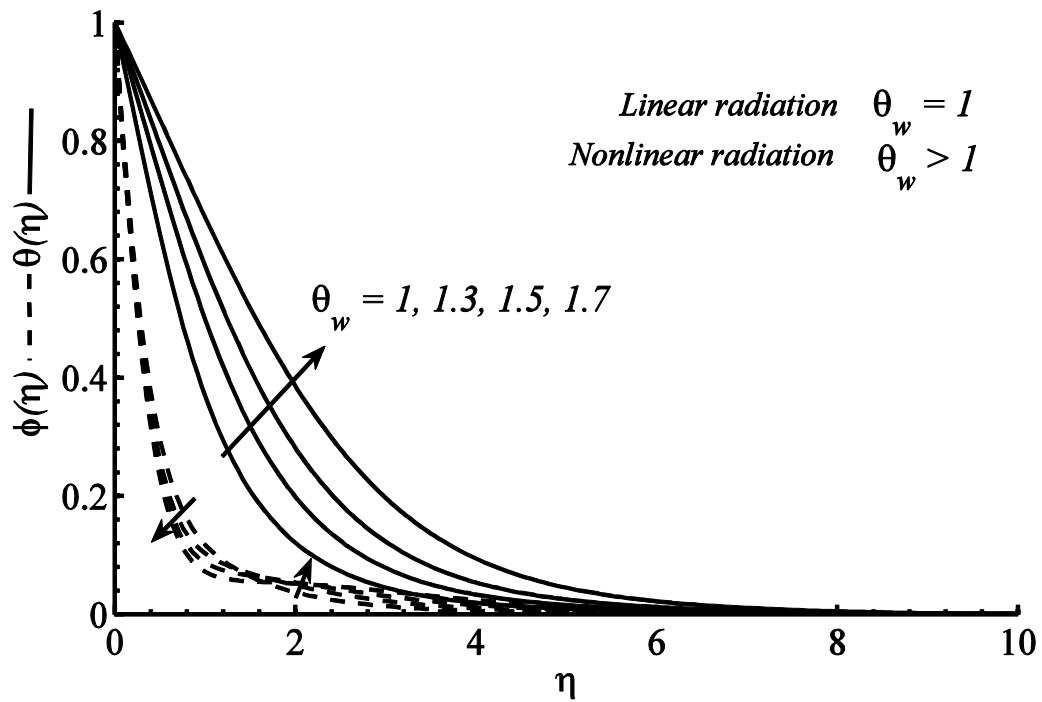


Figure 7.2: Influence of θ_w on $\theta(\eta)$ and $\phi(\eta)$ when $De = 1, \gamma = 0.2, A^* = 0.4, B^* = 0.4, Pr = 6.8, Sc = 1.5, N_t = N_b = 0.1, Rd = 2$.

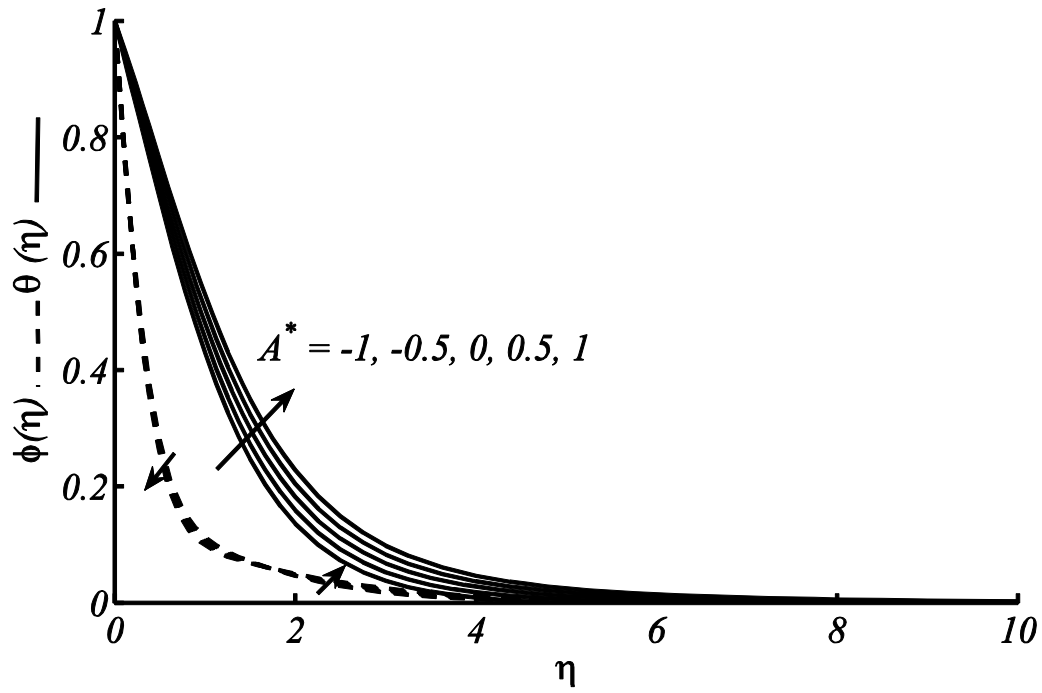


Figure 7.3: Effects of A^* on $\theta(\eta)$ and $\phi(\eta)$ while $De = 1, \gamma = 0.2, Rd = 2, \theta_w = 1.3, B^* = 0.4, Pr = 10, Sc = 10, N_t = 0.1, N_b = 0.1$.

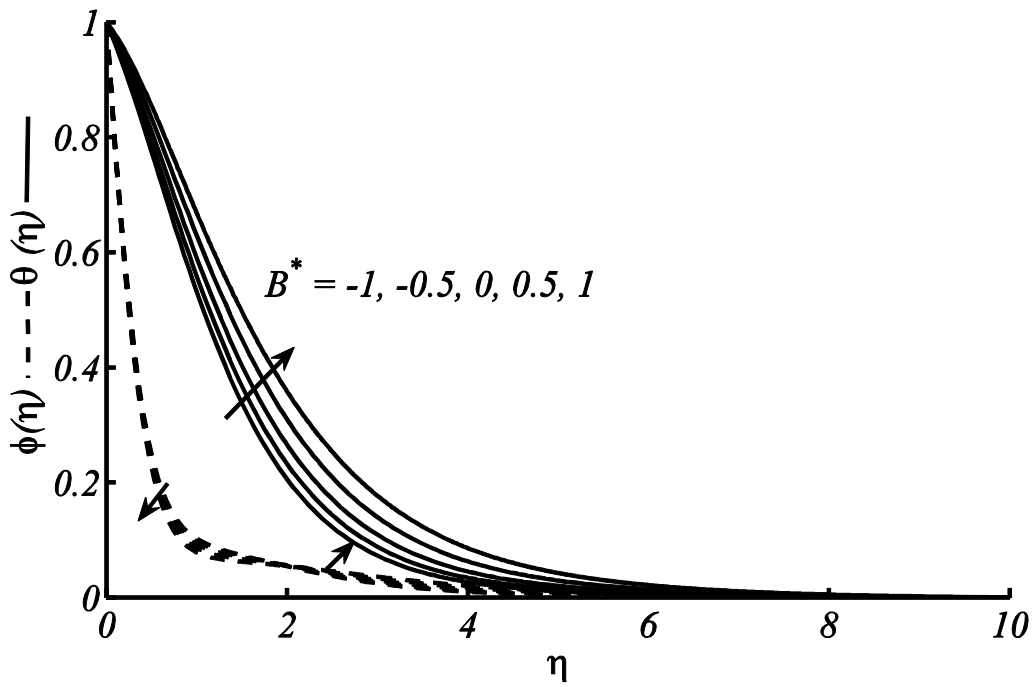


Figure 7.4: Effects of B^* on temperature and concentration profile while $De = 1, \gamma = 0.2, Rd = 2, \theta_w = 1.3, A^* = 0.4, Pr = 10, Sc = 10, N_t = 0.1, N_b = 0.1$.

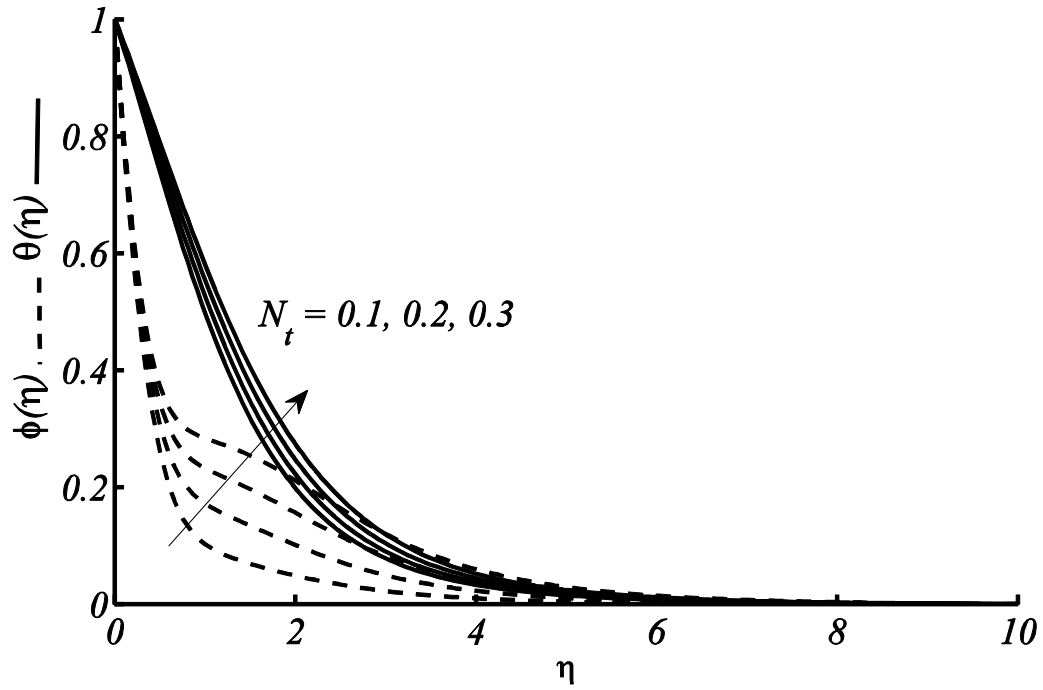


Figure 7.5: Effect of N_t on temperature and concentration profile while $De = 1, \gamma = 0.2, Rd = 2, \theta_w = 1.3, A^* = 0.4, B^* = 0.4, Pr = 10, Sc = 10, N_b = 0.1$.

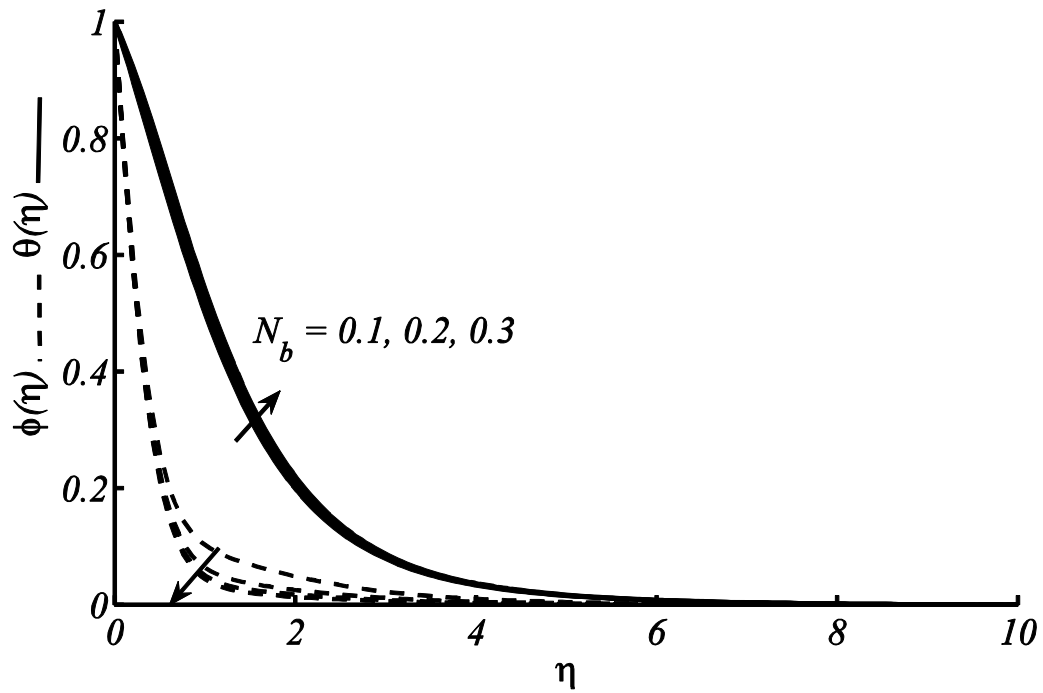


Figure 7.6: Effect of N_b on temperature and concentration profile $De = 1, \gamma = 0.2, Rd = 2, \theta_w = 1.3, A^* = 0.4, B^* = 0.4, Pr = 10, Sc = 10, N_t = 0.1$.

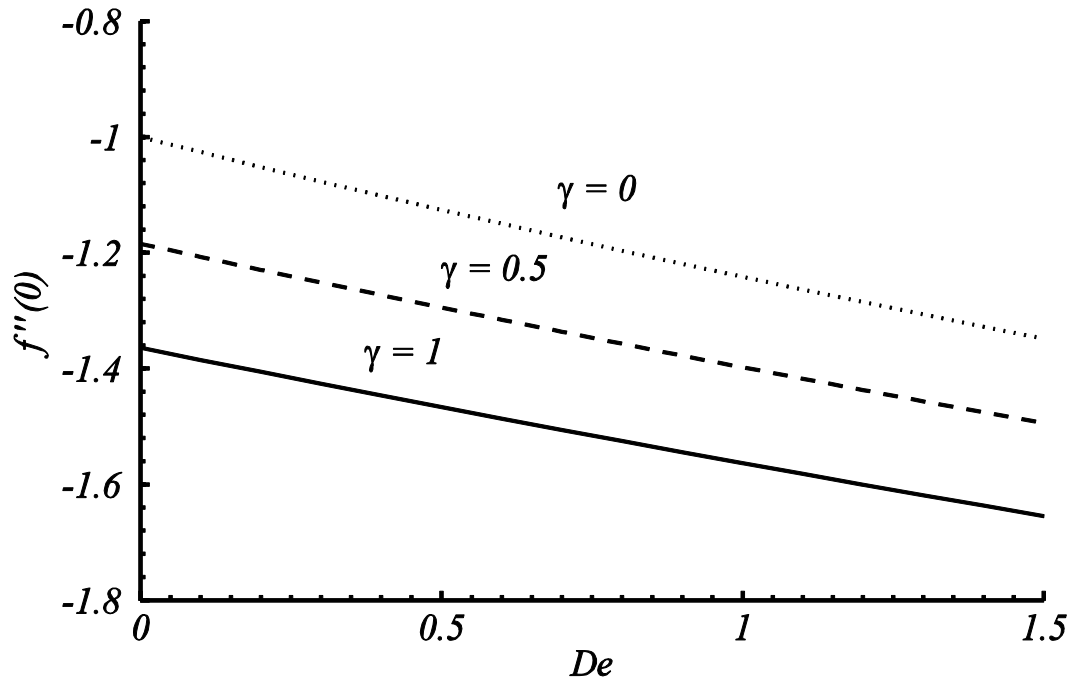


Figure 7.7: Variation in $f''(0)$ against De for different γ at $Rd = 2, \theta_w = 1.3, A^* = 1, B^* = 1, Pr = 10, Sc = 1.5, N_t = N_b = 0.1$.

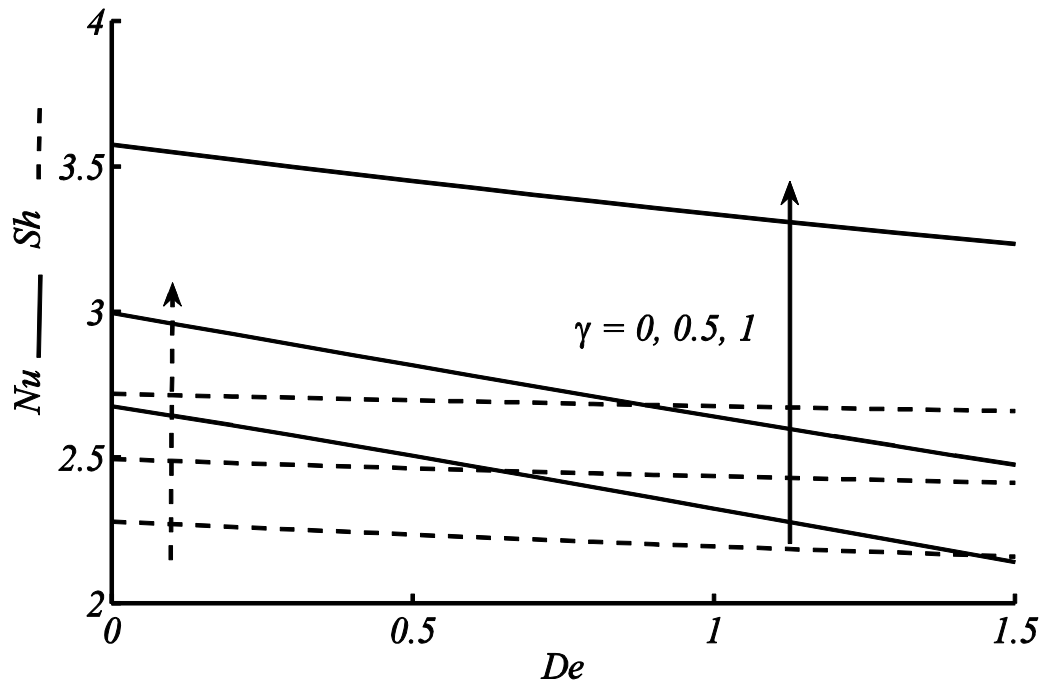


Figure 7.8: Variation in Nu and Sh against β for $Rd = 2, \theta_w = 1.3, A^* = 1, B^* = 1, Pr = 10, Sc = 1.5, N_t = N_b = 0.1$.

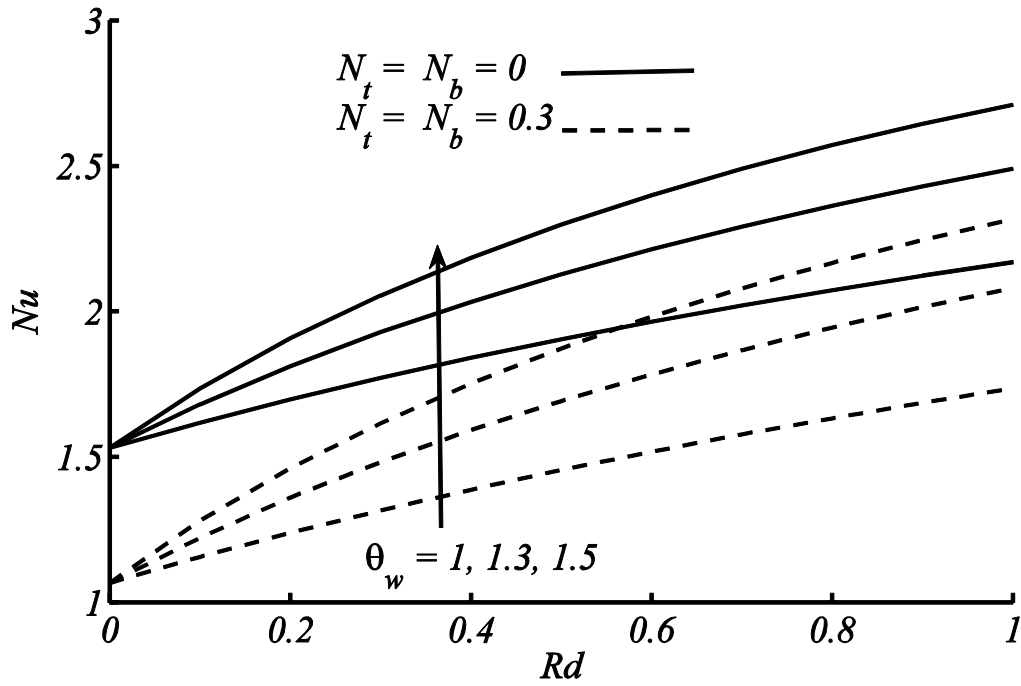


Figure 7.9: Variation in Nu against Rd for different θ_w at $De = 1, \gamma = 0.2, A^* = B^* = 0.4, Pr = 6.8, Sc = 1.5$.

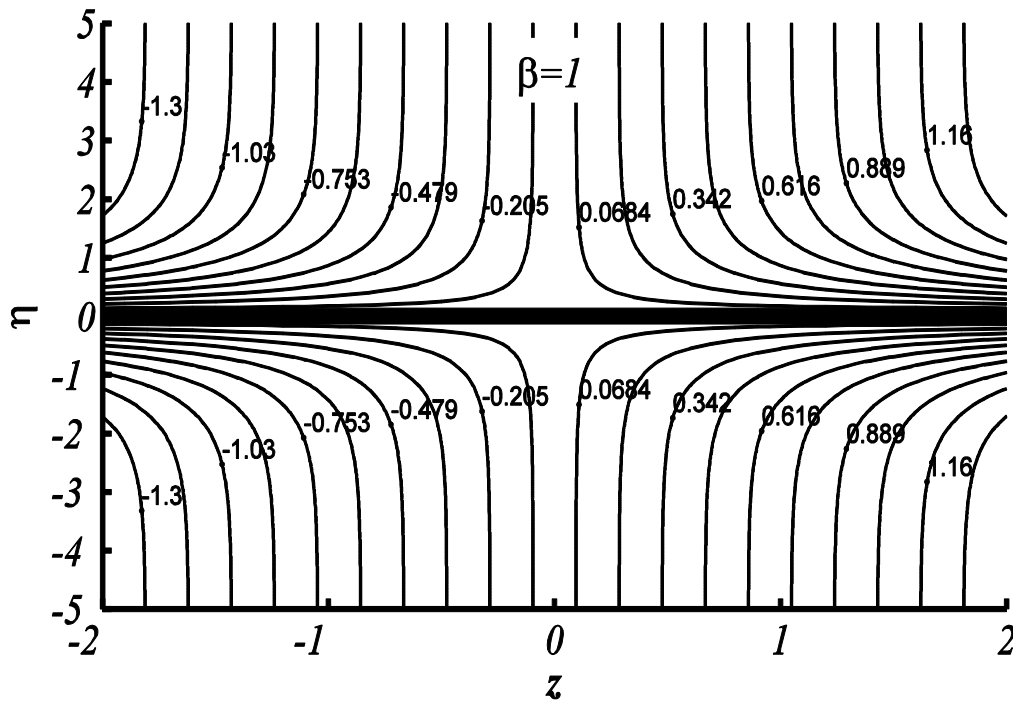


Figure 7.10: Streamlines for $\gamma = 0$ at $De = 1$.

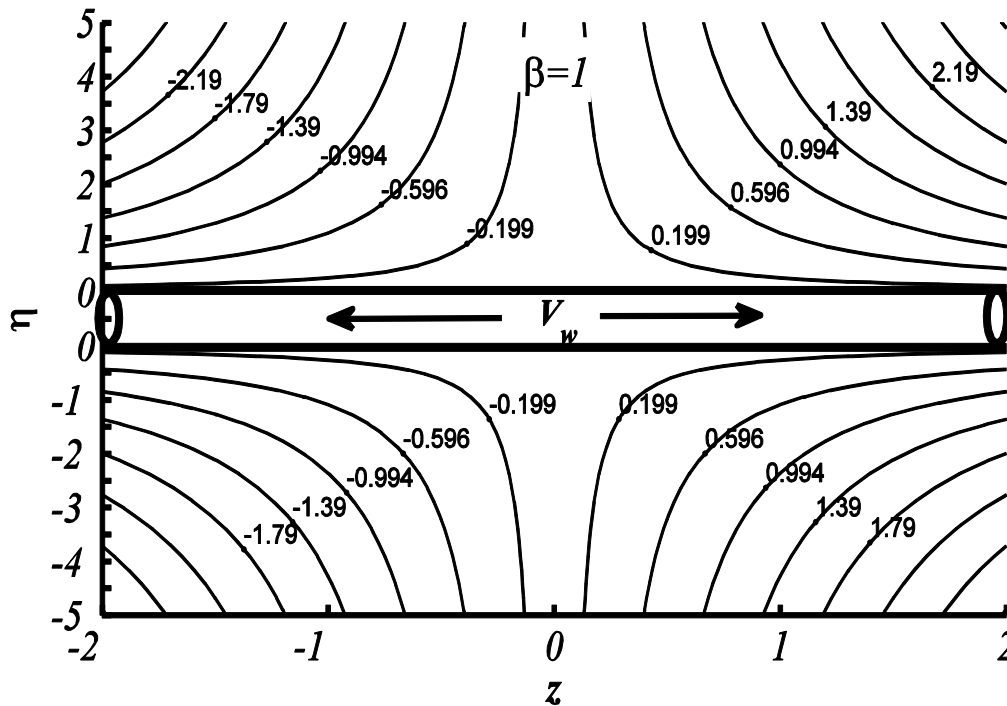


Figure 7.11: Streamlines for $\gamma = 10$ at $De = 1$.

7.4 Conclusion

The non-linear radiation effects on Maxwell nanofluid flow along a stretching cylinder in presence of non-uniform heat generation/absorption is performed. The governed partial differential equations transformed into dimensionless ordinary differential equations, which are then simulated with the help of shooting method. For the validity of applied scheme, the results are first compared with the benchmark studies and then innovative results for the Maxwell nanofluid flowing over stretching cylinder are presented through table and graphs for emerging dimensionless parameters. It is observed the velocity profile shows a decreasing trend with increasing values of Maxwell fluid parameter (De) for both stretching sheet ($\gamma = 0$) and stretching cylinder ($\gamma > 0$) case. Heat transfer rate is decreasing with the increasing strength of Brownian motion and thermophoresis effects. It is important to mention that nonlinear radiation has significantly enhances the radiation as compare to linear radiation.

References:

- Abbas, Z., Majeed, A., and Javed, T. (2013). Thermal Radiation effects on MHD flow over a stretching cylinder. *Heat Transfer Research*, 44, 703–718.
- Abel, M.S., Tawade, J.V., & Nandeppanavar, M. M. (2012). MHD flow and heat transfer for the upper-convected Maxwell fluid over a stretching sheet. *Meccanica*, 47(2), 385–393.
- Abolbashari, M.H., Freidoonimehr, N., Nazari, F., and Rashidi, M. M. (2014). Entropy analysis for an unsteady MHD flow past a stretching permeable surface in nano-fluid. *Powder Technology*, 267, 256–267.
- Ali, M.E. (1994). Heat transfer characteristics of a continuous stretching surface. *Heat and Mass Transfer*, 29, 227–234.
- Ali, N., Khan, S.U., Abbas, Z. and Sajid, M. (2016). Soret and Dufour effects on hydromagnetic flow of viscoelastic fluid over porous oscillatory stretching sheet with thermal radiation. *Journal of Brazilian Society of Mechanical Sciences and Engineering*, DOI 10.1007/s40430-016-0506-x.
- Andersson, H.I., Bech, K.H., and Dandapat, B.S. (1992). Magnetohydrodynamic flow of a power-law fluid over a stretching sheet. *International Journal of Non-Linear Mechanics*, 27(6), 929–936.
- Ariel, P. D. (1994). Stagnation point flow with suction: an approximate solution. *Journal of Applied Mechanics*, 61(4), 976–978.
- Ariel, P.D. (1992). A hybrid method for computing the flow of viscoelastic fluids. *International Journal for Numerical Methods in Fluids*, 14(7), 757–774.
- Bachok, N., and Ishak, A. (2010). Flow and heat transfer over a stretching cylinder with prescribed surface heat flux. *Malaysian Journal of Mathematical Sciences*, 4(2), 159–169.
- Beard, D.W., and Walters, K. (1964). Elastico-viscous boundary-layer flows I. Two-dimensional flow near a stagnation point. *Mathematical Proceedings of the Cambridge Philosophical Society*, 60(3), 667–674.
- Bellman, R.E., and Kalaba, R. (1965). Quasilinearization and Boundary Value Problems. *American Elsevier Publication Company*, New York.
- Benano-Melly, L.B., Caltagirone, J.P., Faissat, B., Montel, F., and Costeseque, P. (2001). Modeling Soret coefficient measurement experiments in porous media considering

- thermal and solutal convection. *International journal of heat and mass transfer*, 44, 1285–1297.
- Buongiorno, J. (2006). Convective transport in nanofluids. *Journal of Heat Transfer*, 128(3), 240–250.
- Burde, G.I. (1995). Nonsteady Stagnation-Point Flows over Permeable Surfaces: Explicit Solutions of the Navier-Stokes Equations. *Journal of fluids engineering*, 117(1), 189–191.
- Canuto, C., Hussaini, M.Y., Quarteroni, A.M., and Zang T.A. (1987). *Spectral methods in fluid dynamics*. Springer, Berlin.
- Cebeci, T., and Bradshaw, P. (1984). *Physical and computational aspects of convective heat transfer*. Springer, New York.
- Chakrabarti, A., and Gupta, A.S. (1979). Hydromagnetic flow and heat transfer over a stretching sheet. *Quarterly of Applied Mathematics*, 37(1), 73–78.
- Chen C.K., and Char, M.I. (1988). Heat transfer of a continuous, stretching surface with suction or blowing. *Journal of Mathematical Analysis and Applications*, 135(2), 568–580.
- Chiam, T.C. (1994). Stagnation point flow towards a stretching plate. *Journal of the physical society of Japan*, 63(6), 2443–2444.
- Choi, S.U.S. (1995). Enhancing thermal conductivity of fluids with nanoparticles. *ASME-Publications-Fed*, 231, 99–106.
- Crane, L.J. (1970). Flow past a stretching plate. *Zeitschrift für angewandte Mathematik und Physik*, 21, 645–647.
- Dalir, N., Dehsara, M., and Nourazar, S.S. (2015). Entropy analysis for magnetohydrodynamic flow and heat transfer of a Jeffrey nanofluid over a stretching sheet. *Energy*, 79, 351–362.
- Dhanai, R., Rana, P., and Kumar, L. (2016). MHD mixed convection nanofluid flow and heat transfer over an inclined cylinder due to velocity and thermal slip effects: Buongiorno's model. *Powder Technology*, 288, 140–150.
- Dursunkaya, Z., and Worek, W.M. (1992) Diffusion-thermo and thermal-diffusion effects in transient and steady natural convection from vertical surface, *International Journal of Heat and Mass Transfer*, 35, 2060–2067.
- Dutta, B.K., Roy, P., and Gupta, A.S. (1985). Temperature field in flow over a stretching sheet with uniform heat flux. *International Communications in Heat and Mass Transfer*, 12, 89–94.

- Eckert E.R.G. (1942). Die Berechnung des Wärmeüberganges in der laminaren Grenzschicht um stromter Körper, *VDI Forschungsheft*, 416, 1–24.
- Eckert, E.R.G., and Drake, D.M. (1972), Analysis of Heat and Mass Transfer, *McGraw Hill*, New York.
- Eijkel, J. (2007). Liquid slip in micro-and nanofluidics: recent research and its possible implications. *Lab on a Chip*, 7(3), 299–301.
- Elbashbeshy, E.M., Emam, T.G., El-Azab, M.S., and Abdelgaber, K.M. (2012). Effect of magnetic field on flow and heat transfer over a stretching horizontal cylinder in the presence of a heat source/sink with suction/injection. *Journal of Applied Mechanical Engineering*, 1000106.
- Garoosi, F., Rohani, B., and Rashidi, M.M. (2015). Two-phase mixture modeling of mixed convection of nanofluids in a square cavity with internal and external heating. *Powder Technology*, 275, 304–321.
- Ghaffari, A., Javed, T., and Labropulu, F. (2015). Oblique stagnation point flow of a non-Newtonian nanofluid over stretching surface with radiation: a numerical study. *Therm. Science*, DOI: 10.2298/TSCI150411163G.
- Gupta, P.S., and Gupta, A.S. (1977). Heat and mass transfer on a stretching sheet with suction or blowing. *Canadian Journal of Chemical Engineering*, 55, 744–746.
- Harris, J. (1977). *Rheology and non-Newtonian flow*, Longman London.
- Hayat, T., Abbasi, F.M., Al-Yami, M. and Monaqueel, S. (2014), Slip and Joule heating effects in mixed convection peristaltic transport of nanofluid with Soret and Dufour effects, *Journal of Molecular Liquids*, 194, 93–99.
- Hayat, T., and Qasim, M. (2010). Influence of thermal radiation and Joule heating on MHD flow of a Maxwell fluid in the presence of thermophoresis. *International Journal of Heat and Mass Transfer*, 53(21), 4780–4788.
- Hayat, T., Anwar, M.S., Farooq, M., and Alsaedi, A. (2015). Mixed convection flow of viscoelastic fluid by a stretching cylinder with heat transfer. *Plos one*, 10(3), e0118815.
- Hayat, T., Asad, S., and Alsaedi, A. (2014). Flow of variable thermal conductivity fluid due to inclined stretching cylinder with viscous dissipation and thermal radiation. *Applied Mathematics and Mechanics*, 35(6), 717–728.

- Hayat, T., Farooq, M., and Alsaedi, A. (2015). Thermally stratified stagnation point flow of Casson fluid with slip conditions. *International Journal of Numerical Methods for Heat and Fluid Flow*, 25(4), 724–748.
- Hayat, T., Fetecau, C., and Sajid, M. (2008). On MHD transient flow of a Maxwell fluid in a porous medium and rotating frame. *Physics letters A*, 372(10) 1639–1644.
- Hayat, T., Gull, N., Farooq, M., and Ahmad, B. (2015). Thermal Radiation Effect in MHD Flow of Powell-Eyring Nanofluid Induced by a Stretching Cylinder. *Journal of Aerospace Engineering*, 29(1), 04015011.
- Hayat, T., Qayyum, A., and Alsaedi, A. (2014). Effects of heat and mass transfer in flow along a vertical stretching cylinder with slip conditions. *The European Physical Journal Plus*, 129(4), 1–16.
- Hayat, T., Qayyum, S., Farooq, M., Alsaedi, A., and Ayub, M. (2015). Mixed convection flow of Jeffrey fluid along an inclined stretching cylinder with double stratification effect. *Thermal Science*, 52–52.
- Hayat, T., Shehzad, S.A., and Alsaedi, A. (2012). Study on three-dimensional flow of Maxwell fluid over a stretching surface with convective boundary conditions. *International Journal of Physical Sciences*, 7(5), 761–768.
- Hiemenz, K. (1911). Die Grenzschicht an einem in den gleichförmigen Flüssigkeitsstrom eingetauchten geraden Kreiszylinder. *Dinglers Polytechn Journal*, 326, 321–324.
- Homann, F. (1936). Der Einfluss grosser Zähigkeit bei der Strömung um den Zylinder und um die Kugel. *ZAMM-Journal of Applied Mathematics and Mechanics/Zeitschrift für Angewandte Mathematik und Mechanik*, 16(3), 153–164.
- Hossain, M.A. and Takhar, H.S. (1996), Radiation effects on mixed convection along a vertical plate with uniform surface temperature, *Heat and Mass Transfer*, 31, 243–248.
- Hossain, M.A., Alim, M.A., and Rees, D. (1999), The effect of radiation on free convection from a porous vertical plate. *International Journal of Heat and Mass Transfer*, 42, 181–191.
- Hussain, T., Shehzad, S.A., Alsaedi, A., Hayat, T., and Ramzan, M. (2015). Flow of Casson nanofluid with viscous dissipation and convective conditions: A mathematical model. *Journal of Central South University*, 22(3), 1132–1140.
- Ishak, A., and Nazar, R. (2009). Laminar boundary layer flow along a stretching cylinder. *European Journal of Scientific Research*, 36(1), 22–29.

- Ishak, A., Nazar, R., and Pop, I. (2008). Magnetohydrodynamic (MHD) flow and heat transfer due to a stretching cylinder. *Energy Conversion and Management*, 49(11), 3265–3269.
- Ishak, A., Nazar, R., and Pop, I. (2008). Uniform suction/blowing effect on flow and heat transfer due to a stretching cylinder. *Applied Mathematical Modelling*, 32(10), 2059–2066.
- Ishak, A., Nazar, R., and Pop, I. (2009). Boundary layer flow and heat transfer over an unsteady stretching vertical surface. *Meccanica*, 44(4), 369–375.
- Javed, T., and Ghaffari, A. (2016). Numerical Study of Non-Newtonian Maxwell Fluid in the Region of Oblique Stagnation Point Flow over a Stretching Sheet. *Journal of Mechanics*, 32(02), 175–184.
- Javed, T., Ghaffari, A., and Ahmad, H. (2015). Numerical study of unsteady MHD oblique stagnation point flow with heat transfer over an oscillating flat plate. *Canadian Journal of Physics*, 93(10), 1138–1143.
- Javed, T., Majeed, A., and Mustafa, I. (2015). MHD effects on natural convection laminar flow from a horizontal circular cylinder in presence of radiation. *Revista Mexicana de Fisica*, 61, 450–457.
- Joneidi, A.A., Domairry, G., Babaelahi, M., and Mozaffari, M. (2010). Analytical treatment on magnetohydrodynamic (MHD) flow and heat transfer due to a stretching hollow cylinder. *International journal for numerical methods in fluids*, 63(5), 548–563.
- Kafoussias, N.G., and Williams, E.W. (1995). Thermal-diffusion and diffusion-thermo effects on mixed free-forced convective and mass transfer boundary layer flow with temperature dependent viscosity, *International Journal of Engineering science*, 33, 1369–1384.
- Khan, W.A., and Pop, I. (2010). Boundary-layer flow of a nanofluid past a stretching sheet. *International Journal of Heat and Mass Transfer*, 53(11), 2477–2483.
- Kuznetsov, A.V., and Nield, D.A. (2010). Natural convective boundary-layer flow of a nanofluid past a vertical plate. *International Journal of Thermal Sciences*, 49(2), 243–247.
- Kuznetsov, A.V., and Nield, D.A. (2011). Double-diffusive natural convective boundary-layer flow of a nanofluid past a vertical plate. *International Journal of Thermal Sciences*, 50(5), 712–717.

- Magyari E., and Pantokratoras, A. (2011). Note on the effect of thermal radiation in the linearized Rosseland approximation on the heat transfer characteristics of various boundary layer flows. *International Communications in Heat and Mass Transfer*, 38, 554–556.
- Mahapatra, T.R., and Gupta, A.S. (2001). Magnetohydrodynamic stagnation-point flow towards a stretching sheet. *Acta Mechanica*, 152(1–4), 191–196.
- Mahapatra, T.R., and Gupta, A.S. (2002). Heat transfer in stagnation-point flow towards a stretching sheet. *Heat and mass transfer*, 38(6), 517–521.
- Mahdy, A. (2015). Heat fluid transfer and flow of a Casson fluid due to a stretching cylinder with Soret and Dufour effects, *Journal of Engineering Physics and Thermophysics*, 88, 897–904.
- Mahdy, A., and Ahmed, S.E. (2015). Thermosolutal Marangoni boundary layer Magnetohydrodynamics flow with the Soret and Dufour effects past a vertical flat plate, *Engineering Science and Technology, an International Journal*, 18 24–31
- Mahmoud, M.A.A. (2007). Thermal radiation effects on MHD flow of a micropolar fluid over a stretching surface with variable thermal conductivity. *Physica A: Statistical Mechanics and its Applications*, 375, 401–410.
- Majeed, A., Javed, T., Ghaffari, A., and Rashidi, M.M. (2015). Analysis of heat transfer due to stretching cylinder with partial slip and prescribed heat flux: A Chebyshev Spectral Newton Iterative scheme, *Alexandria Engineering Journal*, 54, 1029–1036
- Masuda, H., Ebata, A., and Teramae, K. (1993). Alteration of thermal conductivity and viscosity of liquid by dispersing ultra-fine particles. Dispersion of Al_2O_3 , SiO_2 and TiO_2 ultra-fine particles, *Netsu Bussei*, 7(4), 227–233.
- Matin, M.H., Nobari, M.R.H., and Jahangiri, P. (2012). Entropy analysis in mixed convection MHD flow of nanofluid over a non-linear stretching sheet. *Journal of Thermal Science and Technology*, 7(1), 104–119.
- Merkin, J.H., and Pop, I. (2000). Free convection near a stagnation point in a porous medium resulting from an oscillatory wall temperature. *International journal of heat and mass transfer*, 43(4), 611–621.
- Motsa, S.S., and Sibanda, P. (2012). On the solution of MHD flow over a nonlinear stretching sheet by an efficient semi-analytical technique. *International Journal for Numerical Methods in Fluids*, 68(12), 1524–1537.
- Motsa, S.S., Dlamini, P.G., and Khumalo, M. (2014). Spectral relaxation method and spectral quasilinearization method for solving unsteady boundary layer flow

- problems. *Advances in Mathematical Physics*, Article ID 341964.
- Mukhopadhyay, S. (2011). Chemically reactive solute transfer in a boundary layer slip flow along a stretching cylinder. *Frontiers of Chemical Science and Engineering*, 5(3), 385–391.
- Mukhopadhyay, S. (2012). Heat transfer analysis of the unsteady flow of a Maxwell fluid over a stretching surface in the presence of a heat source/sink. *Chinese Physics Letters*, 29(5), 054703.
- Mukhopadhyay, S. (2012). Mixed convection boundary layer flow along a stretching cylinder in porous medium. *Journal of Petroleum Science and Engineering*, 96, 73–78.
- Mukhopadhyay, S. (2013). MHD boundary layer slip flow along a stretching cylinder. *Ain Shams Engineering Journal*, 4(2), 317–324.
- Mukhopadhyay, S., and Gorla, R.S.R. (2013). Slip effects on boundary layer flow and heat transfer along a stretching cylinder. *International Journal of Applied Mechanics and Engineering*, 18(2), 447–459.
- Munawar, S., Ali, A., and Mehmood, A. (2012). Thermal analysis of the flow over an oscillatory stretching cylinder. *Physica Scripta*, 86(6), 065401.
- Mustafa, I., Javed, T., and Ghaffari, A. (2016). Heat transfer in MHD stagnation point flow of a ferrofluid over a stretchable rotating disk. *Journal of Molecular Liquids*, 219, 526–532.
- Mustafa, M., Hayat, T., Pop, I., Asghar, S., and Obaidat, S. (2011). Stagnation-point flow of a nanofluid towards a stretching sheet. *International Journal of Heat and Mass Transfer*, 54(25), 5588–5594.
- Na, T.Y. (1979). *Computational methods in engineering boundary value problems*, Academic Press, New York.
- Nandeppanavar, M.M., Abel, M.S., and Tawade, J. (2010). Heat transfer in a Walter's liquid B fluid over an impermeable stretching sheet with non-uniform heat source/sink and elastic deformation. *Communications in Nonlinear Science and Numerical Simulation*, 15(7), 1791–1802.
- Nazar, R., Amin, N., Filip, D., and Pop, I. (2004). Unsteady boundary layer flow in the region of the stagnation point on a stretching sheet. *International Journal of Engineering Science*, 42(11), 1241–1253.
- Noghrehabadi, A., Saffarian, M.R., Pourrajab, R., and Ghalambaz, M. (2013). Entropy analysis for nanofluid flow over a stretching sheet in the presence of heat

- generation/absorption and partial slip. *Journal of Mechanical Science and Technology*, 27(3), 927–937.
- Pillai, K.M.C., Sai, K.S., Swamy, N.S., Nataraja, H.R., Tiwari, S.B., and Rao, B.N. (2004). Heat transfer in a viscoelastic boundary layer flow through a porous medium. *Computational Mechanics*, 34(1), 27–37.
- Postelnicu, A. (2007), Influence of chemical reaction on heat and mass transfer by natural convection from vertical surfaces in porous media considering Soret and Dufour effects. *Heat and Mass Transfer*, 43 595–602.
- Postelnicu, A. (2010), Heat and Mass transfer by natural convection at a stagnation point in a porous medium considering Soret and Dufour effects. *Heat and Mass Transfer*, 46 831–840.
- Prasad, K.V., Sujatha, A., Vajravelu, K., and Pop, I. (2012). MHD flow and heat transfer of a UCM fluid over a stretching surface with variable thermophysical properties. *Meccanica*, 47(6), 1425–1439.
- Ramzan, M., Farooq, M., Hayat, T., Alsaedi, A., and Cao, J. (2015). MHD stagnation point flow by a permeable stretching cylinder with Soret-Dufour effects. *Journal of Central South University*, 22, 707–716.
- Raptis, A., Perdikis, C., and Takhar, H.S. (2004), Effect of thermal radiation on MHD flow, *Applied Mathematics and Computation*, 153, 645–649.
- Rashidi, M.M., Hosseini, A., Pop, I., Kumar, S., and Freidoonimehr, N. (2014). Comparative numerical study of single and two-phase models of nanofluid heat transfer in wavy channel. *Applied Mathematics and Mechanics*, 35(7), 831–848.
- Rashidi, M.M., Mohammadi, F., Abbasbandy, S., and Alhuthali, M.S. (2015). Entropy Generation Analysis for Stagnation Point Flow in a Porous Medium over a Permeable Stretching Surface. *Journal of Applied Fluid Mechanics*, 8(4), 753–763.
- Reddy, S. and Chamkha, A.J. (2016), Soret and Dufour effects on MHD convective flow of Al_2O_3 -water and TiO_2 -water nanofluids past a stretching sheet in porous media with heat generation/absorption, *Advanced Powder Technology*, doi: 10.1016/j.appt.2016.04.005.
- Rees, D.A.S., and Pop, I. (1995). Boundary layer flow and heat transfer on a continuous moving wavy surface, *Acta Mechanica*, 112, 149–158.
- Rosseland, S. (1931). Astrophysik und atom-theoretische Grundlagen. *Springer-Verlag*.
- Schlichting, H. and Gersten, K. (2003). *Boundary-layer theory*. Eight Edition, Springer-Verlag, Berlin.

- Sharipov, F., and Seleznev, V. (1998). Data on internal rarefied gas flows. *Journal of Physical and Chemical Reference Data*, 27(3), 657–706.
- Sharma, P.R., and Singh, G. (2009). Effects of variable thermal conductivity and heat source/sink on MHD flow near a stagnation point on a linearly stretching sheet. *Journal of Applied fluid mechanics*, 2(1), 13–21.
- Sheikholeslami, M. (2015). Effect of uniform suction on nanofluid flow and heat transfer over a cylinder. *Journal of the Brazilian Society of Mechanical Sciences and Engineering*, 37(6), 1623–1633.
- Siddiqua, S., Hossain, M.A., and Saha, S.C. (2013). Natural convection flow with surface radiation along a vertical wavy surface. *Numerical Heat Transfer, Part A: Applications*, 64, 400–415.
- Soret, C. (1880). Influence de la temperature sur la distribution des sels dans leurs solutions. *Comptes-rendus de l'Académie des Sciences de Paris*, 91, 289–291.
- Tie-Gang, F., Ji, Z., Yong-Fang, Z., and Hua, T. (2011). Unsteady viscous flow over an expanding stretching cylinder. *Chinese Physics Letters*, 28(12), 124707.
- Trefethen, L.N. (2000). *Spectral Methods in MATLAB*. Society for Industrial and Applied Mathematics, Philadelphia USA.
- Tsai, R., and Huang, J.S. (2009). Heat and mass transfer for Soret and Dufour effects on Hiemenz flow through porous medium onto a stretching surface, *International journal of Heat and Mass Transfer*, 52, 2399–2406.
- Vajravelu, K., and Roper, T. (1999). Flow and heat transfer in a second grade fluid over a stretching sheet. *International Journal of Non-Linear Mechanics*, 34, 1031–1036.
- Vieru, D., Fetecau, C., and Fetecau, C. (2008). Flow of a viscoelastic fluid with the fractional Maxwell model between two side walls perpendicular to a plate. *Applied Mathematics and Computation*, 200(1), 459–464.
- Wenchang, T., and Mingyu, X. (2002). Plane surface suddenly set in motion in a viscoelastic fluid with fractional Maxwell model. *Acta Mechanica Sinica*, 18(4), 342–349.
- White, F.M. (2006). *Viscous fluid flow*. Third Edition Mc Graw-Hill, New York.
- Yoshimura, A., and Prud'homme, R.K. (1988). Wall slip corrections for Couette and parallel disk viscometers. *Journal of Rheology*, 32(1), 53–67.